



# WELBORE FRACTURE IMAGING USING INFLOW DETECTION MEASUREMENTS

Final Report  
March 2025



*Sandia National Laboratories is a multimission laboratory managed and operated by National Technology & Engineering Solutions of Sandia, LLC, a wholly owned subsidiary of Honeywell International Inc., for the U.S. Department of Energy's National Nuclear Security Administration under contract DE-NA0003525. SAND#2025-04688R*

# Final Report

**Organization:** University of Utah

**Recipient Organization:** Stanford University

**DUNS Number:** 009214214

**Recipient Address:** 367 Panama St  
Stanford, CA 94305-4007

**Award Number:** 3-2418

**Project Title:** Wellbore Fracture Imaging Using Inflow Detection Measurements

**Project Period:** 10/01/2021 – 03/31/2025

**Principal Investigator:** Roland Horne  
Director, Stanford Geothermal Program  
horne@stanford.edu  
650-723-9595

**Report Submitted by:** Roland N. Horne

**Date of Report Submission:** March 31, 2025

**Project Partners:** Stanford University, Sandia National Lab.

**Topic Leads:** Stuart Simmons, Utah FORGE  
Jon Payne, DOE-GTO  
Angel Nieto, DOE-GTO

# Table of Contents

<b>Chapter 1: Introduction</b> .....	<b>15</b>
1.1 Motivation.....	15
1.2 Project Goal .....	16
1.3 Technical Scope.....	16
1.4 Task Description.....	16
<b>Chapter 2: Tool Fabrication</b> .....	<b>18</b>
2.1 Chemical Sensor Development.....	18
2.1.1 Sensor Fabrication.....	19
2.1.2 Temperature and Pressure Rating for Utah FORGE Conditions.....	23
2.1.2.1 Round 1 Autoclave Testing.....	24
2.1.2.2 Round 2 Autoclave Testing.....	28
2.1.3 Brine Testing.....	31
2.2 Laboratory-scale Tool Development .....	32
2.3 Field-scale Tool Fabrication .....	35
2.3.1 Chemical Sensors and Housing for Field Deployment.....	35
2.3.2 High-Temperature Logging Tool.....	37
<b>Chapter 3: Analytical Formulations and Data-Driven Inference</b> .....	<b>41</b>
3.1 Analytical Formulations.....	41
3.2 Error Estimation and Modeling.....	43
3.3 Nernst Equation.....	45
3.4 Machine Learning (ML) Models for Flow Rate Prediction and Inference .....	46
3.4.1 ML models from numerical simulation data.....	46
3.4.1.1 Dataset Description and Processing.....	47
3.4.1.2 Classification Task to Predict Feed Zone Presence .....	49
3.4.1.3 Regression Task to Predict Feed Zone Inflow Rate.....	51
3.4.1.4 Inference to Determine Statistically Significant Covariates .....	53
3.4.2 ML models from laboratory experiment data .....	56

3.4.2.1	Dataset and Data Augmentation .....	57
3.4.2.2	Methods.....	58
3.4.2.3	Results.....	58
3.4.2.4	Further Analysis on Incorrect Location Prediction.....	66
3.4.2.5	Dual Feed Zone Results .....	68
3.4.2.6	Feature Engineering.....	68
<b>Chapter 4: Laboratory Experiments and Numerical Simulations .....</b>		<b>70</b>
4.1	Round 1 Experiments and Simulations.....	70
4.1.1	Round 1 Laboratory Experiments .....	71
4.1.1.1	Artificial Well Systems Setup.....	71
4.1.1.2	Tool Calibration .....	74
4.1.1.3	Static Laboratory Experiments.....	78
4.1.1.4	Dye Tracer Test.....	83
4.1.1.5	Dynamic Experiments.....	86
4.1.2	Round 1 Numerical Simulation.....	96
4.1.2.1	Simulation Setup.....	96
4.1.2.2	Results of Miniature Scale Simulations .....	98
4.1.2.3	Dye Tracer Test Comparison .....	99
4.1.2.4	Closed Wellhead Simulations .....	101
4.1.2.5	Varying Feed Zone Radius .....	102
4.1.2.6	Varying Log Extraction Position .....	103
4.1.2.7	Log Data at Varying Flow Rates.....	104
4.1.2.8	Effect of Tool Presence.....	105
4.1.2.9	Multiple Feed Zones .....	108
4.1.2.10	ANSYS vs. COMSOL simulations.....	111
4.2	Round 2 Experiments and Simulations.....	113
4.2.1	Round 2 Numerical Simulations.....	113
4.2.1.1	Simulations with Downhole Temperature and Pressure .....	113
4.2.1.2	Housing unit design .....	115
4.2.2	Round 2 Laboratory Experiments .....	122
4.2.2.1	Artificial Well System Modifications .....	122
4.2.2.2	Data Acquisition Modifications .....	127

4.2.2.3	Round 2 Tool Calibration .....	130
4.2.2.4	Round 2 Static and Dynamic Experiments Overview .....	132
4.2.2.5	Chloride Concentration Relative to Tool Positions and Tool Motions.....	140
4.2.2.6	Analysis of the Dynamic Experiment Results .....	152
4.2.2.7	Feed Zone Inflow Rate Sensitivity.....	154
4.2.2.8	Dynamic Experiments on Feed Zone Inflow Rate Sensitivity.....	156
4.2.2.9	Wellbore Flow Rate Sensitivity .....	160
4.2.2.10	Angular Sensitivity .....	165
4.2.2.11	Ion Sensitivity .....	169
<b>Chapter 5: Field Deployment .....</b>		<b>181</b>
5.1	Field Deployment Summary .....	181
5.2	FORGE Well 58-32 Deployment.....	182
5.3	Field Deployment at 16B(78)-32 .....	186
<b>Chapter 6: Post-Deployment Improvements .....</b>		<b>192</b>
6.1	Additional Ion Selective Electrode Studies .....	192
6.2	Scanning Electron Microscope (SEM) .....	196
6.3	Porosity .....	199
<b>Chapter 7: Conclusion and Future Work .....</b>		<b>200</b>
7.1	Conclusion .....	200
7.2	Future Work .....	203
<b>References .....</b>		<b>204</b>
<b>Appendix: Publication List .....</b>		<b>206</b>
	Contribution Authors and Abbreviations.....	206
	Publications.....	210

# Table of Figures

<b>Figure 2-1:</b> Photo of ISE pellets and single-layer AgCl reference pellets.....	20
<b>Figure 2-2:</b> Diagram of the experimental solid-state reference element assembly.....	20
<b>Figure 2-3:</b> Photo of the experimental solid-state multilayered reference pellet.....	21
<b>Figure 2-4:</b> Schematic drawing of the first sealing method.....	21
<b>Figure 2-5:</b> A cross-sectional diagram of the secondary sealing method.....	22
<b>Figure 2-6:</b> Photo of sealing methods 1 and 2.....	22
<b>Figure 2-7:</b> ISE and reference sensor assemblies before (top) and after (bottom) application of Gagekote.....	23
<b>Figure 2-8:</b> Sandia Autoclave and Controller.....	25
<b>Figure 2-9:</b> Multiple ISE and reference electrodes connected to the compression seal feedthrough.....	25
<b>Figure 2-10:</b> The full setup of the Sandia autoclave testing.....	26
<b>Figure 2-11:</b> Voltage vs. temperature at 0.005MCl/L concentration.....	26
<b>Figure 2-12:</b> (a) Testing conditions temperature and pressure vs. time; (b) ISE Voltage vs. time at 0.005 MCl/L concentration.....	27
<b>Figure 2-13:</b> ISE voltage response versus (a) temperature and (b) pressure at 0.005 MCl/L concentration.....	28
<b>Figure 2-14:</b> Upgraded Sandia HPHT autoclave.....	29
<b>Figure 2-15:</b> (a) Testing conditions temperature and pressure vs. time; (b) ISE Voltage vs. time at 0.25 MCl/L concentration.....	30
<b>Figure 2-16:</b> ISE voltage response versus (a) temperature and (b) pressure at 0.25 MCl/L concentration.....	30
<b>Figure 2-17:</b> Calibration of chloride sensors in KCl solution and samples from wells 16A and 16B.....	31
<b>Figure 2-18:</b> schematics of the chloride tool from Gao et al. (2017).....	32
<b>Figure 2-19:</b> Schematics of the updated lab-scale tool fabricated in 2023.....	33

<b>Figure 2-20:</b> Side view (left) and bottom view (right) of the updated lab-scale tool fabricated in 2023. The bottom view shows the sensors' interface. ....	33
<b>Figure 2-21:</b> (left) Side view and (right) bottom view of the lab-scale tool with housing. showing the locations of the (1) reference electrode, (2) ISE probe #2, and (3) ISE probe #3.....	34
<b>Figure 2-22:</b> The (a) SolidWorks® model and (b) printed simulation up-tool component.....	34
<b>Figure 2-23:</b> The (a) SolidWorks® model and (b) printed simulation down-tool component.....	35
<b>Figure 2-24:</b> Field-deployable chloride tool schematics, including an existing PTS tool adapted to the chloride-based wireline tool and high-temperature developed by Sandia National Laboratory.....	35
<b>Figure 2-25:</b> Fabricated sensor housing populated with installed sensors and bulkhead fitting.....	36
<b>Figure 2-26:</b> Sandia's custom high-temperature logging tool with Honeywell's microcontroller and Sandia's custom Application-specific Integrated Circuit or ASIC (left) next to Mitco's PTS module (right). ....	37
<b>Figure 2-27:</b> High-temperature Chemical Buffer Amplifier (CBA) for accommodating additional signal inputs. ....	38
<b>Figure 2-28:</b> Alternative off-the-shelf system microcontroller - EV-HT-200CDAQ1 from Analog Devices.....	39
<b>Figure 2-29:</b> Primary High-Temperature Logging Tools being tested to confirm operation in benchtop test. ....	40
Figure 2-30: LabView User Interface for Field-Scale Chloride Tool.....	40
<b>Figure 3-1:</b> Schematics of a geothermal well with (a) single feed zones and (b) multiple feed zones. ....	42
<b>Figure 3-2:</b> Snapshots of $e$ distribution and resulting volumetric flow rate calculation for a well with single feed zone with (a) rectangular and (b) normal distribution methods. ....	45
<b>Figure 3-3:</b> The simulation result of resulting volumetric flow rate calculations for the different ranges of $e$ : (a) $\pm 1.5\%$ , (b) $\pm 3\%$ , and (c) $\pm 5\%$ . ....	45
<b>Figure 3-4:</b> a) boundary conditions setup and b) example of one of the simulation results. ....	47
<b>Figure 3-5:</b> Snapshot of the dataset after cleanup.....	48
<b>Figure 3-6:</b> Snapshot of the dataset after removing irrelevant columns. ....	48
<b>Figure 3-7:</b> Comparison of different models for the classification task using the Receiver Operating Characteristics (ROC) plot.....	50
<b>Figure 3-8:</b> Receiver Operating Characteristics (ROC) curve for the classification task, fitted using Random Forest classifier on the training and test set.....	51
<b>Figure 3-9:</b> Comparison of different models for the regression task applied to the training set using a plot of predicted versus actual $m\_fz\_abs$ value. ....	52
<b>Figure 3-10:</b> predicted vs. actual plot for the regression task, fitted using the Random Forest model on the (left) training and (right) test set. ....	53

<b>Figure 3-11:</b> Comparison of regression output in the training vs test set. Green boxes indicate significant coefficients that are also found in the test set, while yellow boxes are significant coefficients only found in the training set. The red circle marks the $x_{c1}$ covariate, which is an important covariate in the model. ....	54
<b>Figure 3-12:</b> Comparison of 95% confidence interval obtained via standard error vs bootstrap, applied to the test set. ....	55
<b>Figure 3-13:</b> Significant coefficients on the two-way interaction model with P-value less than 0.001 (three-starred), applied to training and test set. ....	56
<b>Figure 3-14:</b> (left) data augmentation example and (right) dataset snapshot. ....	57
<b>Figure 3-15:</b> Linear regression (left) and logistic regression (right) training and validation set results. ....	59
<b>Figure 3-16:</b> Neural network model accuracy and loss over epochs. ....	59
<b>Figure 3-17:</b> Neural network model accuracy and loss of drop-out rate variation. ....	60
<b>Figure 3-18:</b> Neural network linear regression (left) and neural network classification (right) training and validation set results. ....	61
<b>Figure 3-19:</b> Cross-validation heat map example. ....	61
<b>Figure 3-20:</b> Random Forest regressor (left) and classifier (right) training and validation set results. ....	62
<b>Figure 3-21:</b> XGBoost regressor (left) and classifier (right) training and validation set results. ....	62
<b>Figure 3-22:</b> LGBM regressor (left) and LGBM classifier (right) training and validation set results. ....	63
<b>Figure 3-23:</b> Prediction of LGBM regressor model on the test set. ....	63
<b>Figure 3-24:</b> Test set confusion matrix of random forest classifier. ....	65
<b>Figure 3-25:</b> Test set confusion matrix of LGBM classifier. ....	66
<b>Figure 3-26:</b> Examples of inaccurate prediction from LGBM classifier. ....	67
<b>Figure 3-27:</b> LGBM classifier accuracy vs allowed error range. ....	67
<b>Figure 3-28:</b> Prediction of LGBM classifier on dual feed zone measurement data. ....	68
<b>Figure 3-29:</b> Prediction of LGBM classifier on the test set post feature engineering. ....	69
<b>Figure 4-1:</b> Artificial well system for Round 1 laboratory experiments. ....	71
<b>Figure 4-2:</b> Artificial well system flow loop schematic modified from Kumar (1995). ....	72
<b>Figure 4-3:</b> Injection pump and flowmeter. ....	73
<b>Figure 4-4:</b> Additional reservoir tank (top) and plumbing in the original reservoir tank (bottom). ....	74
<b>Figure 4-5:</b> Tool calibration container: 400 ml (left), 20 L (center), and 100 L(right). ....	75
<b>Figure 4-6:</b> Multimeter (left) and DAQ device (right) to downhole tool connection. ....	76

<b>Figure 4-7:</b> In-house LabVIEW Interface measurement example.....	76
<b>Figure 4-8:</b> Voltage evolution over time during DAQ calibration.....	77
<b>Figure 4-9:</b> Delta voltage evolution over time during DAQ calibration.....	77
<b>Figure 4-10:</b> Tool calibration result. The “Original Tool” and the “New Tool” refers to the tubular tool version 1 and 2, respectively. ....	78
<b>Figure 4-11:</b> Wellbore and reservoir tank voltage readings (top), and concentration actual vs. calculated concentration from voltage (bottom). ....	79
<b>Figure 4-12:</b> One feed zone injection artificial well system assembly. ....	80
<b>Figure 4-13:</b> Injection concentration sensitivity voltage measurement (top) and the calculated chloride concentration result (bottom). ....	81
<b>Figure 4-14:</b> Static measurement assembly (a) Position 1 and (b) Position 2. ....	82
<b>Figure 4-15:</b> Tool placement sensitivity voltage measurement. ....	83
<b>Figure 4-16:</b> Tool position compared to dye injection experiment over time (a) 0.5 second, (b) 1 second, (c) 1.5 seconds, (d) 3 seconds, (e) 3.5 seconds, (f) 4 seconds, (g) 5 seconds, (h) 55 seconds. ....	84
<b>Figure 4-17:</b> Dye tracer test cross-sectional view over time (a) 0 seconds, (b) 0.5 seconds, (c) 1 second, (d) 1.5 seconds, (e) 2 seconds, (f) 2.5 seconds. ....	85
<b>Figure 4-18:</b> Dye injection tracer test (left) 20 ml/s, (center) 50 ml/s, (right) 70 ml/s. ....	86
<b>Figure 4-19:</b> Stepper motor, wire, and rod configuration at the top of wellbore. ....	87
<b>Figure 4-20:</b> Stepper motor driver. ....	87
<b>Figure 4-21:</b> Python CSV data postprocessing visualization.....	88
<b>Figure 4-22:</b> Dynamic measurement tool position cross-section (left) opposite the injection port and (right) centralized. ....	88
<b>Figure 4-23:</b> In-house centralizer, side view (left) and bottom view (right).....	89
<b>Figure 4-24:</b> Dynamic measurement result at the opposite wall from the feed zone port. ....	90
<b>Figure 4-25:</b> Dynamic measurement result at the center of the wellbore. ....	90
<b>Figure 4-26:</b> Dynamic measurement injection flow rate variation. ....	93
<b>Figure 4-27:</b> Dynamic measurement multiple feed zone injection 1. ....	95
<b>Figure 4-28:</b> Dynamic measurement multiple feed zone injection 2. ....	95
<b>Figure 4-29:</b> The geometry setup, boundary conditions, and meshing cross-section of Model S1 (single feed zone), miniature scale.....	97
<b>Figure 4-30:</b> The geometry, boundary conditions, and meshing cross-section of Model S1 (single feed zone), laboratory scale. The laboratory scale mimicked the dimensions of the well system at the Stanford Geothermal Laboratory. Certain aspects of the geometry, such as feed zone radius, would be tweaked as part of the modeling scenarios.....	97

<b>Figure 4-31:</b> Simulation results of S1-Mini1 and S1-Mini2, with the latter case showing blind spot formation away from the inlet. ....	99
<b>Figure 4-32:</b> Comparison between laboratory dye tracer test and the undisturbed state cases at different feed zone inflow rates, shown as pathlines and volume fraction graphics horizontal cross-section along with pathlines vertical cross-section at the inlet location. ....	100
<b>Figure 4-33:</b> Lab experiment results recorded from the top of the well compared with horizontal sections of the undisturbed state base case at different height (z-value) offsets. The contours show the volume fraction of the inflow fluid, which is a NaCl solution of 0.05 mol/L concentration. ....	101
<b>Figure 4-34:</b> Simulation results of flowing (open wellhead) vs. non-flowing wells (closed wellhead). The wellbore flow rate is denoted in kg/s at the top of the graphics, while the feed zone inflow rate is denoted in ml/s at the bottom. ....	102
<b>Figure 4-35:</b> Simulation results in laboratory scale with different feed zone radii. ....	103
<b>Figure 4-36:</b> Comparison of the undisturbed state cases and the chloride concentration change along the wellbore height. The chloride concentration at the feed zone inflow was 0.5 M. ....	104
<b>Figure 4-37:</b> Comparison of the undisturbed state case and the Cl concentration change along the wellbore height at different feed zone flow rates. The results were extracted from the wall-line-4 position across the feed zone inlet. The left image shows the base case inlet flow rate (112.2 ml/s) and higher, while the right image shows the base case flow rate and lower. ....	105
<b>Figure 4-38:</b> Schematics and description for the disturbed state case group (S1-L7). ....	106
<b>Figure 4-39:</b> Comparison of the disturbed state case group, vertical section. The contours show the volume fraction of the inflow fluid, which is a NaCl solution of 0.5 mol/L concentration. ....	107
<b>Figure 4-40:</b> The horizontal section at the feed zone depth of the disturbed state cases compared with the undisturbed state base case. Reference to tool position naming is shown in the top left. The contours show the volume fraction of the inflow fluid, which is a NaCl solution of 0.5 mol/L concentration. ....	108
<b>Figure 4-41:</b> Dye tracer experiments in (a) undisturbed and (b) disturbed states. ....	108
<b>Figure 4-42:</b> scenarios 156 (top) and 158 (bottom) showing the volume fraction vertical cross-section, simulated chloride concentration log data extracted from the center (midline) position, and the corresponding laboratory measurement results. ....	110
<b>Figure 4-43:</b> scenarios 163 (top) and 164 (bottom) showing the volume fraction vertical cross-section, simulated chloride concentration log data extracted from the center (midline) position, and the corresponding laboratory measurement results. ....	110
<b>Figure 4-44:</b> I initial lab-scale modeling results with three different Multiphysics applied. The following boundary conditions were put in: The mass rate at wellbore = 2.09 kg/s; Mass rate at feed zone is 0.1155 kg/s; Concentration at feed zone is 500 mol/m <sup>3</sup> . ....	111
<b>Figure 4-45:</b> modified and iterated lab-scale modeling to mimic phenomena and characteristics observed in the lab experiments. The following boundary conditions were put in: The mass rate at wellbore = 2.09 kg/s; Concentration at FZ = 500 mol/m <sup>3</sup> . ....	112
<b>Figure 4-46:</b> modeling results of the 2-feed zone case in COMSOL. Comparison with previously modeled ANSYS Fluent and dynamic laboratory tests was shown. ....	113

<b>Figure 4-47:</b> Comparison of the laboratory base cases of the undisturbed (a and b) and disturbed (c and d) states at laboratory ambient temperature versus at Utah FORGE downhole pressure and temperature. ....	114
<b>Figure 4-48:</b> Iterations of the housing unit. Version 3 is the final design that was produced for the wireline tool assembly and the updated laboratory prototype. ....	115
<b>Figure 4-49:</b> A summary of fluid flow simulations to evaluate the effectiveness of the field tool designs. Version 3 shows the reliable distribution of chloride concentration all around the sensors, even when the pillar obstructs the inflow.....	115
<b>Figure 4-50:</b> variations of the chloride tool housing unit designs for Version 1. ....	116
<b>Figure 4-51:</b> resulting simulations for Version-1 Modified-1 housing unit design at different tool placements.....	117
<b>Figure 4-52:</b> Original Version 2 housing design (left) and the simplified dimension for numerical simulation purposes (right). ....	118
<b>Figure 4-53:</b> Simulation results of the unobstructed flow case of housing design version 2; (a, b, c) represent the progression of the tool housing penetrating through the wellbore at a certain offset of the feed zone height. The upper graphics show the vertical cross-section, while the lower graphics show the horizontal cross-section at feed zone height. ....	119
<b>Figure 4-54:</b> Simulation results of the free-flow case of the housing design version 2; (a, b, c) represent the progression of the tool housing penetrating through the wellbore at a certain offset of the feed zone height. The upper graphics show the vertical cross-section, while the lower graphics show the horizontal cross-section at feed zone height. ....	119
<b>Figure 4-55:</b> Simplified housing and tool dimension in preparation for numerical simulation cases for tool housing version 3.....	120
<b>Figure 4-56:</b> Five positions of the tool housing relative to the feed zone height labeled from a to e. Positions are chosen to represent the Ream in Hole (RIH) motion of the chloride tool. The number in cm shows the feed zone height offset relative to the center of the housing. Two case groups are simulated: the free-flowing case group (left), where the feed zone inflow faces the opening; and the obstructed case group (right), where the feed zone inflow faces one of the pillars.....	121
<b>Figure 4-57:</b> Modeling results are shown as vertical cross sections; the case group at the top represents the free-flow case, and the case group at the bottom represents the obstructed-flow case.....	122
<b>Figure 4-58:</b> Modeling results are shown as horizontal cross sections at the sensor height, indicated by the orange line; the case group at the top represents the free-flow case, and the case group at the bottom represents the obstructed-flow case.....	122
<b>Figure 4-59:</b> Schematic of the Artificial Well System in the Stanford Geothermal Laboratory. ....	123
<b>Figure 4-60:</b> Labeled image of the Artificial Well System in the Stanford Geothermal Laboratory. ....	124
<b>Figure 4-61:</b> Updated (a) fluid inflow system, (b) Outflow Reservoir, and (c) feed zone injection line for the artificial well system.....	125

<b>Figure 4-62:</b> Updated routing of the shielded electrical cable for the artificial wellbore. ....	126
<b>Figure 4-63:</b> Faraday mesh applied to the power supply transformers of the submersible pumps in the Stanford Geothermal Laboratory .....	127
<b>Figure 4-64:</b> Configuration of the Data Acquisition Device (DAQ).....	128
<b>Figure 4-65:</b> LabVIEW program block front panel and diagram that records voltage outputs from two chloride ISE probes.....	129
<b>Figure 4-66:</b> Experimental configuration for the calibration process .....	130
<b>Figure 4-67:</b> Voltage time series for (a) ISE probe #2 and (b) ISE probe #3 for various chloride concentrations during the calibration process.....	131
<b>Figure 4-68:</b> Linear regression of data points from the calibration process for (a) ISE probe #2 and (b) ISE probe #3 .....	131
<b>Figure 4-69:</b> Position of the chloride tool in reference to the feed zone port for the (a) above, (b) even, and (c) below vertical position .....	134
<b>Figure 4-70:</b> Two instances of varying long-term behavior of ISE probe #2 and ISE probe #3 when submerged in still freshwater in the artificial well. ....	135
<b>Figure 4-71:</b> Voltage time series of dynamic experiments plotted consecutively (a) without and (b) with cleaning the ISE probes between trials. ....	138
<b>Figure 4-72:</b> Concurrent voltage and molarity time series of (a and b) ISE probe #2 and (c and d) ISE probe #3 for a series of dynamic experiments. ....	139
<b>Figure 4-73:</b> Flow dynamics surrounding the chloride tool in the (a) above, (b) even, and (c) below vertical position during feed zone inflow.....	140
<b>Figure 4-74:</b> Voltage time series for ISE probe #2 in the above, even, and below positions for feed zone fluid chloride concentrations of (a, d, and g) $1 \times 10^{-2}$ mol/L, (b, e, and h) $5 \times 10^{-2}$ mol/L, and (c, f, and i) $1 \times 10^{-1}$ mol/L. ....	141
<b>Figure 4-75:</b> Voltage time series for ISE probe #3 in the above, even, and below positions for feed zone fluid chloride concentrations of (a, d, and g) $1 \times 10^{-2}$ mol/L, (b, e, and h) $5 \times 10^{-2}$ mol/L, and (c, f, and i) $1 \times 10^{-1}$ mol/L. ....	142
<b>Figure 4-76:</b> Molarity time series for ISE probe #2 in the above, even, and below positions for feed zone fluid chloride concentrations of (a, d, and g) $1 \times 10^{-2}$ mol/L, (b, e, and h) $5 \times 10^{-2}$ mol/L, and (c, f, and i) $1 \times 10^{-1}$ mol/L .....	143
<b>Figure 4-77:</b> Molarity time series for ISE probe #3 in the above, even, and below positions for feed zone fluid chloride concentrations of (a, d, and g) $1 \times 10^{-2}$ mol/L, (b, e, and h) $5 \times 10^{-2}$ mol/L, and (c, f, and i) $1 \times 10^{-1}$ mol/L .....	144
<b>Figure 4-78:</b> Voltage vs. Depth for ISE probe #2 in the RIH and POOH directions for feed zone fluids with chloride concentrations of (a and b) $1 \times 10^{-1}$ mol/L, (c and d) $5 \times 10^{-2}$ mol/L, and (e and f) $1 \times 10^{-2}$ mol/L.....	146
<b>Figure 4-79:</b> Voltage vs. Depth for ISE probe #3 in the RIH and POOH directions for feed zone fluids with chloride concentrations of (a and b) $1 \times 10^{-1}$ mol/L, (c and d) $5 \times 10^{-2}$ mol/L, and (e and f) $1 \times 10^{-2}$ mol/L.....	147

<b>Figure 4-80:</b> Molarity vs. Depth for ISE probe #2 in the RIH and POOH directions for feed zone fluids with chloride concentrations of (a and b) $1 \times 10^{-1}$ mol/L, (c and d) $5 \times 10^{-2}$ mol/L, and (e and f) $1 \times 10^{-2}$ mol/L.....	148
<b>Figure 4-81:</b> Molarity vs. Depth for ISE probe #3 in the RIH and POOH directions for feed zone fluids with chloride concentrations of (a and b) $1 \times 10^{-1}$ mol/L, (c and d) $5 \times 10^{-2}$ mol/L, and (e and f) $1 \times 10^{-2}$ mol/L.....	149
<b>Figure 4-82:</b> Flow dynamics in the wellbore at high (0.115 kg/s), medium (0.100 kg/s), and low (0.082 kg/s) feed zone flow rates after (a, f, and k) 2 seconds, (b, g, and l) 5 seconds, (c, h, and m) 15 seconds, (d, i, and n) 30 seconds, and (e, j, and o) 60 seconds. ....	155
<b>Figure 4-83:</b> (a) Voltage and (b) molarity time series of ISE probe #2 at high (0.115 kg/s), medium (0.100 kg/s), and low (0.082 kg/s) feed zone flow rates.....	155
<b>Figure 4-84:</b> Molarity vs. Depth for ISE probe #2 and ISE probe #3 in the RIH direction with feed zone inflow rates of (a and b) 0.115 kg/s, (c and d) 0.100 kg/s, and (e and f) 0.082 kg/s.....	158
<b>Figure 4-85:</b> Molarity vs. Depth for ISE probe #2 and ISE probe #3 in the POOH direction with feed zone inflow rates of (a and b) 0.115 kg/s, (c and d) 0.100 kg/s, and (e and f) 0.082 kg/s. ....	159
<b>Figure 4-86:</b> Concurrent voltage time series of ISE probe #2 and ISE probe #3 with wellbore flow rates of (a) 0.753 kg/s, (b) 0.880 kg/s, and (c) 0.992 kg/s. ....	161
<b>Figure 4-87:</b> Molarity vs. Depth for ISE probe #2 and ISE probe #3 in the RIH direction with wellbore flow rates of (a and b) 0.753 kg/s, (c and d) 0.880 kg/s, and (e and f) 0.992 kg/s. ....	162
<b>Figure 4-88:</b> Molarity vs. Depth for ISE probe #2 and ISE probe #3 in the POOH direction with wellbore flow rates of (a and b) 0.753 kg/s, (c and d) 0.880 kg/s, and (e and f) 0.992 kg/s.....	163
<b>Figure 4-89:</b> Chloride Sensor Housing with the labeled pillars and spaces. The varying directions of the feed zone jet tested for the angular sensitivity are denoted as arrows. ....	165
<b>Figure 4-90:</b> Molarity vs. Depth for ISE probe #2 and ISE probe #3 in the RIH motion for angular rotations of (a and b) $0^\circ$ , (c and d) $90^\circ$ , (e and f) $180^\circ$ , and (g and h) $270^\circ$ . ....	167
<b>Figure 4-91:</b> Molarity vs. Depth for ISE probe #2 and ISE probe #3 in the POOH motion for angular rotations of (a and b) $0^\circ$ , (c and d) $90^\circ$ , (e and f) $180^\circ$ , and (g and h) $270^\circ$ . ....	168
<b>Figure 4-92:</b> Voltage time series for ISE probe #2 and ISE probe #3 for feed zone fluid containing $1 \times 10^{-2}$ mol/L concentrations of (a and b) bromide, (c and d) chloride, and (e and f) both bromide and chloride. ....	171
<b>Figure 4-93:</b> Molarity time series for ISE probe #2 and ISE probe #3 for feed zone fluid containing $1 \times 10^{-2}$ mol/L concentrations of (a and b) bromide, (c and d) chloride, and (e and f) both bromide and chloride. ....	172
<b>Figure 4-94:</b> Molarity vs. Depth for ISE probe #2 and ISE probe #3 in the (a and c) RIH and (b and d) POOH directions for a feed zone fluid with $1 \times 10^{-2}$ mol/L concentrations of bromide and chloride.....	173
<b>Figure 4-95:</b> Voltage time series for ISE probe #2 and ISE probe #3 for feed zone fluid containing $1 \times 10^{-2}$ mol/L concentrations of (a and b) sulfate, (c and d) sulfate and chloride, and (e and f) sulfate, chloride, and bromide.....	176

<b>Figure 4-96:</b> Molarity time series for ISE probes #2 and ISE probe #3 for feed zone fluid containing $1 \times 10^{-2}$ mol/L concentrations of (a and d) sulfate, (b and e) sulfate and chloride, and (c and f) sulfate, chloride, and bromide. ....	177
<b>Figure 4-97:</b> Molarity vs. Depth for ISE probe #2 and ISE probe #3 in the (a and c) RIH and (b and d) POOH directions for a feed zone fluid with $1 \times 10^{-2}$ mol/L concentrations of sulfate and chloride. ....	178
<b>Figure 5-1:</b> Utah FORGE site with planned deployment wells circled (left) and geological and heat model of the Utah FORGE site (right). Source: Utah FORGE. ....	181
<b>Figure 5-2:</b> Field-deployable chloride tool schematics, including an existing PTS tool adapted to the chloride-based wireline tool and high-temperature developed by Sandia National Laboratory. ....	182
<b>Figure 5-3:</b> Illustration of tool deployment plan at well 58-32. ....	183
<b>Figure 5-4:</b> (a) the chemical sensor and housing as part of the wireline tool assembly, and (b) the assembly ready to trip in. ....	183
<b>Figure 5-5:</b> logging results during Run in Hole (RIH) at well 58-32. ....	184
<b>Figure 5-6:</b> logging results during Pull Out of Hole (POOH) at well 58-32. ....	185
<b>Figure 5-7:</b> converted molarity from the chemical sensor 1 voltage data during RIH and POOH using Tool 2 calibration curve (blue line on the right chart). ....	186
<b>Figure 5-8:</b> Illustration of tool deployment plan for Utah FORGE Well 16B(78)-32. Perforation stages are shown in highlighted zones, and planned test locations are shown as red stars. ....	187
<b>Figure 5-9:</b> Full chemical tool assembly attached to weight bars and being loaded into lubricators. ....	188
<b>Figure 5-10:</b> Utah FORGE Well 16B test site with lubricator stacks for chemical tool. ....	188
<b>Figure 5-11:</b> well logs from Run in Hole (RIH) run at 16B zonal depths. ....	189
<b>Figure 5-12:</b> well logs from Pull out of Hole (POOH) run at 16B zonal depths. ....	190
<b>Figure 5-13:</b> calibration curve for the chloride sensors used for 16B logging. ....	190
<b>Figure 5-14:</b> Comparison of POOH chloride signal and PLT interpretation performed by SLB on 28 Aug 2024 (around one week later). ....	191
<b>Figure 6-1:</b> Benchtop test setup for ion selective electrode and reference electrode pair. ....	193
<b>Figure 6-2:</b> Calibration test of Platinum-Iridium (Pt-Ir) reference electrode and AgCl/Ag <sub>2</sub> S sensor variations (25:75, 50:50, and 75:25 AgCl:Ag <sub>2</sub> S) in three molar solutions of KCl at ambient temperature. ....	193
<b>Figure 6-3:</b> Calibration test of Platinum-Iridium (Pt-Ir) reference electrode and AgCl/Ag <sub>2</sub> S sensor variations (25:75, 50:50, and 75:25 AgCl:Ag <sub>2</sub> S) in three molar solutions of KCl at elevated temperature (80°C). ....	194
<b>Figure 6-4:</b> Calibration test of Silver Chloride (AgCl) reference electrode and AgCl/Ag <sub>2</sub> S sensor variations (25:75, 50:50, and 75:25 AgCl:Ag <sub>2</sub> S) in three molar solutions of KCl at elevated temperature (85°C). ....	195

**Figure 6-5:** SEM images of three pellet samples obtained under 30 kV beam voltage..... 197

**Figure 6-6:** Comparison of the EDX elemental mapping of chlorine and sulfur atoms in the three pellets..... 198

# Chapter 1

## Introduction

### 1.1 Motivation

One of the most striking measurements taken during DOE's EGS Collab project at the 4850-foot depth location was the so-called 'sewer cam', which enabled direct visualization of the flow of water into the production well through fractures during the stimulation. The ability to see directly which fractures were flowing and (roughly) how much was a breakthrough in understanding the topology of the created fracture network. Achieving this kind of fracture flow imaging at FORGE would be more challenging because of the 225°C temperature, but equally or even more valuable if it could be achieved.

In 2017, a joint project between Sandia and Stanford developed a downhole tool concept to measure the enthalpy of multiphase fluid entering a geothermal well from individual fractures (Gao et al., 2017). For the FORGE project, measuring enthalpy is of less interest because the fluid is expected to be single-phase liquid water. However, the foundation of the device was the measurement of chloride ion concentration, which could form the basis for a direct measurement of inflow from fractures. During the 2017 project, this novel chloride sensing system was implemented into a laboratory test instrument, and we confirmed the capability of the system to measure the ion concentration of fluid entering a model wellbore through a small entry port. The wellbore was a 6-inch diameter model well, and the port was approximately 0.08 inch (2mm) in diameter. The device could measure the chloride concentration accurately even when the well was flowing in a bubbly flow.

Given its accuracy, the tool should be able to identify locations of water entering the wellbore even if the ion concentration differs only slightly from that of the water in the well. It is likely that different fractures may flow slightly different chloride concentrations, which would make it feasible to detect individual fractures as well as to estimate the volume of their flow.

Ultimately, we could also recognize different fractures flowing back significantly different ion concentrations after fracturing in the FORGE wells. This could be realized by adding different ions in the fracturing fluids in different fractures created at different stages of stimulation (and modifying the tool to include different ion specificity).

Sandia's tool was shown during the study to have the capability to withstand the 225°C temperature, and the electrochemical sensing elements were tested in the laboratory to 225°C at 1500 psia for 24 hours. An early implementation of the fully integrated downhole electrochemical tool, including high-temperature electronics, robust housing, and wireline truck interface, had previously been constructed and tested successfully at Sandia; thus, hardware development tasks focused on advancing the technology readiness level (TRL) of this promising technology for FORGE deployment, rather than on developing a new scientific basis for its operation. The data collection electronics in this tool allowed for several other sensors (pressure, temperature, flow spinner) to be implemented in parallel

as well. The research was a new collaboration between Stanford and Sandia to modify and refine the tool for FORGE deployment, to make the downhole measurements, and to characterize the evolving fractures.

## 1.2 Project Goal

The goal of this research was to make measurements in the FORGE wells to map flowing fractures and estimate their flow magnitudes in real-time. Implementation of the project had two substantial goals:

- (1) The ability to locate flowing fractures at FORGE and estimate their flow rates, thereby providing valuable information regarding the FORGE stimulations specifically.
- (2) The demonstration and refinement of a new tool that can achieve an important (and currently missing) measurement in this and future EGS projects.

## 1.3 Technical Scope

- **Phase 1:** The existing Sandia downhole tool was modified and rebuilt for the planned FORGE deployment. The tool underwent stress testing under simulated FORGE conditions to confirm its robustness to expected temperature, pressure, and fluid chemical composition. The analysis methodology was developed to use the tool for flow rate estimation and was analyzed for suitability under the fracture conditions inferred for FORGE by earlier analyses.
- **Phase 2:** The tool was tested at FORGE to investigate the ability to characterize fractures produced during (previous) stimulation efforts. Multiple tests were conducted to test the ability to monitor the fracture network during flow.
- **Phase 3:** Following FORGE deployment, the effectiveness of the tool and interpretation methodology was analyzed in terms of accuracy, response time, resolution, and practical deployment experience. Refinement of the tool elements were investigated, for example, the possible addition of other ion probes, simplified deployment, and increasing robustness to field conditions.

## 1.4 Task Description

### Task 1.1: Phase 1 Tool Configuration and Testing (Sandia)

The electrochemical sensing elements and related high-temperature signal conditioning electronics were implemented in 2017 as add-ons to a previously developed (2002) Sandia downhole tool. This tool has proven reliable but there were several upgrades and part replacements made to ensure success at FORGE in 2021 and beyond. The tool was disassembled and restored. The electronics were fully evaluated for nominal operation and replaced if needed. The supplementary sensors (pressure, temperature, flow spinner) were evaluated and replaced. Additionally, the novel nature of the electrochemical sensing probes means there had never been a long-term shelf-life assessment of their performance. The probes were reconstructed for this project and tested in the laboratory at high temperature and high pressure. Higher temperature-capable probes were also constructed. Each subsystem of the tool was evaluated in environments representative of the planned FORGE deployment.

### Task 1.2: Phase 1 Analysis Method Development (Stanford)

The existing analysis procedures were developed to use chloride measurements for enthalpy estimation (Gao et al., 2017). In the FORGE environment, the goal was the estimation of the presence and magnitude of inflows from specific fractures or zones and the expected fluid flow is single-phase water. The analysis procedures were rederived for the single-phase water case and investigated in terms of the requirements for the physical running of the tool (for example, the proximity of the device to the inflow point and the frequency of the measurements) as well as a preliminary analysis of the accuracy of the inference. Prior to the field tests, experiments with the actual tool elements (the ion-specific probes, as well as a 3D-printed plastic rendition of the whole tool) were conducted in the model test well at Stanford's laboratory. Numerical simulations were conducted to investigate the likely flow configuration around the tool and in the vicinity of the fracture outlets.

### Task 2.1: Phase 2 Tool Deployment at FORGE (Sandia)

The tool was designed for operation with the Sandia-owned wireline truck. The tool was completely integrated with the Sandia truck and tested prior to bringing it to the FORGE site. The downhole tool and all necessary tools for deployment and possible field reconfiguration were loaded in the wireline truck. Sandia personnel drove the truck to the FORGE site and met Stanford personnel on site. The tool was attached and checked for operation and deployment readiness. The truck was positioned near the surface of the borehole, and the sheave system was deployed. The tool was positioned over the center of the hole, and the depth counter zeroed. Data were logged with respect to time and depth throughout the deployment down and back up the borehole. Two deployments were made, one in FORGE well 58-32 and a second one in well 16B.

### Task 2.2: Phase 2 Interpretation of Data Collected at FORGE (Stanford)

Analysis of the data collected during tool deployment at FORGE was used to evaluate the accuracy of the characterization of the fractures. Comparisons were made for consistency with simultaneous PTS measurement techniques, as the Sandia tool itself has the functionality to also log the temperature, pressure and spinner rates.

### Task 3.1: Phase 3 Tool Refinement (Sandia)

Even with as-designed performance in the first deployment, results from the first deployment were used to inform design and procedure reconfigurations for the second deployment. Revisions to the instrumentation package were implemented to achieve a more robust serial communication protocol. The updated tool was tested and deployed as in the first deployment, except that a lubricator system was used because the second test was run while the well was flowing.

### Task 3.2: Phase 3 Interpretation Method Refinement (Stanford)

In concert with the refinement of the tool design, a quantitative analysis of the accuracy improvement was conducted for all candidate modifications. Direct interpretation of data from the deployment of a refined tool was compared to the original Phase 2 results.

# Chapter 2

## Tool Fabrication

This chapter describes the tool fabrication led by Sandia National Laboratory to build and iterate on the lab-scale and field-scale versions of the chemical tool which contain ruggedized chloride ion-selective electrodes (ISE) and a high-temperature logging tool for real-time estimation of the presence and magnitude of inflows from specific fractures or zones and the expected fluid flow in single-phase water. Additional testing post-deployment was conducted on the sensors, which are detailed in Chapter 6. The additional testing includes evaluating the ISE and reference electrode for alternate iterations of the electrode pair, including variations in the ratio of constituent materials of the sensing electrode and alternative reference electrodes, such as a multilayer solid-state sensor pellet and a platinum rod.

### 2.1 Chemical Sensor Development

Ion selective electrodes (ISEs) are specialized electrochemical sensors designed to selectively measure the concentration of specific ions in a solution. They operate by developing a potential difference across a membrane that selectively allows specific ions to pass while blocking other ions. Among these, chloride ion selective electrodes (Cl-ISEs) are analytical devices engineered to measure the concentration of chloride ions in a solution based on ion-selective measurement principles, which relates the measured voltage to the concentration of ions. Chloride was chosen to target as it is commonly found in geothermal systems due to their solubility and mobility in water, making them a significant component of geothermal fluids. The presence of chloride in geothermal systems often originates from the dissolution of minerals in the surrounding rock formations, as well as from the interaction of geothermal fluids with saline groundwater. This potential difference is described by the Nernst equation (Equation 2-1):

$$E = E^0 + \frac{RT}{nF} \ln \left( \frac{[Cl^-]_{sample}}{[Cl^-]_{ref}} \right) \quad (2-1)$$

where  $E$  is the measured potential,  $E^0$  is the standard electrode potential,  $R$  is the universal gas constant,  $T$  is the temperature in Kelvin,  $n$  is the charge of the ion (for  $Cl^-$ ,  $n=1$ ),  $F$  is Faraday's constant,  $[Cl^-]_{sample}$  is the concentration of chloride ions in the sample,  $[Cl^-]_{ref}$  and is the concentration of chloride ions in the reference solution.

Common components of Chloride-ISEs include a sensing membrane, often made from silver chloride (AgCl) or polymeric materials, a reference electrode (typically Ag/AgCl), an internal solution with a known chloride concentration, and an inert body for interfacing with measurement devices. Silver/Silver sulfide ( $Ag_2S$ ) can also be added to the sensing membrane to enhance selectivity, create composite membranes for improved electrochemical properties, participate in redox reactions, increase

sensitivity to low chloride concentrations, and contribute to the stability and longevity of the electrode. The use of Ag<sub>2</sub>S/AgCl as a chloride ion selective material has been demonstrated by Nyachhyon et. al. (2012).

### 2.1.1 Sensor Fabrication

The chloride ion selective electrode used in this study consisted of an equal by mass mixture of AgCl and Ag<sub>2</sub>S powders pressed into cylindrical pellets. The powders were milled by hand in a mortar and pestle and 0.45 g of powder was weighed and transferred to a ¼” diameter die press. The material was then compressed using a Dake 10,000 psi manual hydraulic press outfitted with an Interface Model LBM-20K Force Transducer, to 4000 lbs and held at constant pressure for 15 minutes. The pellets were transferred to a preheated oven at 200°C to sinter the pellet for one hour. The sintered pellet was allowed to cool and stored in a vacuum protected from light until ready for assembly. The ISE pellet after sintering is shown in Figure 2-1.

Multiple iterations of the reference electrode were studied including an experimental solid-state multilayered pellet, and a single layer AgCl pellet. The initial testing was conducted on an experimental solid-state electrode previously developed by Sandia National Laboratories (Egan, 2020) which was built upon a graphene/graphite substrate. The interior components of the reference electrode were composed of materials that were initially separated into four distinct layers, an electrical contact, a transducer, a baffle or reference membrane, and a hydrophobic ion-permeable ceramic membrane composite. The transducer was made from silver-coated graphite spheres, which are synthesized in-house. The baffle was composed of silver chloride and potassium chloride powder. The membrane was made from a mixture of potassium chloride and bonding agents. The material was pressed to 4000 lbs and held at constant pressure for fifteen minutes. The pressed pellet was transferred to a preheated oven at 342°C to sinter the ceramic composite membrane and baffle. Figure 2-2 shows a schematic of the reference electrode pellet and Figure 2-3 shows a photo of the reference electrode pellet.

The alternate reference which was ultimately used in the lab and field-scale testing was based on the commonly used composition for a chloride ion reference electrode of AgCl. This iteration was composed entirely of Silver Chloride powder pressed into a cylindrical pellet. As with the sensing electrode, 0.45 g of powder was weighed and transferred to a ¼” diameter die press. The material was then compressed to 4000 lbs. and held at constant pressure for 15 minutes. The pellets were transferred to a preheated oven at 200°C for one hour and then cooled to room temperature. This reference was selected as it showed comparable results to the solid-state multilayer and significantly reduced the time and complexity of the sensor preparation (Figure 2-1).

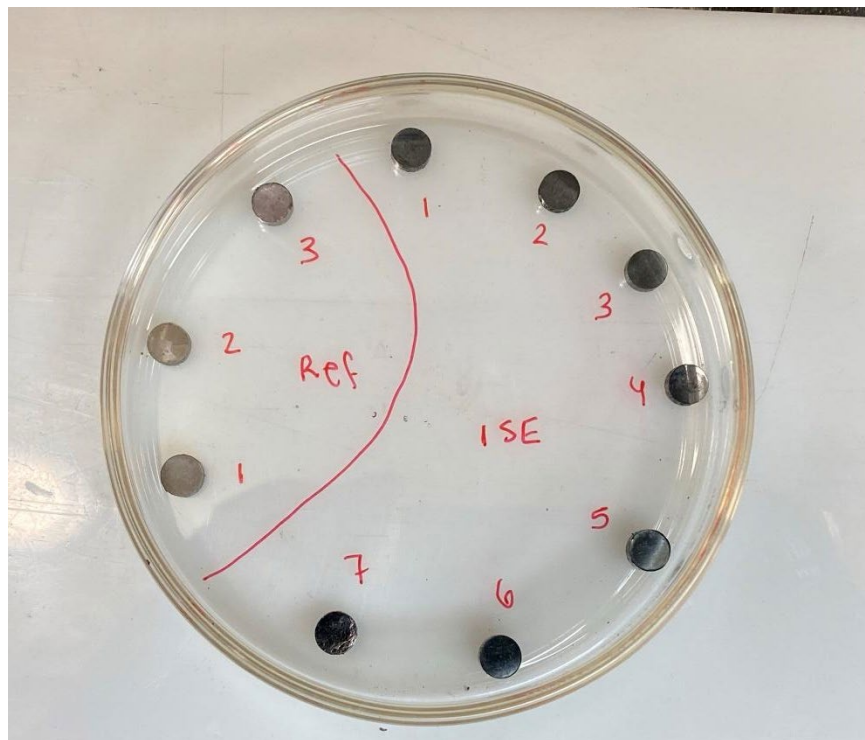


**Figure 2-1:** Photo of ISE pellets and single-layer AgCl reference pellets.

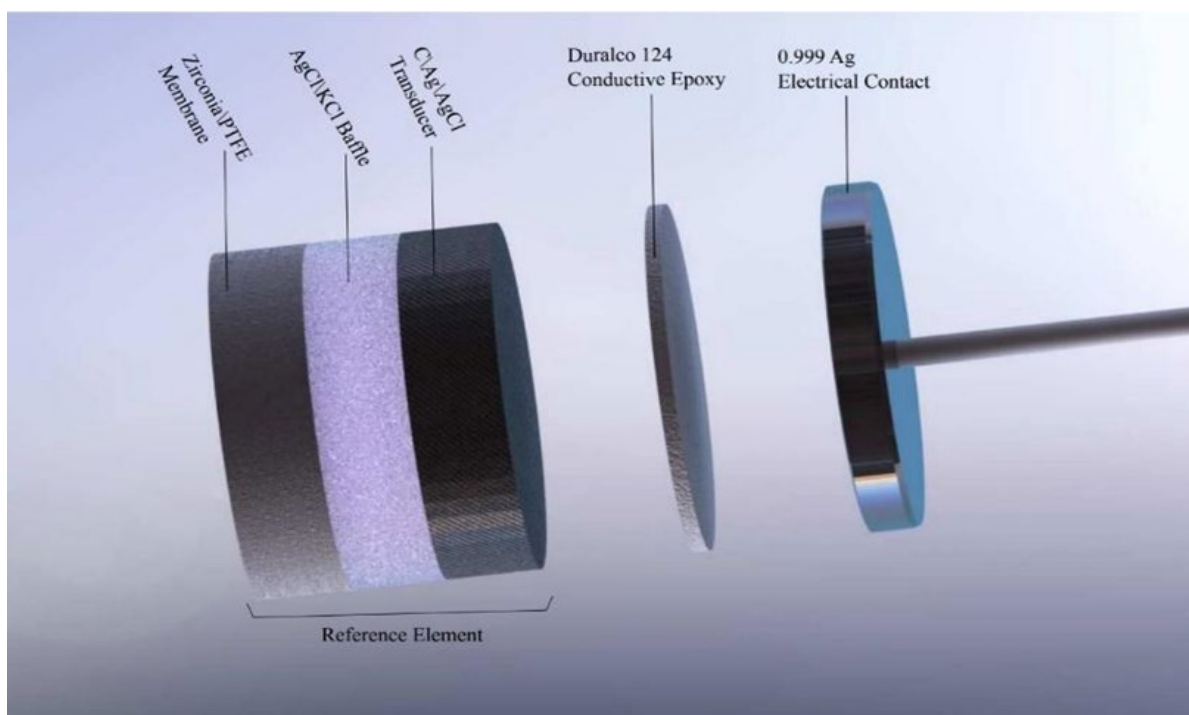


**Figure 2-2:** Diagram of the experimental solid-state reference element assembly.

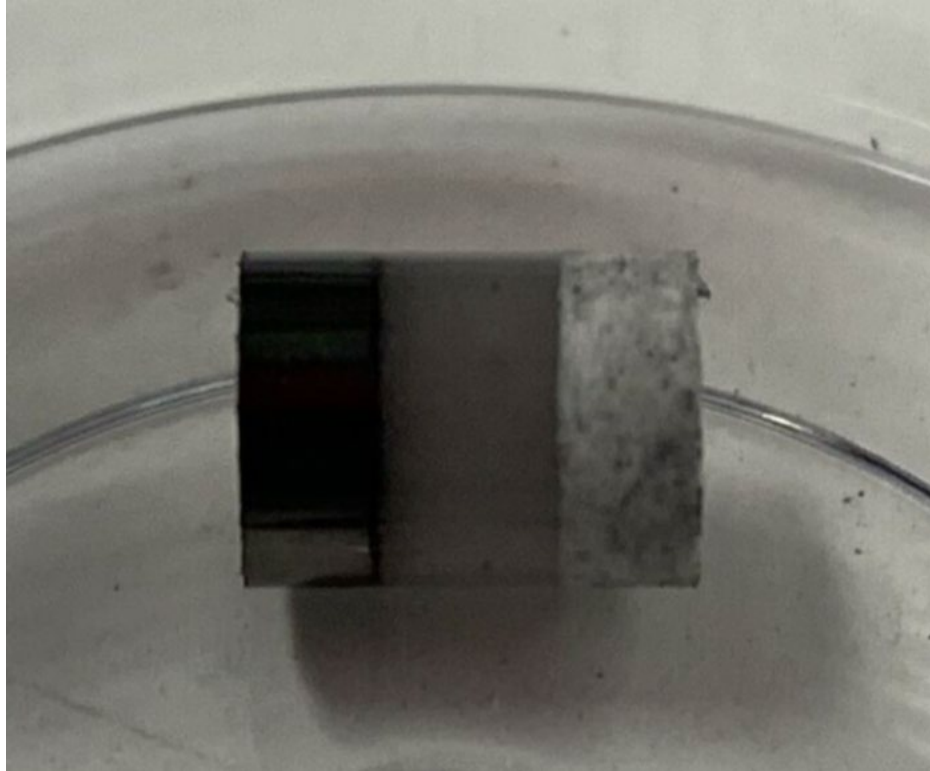


**Figure 2-3:** Photo of the experimental solid-state multilayered reference pellet.

Multiple iterations were evaluated for sealing the electrodes to protect them from the high-temperature and high-pressure environment. In the first iteration, the electrodes were connected to a nickel rod, which served as an electron conductor, using a small amount of silver-based conductive epoxy. The electrodes and the nickel rod were then encapsulated in a tube made of FEP and PTFE. A schematic of this setup is shown in Figure 2-4.

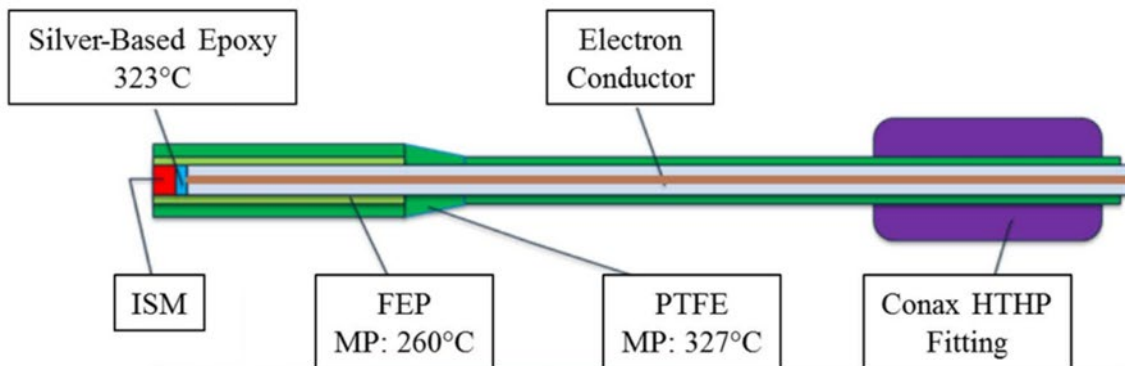


**Figure 2-4:** Schematic drawing of the first sealing method.

In the second sealing method, the electrode pellets were potted using Cotronics Duralco 4460HT Low Viscosity epoxy in a 1-inch long alumina tube with low porosity, an internal diameter of 0.25 inches, and a wall thickness of 0.125 inches. PTFE thread tape was applied to the ends of the tube to prevent the epoxy from leaking out. After potting, the epoxy was step-cured at 248°F for 24 hours and 446°F for 23 hours to enhance its environmental resistance. A protective PTFE round-stock piece,

approximately 2.13 inches long and 0.25 inches in diameter, was fitted over the conductor to shield the epoxy interface from bending and heat during the heat-shrinking process. The assembled electrode, PTFE protector, and lead were covered with layers of Zeus PTFE/FEP Dual-Shrink tubing of increasing diameters to eliminate any leak paths and ensure tight sealing. Care was taken to shrink each layer tightly to prevent air bubbles, which could rupture under heat and pressure. Finally, a 4:1 PTFE heat shrink or PTFE/FEP Dual-Shrink was placed over the entire assembly, allowing enough overhang to melt over the exposed ceramic end. Figure 2-5 shows a schematic drawing of this sealing method and Figure 2-6 shows a photo of the first two iterations of sealing methods.

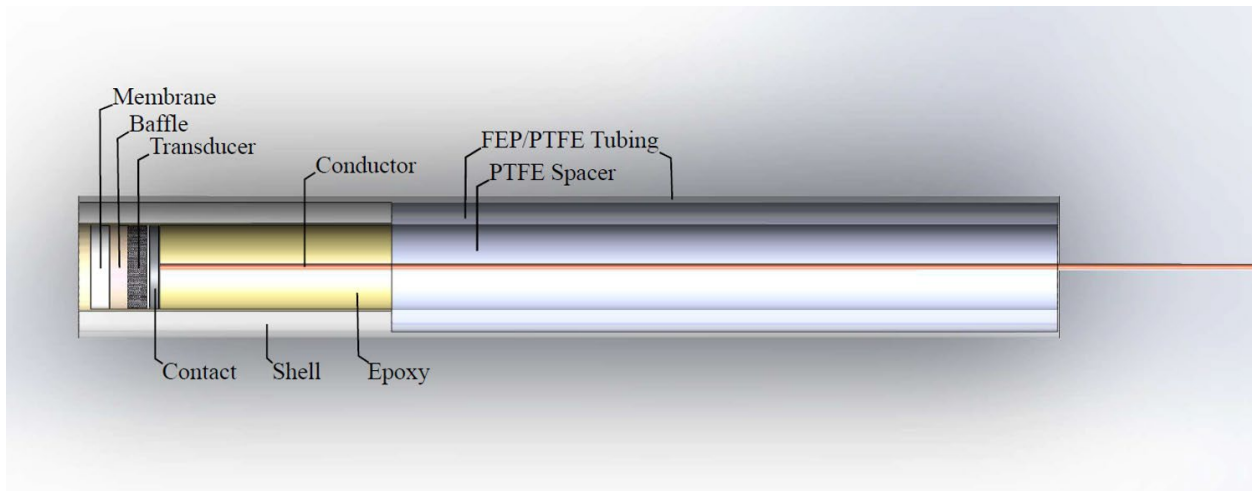


**Figure 2-5:** A cross-sectional diagram of the secondary sealing method.

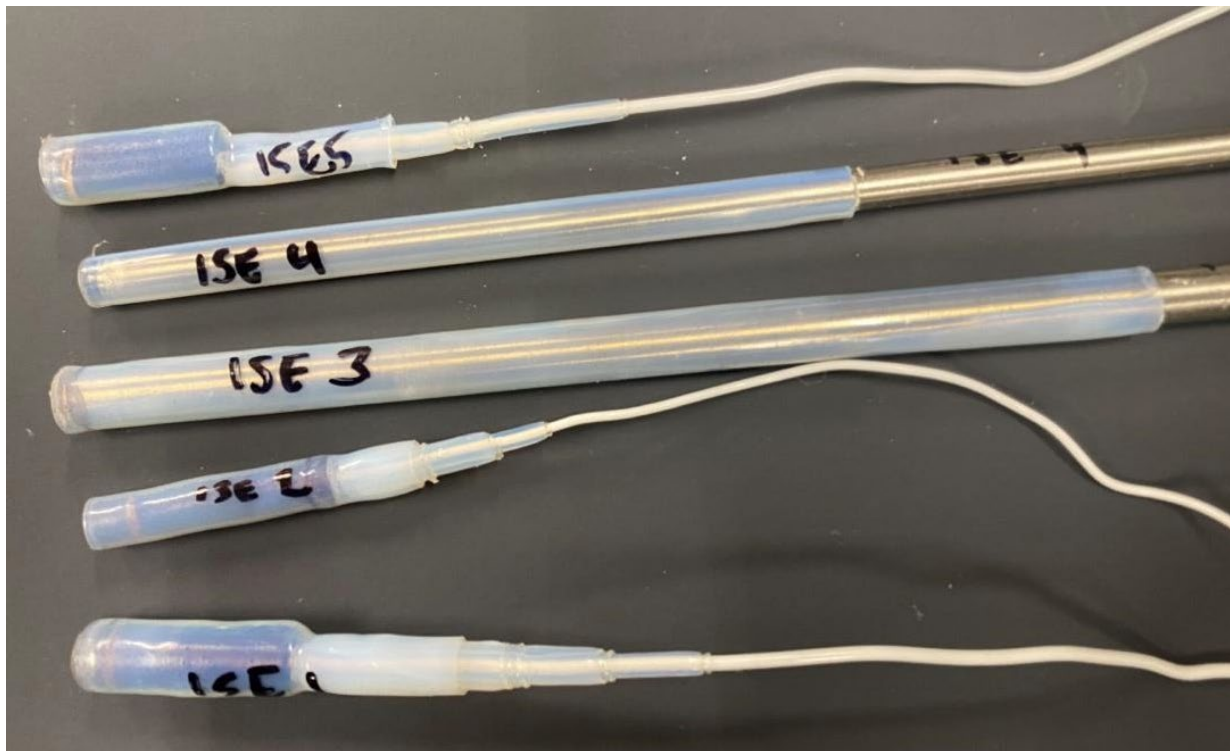


**Figure 2-6:** Photo of sealing methods 1 and 2.

In the final field deployed version of the housing, a CuAg-plated pellet wire adapter was fabricated to centralize a high-temperature nickel-plated copper wire on a conductive surface. The CuAg-plated pellet wire adapter was attached to the pellets using a high-temperature conductive epoxy and cured in a mold to keep the wire adapter centralized on the pellet. The assembled pellets and wire adapters are shown in **Figure 2-7**. The assembled sensors were then coated with Gagekote #1, a protective coating rated up to 455°C.



**Figure 2-7:** ISE and reference sensor assemblies before (top) and after (bottom) application of Gagekote.

### **2.1.2 Temperature and Pressure Rating for Utah FORGE Conditions**

The Go/No-Go decision for the project was based on the chemical sensors' ability to survive and operate effectively under High-Pressure, High-Temperature (HPHT) conditions representative of a geothermal environment, and more specifically, the Utah FORGE conditions as detailed in Table 2-1.

To assess this capability, laboratory tests were conducted using Sandia autoclaves. The successful completion of the temperature and pressure tests validated the capability of the sensors to function in the field trial conditions. These evaluations focused on determining both the mechanical integrity and high-temperature calibration of the sensors.

**Table 2-1:** Target conditions for autoclave testing

Pressure	Up to 34.5 MPa (5000 psi)
Temperature	225°C (437°F)
Chloride concentration	0.005 mol/L - 0.5 mol/L
Duration	24+ hours

### 2.1.2.1 Round 1 Autoclave Testing

In the initial autoclave testing, A Cortest 20420 autoclave (Figure 2-8), was used to evaluate the sensors under high-temperature (225°C) intermediate-pressure (up to 2000 psi) conditions. As illustrated in Figure 2-9, the sensor end of the tool, which includes the bulkhead fitting, ISE, and reference electrodes, was configured to facilitate testing within the autoclave. This setup allows for the simultaneous testing of multiple reference electrode/ISE combinations in a single run, which is essential given that ramp times to reach target temperatures can take several hours per test.

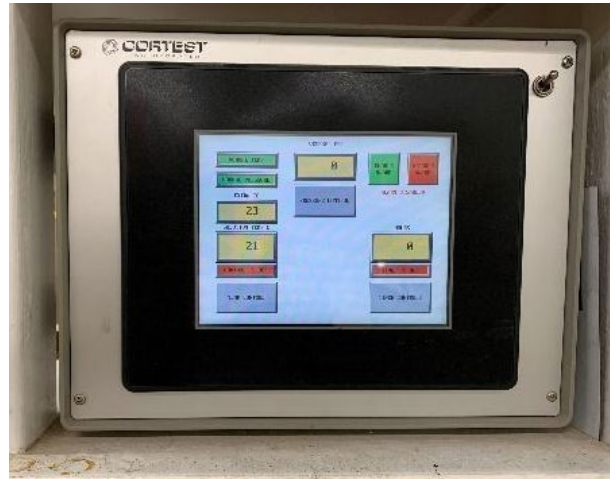
The autoclave is fitted with a polytetrafluoroethylene (PTFE) liner that isolates the electrolyte solution from the inner walls of the pressure vessel. The PTFE liner served two purposes, firstly, to prevent chloride corrosion to the pressure vessel and secondly, to insulate any potential electrical paths from being grounded through the pressure vessel itself.

All cell potentials were measured using National Instruments NI-9238 +/-5 V voltage acquisition modules in differential mode interfaced to a cDAQ-9185 chassis. The reference electrode is connected to a common reference rail shared among the ISEs being tested. The entire test setup is shown in Figure 2-10. During this round of testing, the current configuration was limited to a maximum pressure of approximately 1500 psi due to the constraints of the pressure relief valve, supply pressure, and personnel safety considerations. Upgrading the pressure relief valve and implementing remote operation for the gas bottles enabled higher pressure testing in the subsequent tests.

The minimum and maximum concentrations defined in Table 2-1 were achieved by mixing 0.144 g and 14.4 g of sodium chloride mixed in 500 mL of distilled water, respectively. The test matrix includes evaluations at both the minimum and maximum chloride concentrations (two levels) while stepping through a range of temperatures up to 225 °C. Pressure is maintained at an intermediate level of approximately 500 psi until the maximum temperature is reached, preventing the vaporization of the chloride solution.

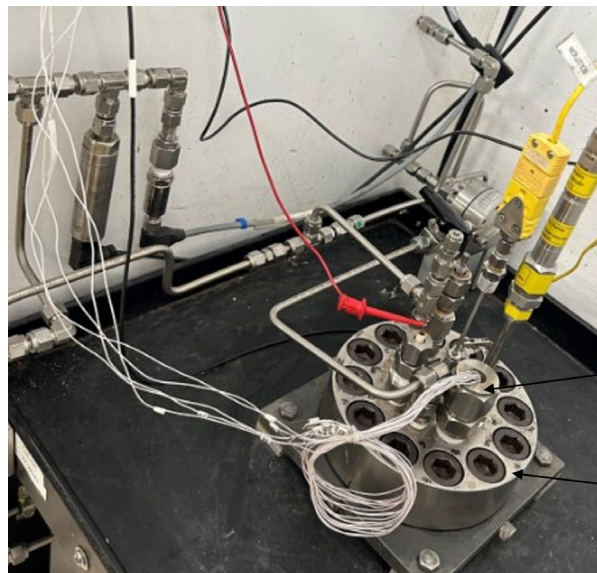
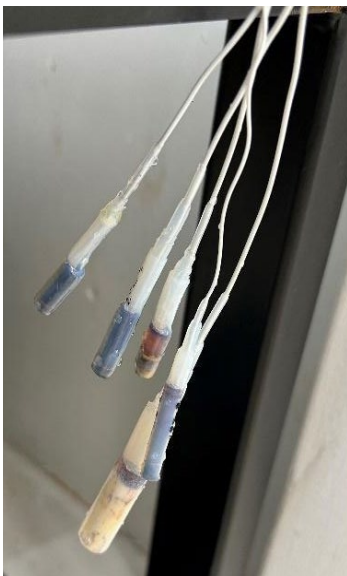


Autoclave



Autoclave controller

**Figure 2-8:** Sandia Autoclave and Controller.



WIRE FEEDTHRU

AUTOCLAVE

**Figure 2-9:** Multiple ISE and reference electrodes connected to the compression seal feedthrough.



**Figure 2-10:** The full setup of the Sandia autoclave testing.

Figure 2-11 presents the results from the initial round of tests conducted at elevated temperatures (up to 200°C). The plot illustrates the temperature dependence of the tool at a fixed chloride concentration, revealing that the voltage output for all three ISEs follows a consistent trend. Notably, there is a discernible voltage offset among the sensors, which is anticipated due to inherent variations arising from the fabrication and assembly processes. Characterizing this offset and understanding the sensors' behavior became integral to the calibration process.

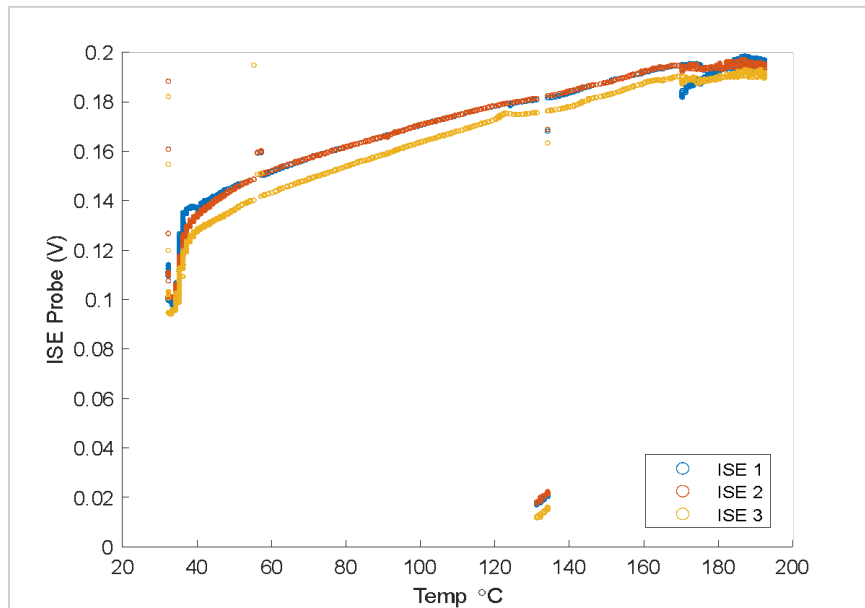


**Figure 2-11:** Voltage vs. temperature at 0.005MCl/L concentration.

Additional tests were conducted on separate probes to evaluate performance under higher pressure and temperature conditions for extended durations. For this testing, the third and final sealing method was used for the preparation of the ISEs and reference sensors using a Gagekote covering of the electrodes as the first two iterations showed damage at higher pressure and temperature. An intermediate pressure test at 1500 psi and a high temperature of 225 °C was performed to subject the tool to more aggressive conditions for over 24 hours, using a chloride concentration of 0.005 M Cl/L.

The results of the first extended-duration test are presented in the following figures. Figure 2-12 illustrates the pressure and temperature over time during the test. The autoclave was initially brought up to the specified test pressure and temperature, and these conditions were maintained for more than 50 hours. The additional time was included to monitor for potential changes following the initial 24-hour period. Upon completion of the test duration, the autoclave heater was turned off, and the system was allowed to cool.

The ISE voltage response over time is plotted in Figure 2-6b. Throughout the duration of the test, a decrease in ISE voltage was observed, a trend that was consistent for both ISEs used. We hypothesize that this decrease may be attributed to variations in the concentration of chloride ions within the sensor body over time; however, further testing is required to confirm this hypothesis. Additionally, a noticeable shift in voltage for both ISEs occurred around the 52-hour mark, which was due to the swapping of reference electrodes at the end of the test window to assess changes in relative voltage resulting from the altered reference.

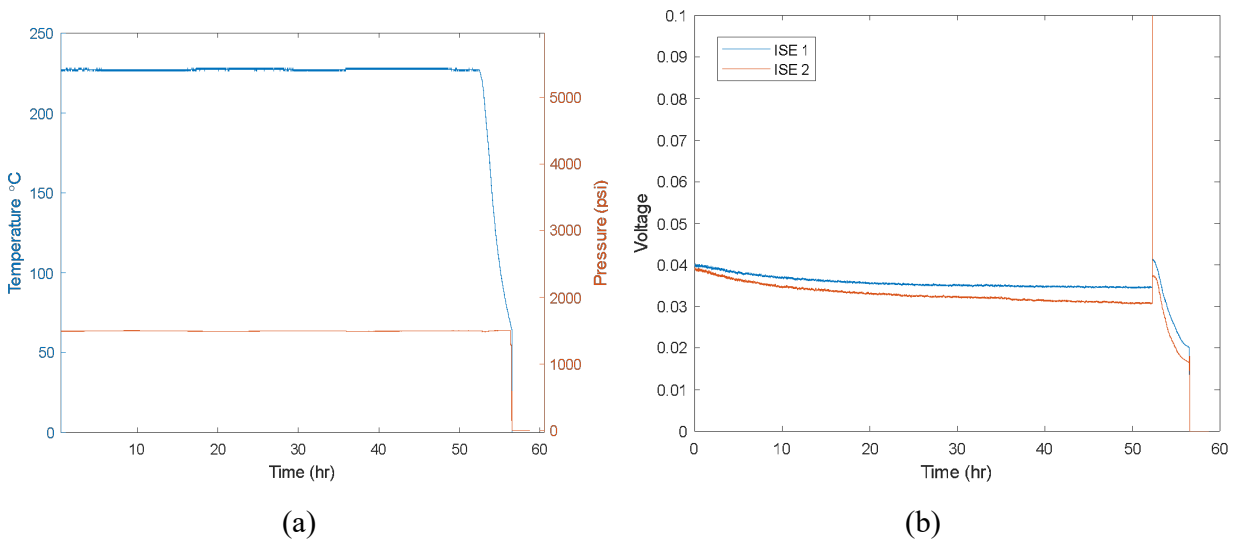


**Figure 2-12:** (a) Testing conditions temperature and pressure vs. time; (b) ISE Voltage vs. time at 0.005 MCl/L concentration.

Figure 2-13 shows the relationship between temperature and pressure and ISE voltage for a fixed chloride concentration. The voltage generated by the probes shows a clear temperature dependence, which is consistent with the previous tests and is a characteristic that will need to be calibrated for each of the probes. Compared to the temperature sensitivity, the probes are relatively insensitive to the pressure for the range of pressures reached in the test. The scatter in the data seen at 1500 psi is due to the change in ISE voltage over time shown in Figure 2-12, as well as the reference electrode swap at the 52-hour mark.

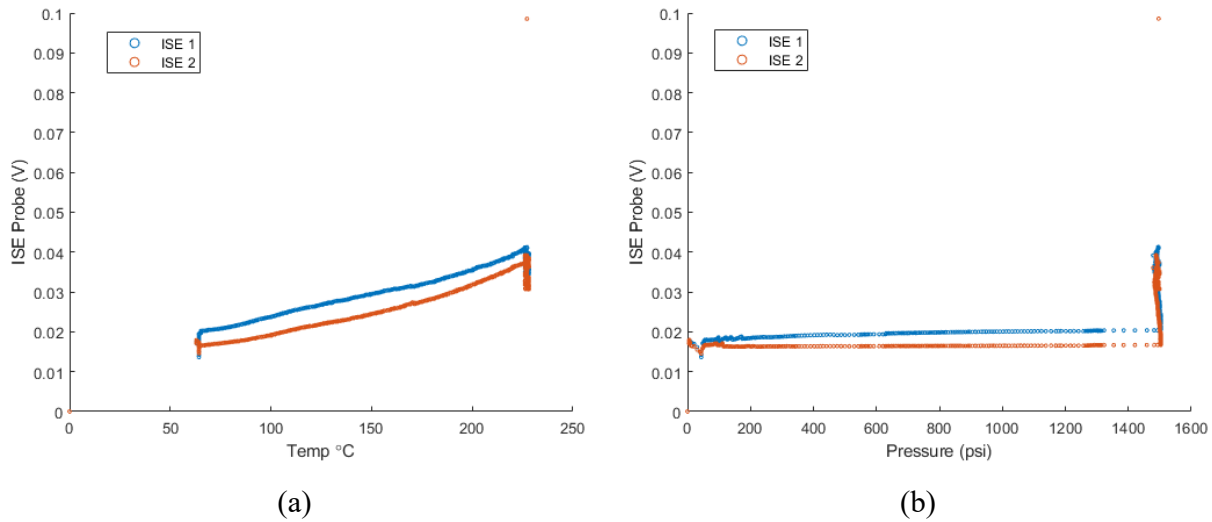


**Figure 2-13:** ISE voltage response versus (a) temperature and (b) pressure at 0.005 MCl/L concentration.

The initial extended-duration tests demonstrated that the chemical tool probes could withstand the targeted temperatures and intermediate pressures specified for the project. The next step involved conducting tests at higher pressures to assess the potential impact of this additional stressor. Consequently, the second round of testing was relocated to a different test chamber due to the pressure limitations of the Cortest autoclave in its previous configuration.

#### 2.1.2.2 Round 2 Autoclave Testing

An upgraded Sandia autoclave was brought online toward the end of Q2 FY23 (Figure 2-14). While it visually resembled the Cortest autoclave, it offered significant usability improvements, including remote operation and enhanced control over both pressure and temperature settings. The test conditions adhered to those outlined in Table 2-1, maintaining a chloride concentration of 0.25 M Cl/L.

Two ion-selective electrodes (ISEs) and a bare wire control were immersed in the brine solution and tested under high-pressure, high-temperature conditions for 24 hours to meet the go/no-go criteria. A description of each sensor element is provided in Table 2-2. ISE 1 was a spare sensor used in previous tests, included in the test sequence to investigate sensor failure modes. ISE 2 served as the primary sensor being tested, while the bare wire was incorporated as a control to determine when the sensors were no longer functioning.

**Table 2-2:** Sensor configuration for Round 2 autoclave testing

Part	Description
ISE 1	Refurbished from previous tests
ISE 2	New sensor with Gagekote sealant applied
Bare wire	Nickel-plated copper (NPC) wire baseline/reference
Reference	Platinum reference sealed with Gagekote

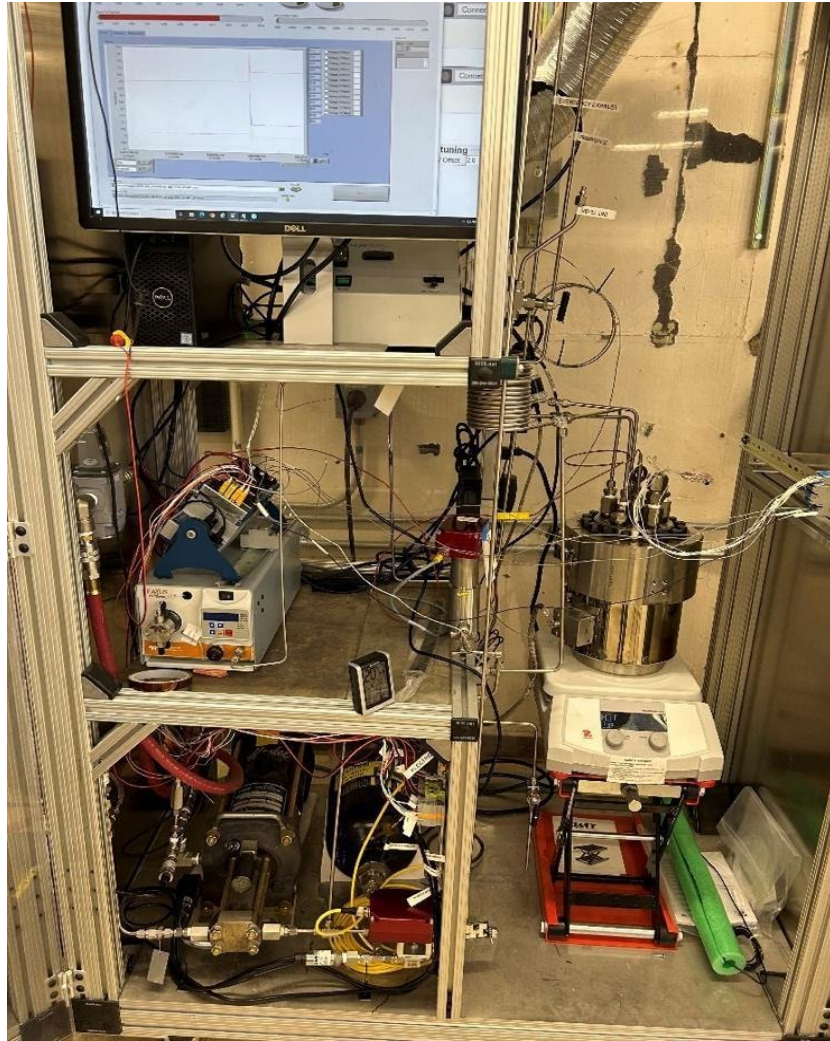


**Figure 2-14:** Upgraded Sandia HPHT autoclave.

Data was collected using the National Instruments data acquisition chassis equipped with voltage input modules. A Parr Instruments 4838 controller regulated the temperature of the fluid. After immersing the sensors in the brine solution, the pressure was increased to between 3000 psi and 4000 psi to check for leaks. Subsequently, the fluid temperature was ramped up to 225 °C to initiate the test, while the pressure was maintained at 5000 psi during the temperature increase. The pressure and temperature versus time plots are shown in Figure 2-15a. The entire data collection occurred over an approximately 30-hour window.

The sensor voltage versus time is illustrated in Figure 2-15b. Each sensor output exhibited transient behavior during the initial pressurization and temperature ramp. The voltage of ISE 1 began to drop almost immediately, and the data from ISE 1 was included in the plot to demonstrate the characteristics of a sensor that was not functioning correctly. In this instance, the behavior of the sensor resembled that of a bare wire, allowing for the identification of the failure mechanism.

In contrast, ISE 2 maintained a nearly steady voltage throughout the entire duration of the test, fluctuating around 0.55 V after steady-state conditions were reached, with a maximum voltage of 0.58 V. A shift in all sensor outputs occurred around the 19-hour mark. Since all sensors reacted similarly,

it was believed that this shift resulted from a change in the behavior of the reference electrode. Additionally, a drop in voltage was observed for ISE 2 around the 25-hour mark, although the fluctuations during that period resolved as the test continued. The cause of this behavior remained uncertain.

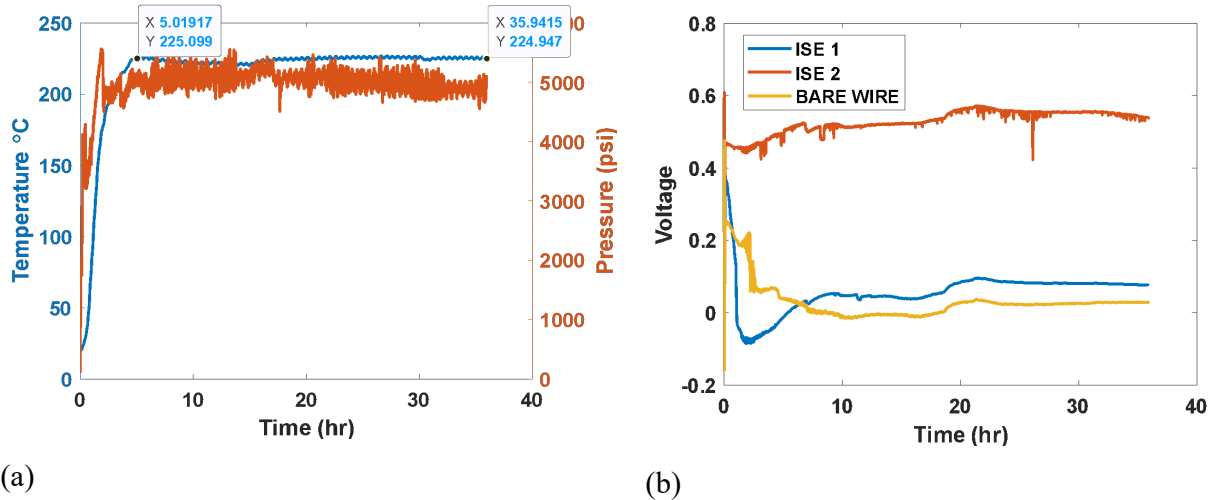


**Figure 2-15:** (a) Testing conditions temperature and pressure vs. time; (b) ISE Voltage vs. time at 0.25 MCl/L concentration.

Figure 2-16 shows the relationship between temperature, pressure, and ISE voltage. For ISE 2, voltage appeared to remain steady across the pressure range. Variations in voltage at the full pressure are due in part to the duration and the natural fluctuations of the sensors over an extended period. Since the sensors are fabricated at pressures much greater than the fluid pressure, it was not expected to see a pressure dependence on the sensor. After reaching steady state conditions, the temperature dependent data shows fluctuations oscillating around the nominal value of 0.55V. Similar to the pressure dependence, the ISEs in this tested configuration do not show a strong dependence on temperature.

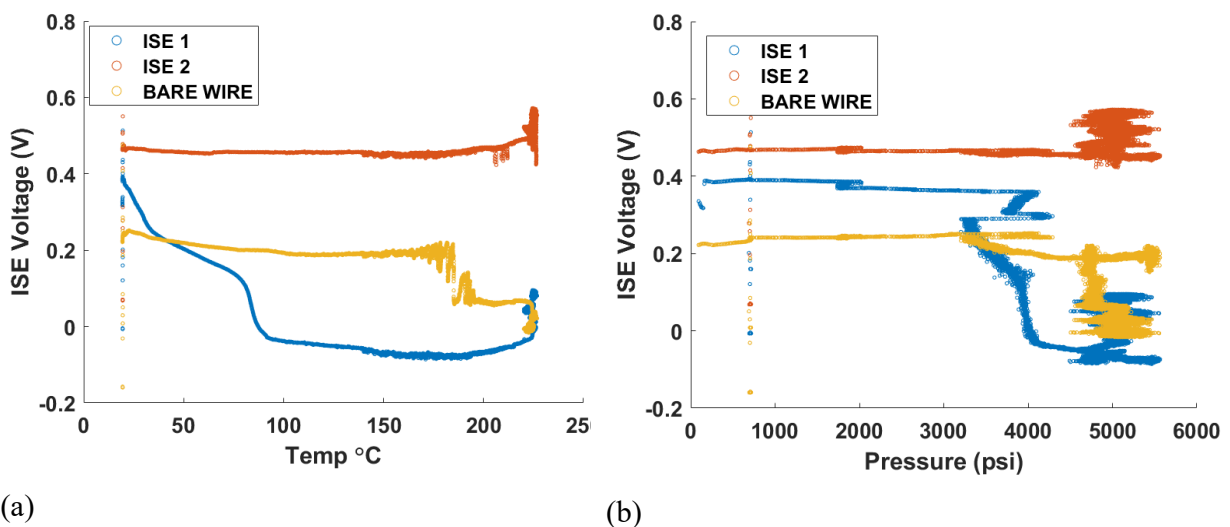


**Figure 2-16:** ISE voltage response versus (a) temperature and (b) pressure at 0.25 MCl/L concentration.

The test demonstrated the ruggedness of the ISE sensor under HPHT conditions. ISE 2 survived nearly 31 hours of continuous exposure to 225°C brine at 5000 psi. Based on our test results and the sensor condition after testing, we are confident the sensors and bulkhead connection design will transfer readily to the final deployable tool.

### 2.1.3 Brine Testing

To demonstrate the capability of the sensor performance in the chemical composition of the brine at Utah FORGE, samples of flowback water from Utah FORGE Well 16A (78)-32 and 16B(78)-32 were collected and tested using the ISE electrode sensors. The chemical composition of the samples is shown in Table 2-3. Figure 2-17 shows the calibration fit of the well samples in comparison to various molarities of Potassium Chloride (KCl) in distilled water.

**Table 2-3:** Chemical composition of well samples from Utah FORGE Wells 16A(78)-32 and 16B(78)-32

DATE TIME	LOCATION	Major (mg/l)									
		pH	Na	K	Ca	Mg	B	SiO <sub>2</sub>	Cl	SO <sub>4</sub>	HCO <sub>3</sub>
7/19/2023 20:00	16A(78)-32 Utah FORGE	7.43	621	80.2	92.3	4.13	2.07	167	1300	162	105
7/20/2023 7:50	16B(78)-32 Utah FORGE	6.69	2871	319	44	0.07	9.05	81	4384	239	383
7/20/2023 15:00	16B(78)-32 Utah FORGE	6.64	81	7	109	3.48	0.32	78	122	115	276

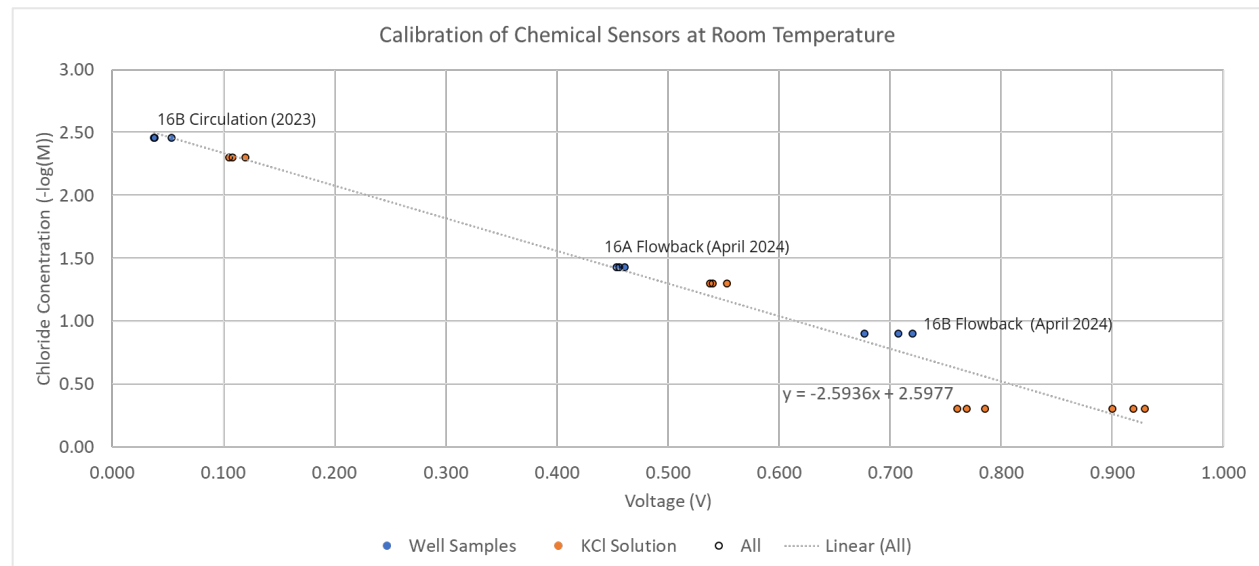


**Figure 2-17:** Calibration of chloride sensors in KCl solution and samples from wells 16A and 16B.

The voltage measurements of the samples from the flow back in both wells are in good agreement with the measurements of the KCl solution. However, the 16B circulation fluid was outside of the linear fit region. This is likely due to the low chloride concentration (0.003 M), which falls outside of the range of the sensors (0.005 – 0.5 M).

## 2.2 Laboratory-scale Tool Development

The initial configuration of the laboratory-scale tool featured a tubular housing unit, which included electrodes at the front end and a data transmission cable at the rear. The initial experiments employed the same tool as Gao et al. (2017) developed by Sandia, as shown in Figure 2-18. The laboratory-scale tool consisted of three electrodes: a chloride-ion selective electrode (ISE), a solid-state bimodal pellet reference electrode, and a graphite ground reference electrode. The measurement of chloride concentration was accomplished by evaluating the voltage difference between the ISE and the reference electrode.

An updated version was fabricated in 2023 (Figure 2-20 and Figure 2-20) to address the calibration mismatch issue of the original tool (detailed in Section 4.1.1.2). Most of the flow behavior investigations in this project, using numerical simulations and laboratory experiments, were conducted with the 2023 tubular lab-scale tool.

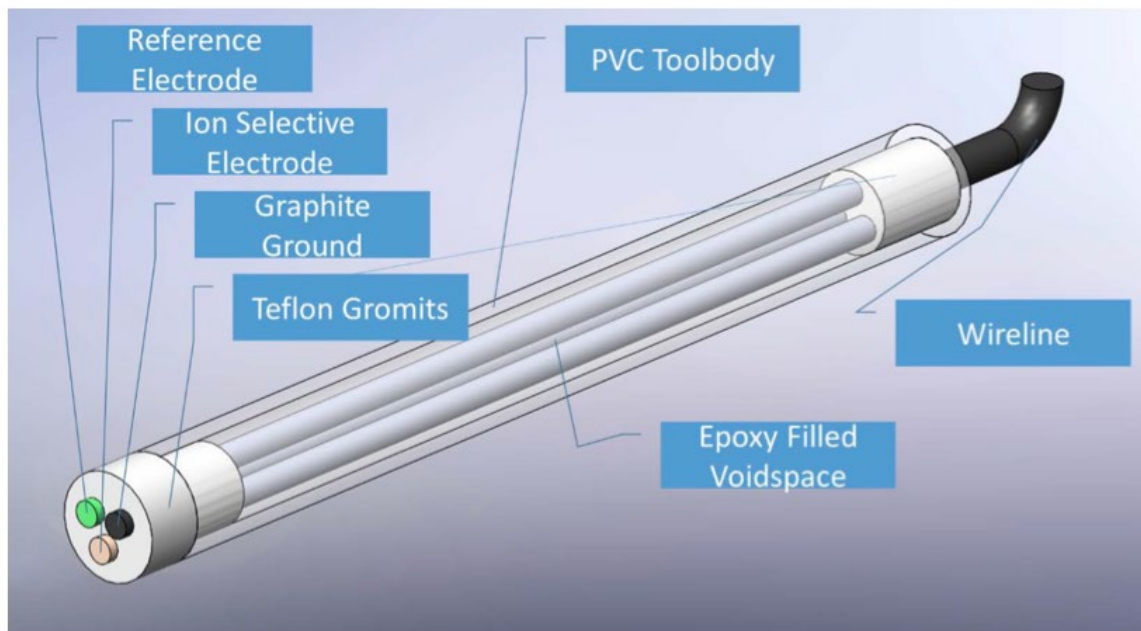


**Figure 2-18:** schematics of the chloride tool from Gao et al. (2017)

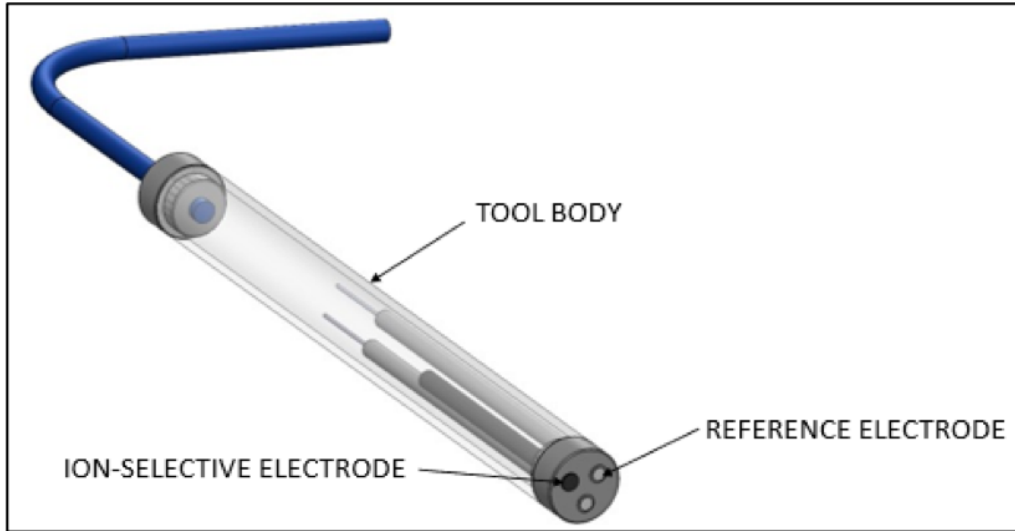


**Figure 2-19:** Schematics of the updated lab-scale tool fabricated in 2023.



**Figure 2-20:** Side view (left) and bottom view (right) of the updated lab-scale tool fabricated in 2023. The bottom view shows the sensors' interface.

In 2024, after the sensor housing design was finalized, an updated version of the lab-scale tool featuring the caged sensor housing (Figure 2-21) fabricated by Sandia was utilized at Stanford to perform additional flow behavior and sensor sensitivity investigations. Additional tubing components (Figure 2-22 and Figure 2-23) were 3D-printed using PLA filament and installed at the top and bottom parts to better represent the wireline tool assembly that would be deployed in the field (see Figure 2-27).

The up-tool component was modified after manufacturing by drilling a hole on the opposite side of the Chloride Sensor Housing. The hole was drilled with a diameter that is slightly larger than the diameter of the shielded electrical cable. After feeding the shielded electrical cable through the hole in the up-tool component, a hose clamp was added to the shielded electrical cable within the up-tool component. This hose clamp suspended the chloride tool to remove tension from the soldered connections to prevent their breakage.

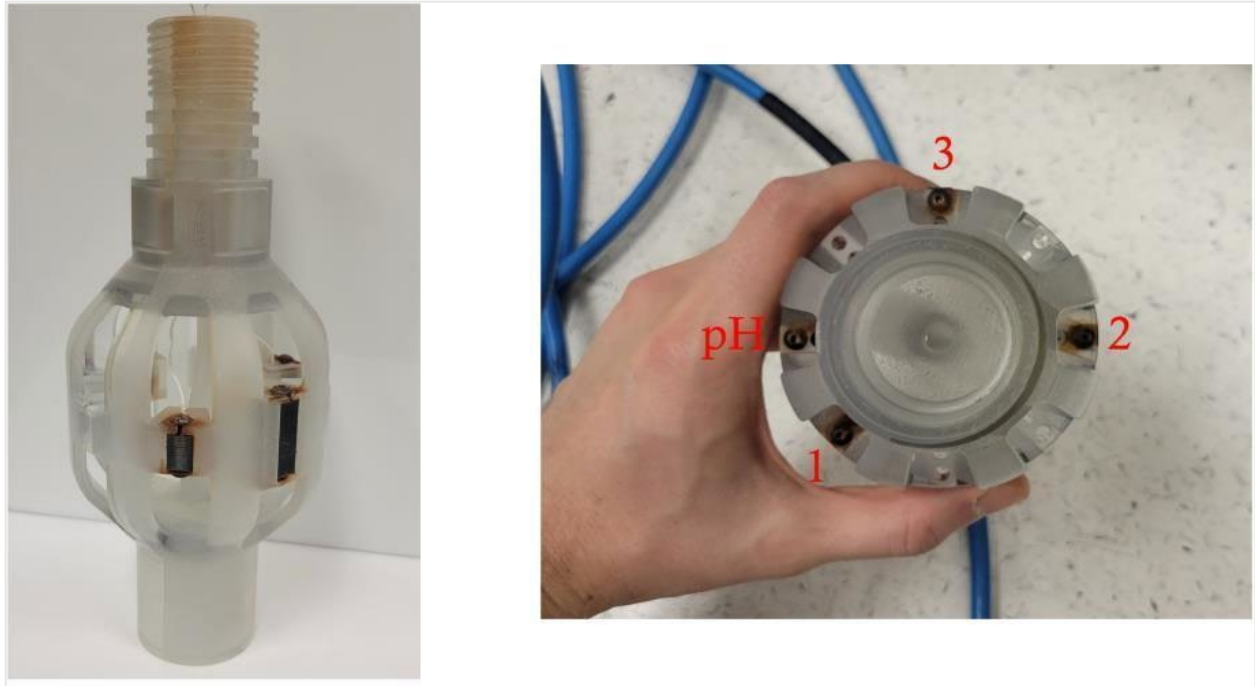


**Figure 2-21:** (left) Side view and (right) bottom view of the lab-scale tool with housing, showing the locations of the (1) reference electrode, (2) ISE probe #2, and (3) ISE probe #3.

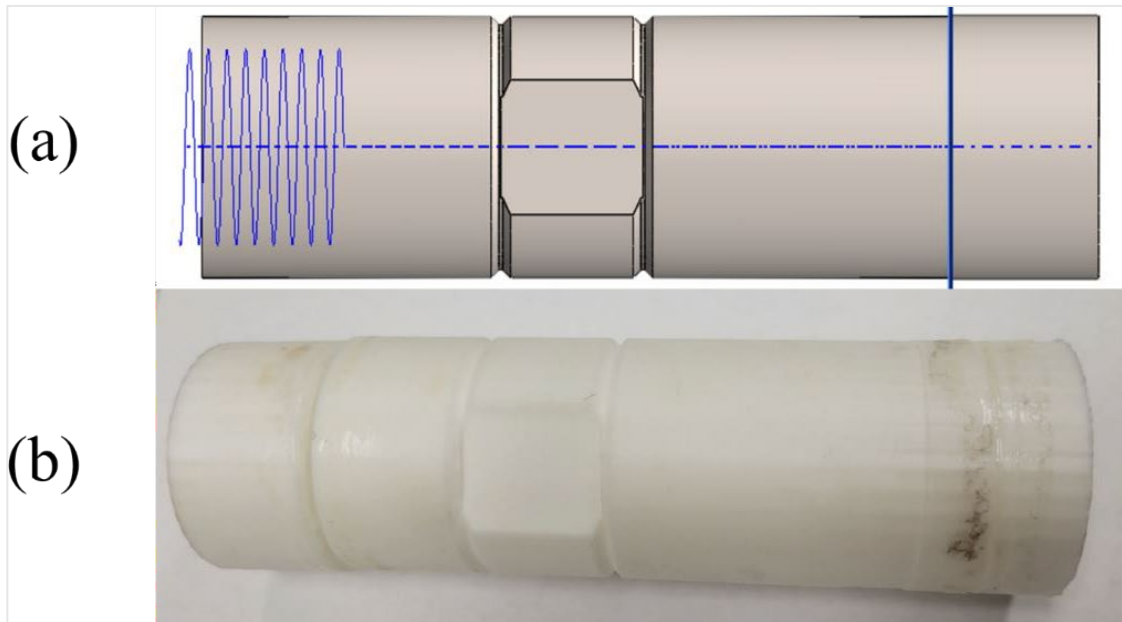


**Figure 2-22:** The (a) SolidWorks® model and (b) printed simulation up-tool component.

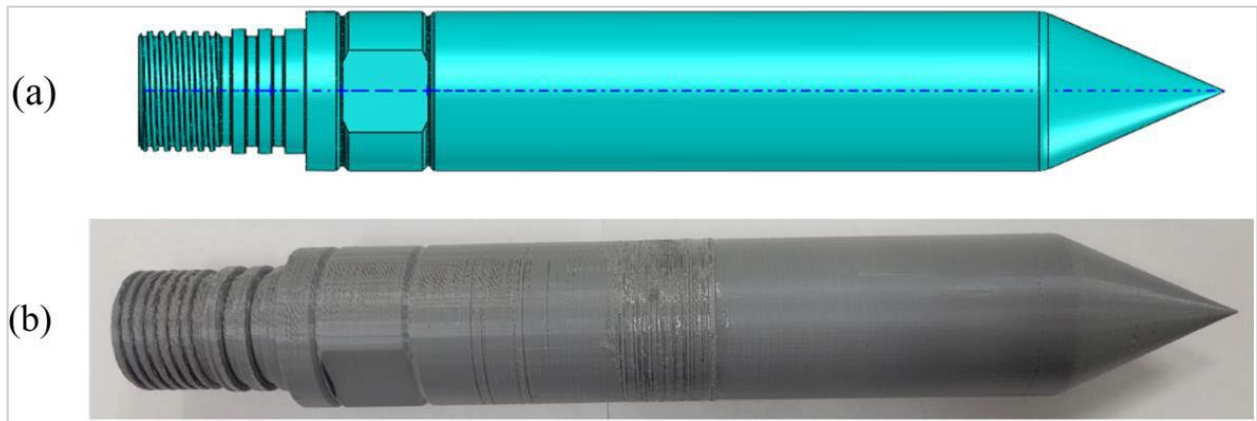


Figure 2-23: The (a) SolidWorks® model and (b) printed simulation down-tool component.

### 2.3 Field-scale Tool Fabrication

The field-deployable chemical tool assembly incorporates the Mitco PTS sensor package and a tip centralizer at the leading edge of the tool. This is used for secondary downhole measurements to compare the geochemistry-based alternative method to the commonly used PTS measurements. A wire guide component was developed to adapt the PTS tool to the FORGE chemical sensor housing. The sensor wires from both the Mitco PTS tool and the chemical sensors pass through a wire feedthrough in the chemical sensor housing to the high-temperature logging tool in the electronics housing. The electronics housing connects to the wireline via a 4-conductor feedthrough that is adapted to a 7-pin conductor feedthrough that matches the wireline connection. The full assembly schematic is shown in Figure 2-24.

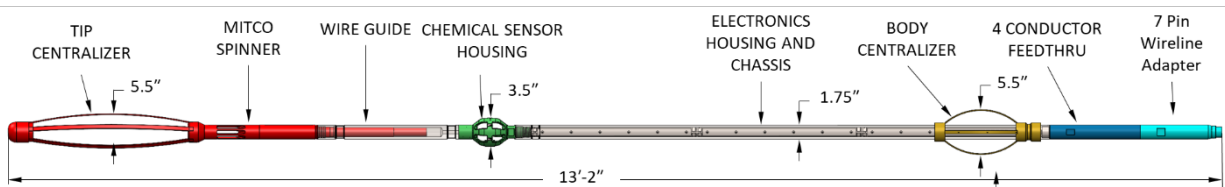


Figure 2-24: Field-deployable chloride tool schematics, including an existing PTS tool adapted to the chloride-based wireline tool and high-temperature developed by Sandia National Laboratory.

#### 2.3.1 Chemical Sensors and Housing for Field Deployment

The field-deployable version of the tool uses the same sensing elements as the lab-scale tool while considering the potential packaging and environmental challenges associated with downhole conditions. The chemical sensor housing was designed and developed to enclose the ion-selective chemical sensors, pH Sensors, and reference electrode sensors. The sensor housing was designed to allow flow to pass through the housing and interact with the chemical sensors uniformly. The housing includes retainer slots to incorporate three Ion-Selective Electrode (ISE) sensors, one reference electrode sensor, and two pH sensors.

The sensors are routed through a wire feed-through and sealed using a Conax Compression Seal Fitting. The Conax Compression Seal Fitting can hold up to four wires; this allows for two ISE sensors, one pH sensor, and one reference electrode; the remaining retainer slots were left empty. The housing also includes a wire feed-thru to accommodate the downstream Mitco PTS sensor used for secondary

measurements. The unique feature combinations (internal tube, pellet slots) are enabled through metal additive manufacturing. The sensor housing with installed sensors is shown in Figure 2-25.



**Figure 2-25:** Fabricated sensor housing populated with installed sensors and bulkhead fitting.

Three sensor housings were manufactured and tested to ensure they were pressure-safe and leak-resistant by including moisture indicators into the wire cavity and loading the capped pressure housing into a pressure vessel. The housing was loaded externally in a water vessel and the moisture indicators confirmed no leaks were present in the pressure housing.

### 2.3.2 High-Temperature Logging Tool

Sandia modified an existing high-temperature (HT) logging tool to deploy the chemical sensors into the Utah FORGE well. The tool uses a previously deployed and tested capability to capture and transmit the data from the chemical sensors to the surface. The tool uses a Honeywell HT HT83C51 microcontroller in parallel with a Sandia custom high-temperature Application-specific Integrated Circuit (ASIC). This tool was developed to capture pressure, temperature, and flow using Mitco's pressure, temperature, spinner module (PTS). The tool uses Frequency Shift Keying (FSK) and a multiconductor wireline to transmit data to the surface. Figure 2-26 shows the electronics for the logging tool placed next to Mitco's PTS module.

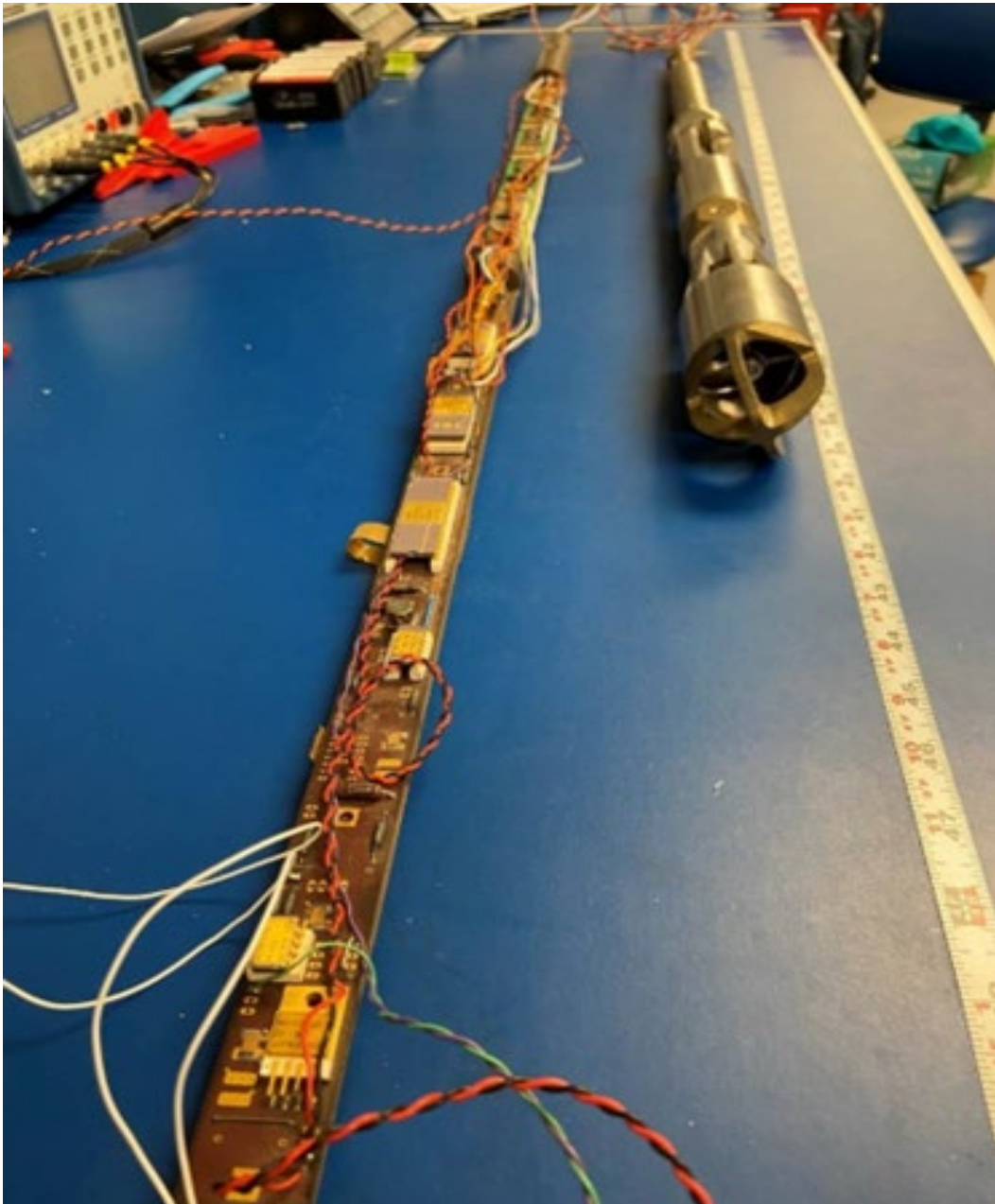


**Figure 2-26:** Sandia's custom high-temperature logging tool with Honeywell's microcontroller and Sandia's custom Application-specific Integrated Circuit or ASIC (left) next to Mitco's PTS module (right).

A new high-temperature expansion board was developed to accommodate the additional signal inputs for the chemical sensors. Figure 2-27 shows the high-temperature Chemical Buffer Amplifier (CBA) board, which was designed to take the high-impedance signal from the sensor to a low impedance while amplifying the signal. Using Sandia's high-temperature tool, the signal is digitized with the onboard Analog-to-digital Converter (ADC). The components of this system are rated to operate at 260 °C. With the populated CBA, the system was tested with the chemical sensors while being heated in the oven to confirm the proper operation of the board. A housing extension was designed and fabricated to incorporate this new board with the high-temperature logging tool.

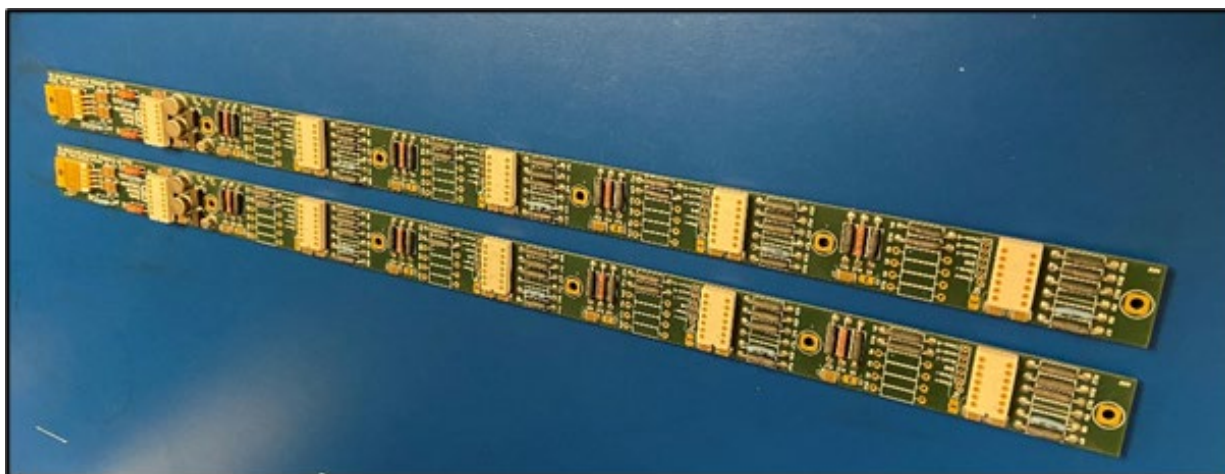


**Figure 2-27:** High-temperature Chemical Buffer Amplifier (CBA) for accommodating additional signal inputs.

In a parallel effort to capture and transmit data from the chemical sensors to the surface using commercial off-the-shelf (COTS) components, Sandia investigated the use of the EV-HT-200CDAQ1 High-Temperature Data Acquisition Reference Design Platform from Analog Devices as an alternative system microcontroller. This device, seen in Figure 2-28, is capable of interfacing with the CBA and the Mitco PTS module and uses an RS485 serial connection to transmit the data it gathers. Software was developed to operate the microcontroller with the high-temperature logging tool and confirming the rated operating temperature of 200 °C over several days of oven testing.

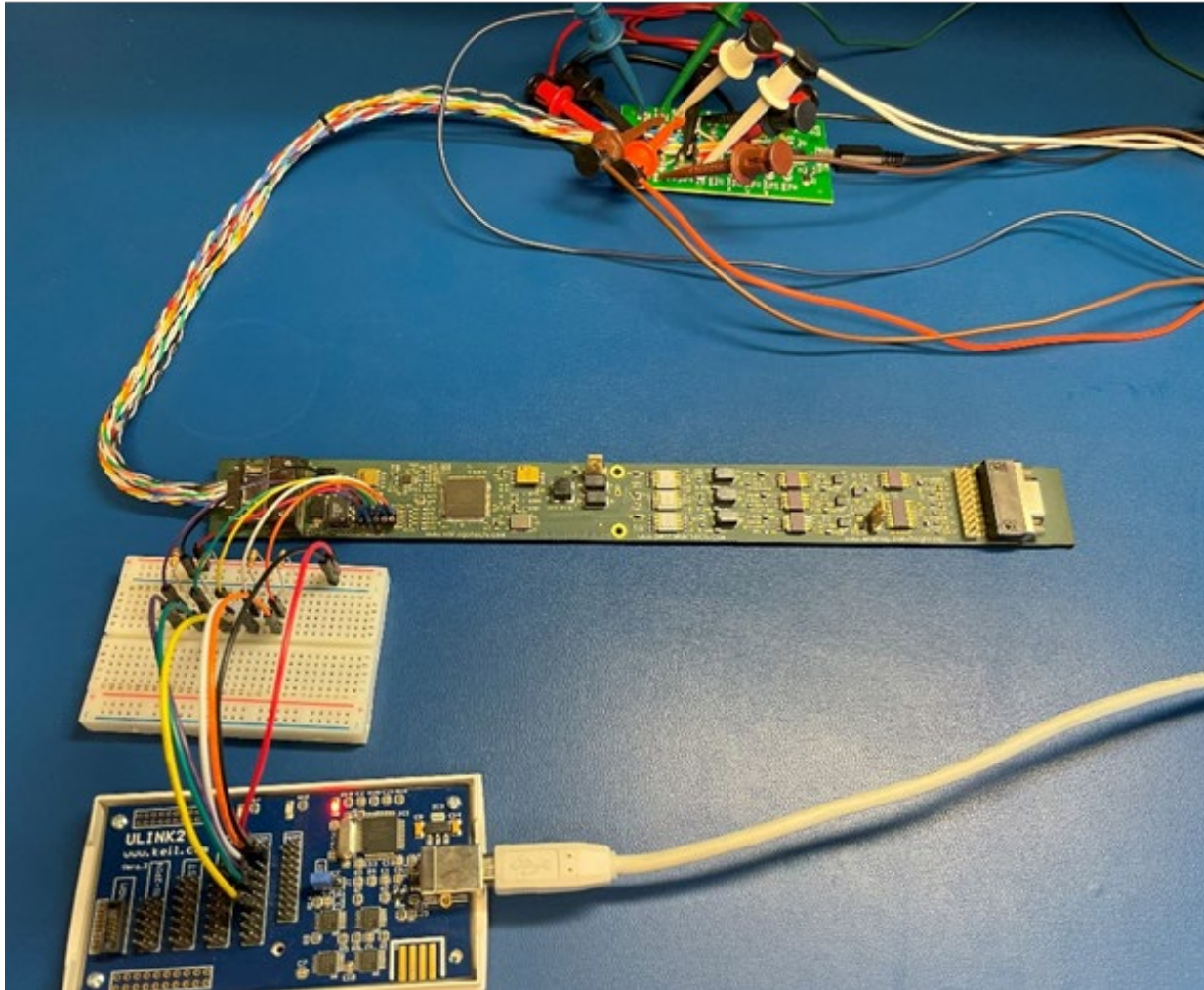


**Figure 2-28:** Alternative off-the-shelf system microcontroller - EV-HT-200CDAQ1 from Analog Devices.

As a result of the high-temperature logging tool experimentations, two versions of the High-Temperature (HT) Logging Tool were developed and assembled to capture and transmit data from the chloride sensors and PTS spinner tool through the wireline to the surface. The primary version incorporates a modified and previously deployed and tested HT electronics package. The system is composed of three main boards: 1) a digital board featuring a Honeywell HT HT83C51 microcontroller, a Sandia custom high-temperature Application-specific Integrated Circuit (ASIC), and memory, 2) an analog board equipped with an analog to digital converter (ADC), multiplexer, and operation amplifiers for the pressure and temperature inputs, and 3) a buffer board that includes a Chemical Buffer Amplifier (CBA) designed to convert the chemical sensor's high input impedance to low impedance. Two full assemblies of the primary HT logging tools were assembled and tested to confirm operation (see Figure 2-29).

The secondary logging tool was constructed to serve as a backup for contingency in the field. This electronic system uses the EV-HT-200CDAQ1 High-Temperature Data Acquisition Reference Design Platform from Analog Devices Inc as an alternative to the digital and analog board in the first system. All three logging tools were tested to confirm they could accurately capture readings from the chloride

and pH sensors, record measurements from the Mitco PTS module, and relay the information through the wireline cable.

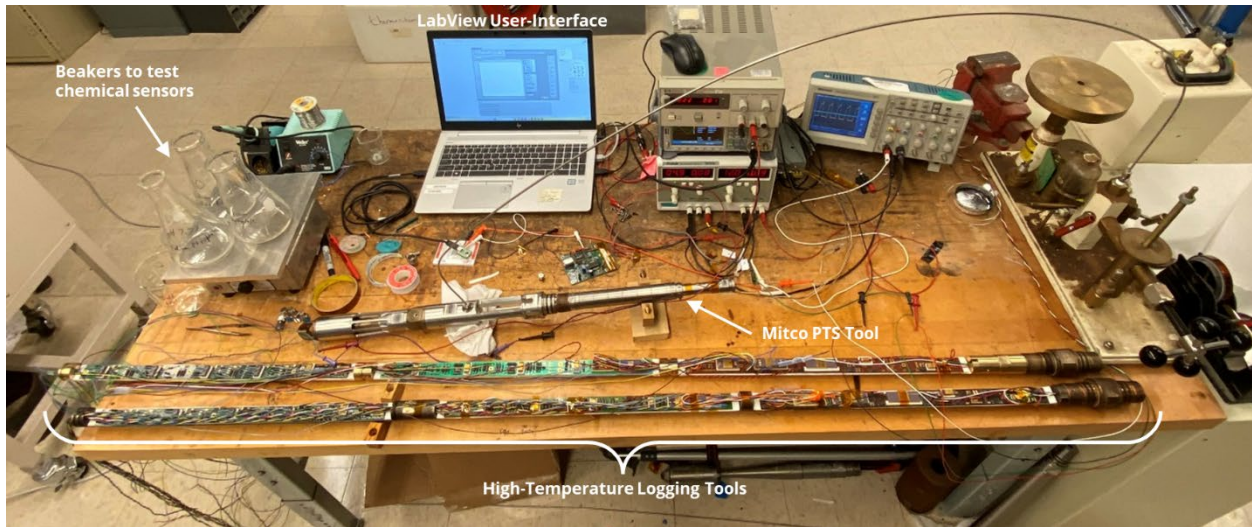


Figure 2-29: Primary High-Temperature Logging Tools being tested to confirm operation in benchtop test.

A LabView user interface was developed (shown in Figure 2-30) to efficiently handle serial data from the tool, offering real-time data display and recording capabilities on a PC. The interface was designed for compatibility with both the primary and secondary High-Temperature Logging tools. This streamlined field operations for each tool configuration.

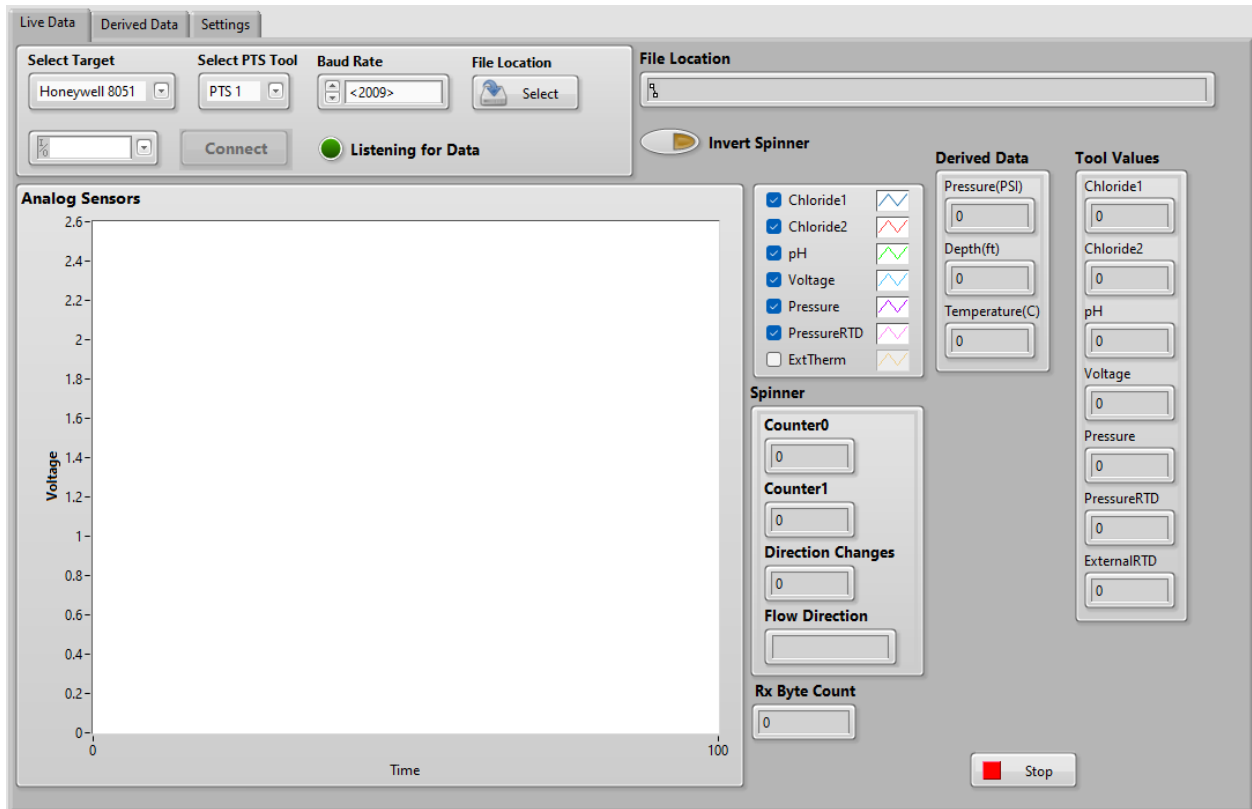


Figure 2-30: LabView User Interface for Field-Scale Chloride Tool.

# Chapter 3

## Analytical Formulation and Data-Driven Inference

### 3.1 Analytical Formulations

Gao (2017) developed an analytical solution for multiphase flow to calculate the flowing enthalpy resulting from the change in chloride concentration. This study modified the solution to calculate the feed zone inflow rate. Additionally, the analytical derivation focused on single-phase fluid (specifically, liquid), as the calculations were applied during field testing at the Utah FORGE site. The nomenclature that is used for deriving the analytical formulas are summarized in Table 3-1.

**Table 3-1:** Nomenclature for the analytical formula derivation.

Symbol	Quantity	Unit
$Cl_x$	Chloride concentration; $x$ denotes certain location or at certain condition	kg/m <sup>3</sup>
$q$	Volumetric flow rate	m <sup>3</sup> /s
$q_x$	Volumetric flow rate of the liquid phase at certain location	m <sup>3</sup> /s
$\rho_{liquid}$	Liquid phase density	kg/m <sup>3</sup>
$\dot{m}_{cl\ x}$	Mass flow rate of chloride; $x$ denotes certain location or at certain condition	kg/s
$\dot{m}_{liquid\ x}$	Mass flow rate of the liquid phase; $x$ denotes certain location or at certain condition	kg/s
$e_f$	Average relative error factor	unitless

Schematics of geothermal wells with single feed zones and multiple feed zones are shown in Figure 3-1. It is assumed that the volumetric flow rate at the wellhead is known and measured independently of the geochemistry-based tool and that the liquid density remains constant.

The mass balance principle can be applied to establish the relationship between the flow rate at the wellhead and above the feed zone using Equation (3-1):

$$d(Cl \cdot q) = 0 \quad (3-1)$$

Thus, for single feed zone case, the mass rate above the feed zone can be described by Equation (3-2):

$$\begin{aligned} \dot{m}_{cl,above} &= \dot{m}_{cl,wellhead} Cl_{above} \cdot q_{above} = Cl_{wellhead} \cdot q_{wellhead} q_{above} \\ &= q_{wellhead} \cdot \frac{Cl_{wellhead}}{Cl_{above}} C q_{above} \cdot \rho_{liquid} \\ &= q_{wellhead} \cdot \rho_{liquid} \frac{Cl_{wellhead}}{Cl_{above}} \\ \dot{m}_{liquid,above} &= q_{wellhead} \cdot \rho_{liquid} \frac{Cl_{wellhead}}{Cl_{above}} \end{aligned} \quad (3-2)$$

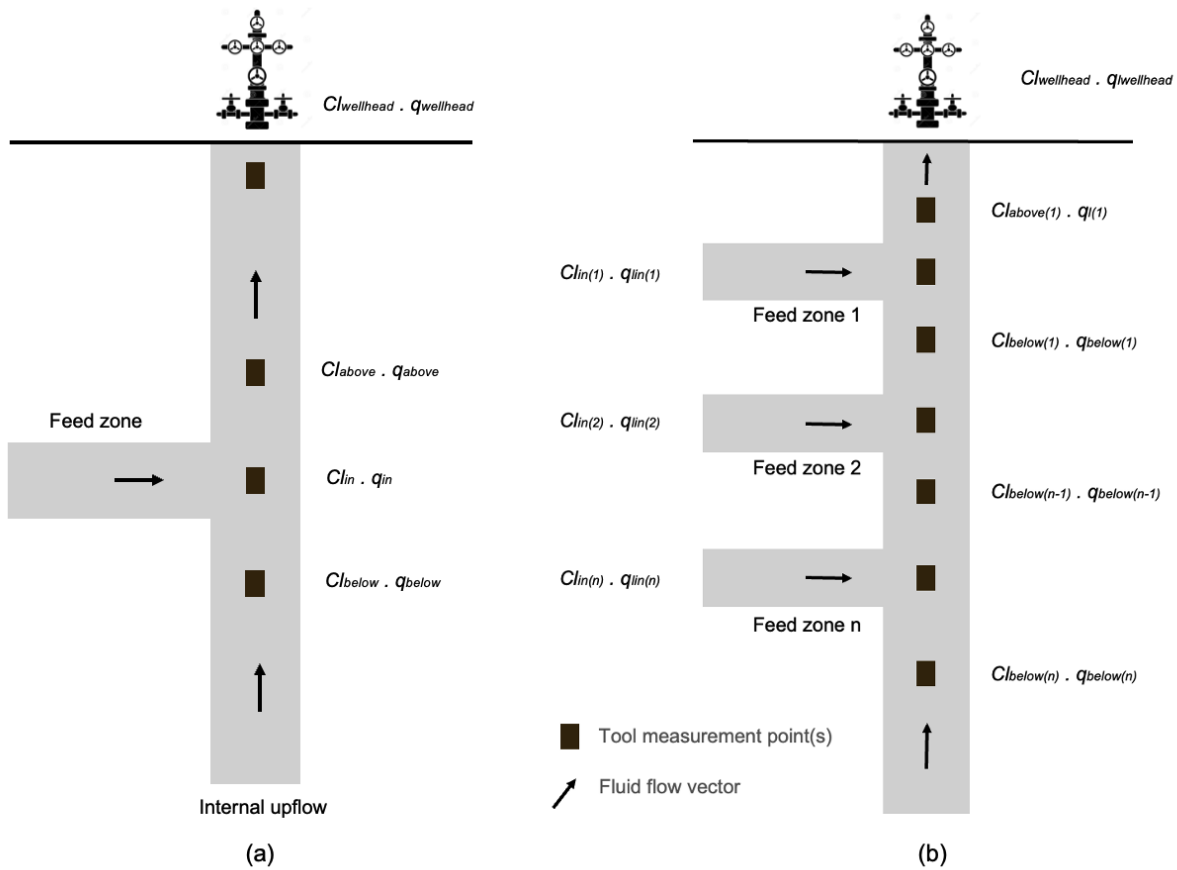


**Figure 3-1:** Schematics of a geothermal well with (a) single feed zones and (b) multiple feed zones.

Considering similar mass balance principles between three places: above the feed zone, at the feed zone, and below the feed zone, the calculation for the mass flow rate from the feed zone could be derived to obtain Equation (3-3):

$$\begin{aligned}
\dot{m}_{cl,in} + \dot{m}_{cl,below} &= \dot{m}_{cl,above} Cl_{in} \cdot q_{in} + Cl_{below} \cdot q_{below} \\
&= Cl_{above} \cdot q_{above} Cl_{below}(q_{above} - q_{in}) + Cl_{in} \cdot q_{in} \\
&= Cl_{above} \cdot q_{above} Cl_{below} \cdot q_{above} - Cl_{below} \cdot q_{in} + Cl_{in} \cdot q_{in} \\
&= Cl_{above} \cdot q_{above} Cl_{in} \cdot q_{in} - Cl_{below} \cdot q_{in} \\
&= Cl_{above} \cdot q_{above} - Cl_{below} \cdot q_{above} (Cl_{in} - Cl_{below})q_{in} \\
&= (Cl_{above} - Cl_{below}) \cdot q_{above} q_{in} \\
&= q_{above} \frac{Cl_{above} - Cl_{below}}{Cl_{in} - Cl_{below}} q_{in} \cdot \rho_{liquid} \\
&= q_{above} \cdot \rho_{liquid} \cdot \frac{Cl_{above} - Cl_{below}}{Cl_{in} - Cl_{below}} \\
\dot{m}_{liquid,in} &= \dot{m}_{above,in} \cdot \frac{Cl_{above} - Cl_{below}}{Cl_{in} - Cl_{below}} \tag{3-3}
\end{aligned}$$

The fraction in Equation (3-3) can be written as  $Cl_{ratio}$  such that:

$$Cl_{ratio} = \frac{Cl_{above} - Cl_{below}}{Cl_{in} - Cl_{below}} \tag{3-4}$$

Incorporating Equation (3-4), Equation (3-3) can then be written as:

$$\dot{m}_{liquid,in} = \dot{m}_{above,in} \cdot Cl_{ratio} \tag{3-5}$$

Upon examining the chloride concentration log pattern, the chloride concentration from below the feed zone to zero could be normalized to zero under ideal conditions. In such case, the  $Cl_{below}$  became zero, and the  $Cl_{ratio}$  in Equation (3-4) could be simplified to:

$$Cl_{ratio} = \frac{Cl_{above}}{Cl_{in}} \tag{3-6}$$

The single feed zone calculation can be expanded to account for multiple feed zones. Denoting the topmost feed zone as feed zone 1, followed by feed zone 2, *et cetera* such that the feed zone can be denoted with  $n$ . The flow rate calculations for feed zone 1 are the same as with the single feed zone calculations, while the subsequent feed zones flow rate are:

$$Cl_{ratio(n)} = \frac{Cl_{below(n-1)} - Cl_{below(n)}}{Cl_{in(n)} - Cl_{below(n)}} \tag{3-7}$$

$$q_{above(n)} = q_{below(n-1)} \tag{3-8}$$

$$q_{in(n)} = q_{below(n-1)} \cdot Cl_{ratio(n)} \tag{3-9}$$

$$q_{below(n)} = q_{below(n-1)} \cdot (1 - Cl_{ratio(n)}) \tag{3-10}$$

## 3.2 Error Estimation and Modeling

Gao (2017) did a series of experiments to determine the average relative error of measured chloride concentration versus actual known chloride concentration with respect to different gas flow rates. It was found that for liquid flow, the measurement underestimated the actual chloride concentration by around 1.2%. However, the noise level at the feed zone could be different than at the well head or above or below the feed zone. Therefore, relative error of chloride measurement at various points at the wellbore and its effect to the resulting flow rate calculations need to be understood.

The average relative error of the chloride measurement can be represented with error factor  $e_f$ , which upon multiplying with the measured value, will give the corrected chloride measurement, such that:

$$Cl_{corr} = Cl_{measured} \cdot e_f \quad (3-11)$$

where  $Cl_{corr}$ ,  $Cl_{measured}$ , and  $e_f$  are corrected chloride measurement, measured chloride measurement, and average relative error factor, respectively. The chloride ratio in Equation (3-7) can then be corrected accordingly to account for relative error fluctuating at different points in the wellbore:

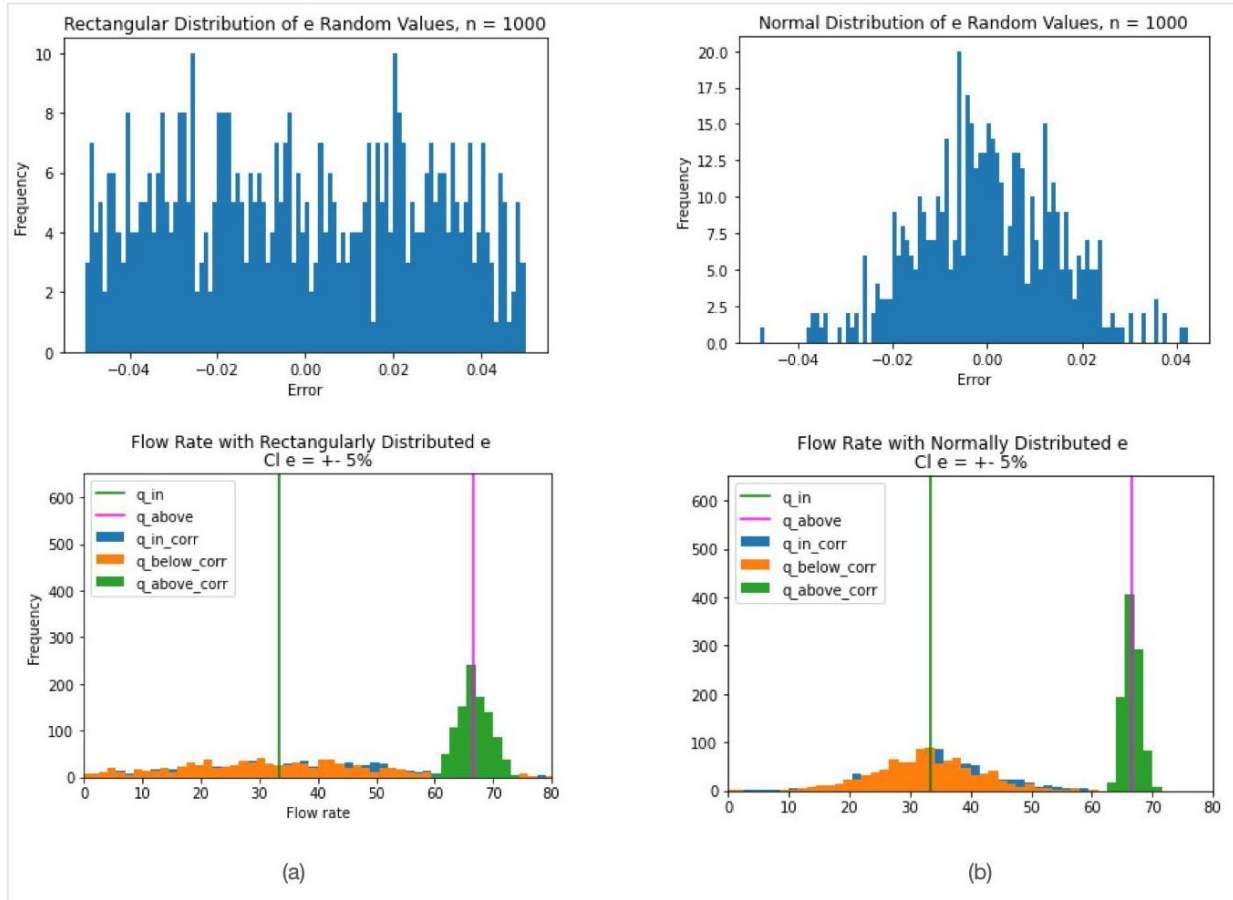
$$Cl_{ratio(corr)} = \frac{Cl_{above} \cdot e_{fabove} - Cl_{below} \cdot e_{fbelow}}{Cl_{in} \cdot e_{fin} - Cl_{below} \cdot e_{fbelow}} \quad (3-12)$$

The volumetric flow rate calculations for both single feed zone and multiple feed zones can be corrected in a similar manner, where each of the measured flow rate concentration is multiplied by its error factor.

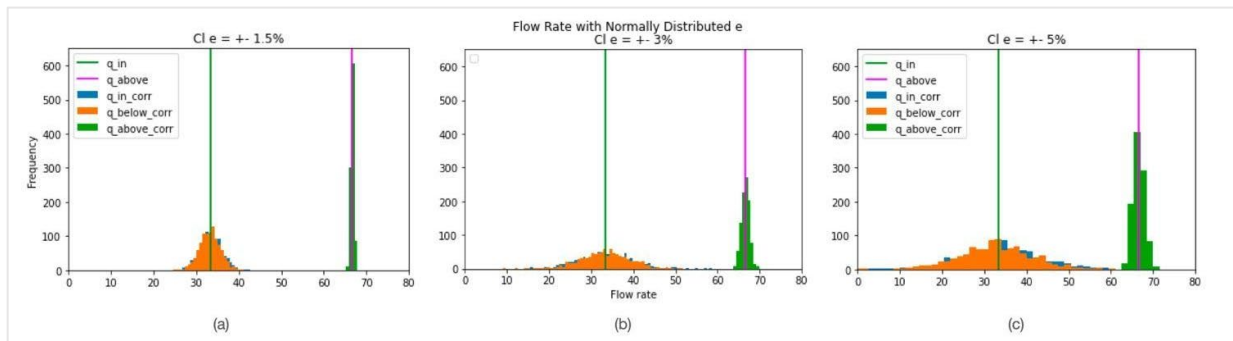
Taking the formulas defined in Section 3.1, the range of discrepancies between uncorrected and corrected chloride measurements at various points of the wellbore were modeled stochastically to understand their effect on the resulting flow rate calculations. Numerical simulations involving 1000 runs of flow rate calculations were performed with randomly distributed  $e$  values, using rectangular and normal distribution methods for comparison.

Figure 3-2 shows a snapshot of the  $e$  value distribution for each type of random distribution and the resulting mass flow rate calculations in a well with single feed zone. As expected, the simulation results show that normally distributed error value yields narrower volumetric flow rate range compared to rectangular distribution. The range of  $q_{above}$  is consistently narrower than  $q_{in}$  and  $q_{below}$  with the latter pair being similar in range to each other. For each distribution, different error ranges were tested, namely  $\pm 1.5\%$ ,  $\pm 3\%$ , and  $\pm 5\%$ , all with 500 intervals (Figure 3-3). There is a positive correlation between increasing error ranges and increasing the flow rate ranges, and  $q_{above}$  consistently has a narrower range compared to  $q_{in}$  and  $q_{below}$ , with the latter pair being similar in range to each other.

From the error modeling for the single feed zone case, it can be concluded that measurement error will adversely affect the accuracy of volumetric flow rate calculations at and below the feed zone but not so much above the feed zone.



**Figure 3-2:** Snapshots of  $e$  distribution and resulting volumetric flow rate calculation for a well with single feed zone with (a) rectangular and (b) normal distribution methods.



**Figure 3-3:** The simulation result of resulting volumetric flow rate calculations for the different ranges of  $e$ : (a)  $\pm 1.5\%$ , (b)  $\pm 3\%$ , and (c)  $\pm 5\%$ .

### 3.3 Nernst Equation

The Nernst equation yields the voltage at which electrochemical reactions occur. Relevant to this research, the Nernst Equation relates the potential difference between a reference electrode and a chloride ISE probe to the ion concentration in the surrounding solution. In short, the Nernst Equation

is used to assess the chloride concentration of the fluid in a well using the voltage produced by a chloride ISE probe.

Further discussion on the application of the Nernst Equation as the basis of the sensor development is detailed in Section 2.1. The equation is shown as Equation (2-1), which is once again detailed here:

$$E = E^0 + \frac{RT}{nF} \ln \left( \frac{[Cl^-]_{sample}}{[Cl^-]_{ref}} \right) \quad (3-13)$$

Using the Nernst Equation with the assumption that fluid solutions in the Stanford Geothermal Laboratory are at 70°F (294 K), the relationship between the negative common (base 10) logarithm of the chloride concentration and the voltage reading of a chloride ISE probe is  $-17.13 - \log_{10}(\text{mol/L})/V$ . An experimental determination of this relationship for the chloride tool used for this project is described later in Section 4.2.2.3. This empirical relationship was then used to infer the chloride concentration of the wellbore fluid for the experiments.

### 3.4 Machine Learning (ML) Models for Flow Rate Prediction and Inference

Machine Learning (ML) models were developed using data from numerical simulations and laboratory experiments, as detailed in the following sections.

#### 3.4.1 ML models from numerical simulation data

Two types of ML models were constructed from numerical simulation data: a classification task to predict feed zone presence and a regression task to predict feed zone inflow rate. The ML models provided additional verification and validation to the deterministic analytical approach described in Section 3.1.

Important variables for the ML models were wellbore flow rate  $m_w$ , volume fraction  $X_{vol}$ , feed zone inflow rate  $m_{fz}$ , as illustrated in Figure 3-4. The continuous outcome variable was the feed zone flow rate (i.e. `m_fz_abs`), taken from the feed zone mass flow rate data (i.e. `saline.mass_flow`) at absolute value. This variable was chosen to be predicted for the regression task. In the simulation dataset, the  $m_{fz}$  variable was typically positive;  $m_{fz}$  could be negative in rare conditions where the wellbore mass flow ( $m_w$ ) was much larger.

The binary outcome variable was the Chloride/No-chloride indicator (CNC), which was chosen to be predicted for the classification task. The variable described the presence of chloride concentration above the  $x_{vol} = 0.3$  threshold. The choice was made because another purpose of the tool development was to detect feed zone presence, which the elevated value of measured chloride concentration would indicate.

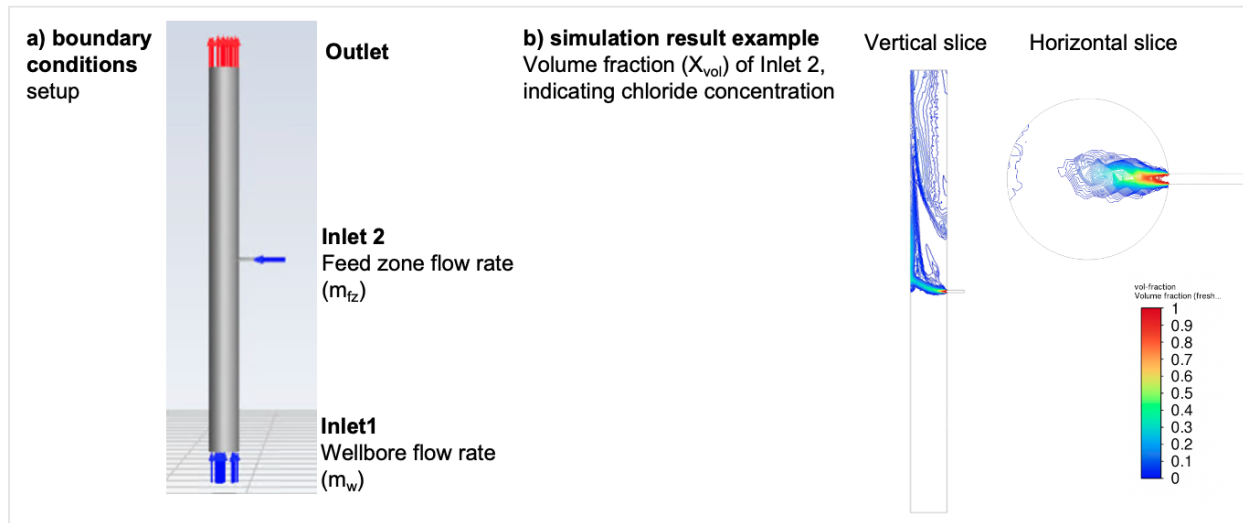


**Figure 3-4:** a) boundary conditions setup and b) example of one of the simulation results.

### 3.4.1.1 Dataset Description and Processing

The dataset was exported simulation data from ANSYS Fluent for the single feed zone, laboratory scale group, with different inflow rates ranging from 20 to 200 ml/s. The raw dataset consisted of nine CSV files representing five levels of  $\Delta m$ , which was the difference between  $m_w$  and  $m_{fz}$ . Each CSV file was comprised of 102 columns and 55,293 rows. Then, preliminary cleanup steps were performed:

- removing All-NULL or all-zero columns, duplicate columns, and ID columns
- removing artifacts from column names
- removing rows with  $Z$  values 5 cm above and below the feed zone

After the basic cleanup, the columns and rows were reduced to 86 and 4748, respectively. Then, the data was combined into a dataset with `delta_m` as a categorical variable. Figure 3-7 shows a snapshot of the dataset after cleanup.

While the preliminary cleanup removed metadata and columns with no content, irrelevant columns still existed and could be categorized as follows:

- Columns representing physical properties that were known to be constant and/or did not influence outcome variables, such as fluid density, viscosity, and wall terms.
- Columns describing wellbore inlet (Inlet1) properties, denoted by `Fresh_water.[property]`. This study was primarily interested in feed zone inlet (Inlet2) properties, represented by `saline.[property]`.
- Redundant vector-scalar property pair such as `velocity` and `velocity u`. These columns had the same values, albeit different signs. Variations of velocity derivation were also redundant.

The columns fitting the above categories were removed from the dataset, reducing the size to 15 columns before feature engineering. Figure 3-6 shows a dataset snapshot after removing the irrelevant columns.

	X	Y	Z	Connectivity Number	Density [ kg m <sup>-3</sup> ]	Eddy Viscosity [ Pa s ]	Edge Length Ratio	Element Volume Ratio	Fresh_water.Density [ kg m <sup>-3</sup> ]	Fresh_water.Mass Flow [ kg s <sup>-1</sup> ]	Fresh_water.Mass Flux [ kg s <sup>-1</sup> m <sup>-2</sup> ]
1	0.098068073	-0.0022603711	-2.973052e-03	24	998.2291	0.020689894	1.417972	1.910224	998.2001	NA	NA
2	0.113533482	-0.0007919451	3.603640e-03	20	998.2288	0.023361050	1.736969	2.729046	998.1998	NA	NA
3	0.131113410	-0.0024787444	2.794762e-03	26	998.2292	0.022379782	1.450702	2.502663	998.2001	NA	NA
4	0.082295090	0.0023520801	2.765230e-03	28	998.2288	0.020518860	1.488371	2.214659	998.2000	NA	NA
5	0.140606761	-0.0014158504	3.433708e-03	26	998.2289	0.017396051	1.543976	2.246444	998.2000	NA	NA
6	0.101994127	-0.0035862613	1.469180e-03	24	998.2291	0.022395393	1.568359	2.185542	998.2002	NA	NA
7	0.091810815	-0.0010813997	-3.631525e-03	34	998.2290	0.018575089	1.629777	1.915058	998.2001	NA	NA
8	0.143021718	-0.0037759561	-2.885023e-04	24	998.2289	0.017472154	1.681235	2.436030	998.2001	NA	NA
9	0.122767076	0.0009102449	-3.701310e-03	24	998.2289	0.021677509	1.417120	1.974428	998.2000	NA	NA
10	0.073727682	0.0011773282	-5.629330e-03	22	998.2057	0.013648283	1.401605	2.064891	998.2000	NA	NA
11	0.033005368	-0.0598742738	1.469044e-02	24	998.1999	0.010351501	1.562315	2.232014	998.1999	NA	NA
12	0.110131837	-0.0008804951	-3.582205e-03	26	998.2291	0.022085542	1.708438	1.835510	998.2000	NA	NA
13	0.108592220	-0.0034403081	9.241738e-04	26	998.2291	0.023094615	1.535854	3.395489	998.2000	NA	NA
14	0.137021706	-0.0033052994	-1.960083e-03	24	998.2290	0.016614107	1.463132	1.647898	998.2002	NA	NA
15	0.143170163	-0.0027735164	2.008910e-03	32	998.2291	0.018252600	1.648979	2.808631	998.2001	NA	NA
16	0.143667817	-0.0008755475	3.654723e-03	26	998.2291	0.015266401	1.626567	2.894251	998.2000	NA	NA
17	0.075645320	-0.0019787759	-3.162856e-03	26	998.2293	0.020779779	1.488478	2.109255	998.2001	NA	NA
18	0.047954284	0.0460385606	-2.063737e-03	30	998.2002	0.010305638	1.505907	2.326880	998.2002	NA	NA
19	-0.066250309	-0.0138883628	1.710731e-03	26	998.2001	0.012837728	1.615620	2.061676	998.2000	NA	NA

Figure 3-5: Snapshot of the dataset after cleanup.

	X	Y	Z	Mass Flow [ kg s <sup>-1</sup> ]	Mass Flux [ kg s <sup>-1</sup> m <sup>-2</sup> ]	Maximum Face Angle [ degree ]	Minimum Face Angle [ degree ]	Pressure [ Pa ]	Saline.Mass Flow [ kg s <sup>-1</sup> ]	Saline.Mass Flux [ kg s <sup>-1</sup> m <sup>-2</sup> ]	Saline.Velocity [ m s <sup>-1</sup> ]	Saline.Volum Fraction
1	0.098068073	-0.0022603711	-2.973052e-03	NA	NA	82.05474	41.87951	176.0166170	NA	NA	1.43029368	1.00000
2	0.113533482	-0.0007919451	3.603640e-03	NA	NA	90.84691	46.17827	257.1559140	NA	NA	1.46380281	1.00000
3	0.131113410	-0.0024787444	2.794762e-03	NA	NA	81.48926	41.76652	359.0093080	NA	NA	1.48106539	1.00000
4	0.082295090	0.0023520801	2.765230e-03	NA	NA	84.91945	38.48277	99.0095673	NA	NA	1.46314287	1.00000
5	0.140606761	-0.0014158504	3.433708e-03	NA	NA	93.52994	42.11637	421.7272950	NA	NA	1.48552752	1.00000
6	0.101994127	-0.0035862613	1.469180e-03	NA	NA	86.65047	43.10387	202.9893650	NA	NA	1.45495737	1.00000
7	0.091810815	-0.0010813997	-3.631525e-03	NA	NA	89.60238	34.10569	152.8173520	NA	NA	1.41592240	1.00000
8	0.143021718	-0.0037759561	-2.885023e-04	NA	NA	91.74816	35.41196	421.4381710	NA	NA	1.48401940	1.00000
9	0.122767076	0.0009102449	-3.701310e-03	NA	NA	90.18155	39.34724	309.8617550	NA	NA	1.45004892	1.00000
10	0.073727682	0.0011773282	-5.629330e-03	NA	NA	97.71808	40.71163	-14.5738649	NA	NA	0.28008309	1.9167C
11	0.033005368	-0.0598742738	1.469044e-02	NA	NA	88.20708	38.34227	2.1404934	NA	NA	0.11585496	0.00000
12	0.110131837	-0.0008804951	-3.582205e-03	NA	NA	85.94926	44.92817	243.9728550	NA	NA	1.46470046	1.00000
13	0.108592220	-0.0034403081	9.241738e-04	NA	NA	76.72916	35.81797	230.4454350	NA	NA	1.48237276	1.00000
14	0.137021706	-0.0033052994	-1.960083e-03	NA	NA	93.13265	43.41930	393.5093380	NA	NA	1.47828448	1.00000
15	0.143170163	-0.0027735164	2.008910e-03	NA	NA	75.16069	34.79697	421.4857480	NA	NA	1.48953104	1.00000
16	0.143667817	-0.0008755475	3.654723e-03	NA	NA	89.49286	38.00690	431.3360290	NA	NA	1.48975396	1.00000
17	0.075645320	-0.0019787759	-3.162856e-03	NA	NA	81.00785	34.00116	89.8146210	NA	NA	1.40553331	1.00000
18	0.047954284	0.0460385606	-2.063737e-03	NA	NA	74.53063	37.02788	-0.6915364	NA	NA	0.14495088	0.00000
19	-0.066250309	-0.0138883628	1.710731e-03	NA	NA	82.76974	35.52559	6.9743714	NA	NA	0.04925372	1.33455

Figure 3-6: Snapshot of the dataset after removing irrelevant columns.

While the no-content columns were removed during the preliminary data cleanup, some still contained null values. However, these null values were relevant to the analysis—for instance, the null values at `saline.volume_fraction` represented locations without chloride and part of the outcome variable CNC. Thus, these null values would be kept intact, and an engineered feature would be created to capture the null values in a binary fashion.

Engineered features were essential for this dataset, as the raw simulation data were quite rudimentary in capturing the physical properties. Some of the engineered features that were created:

- A categorical variable `delta_m` was created to represent the different delta levels between the feed zone flow rate ( $m_{fz}$ ) and the wellbore flow rate ( $m_w$ ).
- The binary outcome variable `CNC` was created using the threshold of `saline.volume_fraction` variable of equal or more than 0.3

Additionally, a few categorical variables were created to describe the visual properties of the volume fraction distribution seen from the horizontal slice. With these additional engineered features, the dataset size became 18-20 columns. Finally, 25% of the cleaned and processed dataset was set aside as the test set, while the remaining 75% was purposed for the training set.

### 3.4.1.2 Classification Task to Predict Feed Zone Presence

Four ML algorithms were used to create prediction models for the classification task to predict the feed zone presence. The description of each algorithm is as follows:

- **Logistic regression:** analyzes the effect of a group of independent variables on a binary outcome by quantifying each independent variable's unique contribution. Using components of linear regression reflected in the logit scale, logistic regression iteratively identifies the strongest linear combination of variables with the greatest probability of detecting the observed outcome (Stolzfus, 2011).
- **k-Nearest Neighbor (KNN):** a straightforward classifier that identifies the nearest neighbors to a query example and uses those neighbors to determine the class of the query (Cunningham and Delany, 2020)
- **Random Forest:** constructs an ensemble of decision trees and combines their predictions to improve accuracy and reduce overfitting. Random Forest easily adapts to nonlinearities found in the data. Generally, ensemble learning algorithms like Random Forest are well suited for medium to large datasets (Schonlau and Zou, 2020).
- **Linear Support Vector Machine (SVM):** binary classifiers based on vector representations of training instances that find a hyperplane between two classes such that the distance (margin) between the closest training examples and the hyperplane is maximized (Gholami and Fakhari, 2017).

Logistic regression was used for the classification task base model with all variables included except those causing collinearity. The performance was evaluated by comparing the Accuracy score and Cohen's Kappa coefficient.

The Accuracy score is a performance metric that measures how often a model correctly predicts the class label of an instance. It is calculated by dividing the number of correctly classified instances by the total number of instances in the dataset.

Cohen's Kappa coefficient measures agreement that can take values between -1 and 1. A score of 1 means that there is a perfect agreement, 0 means that agreement is due to chance, and negative values indicate less agreement than expected by chance. Typically, a Cohen's Kappa coefficient greater than 0.75 is considered an excellent agreement, while a value less than 0.4 indicates poor agreement.

The performance of four ML models applied to the training set for the binary outcome variable CNC is presented in Table 3-2, and the Receiver Operating Characteristics (ROC) plot is shown in Figure 3-7.

**Table 3-2:** Accuracy and Cohen’s Kappa performance metrics of the classification task applied to the training set with target variable CNC. The numbers colored green indicated that the error was lower than the base model, while the numbers colored red indicated a higher error than the base model.

Model Strategy	Accuracy after cross validation with K = 9	Cohen’s Kappa after cross validation with K = 9	Accuracy standard deviation	Cohen’s Kappa standard deviation
Base: logistic regression	0.9996372	0.9991198	0.0008161409	0.001980641
K-nearest neighbor	0.9804232	0.9531897	0.003546972	0.008343481
Random Forest	0.9997583	0.9994138	0.0005095314	0.001235728
Linear Support Vector Machine (SVM)	0.9995169	0.9988316	0.0008444516	0.002041898

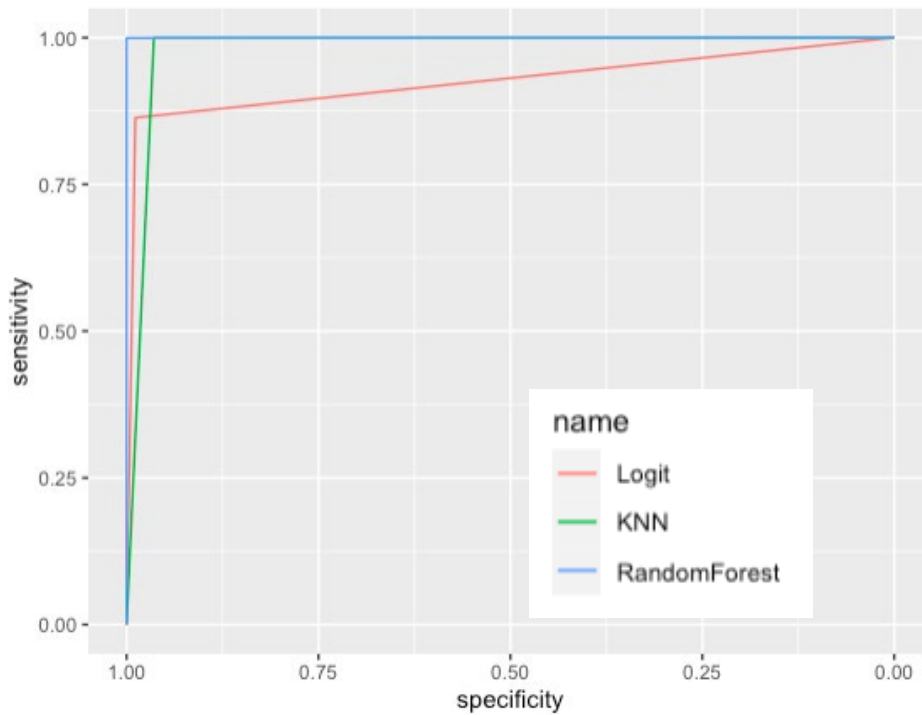


**Figure 3-7:** Comparison of different models for the classification task using the Receiver Operating Characteristics (ROC) plot.

When applied to the training set, the Random Forest model performed the best for the classification task, with the Accuracy score and Cohen’s Kappa coefficients 0.9997583 and 0.9994138, respectively. These scores were higher than the base model. In comparison, the test set prediction yielded the accuracy score and Cohen’s Kappa of 0.9997596 and 0.9994146, respectively, close to the results obtained from the training set. Figure 3-8 shows the ROC curve of the test versus training set fit using

the Random Forest classifier. It can be concluded that the Random Forest ML model was accurate in predicting feed zone presence, with an accuracy of up to 99.94%.

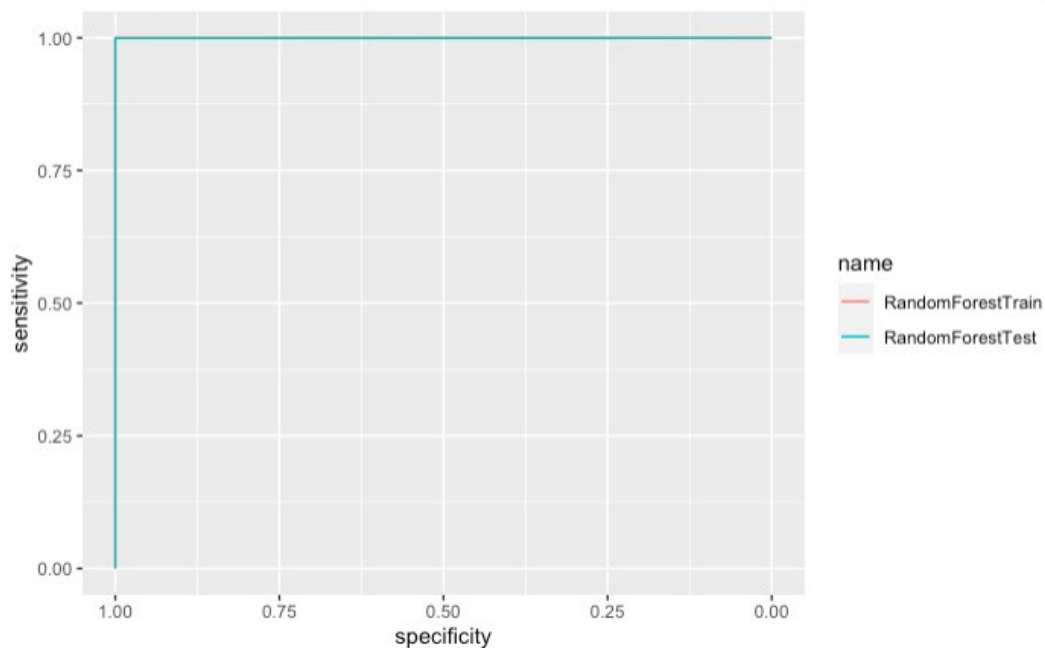


**Figure 3-8:** Receiver Operating Characteristics (ROC) curve for the classification task, fitted using Random Forest classifier on the training and test set.

### 3.4.1.3 Regression Task to Predict Feed Zone Inflow Rate

Five ML algorithms were used to create prediction models for the regression task to predict the feed zone inflow rate. The description of each algorithm is as follows:

- **Ordinary Least Squares (OLS):** a straightforward regression method that builds a line of best fit that depicts the spread of the data point with a single line. The line has the smallest value of summed squared errors for each data point (Burton, 2021).
- **Two-way Interaction:** a type of regression that factors in the two-way interaction among the predictor variables in determining the outcome variable (Yurochkin et al., 2017). In other words, the impact of one variable on the dependent variable depends on the specific value of the other variable.
- **Lasso Regularization:** Least Absolute Shrinkage and Selection Operator (LASSO, often stylized as Lasso) is a shrinkage and variable selection method for regression models to handle multicollinearity and prevent overfitting (Ranstam and Cook, 2018). The penalty term is the absolute value of coefficients and encourages some of them to be zero, leading to sparser models.
- **Ridge Regularization:** similar to Lasso, Ridge Regularization handles multicollinearity and prevents overfitting. The difference is that Ridge does not force coefficients to be zero but shrinks them towards zero while keeping all features in the models.
- **Random Forest:** similar to what has been described in Section 3.2.2, Random Forest can also be applied to regression tasks.

To evaluate the regression task ML models, the Root Mean Square Error (RMSE) obtained from cross-validations, including the base model, were compared to each other. The base model for the regression task used Ordinary Least Squares (OLS) using all covariates except for those knowingly caused multicollinearity. The performance of the ML models applied to the training set is summarized in Table 3-3, while the predicted versus actual plot of some of the models is shown in Figure 3-9.

**Table 3-3:** Root Mean Square Error (RMSE) of the regression task applied to the training set with target variable `m_fz_abs`. The numbers colored green indicated that the error was lower than the base model, while the numbers colored red indicated a higher error than the base model.

Model Strategy	RMSE cross validation with K = 5	RMSE cross validation with K = 10	RMSE cross validation with K = 30
Base model (Ordinary Least Square)	1.620875e-04	1.638290e-04	1.630212e-04
2-way interaction	2.410748e-18	3.464027e-18	3.139996e-18
Regularization, Lasso	1.830547e-04	1.838429e-04	1.832127e-04
Regularization, Ridge	3.567066e-04	3.569010e-04	3.571469e-04
Random Forest	4.569285e-05	3.107511e-05	3.086787e-05

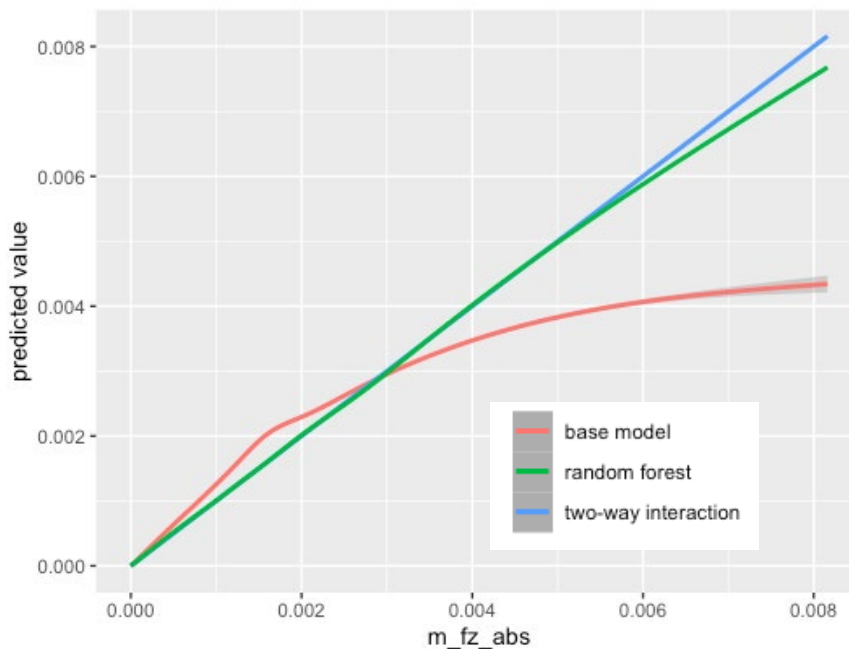


**Figure 3-9:** Comparison of different models for the regression task applied to the training set using a plot of predicted versus actual `m_fz_abs` value.

When applied to the training set of the regression task, the Random Forest model once again performed the best. The Random Forest model yielded an RMSE of  $3.1 \times 10^{-5}$  in the training set, calculated using 10-fold cross-validation. Even though the two-way interaction model had the smallest error, the error was erroneously too small, indicating overfitting. Thus, the Random Forest model was selected as the best model for the regression task instead.

Figure 3-10 shows the predicted vs. actual plot of the test and training set fit using the Random Forest algorithm. When the Random Forest model was applied to the test set, the RMSE became  $6.440249 \times 10^{-5}$ . This doubling in the error size was expected, as the test set was only a quarter in size compared to the training set, and thus the error would typically be twice in size.

It can be concluded from the model evaluation criteria that the Random Forest model was the best for the regression task in predicting the feed zone inflow rate. Furthermore, it was discovered that Random Forest was a robust model that performed the best for classification and regression tasks in this study. Indeed, Random Forest has consistently delivered excellent results in various geothermal use cases, including geothermal well flow rate prediction, well placement optimization, and reservoir mineralogy segmentation.

The literature supported Random Forest robustness for geothermal applications, such as Tamburello et al. (2022), who employed the Random Forest algorithm to map the global distribution of thermal springs and its relationship with endogenous and exogenous factors. Okoroafor et al. (2022) documented various ML applications in geothermal over the past two decades, including research by Shahdi et al. (2021), where Random Forest and Gradient Boost achieved the highest accuracy in subsurface temperature prediction.

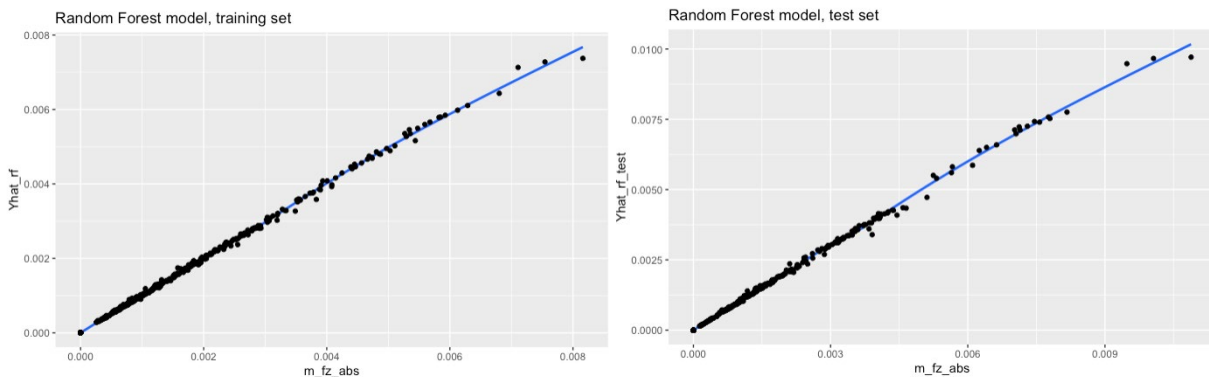


**Figure 3-10:** predicted vs. actual plot for the regression task, fitted using the Random Forest model on the (left) training and (right) test set.

#### 3.4.1.4 Inference to Determine Statistically Significant Covariates

Inference analysis was done to gain insights into the primary variables (i.e., covariates) that determine the accuracy of the feed zone inflow rate prediction. Statistically significant coefficients were determined using a probability value or p-value cutoff against the null hypothesis, i.e., the statement that there was no effect in the population parameter being studied.

A low p-value (typically less than a predefined significance level, often 0.05) suggests that the observed results are unlikely to have occurred under the null hypothesis, providing evidence against the null hypothesis. A high p-value indicates that the observed results could easily have occurred due to random chance, and there is insufficient evidence to reject the null hypothesis.

The base model of the regression task, the Ordinary Least Square model, was chosen for the first inference analysis even though the Random Forest model was the best-performing model due to the Random Forest algorithm’s “black-box” nature. The base model included all but six covariates known to cause collinearity.

From the regression output (see Figure 3-11), nine out of 17 coefficients were deemed statistically significant based on the p-value cutoff (i.e.,  $\alpha$ ) of 0.05. In particular, six coefficients were denoted with three-star (p-value < 0.001), followed by two coefficients with two stars (p-value < 0.01), and one coefficient with one star (p-value < 0.05).

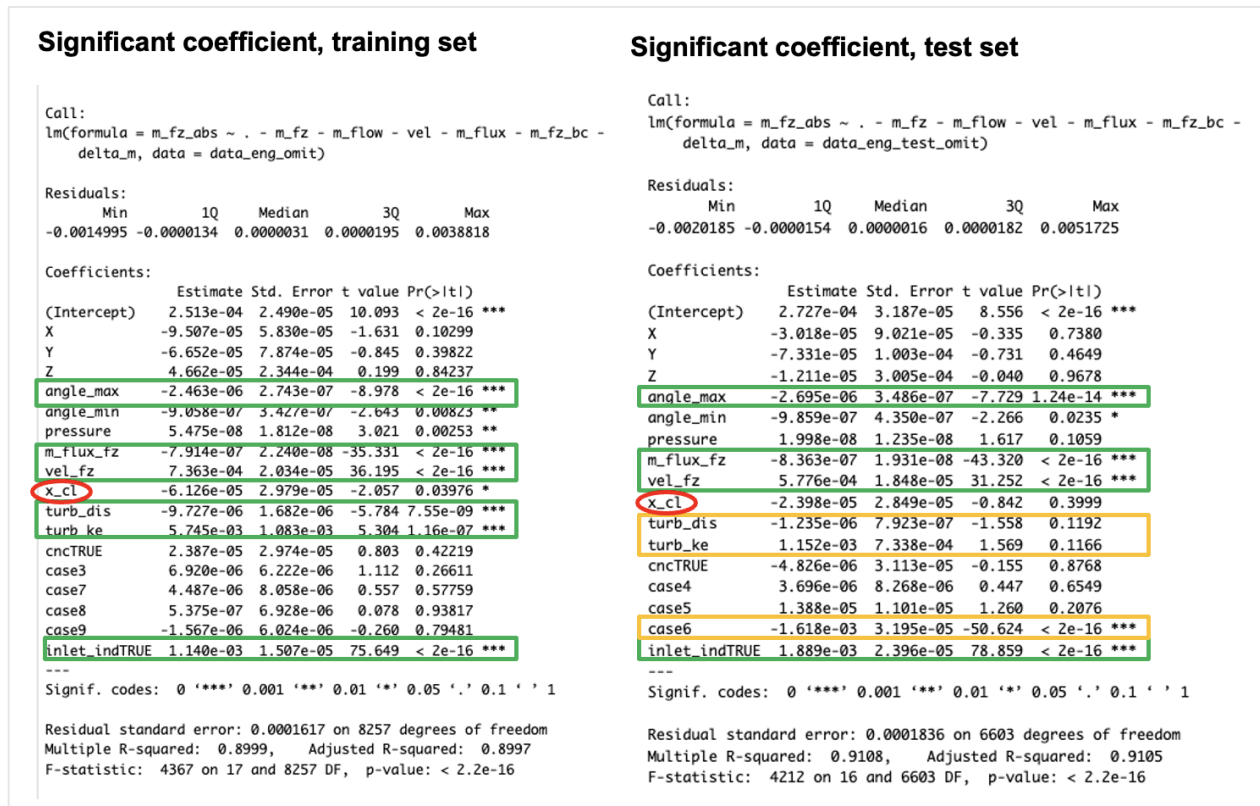


**Figure 3-11:** Comparison of regression output in the training vs test set. Green boxes indicate significant coefficients that are also found in the test set, while yellow boxes are significant coefficients only found in the training set. The red circle marks the  $x_{cl}$  covariate, which is an important covariate in the model.

Looking at the p-value results and knowing what was important in the chloride tool research, there was a discrepancy between the statistical versus practical significance, especially if a more conservative  $\alpha$  cutoff was used. Consider  $x_{cl}$  (i.e., chloride concentration), one of the most important variables in the research and a property that we could measure in the field. Only when  $\alpha = 0.05$  was used would the  $x_{cl}$  be deemed statistically significant; a more conservative  $\alpha$  cutoff of 0.01 and 0.005 would entirely miss  $x_{cl}$ . On the other hand, some coefficients already known to be practically significant in the research made it to the significant coefficient list. For example, the feed zone indicator,  $inlet\_indTRUE$ , was denoted by three stars.

Therefore, we needed to be cautious of extending the statistical significance into practical significance – the former indicated that the coefficient was significant in the context of the specific model (i.e., the base model in our case) but not necessarily in the population.

Upon fitting the base model to the test set, a change was observed in the significant coefficients. Only six out of 17 coefficients passed the  $\alpha = 0.005$  cutoff. Specifically, five coefficients had three stars, and one coefficient had one star. Furthermore, out of the nine statistically significant coefficients in the training set, only five were carried over to the test set fit. The turbulence coefficients,  $turb\_dis$  and

turb\_ke did not make it into the list, nor did x\_cl, a practically significant coefficient. Additionally, one new coefficient showed up as a statistically significant coefficient in the test set which is the case group indicator (case6).

Overall, the test set had fewer coefficients deemed statistically significant compared to the training set, indicating an overfitting of the model in the training set. Indeed, the residual standard error of the test set fitting was larger than the training set fitting (0.0001617 vs. 0.0001836), indicating an overfit in the training set.

The bootstrap method was then applied to the test set fit using 1000 replicates, followed by construing each regression coefficient's 95% confidence interval. A comparison between the confidence interval obtained from standard regression and the bootstrap is shown in Figure 3-12.

	95% confidence interval via standard output		idx	95% confidence interval via bootstrap		Difference		
	2.5 %	97.5 %		2.5%	97.5%			
(Intercept)	2.024995e-04	3.001169e-04	1	1	1.881109e-04	3.184456e-04	1	6.11%
X	-2.093610e-04	1.921457e-05	2	2	-1.287542e-04	-5.577673e-05	2	190.28%
Y	-2.208693e-04	8.782535e-05	3	3	-9.215396e-05	-3.970280e-05	3	-54.79%
Z	-4.129169e-04	5.061555e-04	4	4	-1.197936e-04	2.173488e-04	4	-57.06%
angle_max	-3.000198e-06	-1.924901e-06	5	5	-3.153646e-06	-1.811548e-06	5	-5.89%
angle_min	-1.577671e-06	-2.339763e-07	6	6	-1.652869e-06	-1.458569e-07	6	-37.66%
pressure	1.922488e-08	9.028228e-08	7	7	2.985876e-08	7.685829e-08	7	-14.87%
m_flux_fz	-8.353605e-07	-7.475366e-07	8	8	-9.083465e-07	-6.770232e-07	8	-9.43%
vel_fz	6.964673e-04	7.762246e-04	9	9	5.875091e-04	8.981373e-04	9	15.71%
x_cl	-1.196587e-04	-2.869417e-06	10	10	-8.789706e-05	-2.353824e-05	10	720.31%
turb_dis	-1.302385e-05	-6.430820e-06	11	11	-1.403124e-05	-4.865404e-06	11	-24.34%
turb_ke	3.621779e-03	7.868419e-03	12	12	2.899053e-03	8.253830e-03	12	4.90%
cncTRUE	-3.442163e-05	8.215693e-05	13	13	-2.281696e-06	4.227461e-05	13	-48.54%
case3	-5.277281e-06	1.911743e-05	14	14	-7.643053e-06	2.069546e-05	14	8.25%
case7	-1.130727e-05	2.028221e-05	15	15	-8.071087e-06	1.616292e-05	15	-20.31%
case8	-1.304360e-05	1.411852e-05	16	16	-9.087600e-06	1.060134e-05	16	-24.91%
case9	-1.337508e-05	1.024174e-05	17	17	-1.209272e-05	9.542986e-06	17	-6.82%
inlet_indTRUE	1.110155e-03	1.169220e-03	18	18	1.013792e-03	1.262327e-03	18	7.96%

**Figure 3-12:** Comparison of 95% confidence interval obtained via standard error vs bootstrap, applied to the test set.

Some coefficients, notably the mesh location indicator X and the chloride concentration indicator x\_cl showed a significant widening of confidence interval when the bootstrap method was used – almost two-fold and seven-fold widening, respectively. The depth indicator Z showed a shrinking of the confidence intervals, albeit not as severe as the widening observed.

The Bootstrap method involved making minimal assumptions about the characteristics of the population model. While this approach resulted in wider intervals, it was a trade-off for making fewer assumptions than the parametric approach.

Another inference analysis was done using the two-way interaction model to compare with the results from the base model. The significant coefficients for the two-way interaction model are shown in Figure 3-13. In this context, the three-star coefficients (p-value < 0.001) were considered.

Compared with the base model's significant coefficients described earlier, all the statistically significant interaction terms contained one or more covariates that showed up as significant in the base model: the angle terms (angle\_min, angle\_max), the turbulence terms (turb\_dis, turb\_ke), case

indicators, pressure term (pressure), feed zone indicator (cncTRUE), and most importantly, the chloride concentration (x\_cl).

The consistency of the significant coefficients between the base model and the two-way interaction model was reassuring, and these coefficients might indeed reflect practical significance in the population model.

<b>Three-star significant coefficient (P-value &lt; 0.001), training set</b>			
m_flow	X:case3	m_flow:inlet_indTRUE	angle_max:x_cl
0.000000e+00	9.884705e-10	0.000000e+00	6.650931e-04
angle_max:cncTRUE	angle_min:x_cl	angle_min:cncTRUE	pressure:x_cl
7.950866e-04	4.493843e-04	3.440112e-04	1.915067e-14
pressure:cncTRUE	x_cl:turb_dis	x_cl:case3	x_cl:case9
3.339683e-18	2.567708e-04	2.751035e-21	2.940472e-05
turb_dis:case3			
8.378711e-04			
<b>Three-star significant coefficient (P-value &lt; 0.001), test set</b>			
m_flow	m_flow:inlet_indTRUE	angle_max:x_cl	angle_max:cncTRUE
0.000000e+00	0.000000e+00	2.873904e-16	2.602341e-19
angle_min:x_cl	angle_min:cncTRUE	pressure:case4	pressure:case5
1.467687e-13	9.484424e-16	3.304184e-04	5.521639e-04
turb_ke:cncTRUE	cncTRUE:case4	cncTRUE:case5	
7.605116e-07	4.934311e-15	1.307290e-13	

**Figure 3-13:** Significant coefficients on the two-way interaction model with P-value less than 0.001 (three-starred), applied to training and test set.

### 3.4.2 ML models from laboratory experiment data

A second machine learning approach was developed to try to improve the identification and quantification of feed zones based on the voltage measurements obtained in the laboratory experiments. Two distinct models were constructed: a regression model for quantifying fracture inflow and a classification model for determining the presence of a fracture. The data collected from the single fracture inflow measurements shown in Chapter 5 served as the foundation for this approach. A data augmentation technique was employed to enhance the reliability of the original data.

Various methods and models were evaluated, including linear regression, logistic regression, random forest, XGBoost, Neural Network, and LGBM. After careful evaluation, the LGBM model demonstrated the highest performance scores on the validation set for both the regression and classification models. Moreover, LGBM predictions on the test set closely aligned with those on the validation set, indicating robust predictive capabilities.

Subsequently, it was discovered that incorporating a featured parameter, namely the delta of each measurement point, significantly improved the classification accuracy of the models. It is important to note that this approach is currently limited to single feed zone characterization. The application of the models to dual feed zone data did not yield satisfactory results.

### 3.4.2.1 Dataset and Data Augmentation

The dataset used in this approach was obtained from the measurements conducted during the Round 1 single fracture flow experiment described in Section 4.1.1.3. To facilitate the analysis, all the measured data was processed to create a standardized set of 100 voltage values for each RIH and POOH measurement.

In order to expand the dataset and improve the robustness of the machine learning model, data augmentation techniques were applied. This involved generating additional artificial data points based on the original measurements. The augmentation process included shifting the assumed feed zone location along the depth of the wellbore and shifting the actual measurements accordingly. This resulted in an augmented dataset that encompassed a wider range of scenarios and variations in feed zone positions.

To illustrate the data augmentation process, Figure 3-14 provides a visualization of an example where the original measurement is augmented by shifting the feed zone location and corresponding measurements. This technique allowed for a more comprehensive training dataset and increased the model's ability to accurately predict feed zone locations and quantify their characteristics. By incorporating data augmentation, the machine learning models were trained on a more diverse and extensive dataset, enabling them to generalize well and provide robust predictions even for scenarios beyond the original measurements.

After data augmentation, the dataset consists of a total of 2208 examples, which were divided into three sets: 60% for the training set, 20% for the validation set, and 20% for the test set. All features (103) are considered as input for the machine learning model. The 100 points of tool measurement range from 1 to -1, the total flow rate ranges from ~100 to ~900, and measurement conditions are presented as 1 if the measurement was taken upwards (POOH) and 0 if the measurement was taken downward (RIH). Lastly, cable speed was specified as float values between 1-3 cm/s. Normalization was used as a data preprocessing step to ensure that the features have a consistent range, which is important for most machine learning models to work effectively.

The expected output from each example for the logistic regression problem is a vector of 25 points, which describes whether there is fracture inflow (1) or not (0) at that section of the measurement. For the regression problem, the objective is to predict the continuous value of the flow rate from the fracture. A snapshot of a section of the data after normalization can be seen in Figure 3-14.

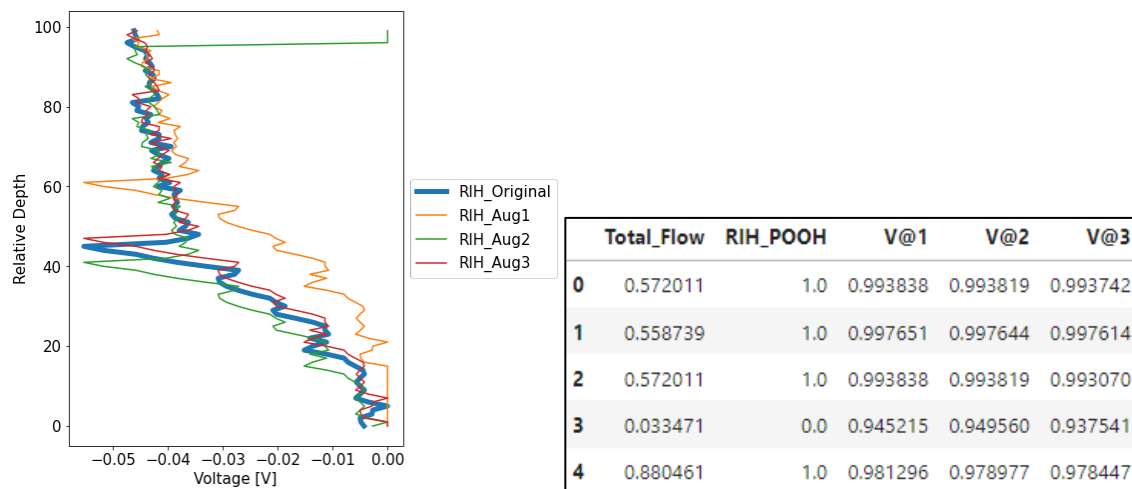


Figure 3-14: (left) data augmentation example and (right) dataset snapshot.

### 3.4.2.2 Methods

As a baseline model for the problem, linear regression and logistic regression were implemented first due to their simplicity compared to other algorithms. Afterward, more complex machine learning models, neural networks, decision trees, and gradient boosting were further evaluated. Explanation on the algorithms are as follows:

- **Neural networks** are a class of machine learning models that consist of multiple interconnected layers of nodes (neurons). Each node processes and transforms the input data to produce an output. Neural networks are trained using back-propagation, which is a gradient descent algorithm, to optimize the weights and biases of the nodes and minimize the prediction error. In the case of multiclass classification problems, the last layer of the neural network typically utilizes the softmax activation function to compute the probabilities for each class.
- **Decision trees**, on the other hand, are supervised machine-learning algorithms used for both classification and regression problems. They create a tree-like model of decisions and their potential consequences. The algorithm recursively partitions the data based on the values of the input features, resulting in a tree structure where each leaf node represents a decision or a prediction.
- **Gradient boosting** is a machine learning technique that builds a predictive model by sequentially adding weak learners to an ensemble. It adjusts the weights of these learners based on the errors made by the previous models. The goal is to iteratively reduce the prediction error by focusing on the hardest-to-predict cases. Gradient boosting utilizes gradient descent to minimize the prediction error and improve the model's performance. The resulting model is a weighted combination of the individual weak learners.

The performance of the fracture flow rate prediction models was evaluated using mean squared error (MSE), which measures the average squared difference between the predicted and actual values. A lower MSE indicates a better prediction performance.

For the classification task, the performance was evaluated based on accuracy, which measures the percentage of correctly classified instances. A higher accuracy indicates a better classification performance.

### 3.4.2.3 Results

As baseline models, linear regression and logistic regression were used to compare the performance of the more complex models. However, the results obtained from these baseline models were not satisfactory. The baseline model results are shown in Figure 3-15.

In the case of linear regression, it was observed that solely using gradient descent did not accurately predict the fracture inflow. This indicates that a linear relationship between the predictors and the outcome variables is not sufficient to capture the complexity of the problem. The logistic regression baseline showed a rough correlation between the predictors and the presence of fracture inflow, and the accuracy achieved for the test set was only 33%, which is far from satisfactory. This indicates that the logistic regression model alone was not able to effectively classify the instances. These results highlight the need for more complex models that can capture the nonlinear relationships and patterns in the data.

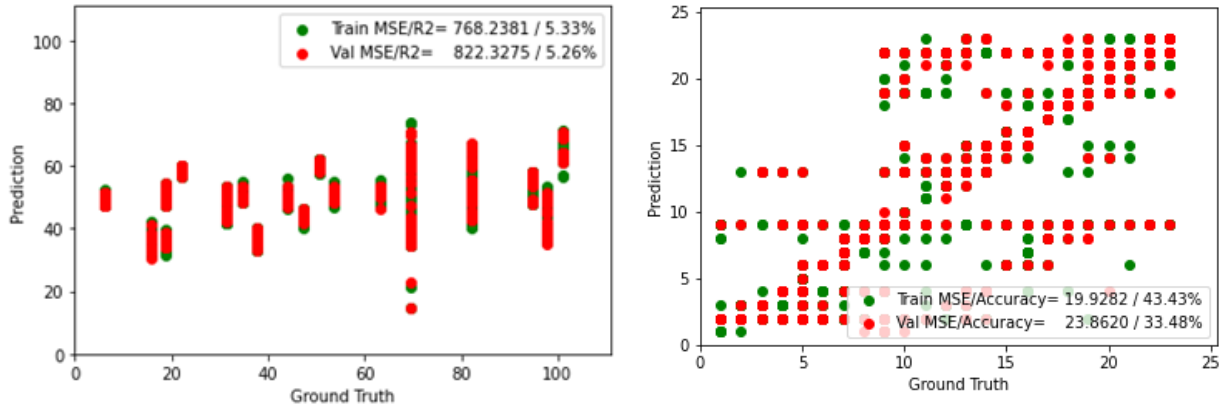


**Figure 3-15:** Linear regression (left) and logistic regression (right) training and validation set results.

The neural network was tuned by adjusting the number of layers, number neurons, epochs, batch size, learning rate and by applying regularization and dropout layer to reduce overfitting. As shown in Figure 3-17, it is seen that during the initial training epochs, the validation loss initially decreases but increase again halfway through the epochs indicating that model start to overfit given that the training loss keeps decreasing. However, in this case the accuracy, keeps increasing although validation loss increases, therefore both are evaluated at the same time.

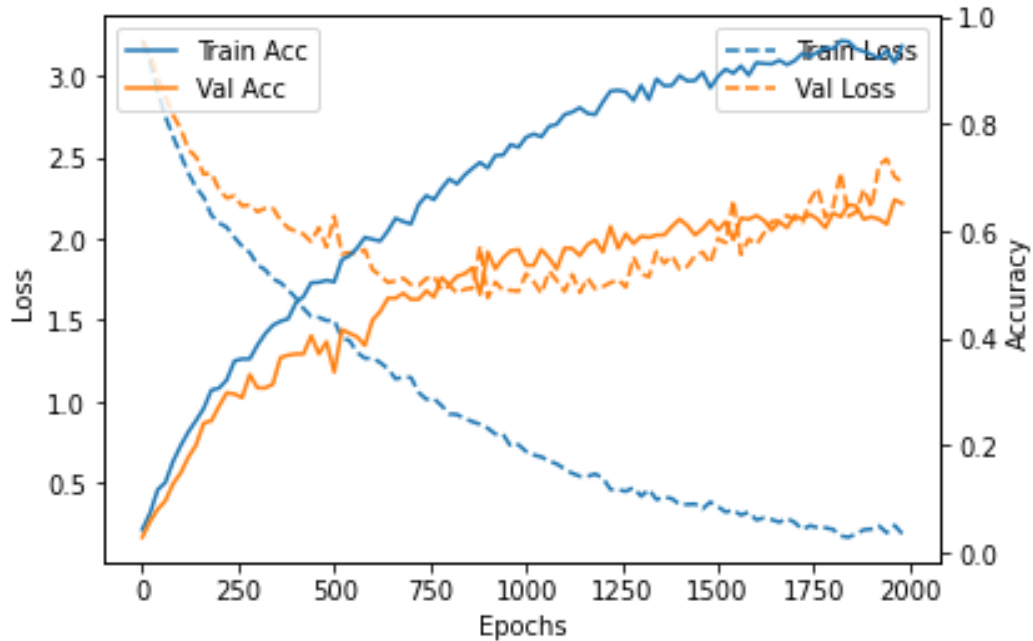


**Figure 3-16:** Neural network model accuracy and loss over epochs.

An example of the dropout rate sensitivity analysis is shown in Figure 3-17, it can be seen that the higher the dropout rate, the validation loss also decreases while the train loss is still quite stable. It is also noticed that the higher dropout rate resulted in more training accuracy reduction, therefore the rate was adjusted accordingly. All the parameters were tuned to achieve the best evaluation metric from validation set for both fracture flow rate and the classification problem.

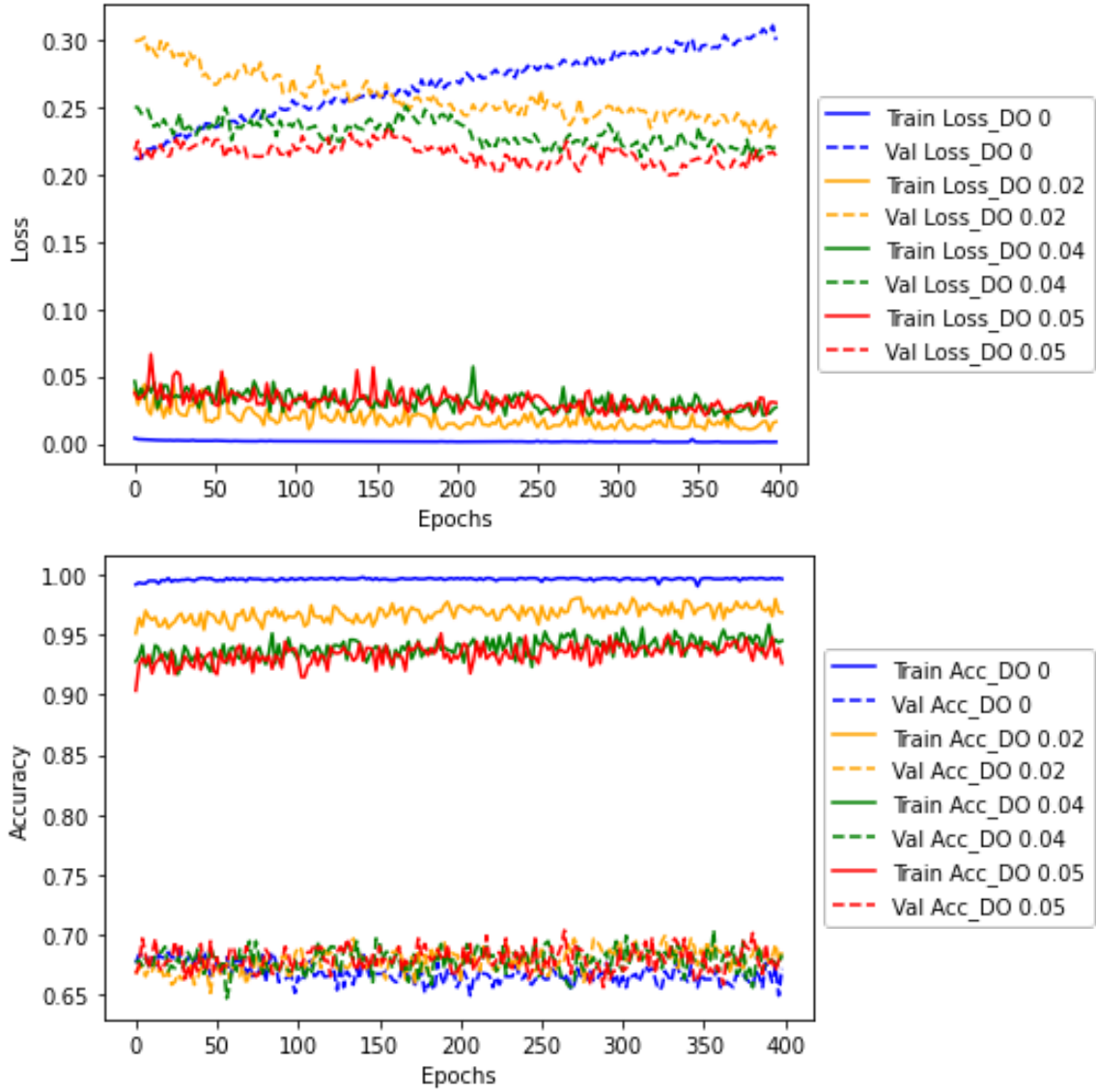


**Figure 3-17:** Neural network model accuracy and loss of drop-out rate variation.

The result of the model with tuned hyperparameters are shown where the injection regression converges to the best MSE from parameter testing. The hyperparameters optimized for the neural network were six layers with 10-100 neurons on each layer and a dropout rate of 0.06. The result shows the best MSE of 14.68 for the validation set. With the same workflow as the fracture flow prediction, the classification prediction using neural network achieve the best accuracy of 66.5%. Comparison between actual and predicted results of the fracture flow model fracture prediction is shown in Figure 3-18.

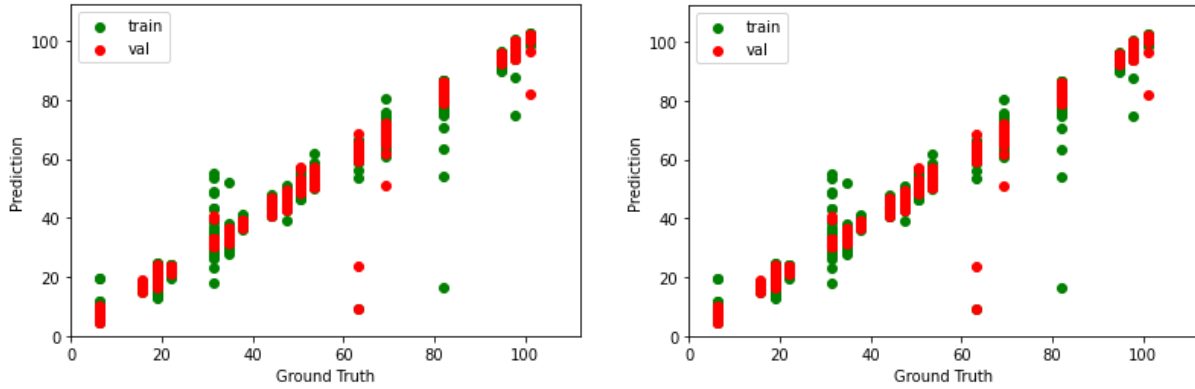


**Figure 3-18:** Neural network linear regression (left) and neural network classification (right) training and validation set results.

For decision trees and gradient boosting, the hyperparameter tuning workflow uses cross validation of fivefold with ranges for every parameter. Every combination was then tested and chosen based on the best average accuracy. An example of the result of testing every parameter can be seen in the heatmap shown Figure 3-19 where yellow correlates to a better result of average accuracy in between the folds.



**Figure 3-19:** Cross-validation heatmap example.

The result of the random forest regression converged to the best validation result of `max_depth` of 7 and `n_estimator` of 17. The result of the random forest classification converged to the best validation result of `Bootstrap: true`, `Max_depth: 50`, `Max_features: 0.5`, `N_estimators: 200`, `Min samples split: 1`, `Min samples leaf: 2`. The comparison between the actual and predicted values can be seen in Figure 3-20.

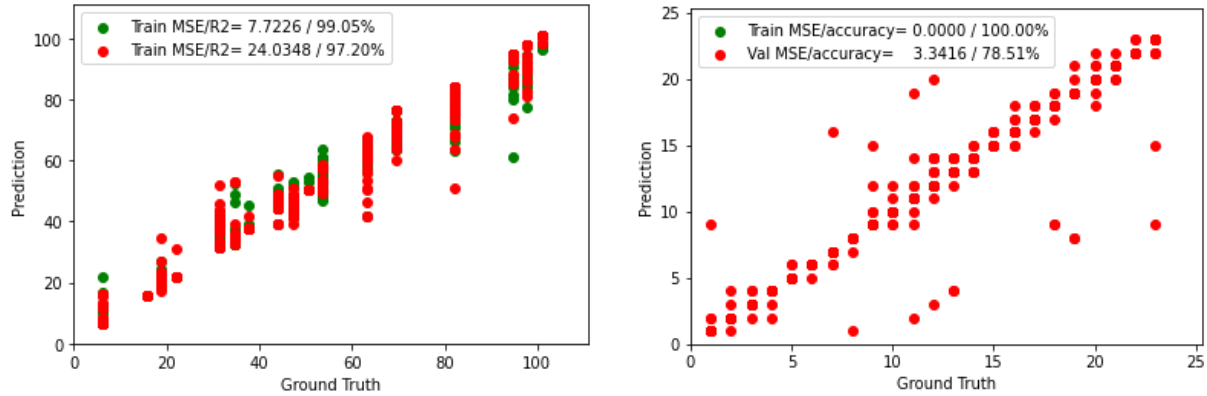


**Figure 3-20:** Random Forest regressor (left) and classifier (right) training and validation set results.

Hyperparameters for the XGBoost regressor model after tuning are `colsample_bytree`: 0.1, `gamma`: 0.5, `learning_rate`: 0.05, `max_depth`: 12, `n_estimators`: 750, `reg_alpha`: 5.8, `reg_lambda`: 2.7, `subsample`: 0.5. while hyperparameters for XGBoost classifier model after tuning are `max_depth`: 7, `learning_rate`: 0.1, `n_estimators`: 200, `reg_lambda`: 1.0, `subsample`: 1. The comparison between the actual and predicted values can be seen in Figure 3-21.

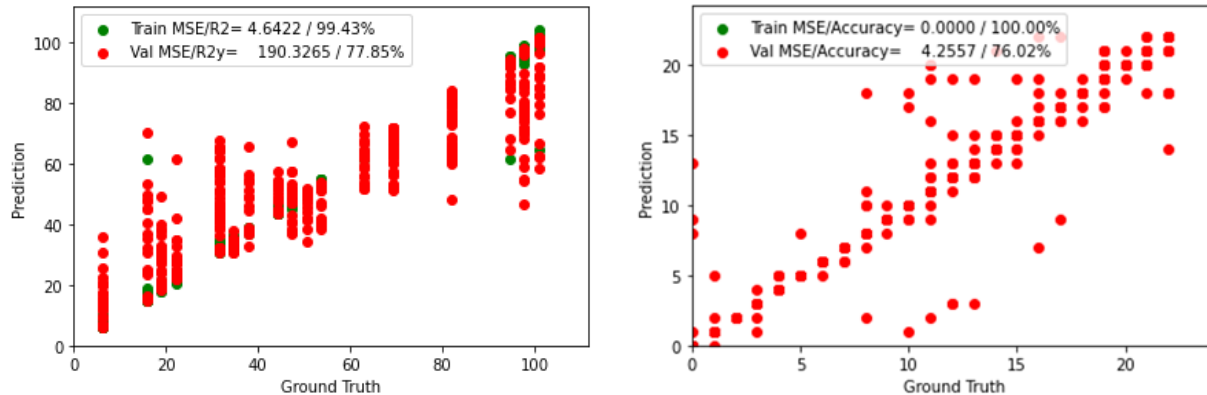


**Figure 3-21:** XGBoost regressor (left) and classifier (right) training and validation set results.

Hyperparameters for LGBM regressor model after tuning are `colsample_bytree`: 1, `learning_rate`: 0.04, `max_depth`: 3, `min_child_samples`: 11, `n_estimators`: 900, `reg_alpha`: 1.2, `reg_lambda`: 1.4, `subsample`: 0.8. While the hyperparameters for LGBM classifier model after tuning are `learning_rate`: 0.1, `max_depth`: 5, `n_estimators`: 200, `reg_lambda`: 0, `subsample`: 0.6. The comparison between the actual and predicted values can be seen in Figure 3-22.

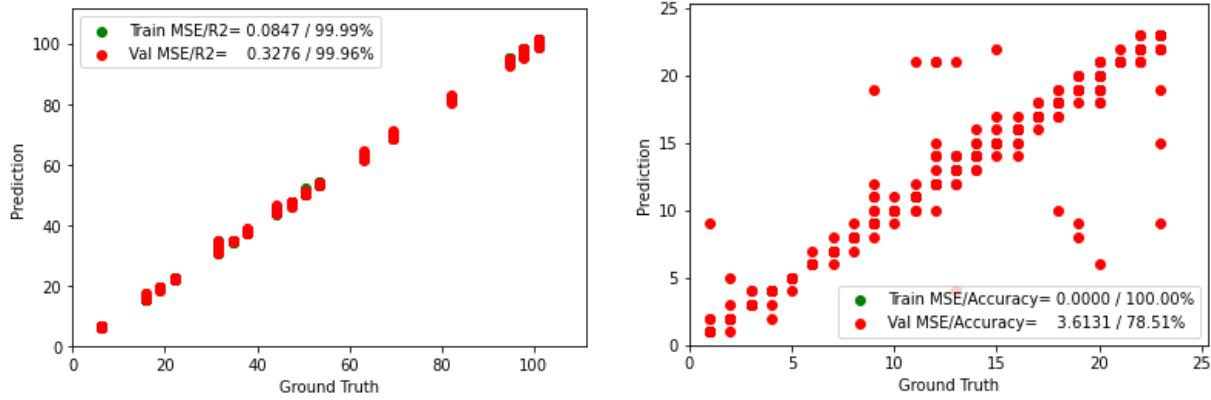


**Figure 3-22:** LGBM regressor (left) and LGBM classifier (right) training and validation set results.

According to the validation set summary of the regression model predicting the fracture flow rate presented in **Table 3-4**, the LGBM model exhibited the lowest mean squared error (MSE), indicating its superior performance in regression tasks. On the other hand, both LGBM and random forest models achieved the highest accuracy score in the validation test. These models were then evaluated using the test set to further assess their performance. The LGBM regressor model demonstrated satisfactory results, achieving an MSE of 0.36 and an R2 score of 99.96%. These metrics indicate the model's ability to accurately predict the fracture flow rate with a high degree of precision. The comparison between the actual and predicted value of the test set is shown in Figure 3-23.

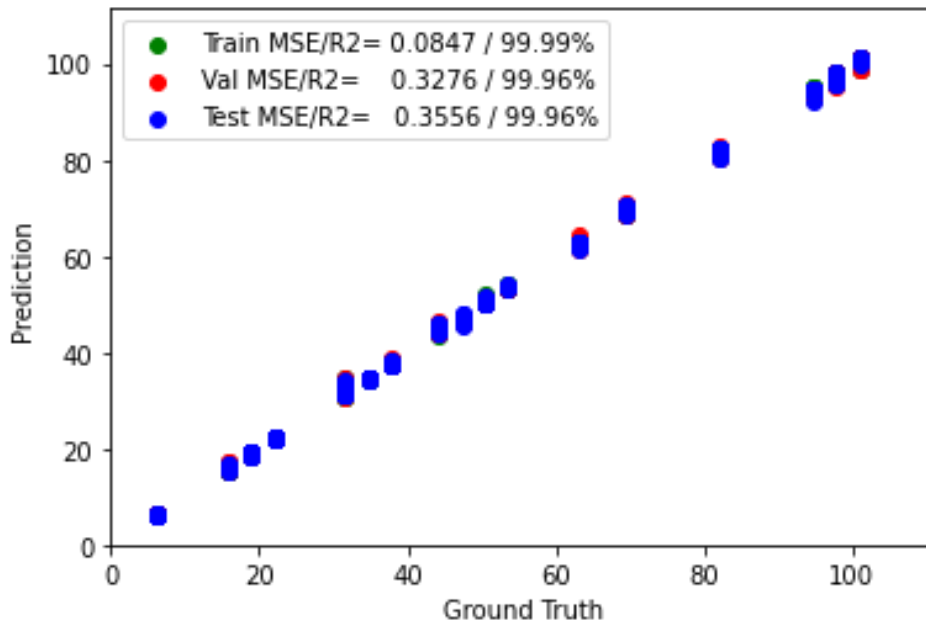


**Figure 3-23:** Prediction of LGBM regressor model on the test set.

**Table 3-4:** Feed zone flow rate machine learning approach result summary.

Model	Training		Validation	
	R <sup>2</sup>	MSE	R <sup>2</sup>	MSE
SGD Regressor (Baseline)	6.24%	760.88	5.75%	809.76
RF Regressor	99.28%	5.77	97.82%	18.79
NN	99.99%	0.08	99.96%	0.33
LGBM	98.45%	12.63	98.29%	14.68
XGBRegressor	99.43	4.6421	77.85%	190.33

The performance of the random forest classifier on the test set exhibited higher MSE (3.36) compared to the validation set, indicating a less accurate prediction of the fracture flow rate. The log loss value of 8.59 and accuracy of 75.11% further confirm the suboptimal performance of the model. The confusion matrix shown in Figure 3-24. provides additional insight into the model's performance.

On the other hand, the LGBM classifier demonstrated improved performance on the test set compared to the validation set. The MSE value of 4.70 indicates a relatively accurate prediction of the fracture flow rate. The log loss value of 6.95 and accuracy of 79.86% further support the model's better performance. The confusion matrix shown in Figure 3-25 provides a visual representation of the model's classification accuracy.

It is worth noting that while the random forest classifier may have better MSE, the LGBM classifier outperformed it in terms of accuracy. In this specific project, where predicting the location closer is considered important, MSE can be considered a valid metric. However, accuracy is also crucial as it determines the overall correctness of the model's predictions.

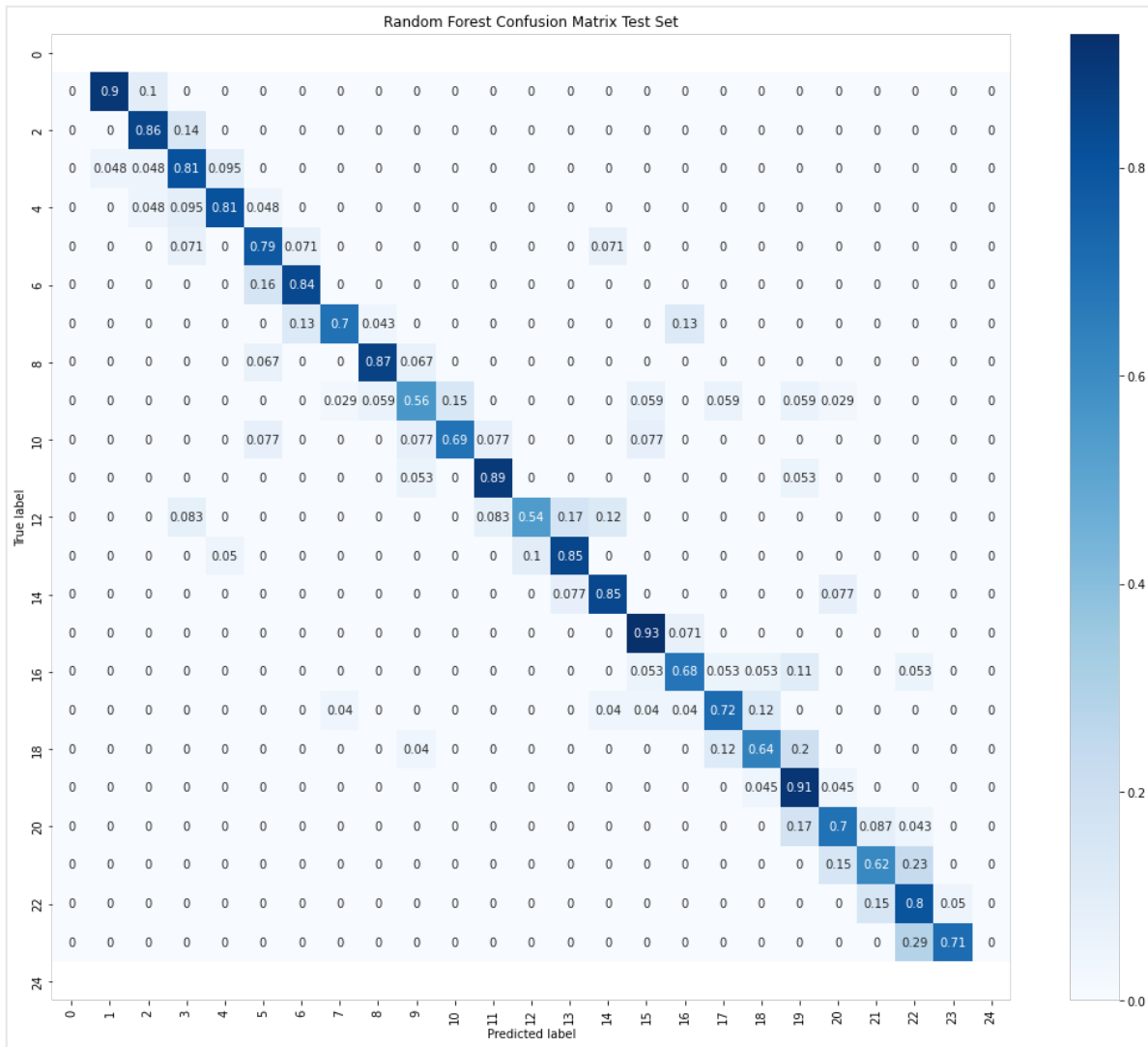


Figure 3-24: Test set confusion matrix of random forest classifier.

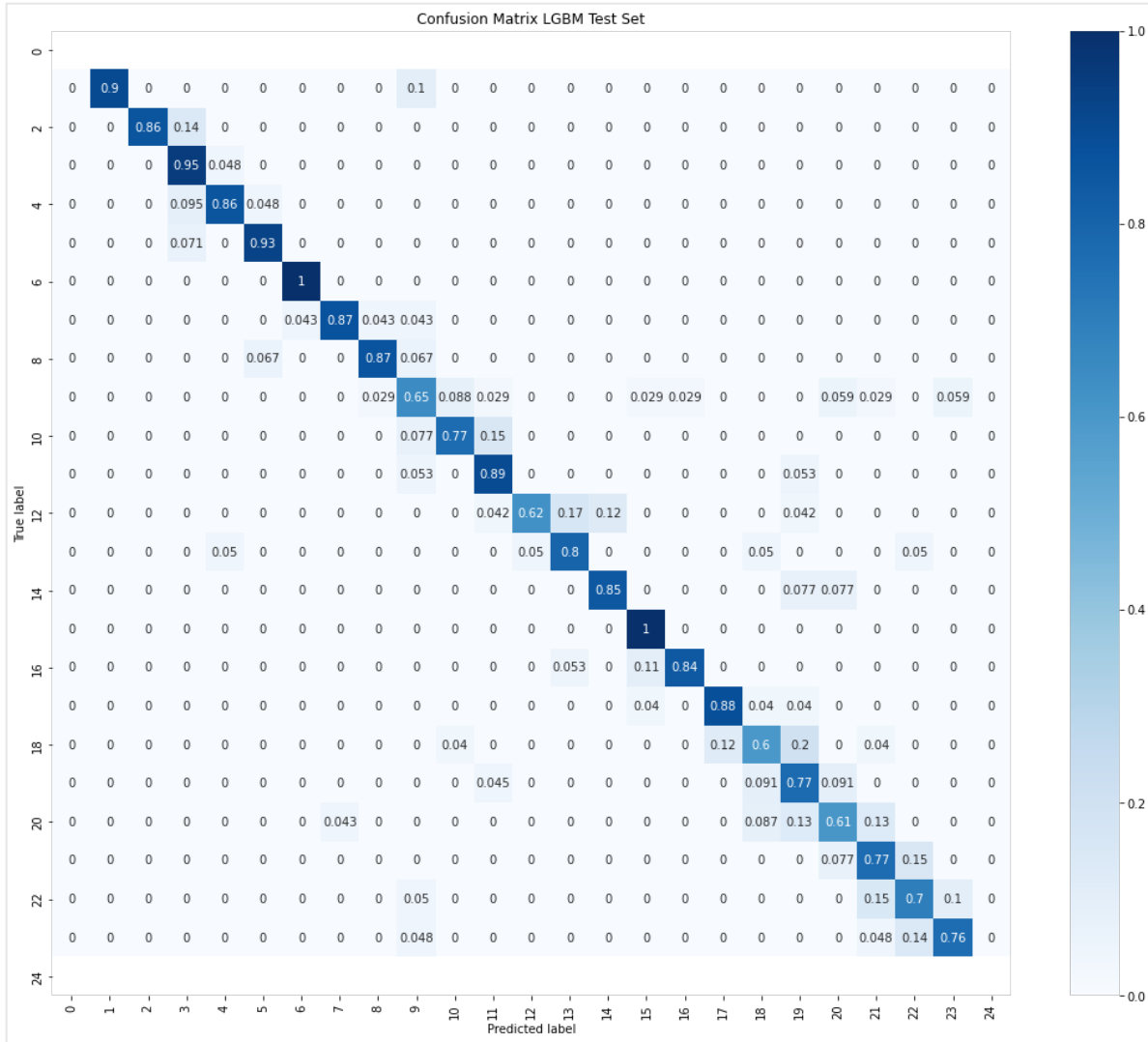


Figure 3-25: Test set confusion matrix of LGBM classifier.

### 3.4.2.4 Further Analysis on Incorrect Location Prediction

To analyze the incorrect predictions made by the LGBM classifier, a detailed examination was conducted. The data points that were inaccurately predicted were collected and studied. It was observed that a majority of these predictions were in close proximity to the actual feed zone location. In several examples (Figure 3-26), it was noted that three out of four inaccurate predictions were off by just one group. For instance, if the actual group was 19, most of the incorrect predictions were either 18 or 20.

Considering that the laboratory wellbore scale height was 60 inches (152.4 cm), and the classification problem divided the height into 25 groups, missing a prediction by one group corresponds to a deviation of approximately 2.5 inches (6.35 cm). Consequently, the accuracy of the model was further evaluated based on the acceptable range of errors.

The results revealed a significant improvement in accuracy when allowing for one error range tolerance. The accuracy increased from 78% to 93%, indicating that the majority of inaccurate predictions were still in close proximity to the actual feed zone. This finding highlights the model's

capability to predict the feed zone location with a high degree of precision, considering the small margin of error.

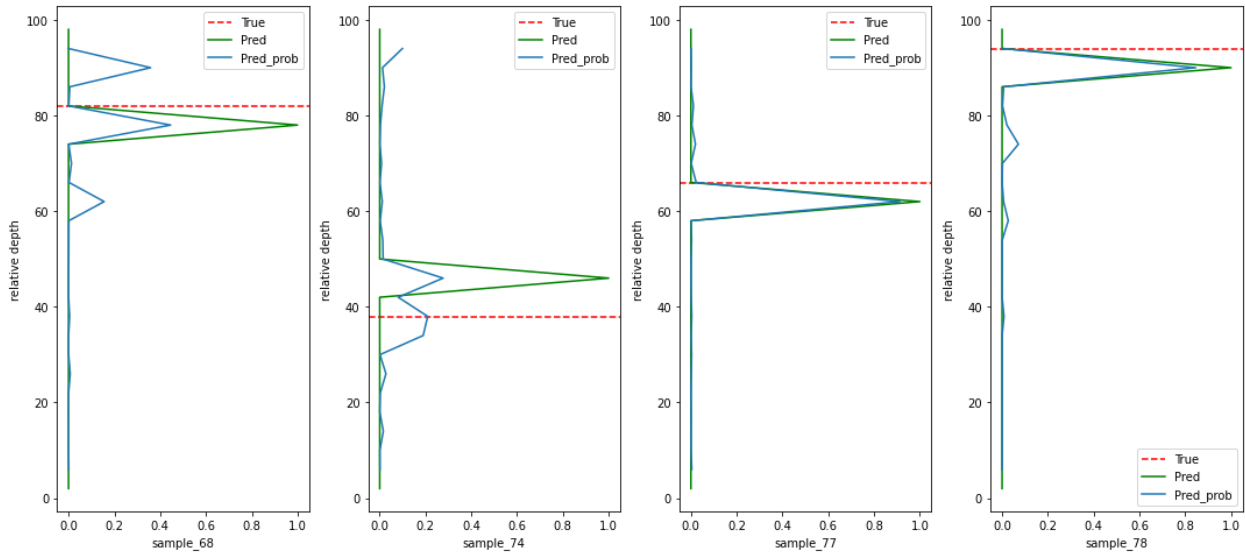


**Figure 3-26:** Examples of inaccurate prediction from LGBM classifier.

The results demonstrate a substantial increase in accuracy from 78% to 93% when allowing for a tolerance of one error range. This indicates that the majority of inaccurate predictions are in close proximity to the actual group. Moreover, the accuracy remains relatively consistent at around 96-97% until a tolerance of five error ranges, suggesting that the remaining inaccurate predictions are likely outliers. This relationship between accuracy and error range tolerance is visualized in Figure 3-27.

It is important to note that the appropriate error tolerance may vary depending on the specific object or situation being analyzed. Different applications may require different levels of precision, and the tolerance should be adjusted accordingly.

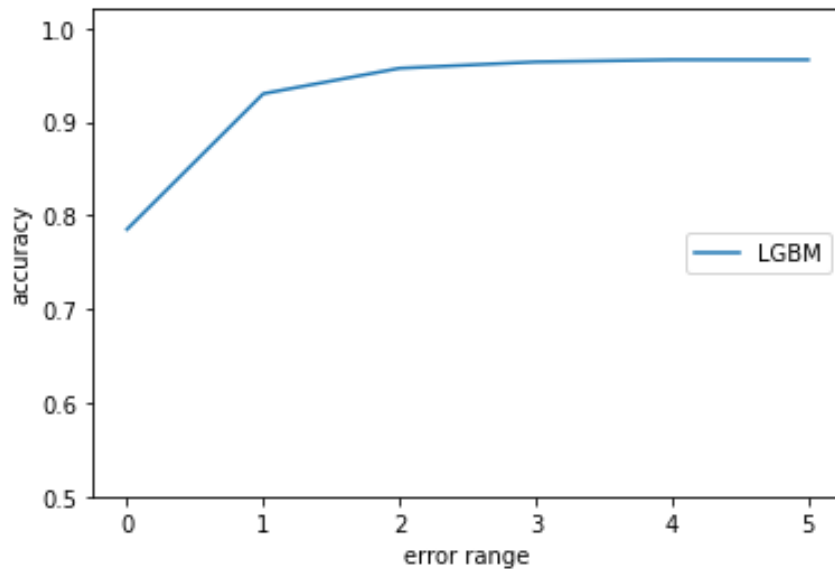


**Figure 3-27:** LGBM classifier accuracy vs allowed error range.

### 3.4.2.5 Dual Feed Zone Results

In an attempt to extend the application of the developed model, an implementation was made to predict dual feed zone measurements. However, the results were not satisfactory, yielding an accuracy of correctly predicting fractures at 58% and an accuracy of accurately predicting scenarios at 37%. It is important to note that this outcome was obtained without including the dual feed zone measurement data in the training set of the model. Examples of the dual feed zone prediction results can be seen in Figure 3-28, where the dashed red lines are the actual fractures at x axis equal 1 while the yellow lines are the model predictions.

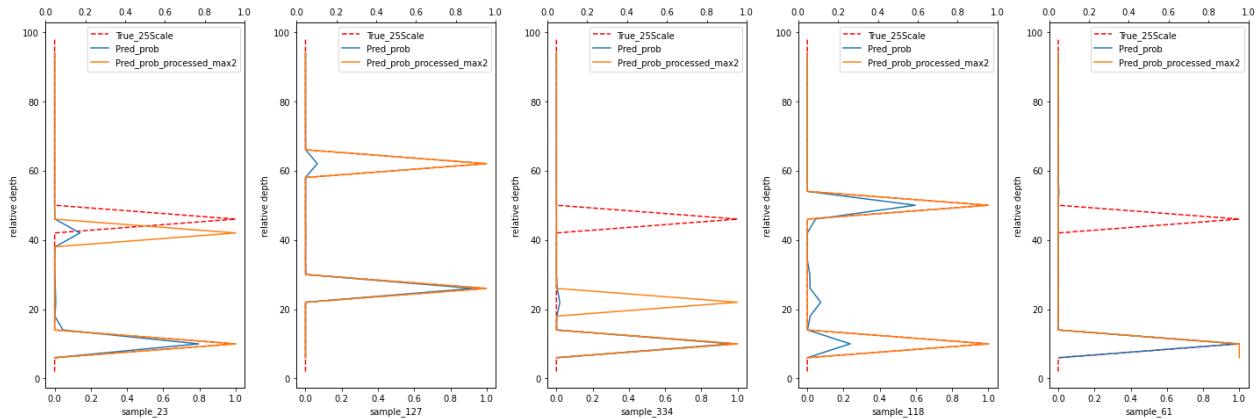


**Figure 3-28:** Prediction of LGBM classifier on dual feed zone measurement data.

To improve the performance of the machine learning model in predicting dual feed zone measurements, it is recommended to include some of the dual feed zone data in the training set. This will allow the model to learn and capture the patterns specific to dual feed zone scenarios, potentially enhancing its ability to predict such cases accurately.

### 3.4.2.6 Feature Engineering

In the later stages, feature engineering was implemented specifically to the LGBM model classifier to improve the accuracy in locating the actual feed zone. The feature engineering process involved adding the delta (change) of each voltage data point to the next data point. As there are 100 points of voltage measurement, this resulted in the addition of 99 data points as an additional parameter for each example.

Following a similar process of hyperparameter tuning, the results demonstrated significant improvement. The validation set achieved an accuracy of 87.33% and a mean squared error (MSE) of 5.457, surpassing the previous results without feature engineering, which achieved an accuracy of 78.51% and an MSE of 3.61. Moreover, the prediction performance on the test set was also satisfactory, with an accuracy of 87.56% and an MSE of 3.4977 (Figure 3-29).

These results indicate that incorporating the change in voltage through the wellbore as a feature significantly enhanced the performance of the machine learning model, aligning with the concept and relationship between voltage changes and existing feed zones.

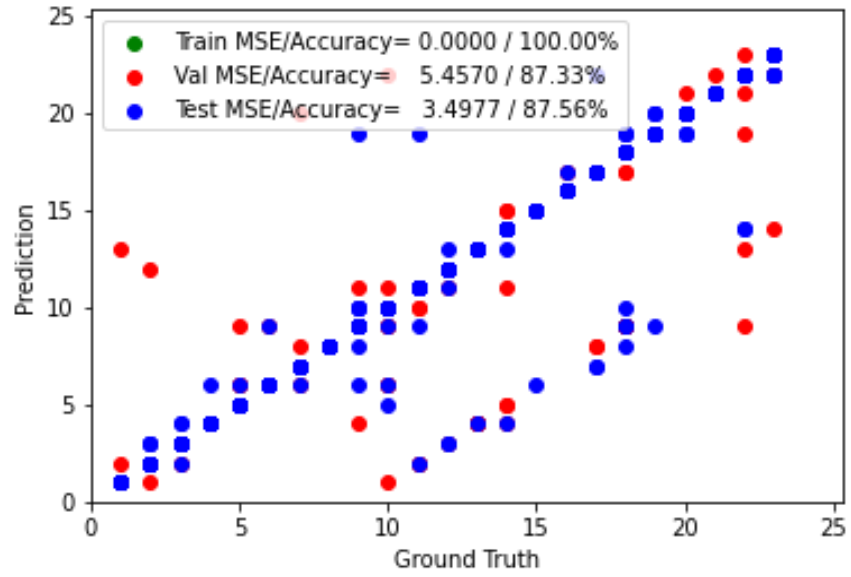


**Figure 3-29:** Prediction of LGBM classifier on the test set post feature engineering.

## Chapter 4

# Laboratory Experiments and Numerical Simulations

We conducted laboratory experiments and numerical simulations to investigate fluid flow behavior and understand the tool's capabilities and limitations, particularly in preparation for field deployment. Laboratory experiments were conducted using several iterations of the chloride tool, as detailed in Section 2-6. The artificial well system was used for testing involving flow, while the bench was used for calibration. Accompanying numerical simulations were conducted as appropriate to expand the test scenarios that are difficult to perform in laboratory settings. The laboratory experiments and numerical simulations can be categorized into three rounds:

- Round 1, which used the tubular lab-scale tools and the initial artificial well system
- Round 2, which used the tool with housing and the modified artificial well system
- Round 3, post-field deployment, as detailed in Chapter 6.

This chapter outlines the laboratory experiments and numerical simulations prior to the field data acquisition at Utah FORGE Wells, i.e., Round 1 and Round 2.

### 4.1 Round 1 Experiments and Simulations

In Round 1, tubular lab-scale tools were used for the laboratory experiments and subsequent comparative simulations. Initial tests were conducted using the original version reported by Gao (2017), identifiable by its white epoxy body. In 2023, Sandia sent an updated version of the tubular tool with a transparent epoxy body. In this report, we will refer to them as tubular tool version 1 and version 2, respectively.

Calibrations and flow experiments were initially performed with version 1 and were subsequently repeated and expanded using version 2. Additionally, the existing artificial well system was enhanced with new pumps and reservoirs as will be detailed in the following section.

## 4.1.1 Round 1 Laboratory Experiments

### 4.1.1.1 Artificial Well Systems Setup

Kumar (1995) designed and constructed the artificial well and its accompanying system, which Gao (2017) also used for the initial work of the chloride tool research project pre-FORGE. The artificial well system has four main components: the main wellbore, the feed zone system, the fluid inflow apparatus, and the fluid outflow apparatus. The annotated images and schematic are shown in Figure 4-1 and Figure 4-2, respectively.

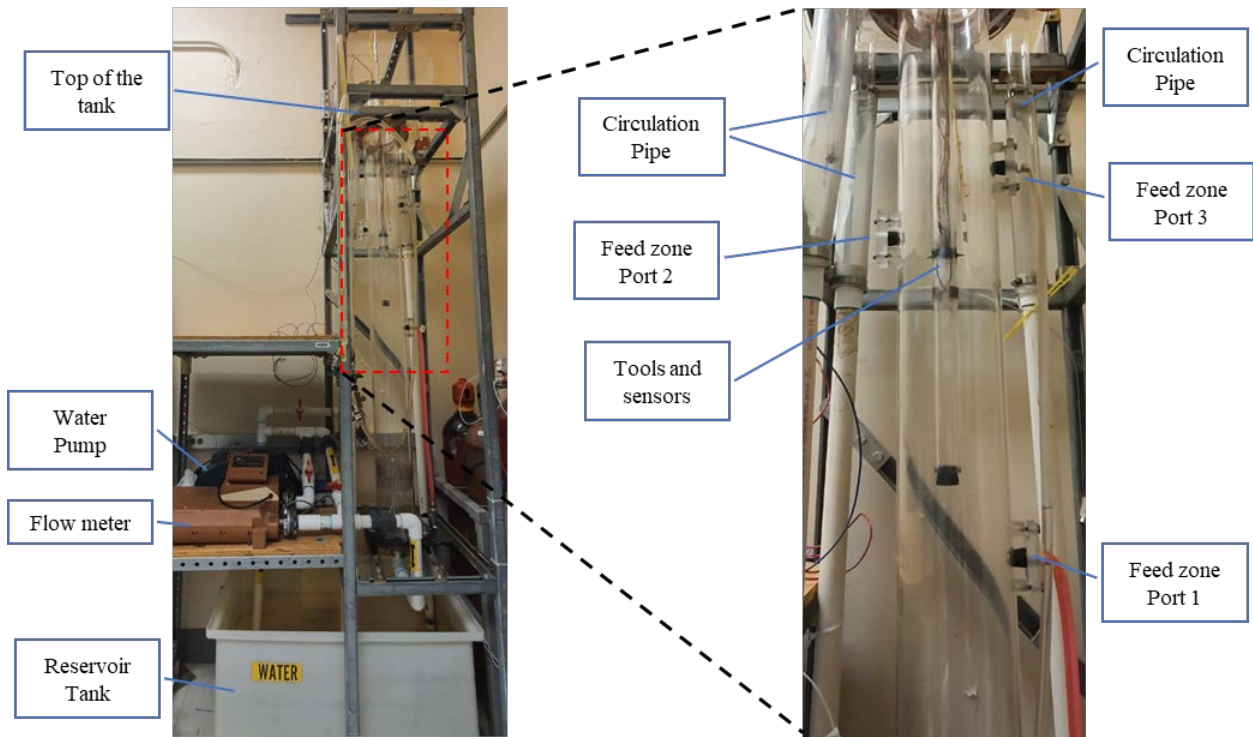


**Figure 4-1:** Artificial well system for Round 1 laboratory experiments.

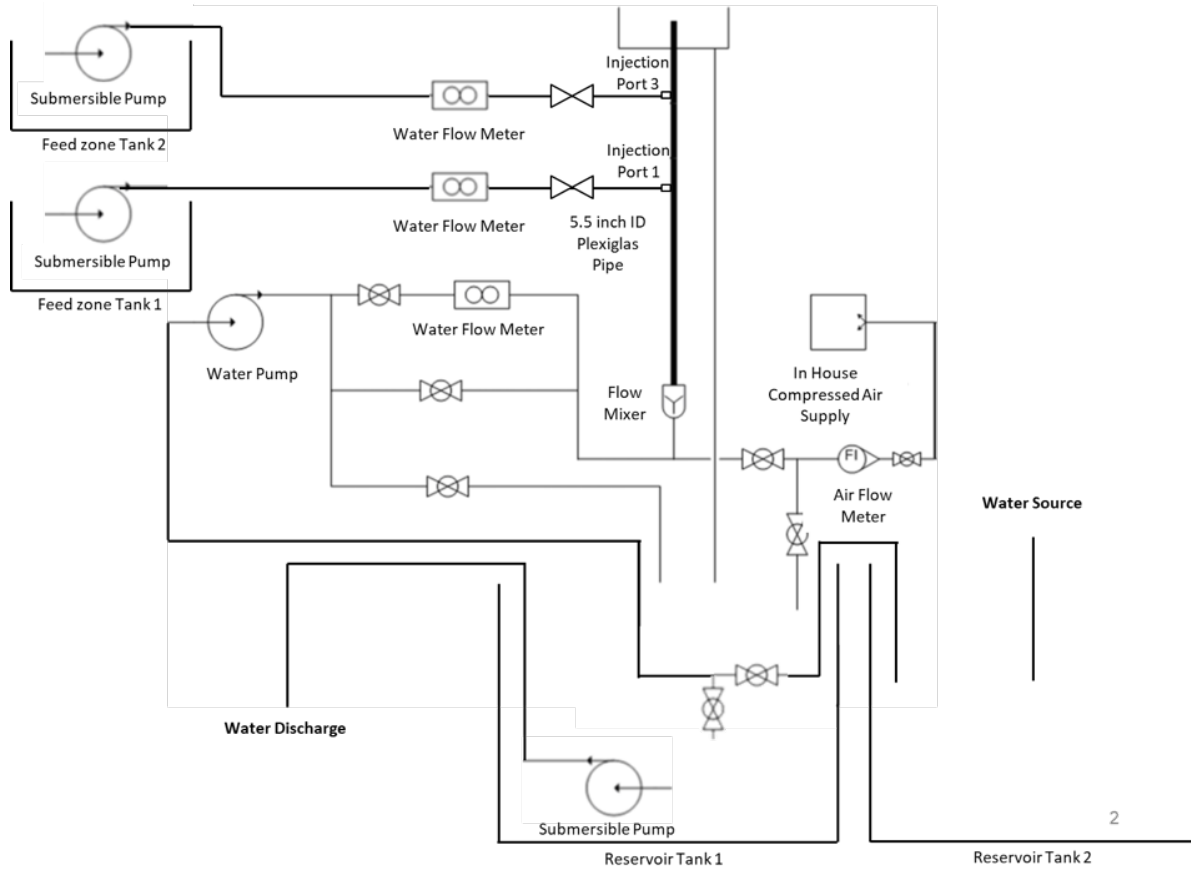


**Figure 4-2:** Artificial well system flow loop schematic modified from Kumar (1995).

The artificial well system's main wellbore is a 78-inch-tall (198 cm) acrylic cylinder with an inner diameter of 6.0 inches (15.2 cm) and an outer diameter of 6.5 inches (16.5 cm). The bottom 4.5 inches (11.4 cm) of the wellbore houses a flow diffuser, which regulates the velocity of the fluid flow to minimize turbulence and ensure smooth and even flow. To simulate feed zone inflow into the main wellbore, the artificial well system has three ports for feed zones at varying heights along its side. On the right of the wellbore, Feed Zone 1 and Feed Zone 3 are located 34 and 60 inches (86.4 and 152 cm) above the bottom of the wellbore, respectively. On the left side of the wellbore, Feed Zone 2 is located 50 inches (127 cm) above the bottom of the wellbore.

A water pump and flow meter were installed to facilitate and measure the circulation of water within the system. The water pump was powered by a capacitor-start motor (Dayton 6K232C) with a power of 1 hp (0.75 kW). Three circulation pipes were used to connect the top of the well and the water tank, enabling water pumped through the system to flow back into the bottom reservoir tank.

Additionally, to accommodate the flow of injection from the feed zone ports 1 and 3 a 0.5-inch (1.27 cm) clear vinyl tubing was used to connect these ports to a water flow meter (ICS006 RainPoint). The other end of the flow meter connected to feed zone port 1 was then linked to an 85W 3200 GPH (3.36 L/s) submersible pump (AQQA 110V). Similarly, the flow meter connected to feed zone port 3 was attached to a 3170 GPH (3.33 L/s) submersible pump (eFlux DC Flow Pump). Both pumps were placed within separate containers, with capacities of 30 L and 54 L, respectively. A picture of the submersible pump, flowmeter, and container connected to the feed zone port can be seen in Figure 4-3.

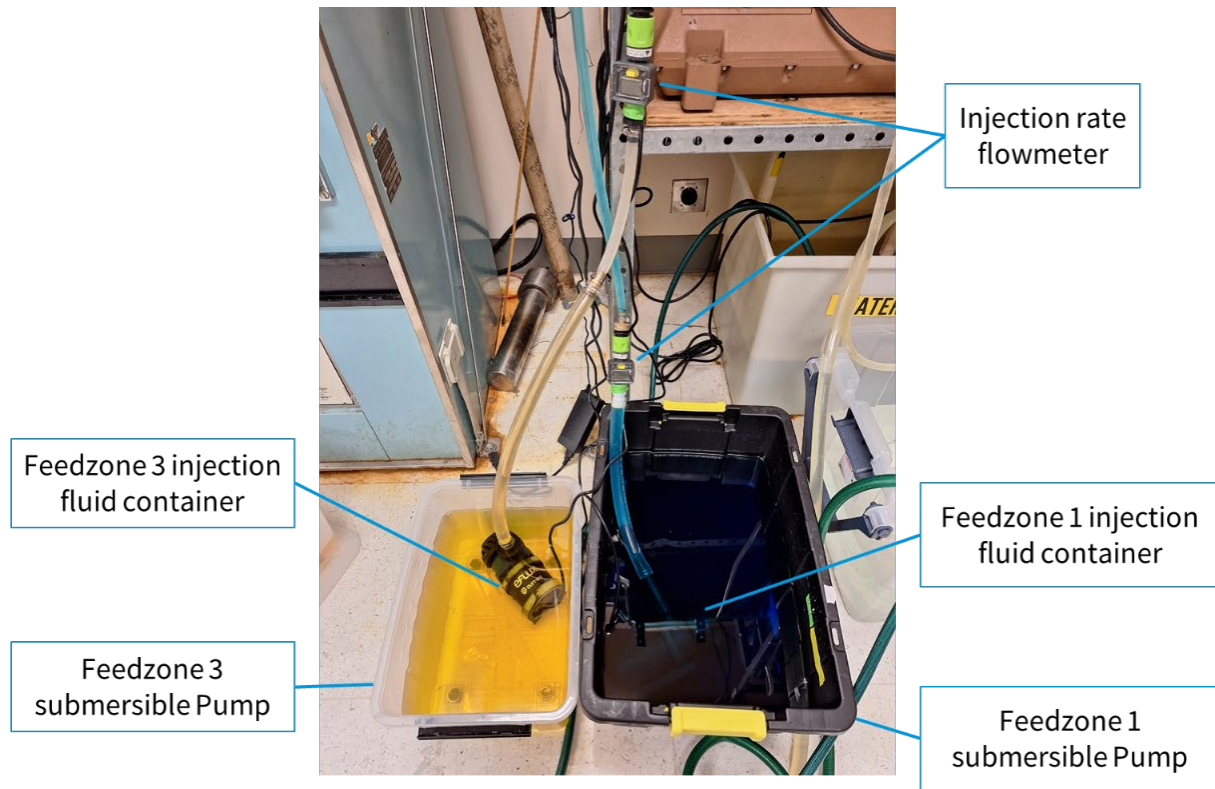


**Figure 4-3:** Injection pump and flowmeter.

The extra reservoir tank and the corresponding plumbing enhancements were aimed at ensuring a constant and untainted water supply, thereby preventing any potential cross-contamination of chloride-concentrated water from the downhole flow. The installation of the reservoir tank was intended to maintain the integrity of the experimental setup and ensure accurate and reliable results. A picture of the additional reservoir tank and the connection to the intake of the original well system can be seen in Figure 4-4.

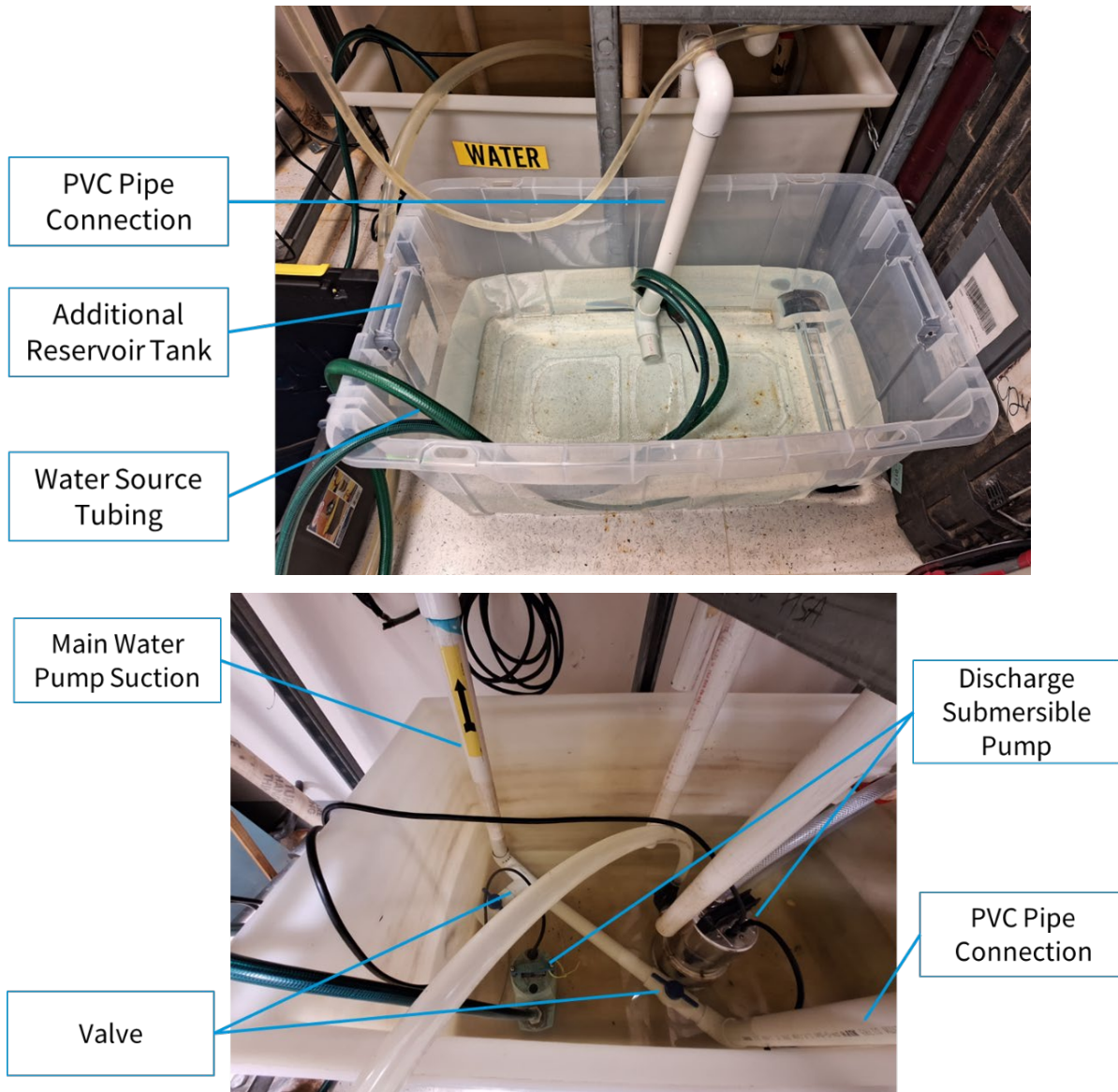


**Figure 4-4:** Additional reservoir tank (top) and plumbing in the original reservoir tank (bottom).

#### 4.1.1.2 Tool Calibration

Round 1 calibration was first done with the tubular tool version 1 and then subsequently with version 2. With both tool versions, the calibration began by submerging the tubular tool in a saturated chloride solution for 24 hours to allow for rehydration. The calibrations were conducted by preparing various chloride-concentrated solutions by dissolving sodium chloride in water with the respective weight and volume under ambient conditions to achieve the desired concentration. A chloride concentration ranging from  $10^{-6}$  mol/L to 2 mol/L was formulated.

During one of the calibration processes, deionized and distilled water were used to observe if there were any differences. However, the results obtained using deionized and distilled water did not show any significant difference compared to using tap water, so tap water was used thereafter.

An electrical balance (Sartorius SECORA5102-1S) with a resolution of 0.01 g was used to measure the weight of sodium chloride. Three different volumes were utilized: 400 ml in a graduated cylinder, 20 L in a water tank, and 100 L in another water tank. These container setups are shown in Figure 4-5. Generally, lower-concentration solutions were prepared in larger-volume containers. The body of the tool was then fully submerged in each solution while the wireline connected to the upper end of the tool body was linked to a voltmeter or data acquisition (DAQ) device for voltage measurement. The voltage reading for each solution concentration was observed until the voltage reading was stable.



**Figure 4-5:** Tool calibration container: 400 ml (left), 20 L (center), and 100 L(right).

The calibration measures the voltage difference between the Cl-ISE and the reference electrode with a digital multimeter (KAIWEETS Digital Multimeter TRMS 6000). The Cl-ISE was connected to the V $\Omega$ Hz and the reference electrode was connected to the Common (COM). The potential difference between the two electrodes was measured under the DC Voltage mode within the range of mV. The multimeter connection can be seen in Figure 4-6. Measurements were taken after the sodium chloride was completely dissolved, and the reading from the voltmeter became relatively stable. During the multimeter calibration process, it was observed that the time required to reach equilibrium was longer for lower concentrations compared to higher concentrations.

In addition to the multimeter calibration measurements, calibration utilizing a data acquisition (DAQ) device was conducted for tubular tool version 2. The connections between the downhole tool and the DAQ device were made by connecting the Cl-ISE to one of the positive input ports of the DAQ device. The reference electrode was connected to the affiliated negative input port of the DAQ device, as shown in Figure 4-6. During the calibration phase of the tubular tool version 2, it was found that the impedance of the DAQ device strongly affects the consistency of the voltage measurement from the tool, so it is recommended to use a higher impedance DAQ device for the downhole tool. For reference, the impedance of the DAQ device used (NI USB 6001) was  $>1\text{G}\Omega$ .

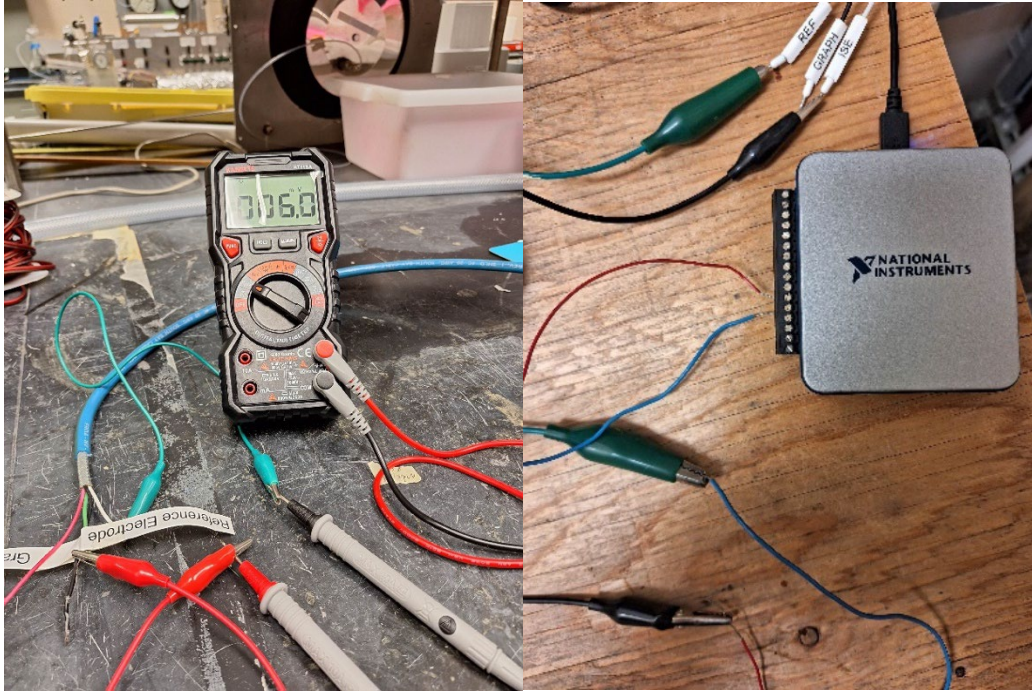


**Figure 4-6:** Multimeter (left) and DAQ device (right) to downhole tool connection.

The USB port from the DAQ device was then connected to a computer and interrogated using the software LabVIEW. An in-house code in LabVIEW was made to record and visually display the dynamic measurements and automatically save the measurements into a CSV file. The DAQ device for the experiments conducted was set to read 100 to 1000 data per second. Each calibration point was observed for 30 minutes to evaluate the time needed to establish equilibrium. The in-house LabVIEW code and visualization are presented in Figure 4-7.

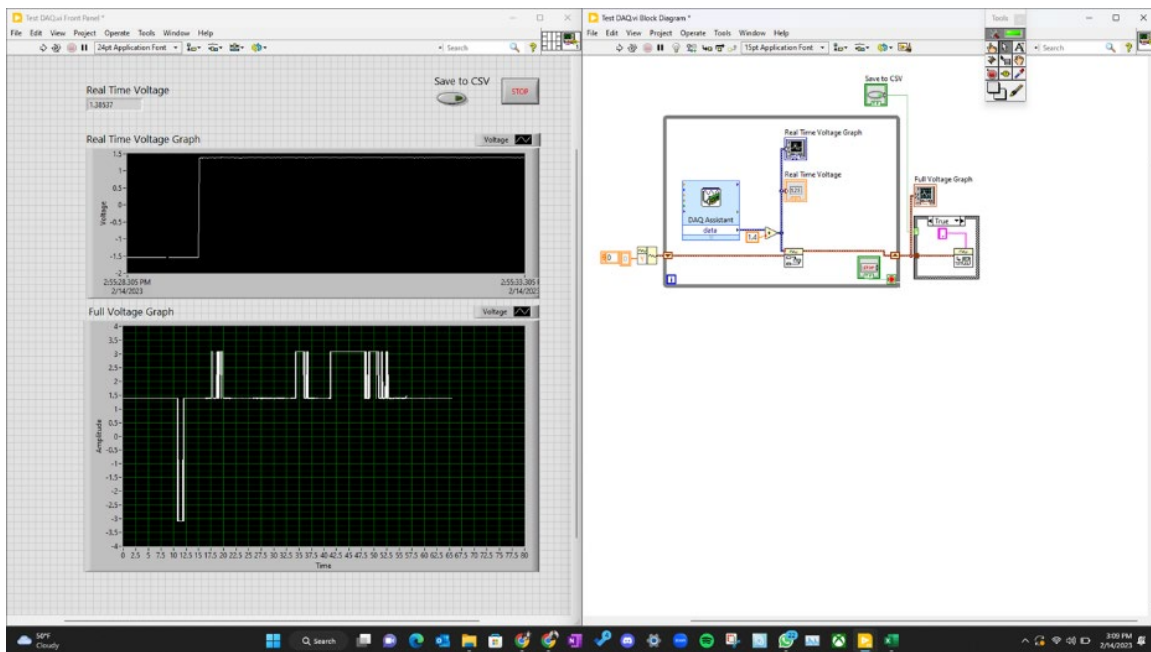


**Figure 4-7:** In-house LabVIEW Interface measurement example.

During the DAQ calibration process, it was observed that the downhole tool measurement took approximately 15 minutes to reach equilibrium, as shown in Figure 4-8. Further analysis of the voltage changes over time revealed that, upon reaching equilibrium, a predominant change of 0.001 V was observed compared to the initial measurement. The maximum change recorded during this process was 0.04 V, as illustrated in Figure 4-9.

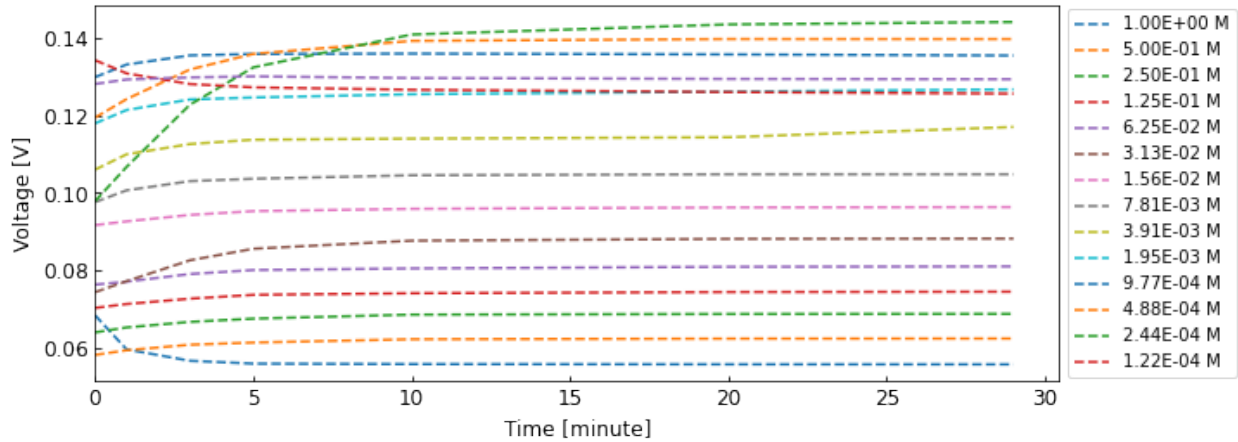


**Figure 4-8:** Voltage evolution over time during DAQ calibration.

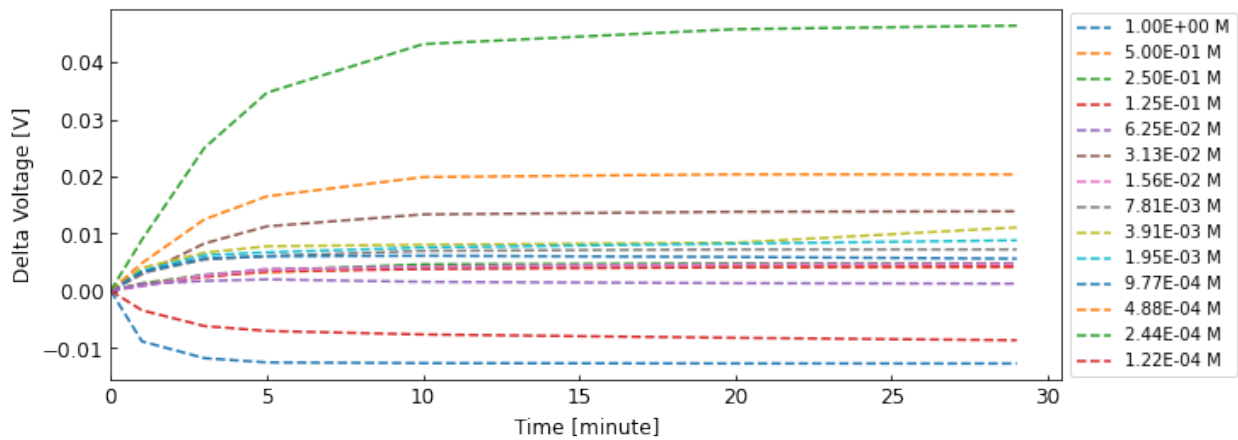


**Figure 4-9:** Delta voltage evolution over time during DAQ calibration.

The calibration results for both the tubular tool version 1 and 2 are shown in Figure 4-10. The relationships between voltage readings and chloride concentrations for the original tool using the multimeter, the new tool using multimeter and the new tool using DAQ device are shown in Equation (4-1), Equation (4-2) and Equation (4-3) respectively.

$$-\log(M) = 98.58V + 0.2998 \quad (4-1)$$

$$-\log(M) = 35.168V - 1.4265 \quad (4-2)$$

$$-\log(M) = 38.15V - 1.9598 \quad (4-3)$$

where,  $M$  is chloride concentration in mol/L and  $V$  is the electrical potential difference between the reference and the CL-ISE electrode in volt. The regression coefficient ( $R^2$ ) of the three calibrations were 0.9047, 0.9727 and 0.9783 respectively. Equation (4-1) established an updated correlation

between chloride concentration and voltage, and this relationship was subsequently utilized in later experiments for measuring chloride concentration.

In comparison to the previous calibration conducted by Gao (2017) shown as the red line in Figure 4-10, the updated calibration results obtained using tubular tool version 1, represented by the blue line in the same figure, confirmed the inverse relationship between chloride concentration and voltage. However, the result shows smaller voltage measurements for similar chloride concentrations, which appears to show a change in the tool performance over the five years since the previous calibration. It was further noted that the updated calibration exhibited a steeper slope, indicating that a given voltage change would yield a proportionally larger change in chloride concentration.

The calibration results obtained using both the multimeter and the DAQ device for the version 2 tool closely aligned with the findings reported by Gao (2017). However, measurements of chloride concentration below  $10^{-4}$  exhibited high variance, rendering them inconclusive. As a result, further experiments were not conducted for chloride concentrations lower than  $10^{-4}$ .

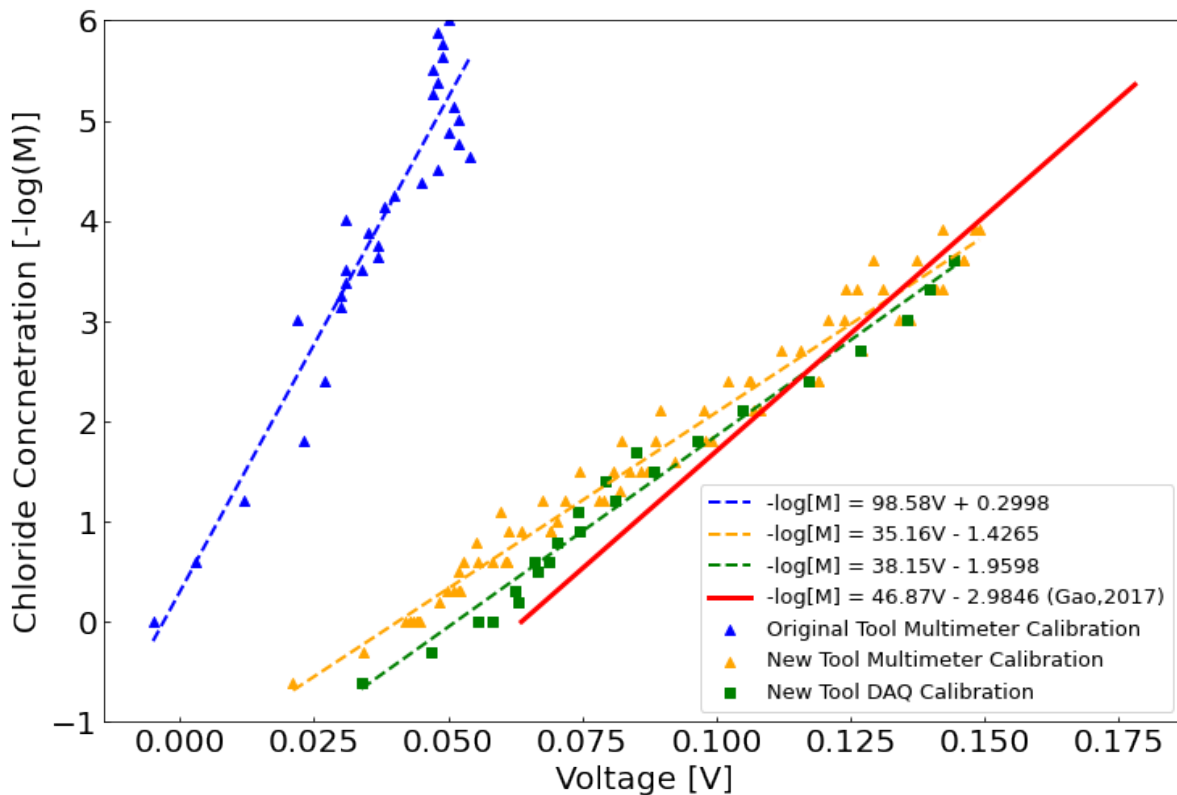


**Figure 4-10:** Tool calibration result. The “Original Tool” and the “New Tool” refers to the tubular tool version 1 and 2, respectively.

#### 4.1.1.3 Static Laboratory Experiments

##### ***Downhole Flow***

Static experiments involved placing the tool inside the artificial wellbore in a stationary position. Commencing the experiments, measurements were conducted to test the chloride measurement in bulk vs. inside the wellbore. A single-phase flow with different chloride concentrations was circulated

through the artificial wellbore with water containing chloride concentrations ranging from 0.5 mol/L to 0.0625 mol/L. Voltages were measured both in the reservoir tank and inside the well while the water was circulating using the multimeter similar to during calibration. The measurement inside the well was obtained by attaching the tool to a 36-inch metal rod and inserting the rod into the well from the top.

A comparison between the voltage readings from the reservoir tank and inside the well is shown in **Figure 4-11**. While the voltage measurements in the wellbore showed a slightly higher reading, generally, the measurements of voltage between the wellbore and reservoir tanks were consistent. The voltage measurements gathered were then processed to chloride concentration by using Equation (4-1), and the converted result is shown in **Figure 4-11**. The actual concentration was obtained by diluting a 0.5 M solution with water to double the volume, resulting in half the concentration. The procedure was repeated until reaching the data point with the least concentration. The result shows a relatively good match between the actual concentrations and the calculated concentrations for concentrations lower than 0.3 mol/L. However, chloride concentration higher than 0.3 mol/L only has one data point showing a result of 0.7 mol/L calculated concentration from the actual 0.5 mol/L actual concentration. This is a variance of the voltage-chloride relationship from Equation (3-1) as the regression is less than the previous study. This result shows promising results for chloride concentration calculation under flowing and static condition.

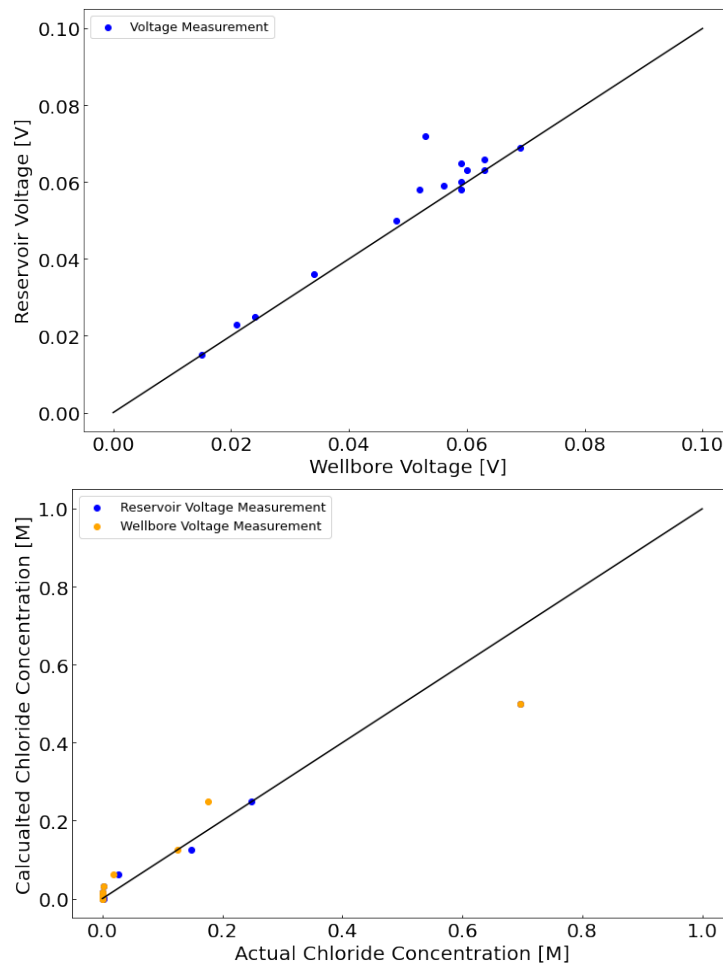


**Figure 4-11:** Wellbore and reservoir tank voltage readings (top), and concentration actual vs. calculated concentration from voltage (bottom).

### ***Single Fracture Inflow***

For the single fracture inflow experiments, the tool was positioned in the middle of the wellbore, two inches (5 cm) above the first injection port. The reservoir tank was filled with 200 liters of water, and the injection port was connected to a tubing, a valve, and a submersible pump placed inside a 20 L vessel containing the chloride solution to be injected. The artificial well system and tool assembly for the one feed zone injection experiment are shown in Figure 4-12.

To initiate the experiment, the main well flow pump was turned on until the circulation reached a stable state. The downhole flow rate of the circulation system was measured and found to be 2.09 kg/s. Once the circulation was stable, the submersible pump connected to the feed zone solution was turned on, and the valve for the injection port was opened, allowing the solution to be injected into the feed zone port. The valve was then closed once the 20 L feed zone solution vessel was empty. During the injection process, the flow rate of the injected solution from the feed zone port was measured and determined to be approximately 100 ml/s.

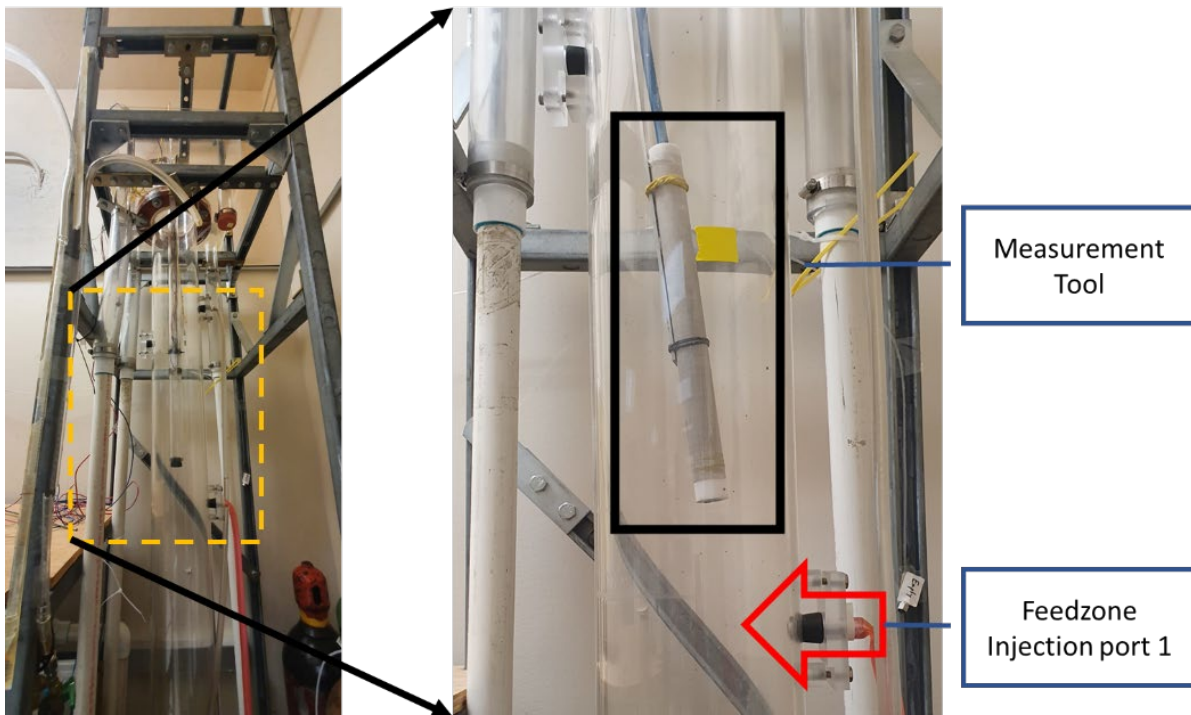


**Figure 4-12:** One feed zone injection artificial well system assembly.

For the single feed zone injection chloride concentration sensitivity analysis, three different chloride concentration solutions were utilized, 0.1, 0.5, and 1 M. The voltage measurements of the 0.1, 0.5, and 1 M injected solutions were recorded over the span of around 3 minutes. The results, shown in Figure 4-13, demonstrated a gradual reduction in voltage reading as time progressed. This reduction can be attributed to the introduction of higher chloride concentration solutions through the feed zone port, which gradually increased the initial zero chloride concentration solution within the reservoir tank and the recirculating wellbore system.

The experiment showed that higher chloride concentration injections resulted in smaller voltage readings, which aligns with the calibration results described earlier. Additionally, the experiment

indicated a relatively stable voltage reading after approximately 2.5 minutes following the initiation of injection. This stability suggests that the system reached a state of equilibrium, where the concentration of chloride in the wellbore system remained relatively constant. It is also observed that the higher concentration of chloride injection tends to stabilize faster.

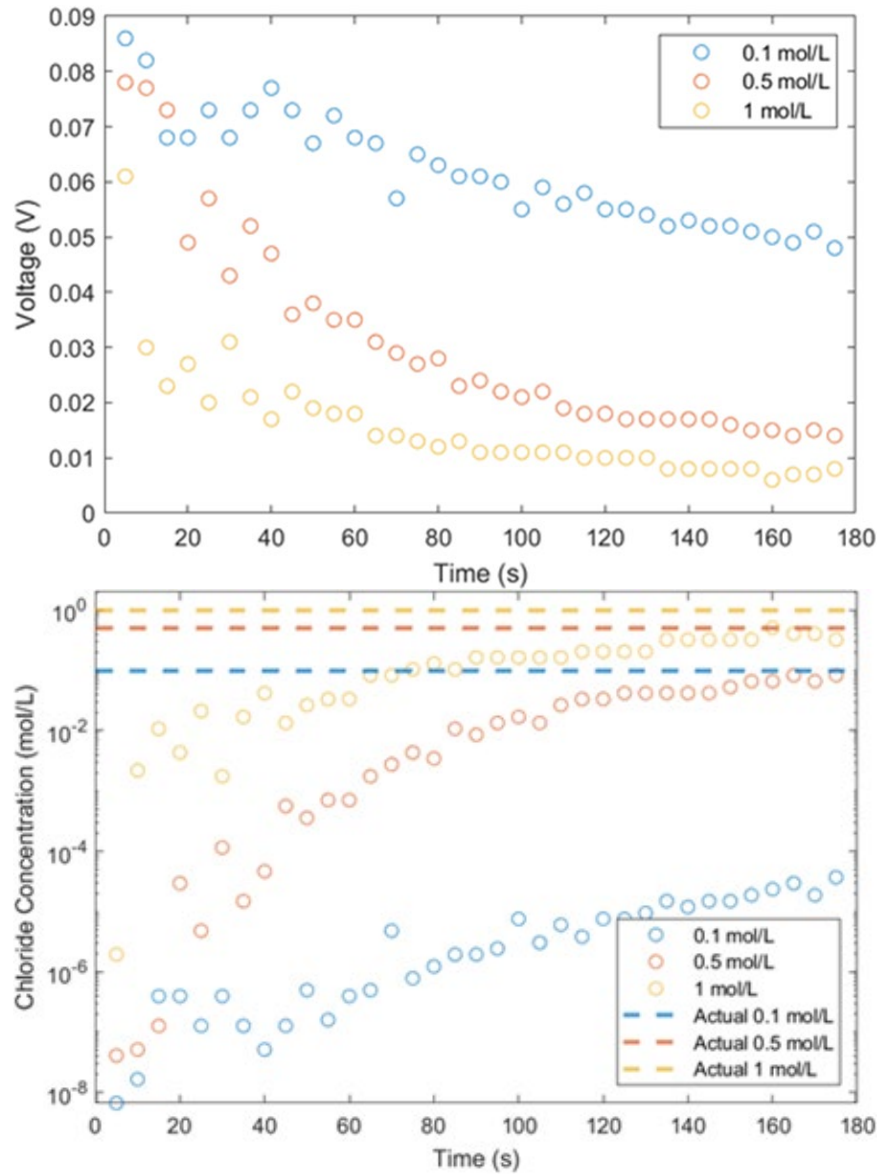


**Figure 4-13:** Injection concentration sensitivity voltage measurement (top) and the calculated chloride concentration result (bottom).

The calculated chloride concentrations, represented by the dots in Figure 4-13, increase over time as expected. However, these values are consistently below the actual injected chloride concentrations, indicated by the horizontal lines with the corresponding color. For the 1 Mol/L solution, the indicated concentration was 0.511 Mol/L. Similarly, for the 0.5 Mol/L solution, the measurement indicated a concentration of 0.104 Mol/L. This suggests that the accuracy of the measurement decreases for lower chloride concentrations. This inaccuracy is not necessarily associated with the chloride measurement itself but rather the variation of chloride concentration in the flowing wellbore system.

The underestimation observed in this experiment can be attributed to several factors. Firstly, the nonuniform mixing of the injected solution within the downhole flow fluid from the reservoir tank inside the wellbore might have influenced the chloride concentration. Additionally, the positioning of the tool, being two inches (5 cm) above the injection port and placed in the center of the well, could have also impacted the indicated values in the measurements.

To investigate the effect of tool placement on measurement accuracy, two different positions were considered: Position 1, corresponding to placing the tool at the center of the wellbore, and Position 2, involving placing the tool directly in front of the feed zone. The positions are depicted in Figure 4-14. For this experiment, a chloride concentration of 0.1 mol/L was chosen for the feed zone injection solution. This decision was based on the previous experiments which indicated that lower concentrations were associated with lower accuracy. The injected solution had an average flow rate of 100 ml/s, while the downhole flow rate of the main wellbore circulation system was measured at 2.09 kg/s.

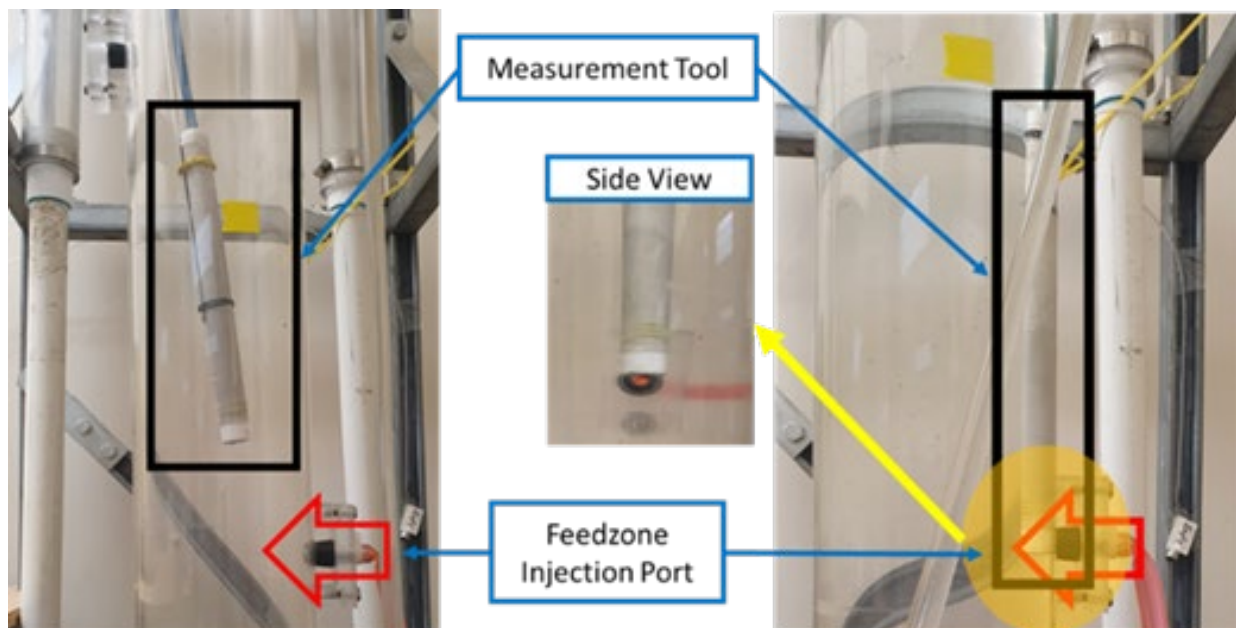


**Figure 4-14:** Static measurement assembly (a) Position 1 and (b) Position 2.

The voltage measurements and calculated chloride concentrations obtained from the static measurement experiment are shown in Figure 4-14. The graph illustrates that when the tool was placed at Position 1 (center of the wellbore), the voltage readings decreased gradually over time but not significantly. Conversely, when the tool was positioned at Position 2 (directly in front of the feed zone), the voltage measurements exhibited a rapid decline right from the beginning shown by the red dashed arrow. This indicates Position 2 was more sensitive to the changes in chloride concentration. Position 2 also yielded significantly better accuracy in determining the inflowing chloride concentration.

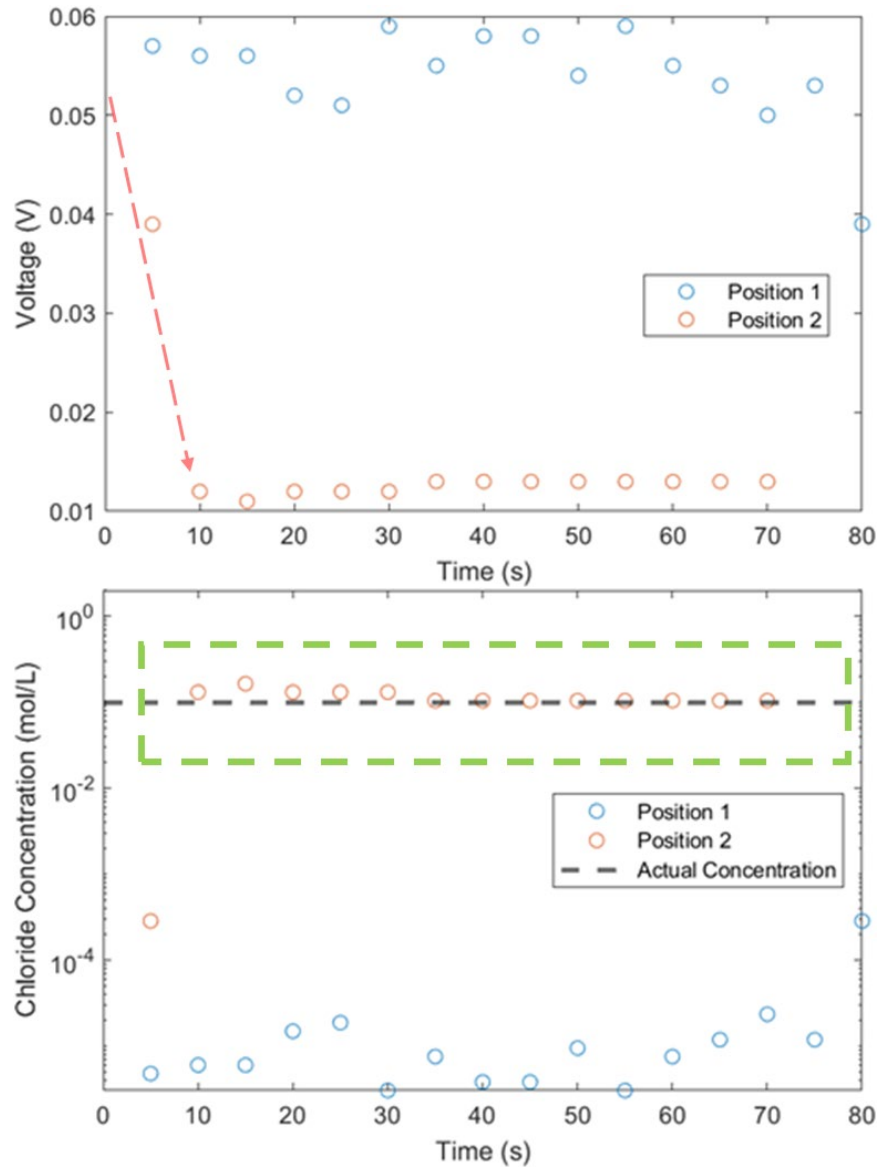


**Figure 4-15:** Tool placement sensitivity voltage measurement.

#### 4.1.1.4 Dye Tracer Test

A dye tracer test was conducted to gain insight into the behavior of the chloride-concentrated solution injected through the feed zone port. Blue food coloring was added to a 20-liter water solution with no dissolved chloride, mimicking the injected solution. The dye solution was then injected using a similar procedure as in the single feed zone injection experiments. The observations of the injected solution behavior over time in relation to the tool position are presented in Figure 4-16.

In Figure 4-16 (b) to Figure 4-16 (d), it can be seen that the injected flow, at a rate of 100 ml/s and downhole flow of 2.09 kg/s, initially tends to flow across the wellbore to the other side and then moves upwards following the downhole flow from the well system. As time progresses, Figure 4-16 (e) to Figure 4-16 (h) reveal the emergence of a blind spot, indicated by the red circle, where the injected fluid appears less concentrated compared to the surrounding areas. This blind spot occurs around the center of the wellbore, slightly above the feed zone height. This nonuniform mixing phenomenon

aligns with the suspicion raised in Section 4.2 as one of the reasons why the calculated chloride concentration was underestimated when measurements were conducted in the center of the wellbore, 2 inches (5 cm) above the feed zone.

Furthermore, turbulent flow was observed during the experiment, as demonstrated by a portion of the injected solution flowing downwards and then upwards again (marked by the black box) in Figure 4-16 (e) to Figure 4-16 (h). Moreover, Figure 4-16(g) indicates that after 55 seconds, the downhole flow from the reservoir tank has already become fully blue in color, showing that the reservoir tank had been thoroughly mixed with the injected solution, which then flowed back into the wellbore. This happened because, during this stage of the experiments, the second reservoir tank was not yet installed, resulting in contamination of the injection fluid being pumped back again into the main wellbore as the downhole flow.

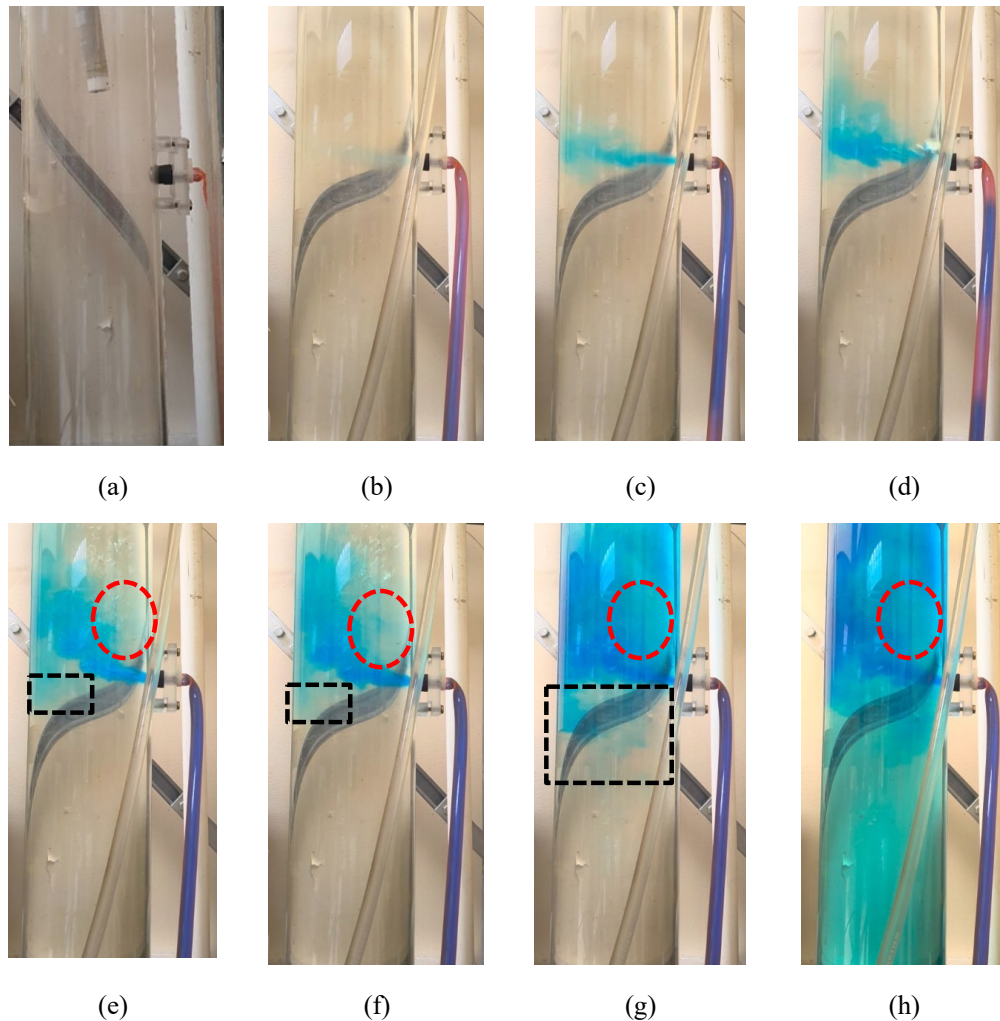


**Figure 4-16:** Tool position compared to dye injection experiment over time (a) 0.5 second, (b) 1 second, (c) 1.5 seconds, (d) 3 seconds, (e) 3.5 seconds, (f) 4 seconds, (g) 5 seconds, (h) 55 seconds.

In addition to the side view observation of the dye-tracer test, a cross-sectional perspective was also achieved by lowering an underwater camera into the flow. Figure 4-17 shows the cross-sectional view of the blue injection fluid mixed into the wellbore with a 0.5-second increment. The left column shows the actual footage, the middle column shows brightness- and contrast-adjusted footage, and the right

column shows the distribution of the blue dye indicated in black after data processing to focus and mark the blue pixels. The small red rectangle represents the point where the fluid is being injected, and the circle represents the circumference of the well at that depth. The clarity of the view is somewhat affected by white rings, which are bubbles on the camera lens. However, the original footage still captures the mixing of the dye in the wellbore.

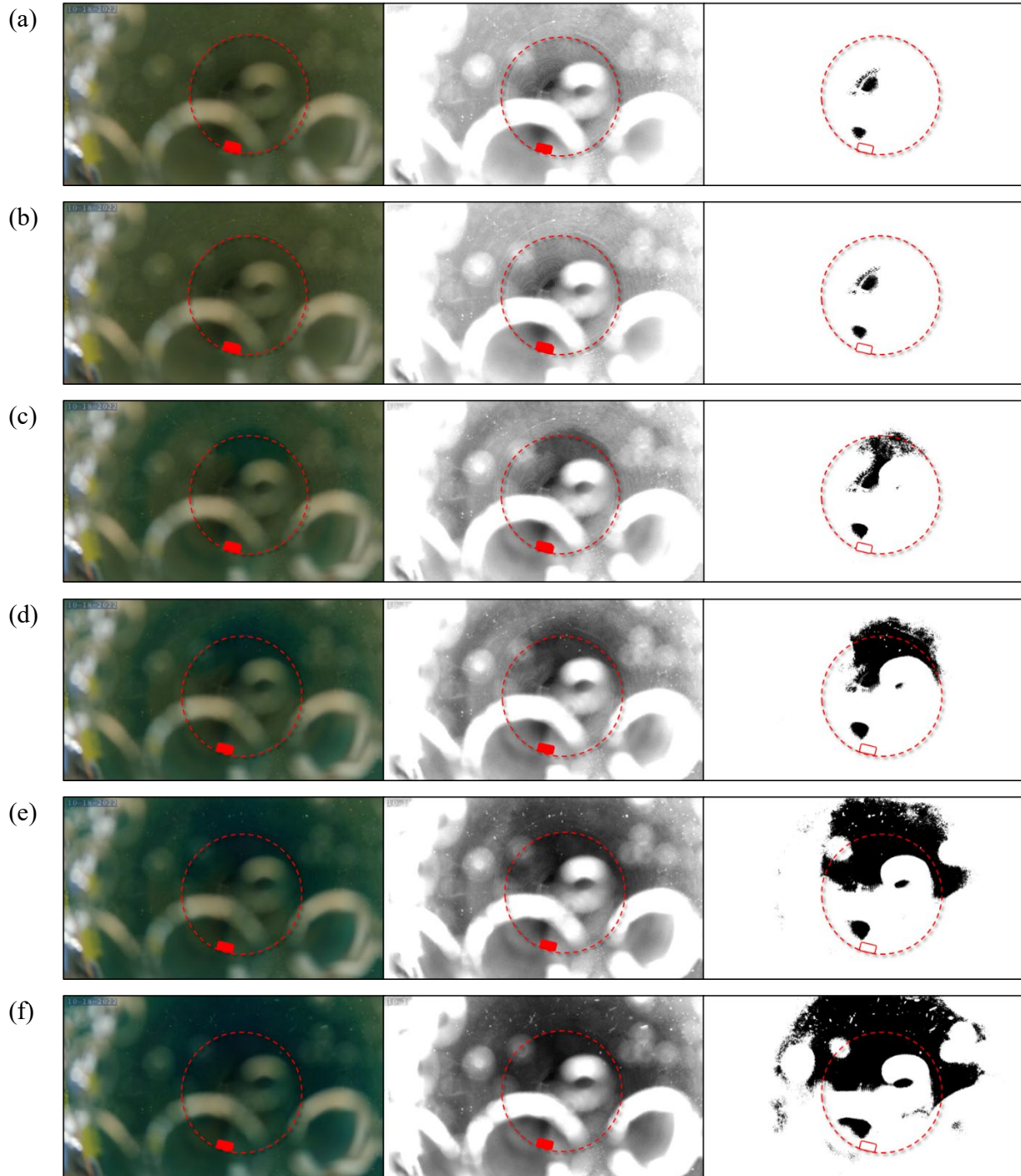


**Figure 4-17:** Dye tracer test cross-sectional view over time (a) 0 seconds, (b) 0.5 seconds, (c) 1 second, (d) 1.5 seconds, (e) 2 seconds, (f) 2.5 seconds.

Analyzing the cross-sectional view captured 1 second after the injection started (Figure 4-17c), it is evident that the injection fluid reaches the opposite side from the injection port and swirls towards the sides, confirming the observation from the side view. As time progresses, the swirling motion of the dye around the wellbore perimeter becomes more extensive, resulting in a significantly higher distribution of dye around the circumference, as seen in Figure 4-17f.

To gain a better understanding of the flow behavior within the wellbore, multiple dye tracer tests were conducted at different injection flow rates of 20, 50, and 70 ml/s while maintaining similar downhole flow conditions. The side view capture of these experiments is shown in Figure 4-18. As the flow stabilized, a blind spot was observed directly above the feed zone port in the 70 ml/s test (Figure 4-18c), as indicated by the red circle. However, this blind spot did not appear in the 20 and 50 ml/s cases.

In the 20 ml/s test (Figure 4-18a), the injected fluid tended to stay on the closer side wall of the injection port and exhibited less mixing with the downhole flow. In the 50 ml/s test (Figure 4-18b), the injected fluid traveled upward, covering approximately one-third of the well diameter, while leaving an area without significant mixing at the opposite end of the well diameter. It should also be noted that this injection rate behavior corresponds to a downhole flow rate of 2.09 kg/s which equals 2090 ml/s. Therefore, these behaviors are related to an injection rate of approximately 1%, 2.5%, and 3.5% of the main wellbore downhole flow, respectively, for the 20, 50 and 70 ml/s injection rates. These results suggest that a higher relative injection flow rate leads to the formation of a blind spot directly above the feed zone inlet. On the other hand, a lower flow rate produces a blind spot across from the injection port. Numerical simulations were performed to better understand the flow behavior observed in the dye tracer tests. The results are discussed in Section 4.1.2.2.



**Figure 4-18:** Dye injection tracer test (left) 20 ml/s, (center) 50 ml/s, (right) 70 ml/s.

#### 4.1.1.5 Dynamic Experiments

Dynamic measurement experiments were conducted to replicate the actual field deployment, where measurements will be taken along the wellbore using a downhole logging tool attached to a wireline that is in motion during logging. The measurements were conducted by running the tool into the

artificial wellbore system, starting from the top to the bottom of the well (run-in hole or RIH) and then pulling the tool back up (pull-out of hole or POOH).

A dynamic pulley system was constructed by attaching the tubular tool to a wire that was connected to a rod at the top of the wellbore. This rod is connected to a bipolar 2A stepper motor (Nema 17). This stepper motor was controlled using a 4A stepper motor driver (TB6600) and a 160V stepper motor drive. These devices are used to control and adjust the speed and direction of the stepper motor rotation as well as the turn on the stepper motor. These drivers were connected to a power source up to 12 volts. The downward and upward motion was achieved by rotating the rod that pulls the wire up and down.



**Figure 4-19:** Stepper motor, wire, and rod configuration at the top of wellbore.

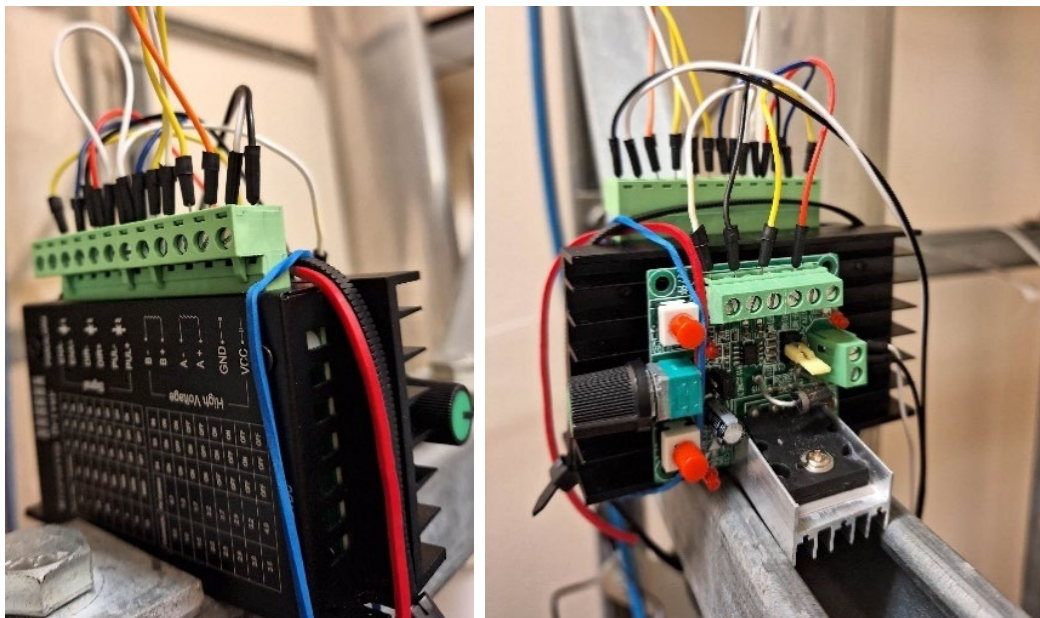


**Figure 4-20:** Stepper motor driver.

A data acquisition (DAQ) device was also installed to record the voltage from the tool. The devices used were NI USB 6009 for the original tool and NI USB 6001 for the new tool. The connections between the tool and the DAQ device were explained in Section 4.1.1.2, as shown in Figure 4-6. The DAQ device was set to read 100 to 1000 times per second. The in-house LabVIEW code is presented in Figure 4-7.

An in-house Python code was developed to divide the data into downward and upward motion data segments to process the recorded CSV file from the LabView output. These upward and downward data were then smoothened by averaging the data into a certain number of points along the wellbore to remove noise, resulting in a visually clearer data set for analysis. The visualization example of how the CSV data were being processed is shown in Figure 4-21.

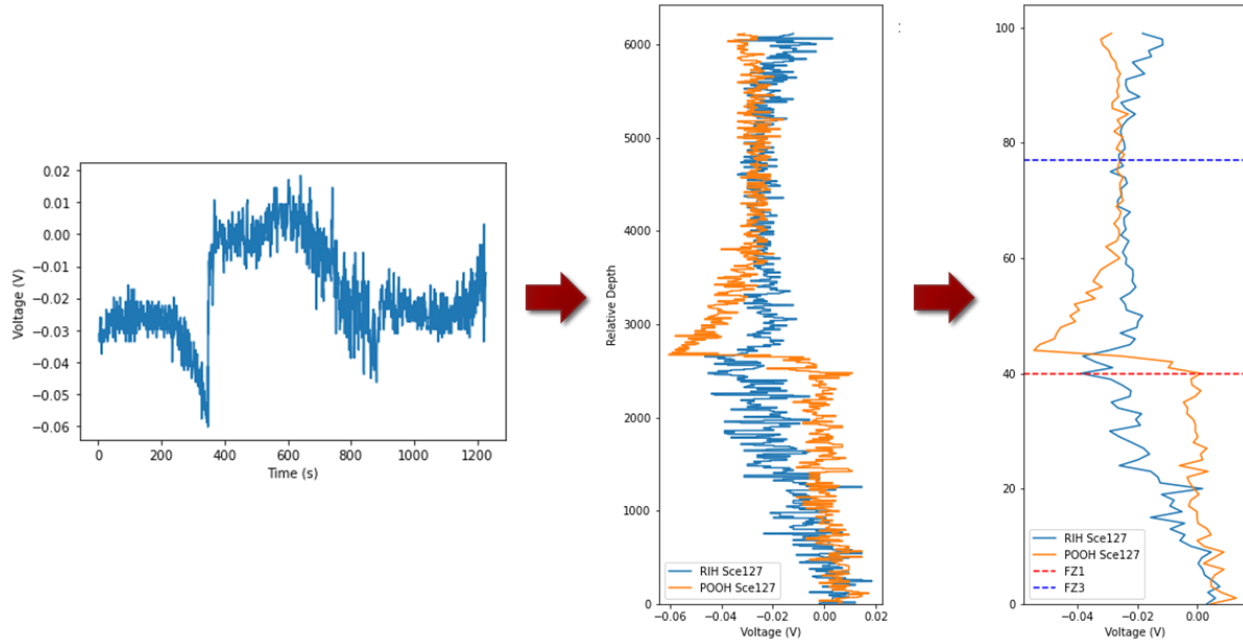


**Figure 4-21:** Python CSV data postprocessing visualization.

### *Single Fracture Inflow*

Initially, the DAQ device and reservoir tank 2 were not yet installed, and thus the voltage measurement was conducted using the voltmeter. Two different tool positions were evaluated. The first measurement was conducted with the tool close to the opposite wall from the injection, and the second measurement was run with the tool placed at the center of the wellbore (Figure 4-22). A centralizer was built around the tool to achieve the centralized position while conducting the dynamic measurement (Figure 4-33). The centralizer consists of plastic rods to keep the tool in the center of the wellbore. At the ends of the rods, wheels are attached at two points of the downhole tool, and wheels are attached to the rod to avoid running friction during upward and downward motion.

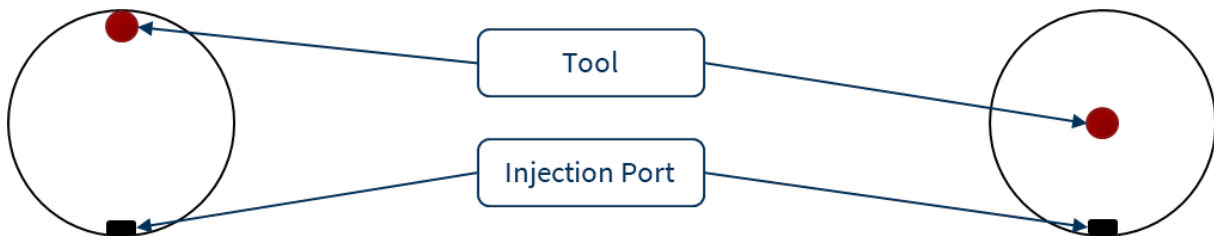


**Figure 4-22:** Dynamic measurement tool position cross-section (left) opposite the injection port and (right) centralized.

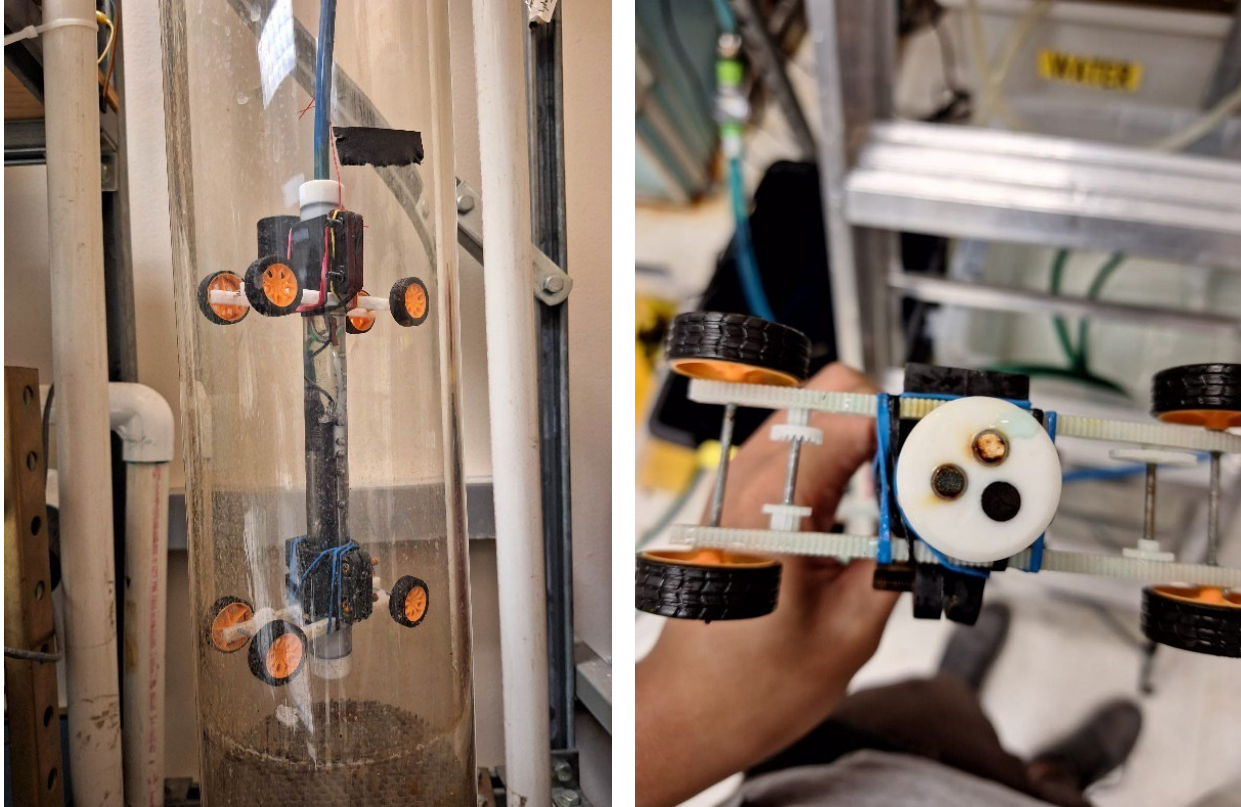


**Figure 4-23:** In-house centralizer, side view (left) and bottom view (right).

During this experiment, the fluid concentration from the injection port was 0.05 mol/L with a flow rate of around 100 ml/s, while the main wellbore flow had zero chloride concentration with a 2.09 kg/s mass rate. Due to limitations of the artificial well system and centralizer dimension, the dynamic measurements were limited to a specific section of the wellbore. The measured section had a total length of 58 inches, excluding 11 inches of the bottom part and 2 inches of the top part of the wellbore.

The result of the dynamic measurements taken across from the injection port is shown in Figure 4-24, while the result of the centralized position is shown in Figure 4-25. Both measurements successfully captured the drop in voltage around the injection port, indicating a spike of chloride concentration around that depth. However, it was noticed that there was a delay in response of the tool shown by the consistently different depth of calculated chloride concentration peak between the RIH and POOH. The RIH measurement registered a peak below the feed zone, while the POOH showed it above the feed zone.

After the conversion from voltage measurements, the calculated chloride concentration also showed promising results, being close to zero below the feed zone, but with higher values around and above the feed zone. However, a portion of the calculated chloride concentration around and above the feed zones was found to be higher than the possible value of 0.05 mol/L, which is the chloride concentration that was being injected. It was suspected that the calibration result needed to be refined.

Additionally, it was also observed that the centralized position generally measured higher concentration at similar depths compared to the opposite position, which indicated that less mixing happened further away from the feed zone. These findings are in agreement with the static measurements, suggesting closer measurement of the injection source results in more accurate results.

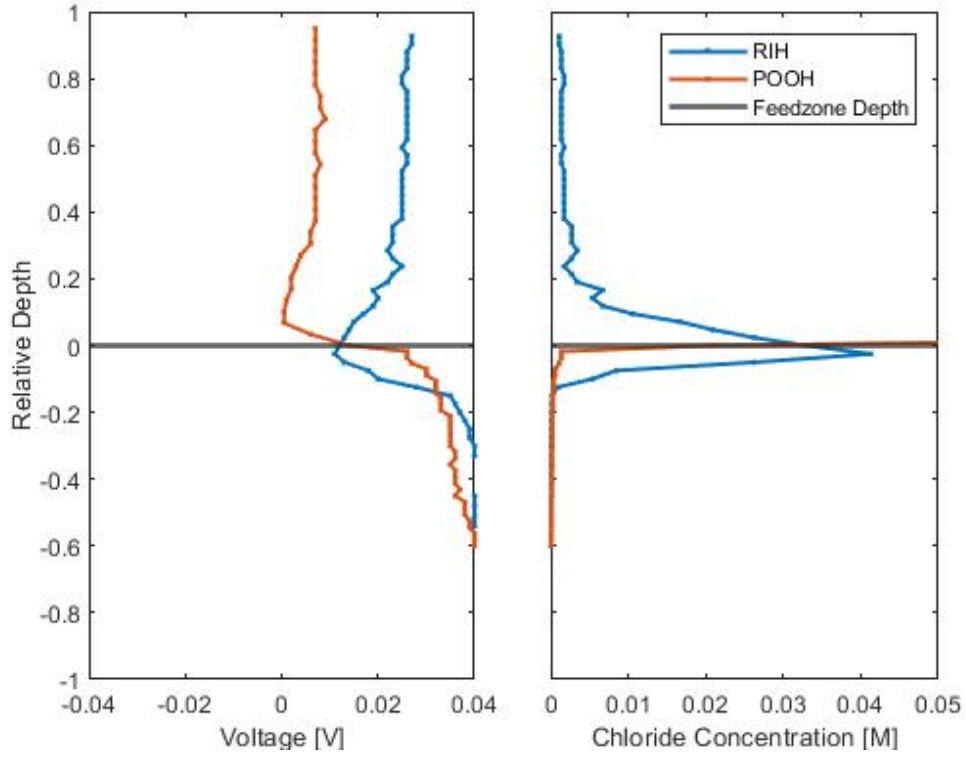


**Figure 4-24:** Dynamic measurement result at the opposite wall from the feed zone port.

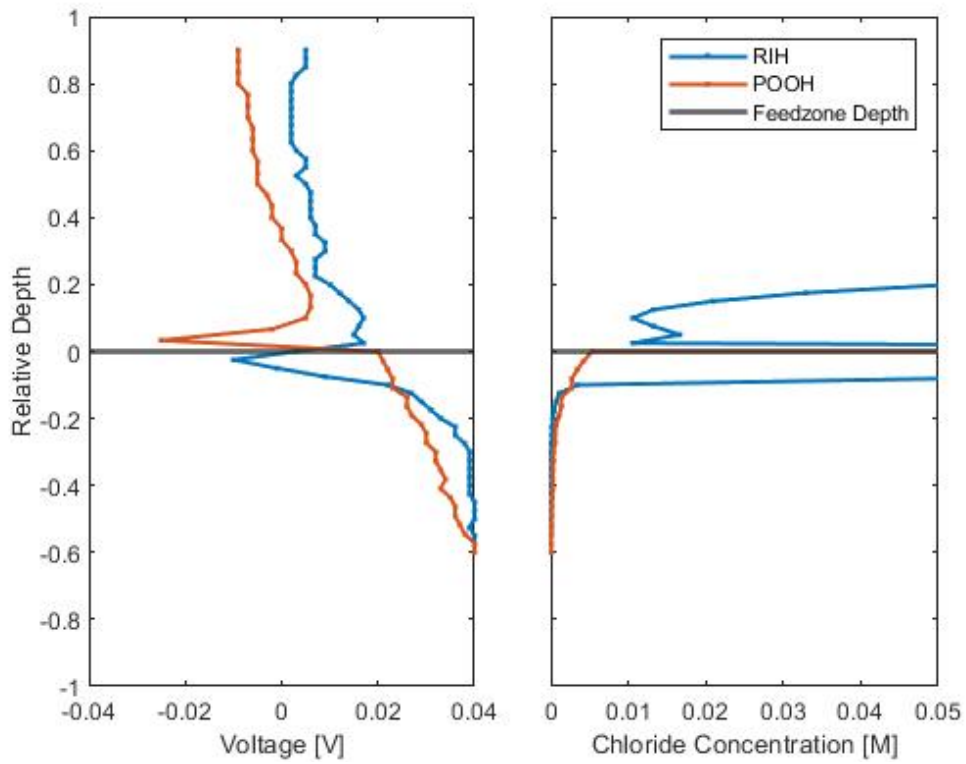


**Figure 4-25:** Dynamic measurement result at the center of the wellbore.

In addition to the multimeter measurements, single fracture inflow measurements were conducted using the DAQ (data acquisition) device at a later stage of the laboratory experiments. These measurements were carried out under the condition that reservoir tank 2 was installed to prevent cross-contamination of water in the reservoir tank.

A total of 25 measurements were performed, covering a range of different parameters. The feed zone port injection rates ranged from 6.31 to 100.94 ml/s, the downhole flow rates varied between 181.44 and 907.18 ml/s, and the chloride concentrations injected from the feed zone ports ranged from 0.001 to 0.5 M. The measurements were conducted using either feed zone port one or feed zone port 3, and the downhole tool was positioned centrally in the wellbore.

The comprehensive overview of all the scenarios measured can be seen in Table 4-1, which provides detailed information on each measurement case, including the specific combinations of injection rates, flow rates, chloride concentrations, and feed zone ports used.

**Table 4-1:** Single fracture dynamic measurement scenario details.

Scenario	Injection Flow Rate (ml/s)		Down Hole Flow Rate (ml/s)	Injection Concentration (M)	
	Feed zone 1	Feed zone 3		Feed zone 1	Feed zone 3
1	97.79	0.00	385.55	0.05	0.00
2	82.02	0.00	381.77	0.05	0.00
3	69.40	0.00	381.77	0.05	0.00
4	47.32	0.00	381.77	0.05	0.00
5	31.55	0.00	381.77	0.05	0.00
26	100.94	0.00	755.99	0.01	0.00
27	82.02	0.00	755.99	0.01	0.00
28	69.40	0.00	748.43	0.01	0.00
29	50.47	0.00	755.99	0.01	0.00
30	22.08	0.00	755.99	0.01	0.00
101	97.79	0.00	185.22	0.1	0.00
102	69.40	0.00	185.22	0.1	0.00
103	37.85	0.00	181.44	0.1	0.00
104	18.93	0.00	181.44	0.1	0.00
105	15.77	0.00	181.44	0.1	0.00
126	94.64	0.00	506.51	0.5	0.00
127	82.02	0.00	498.95	0.5	0.00

128	63.09	0.00	502.73	0.5	0.00
129	44.16	0.00	498.95	0.5	0.00
130	31.55	0.00	498.95	0.5	0.00
151	0.00	53.63	548.09	0.00	0.10
152	0.00	18.93	555.65	0.00	0.10
153	0.00	6.31	555.65	0.00	0.10
154	0.00	34.70	555.65	0.00	0.10
155	0.00	37.85	638.81	0.00	0.10

An example of the dynamic measurement using the DAQ device can be seen in Figure 4-26. Scenarios 127, 128, and 129 were measured under similar conditions where chloride concentration injection of 0.5 mol/L was injected through feed zone 1 (FZ1), and the downhole flow rate was around 500 ml/s. The only difference between the three scenarios was the injection rate with 82, 63, and 44 ml/s correlates to scenarios 127, 128, and 129, respectively.

From the measurement, it was observed that the downhole tool successfully captured the voltage drop around the depth of the feed zone port, both during the upward motion (POOH - Pull Out of Hole) and downward motion (RIH - Run in Hole) of the tool. However, the change in voltage was more pronounced during the upward motion compared to the downward motion. This indicates that the tool was more sensitive to detecting changes in voltage during the POOH motion, perhaps indicating that it responds faster to increasing chloride concentrations than to decreasing chloride concentrations. Additionally, it was noted that there was a delay in the voltage response between the POOH and RIH motions. The voltage drops during the POOH motion occurred at a greater depth than the voltage drop during the RIH motion, suggesting a lag in the measurement response similar to the multimeter measurement.

Furthermore, the injection flow rate impacted the voltage measurement. Higher injection rates, such as in Scenario 127, resulted in a greater drop in voltage compared to the other two measurements (Scenarios 128 and 129), which had lower injection rates. This observation indicates that the injection flow rate influenced the magnitude of the voltage drop, with higher injection rates leading to more significant changes in voltage.

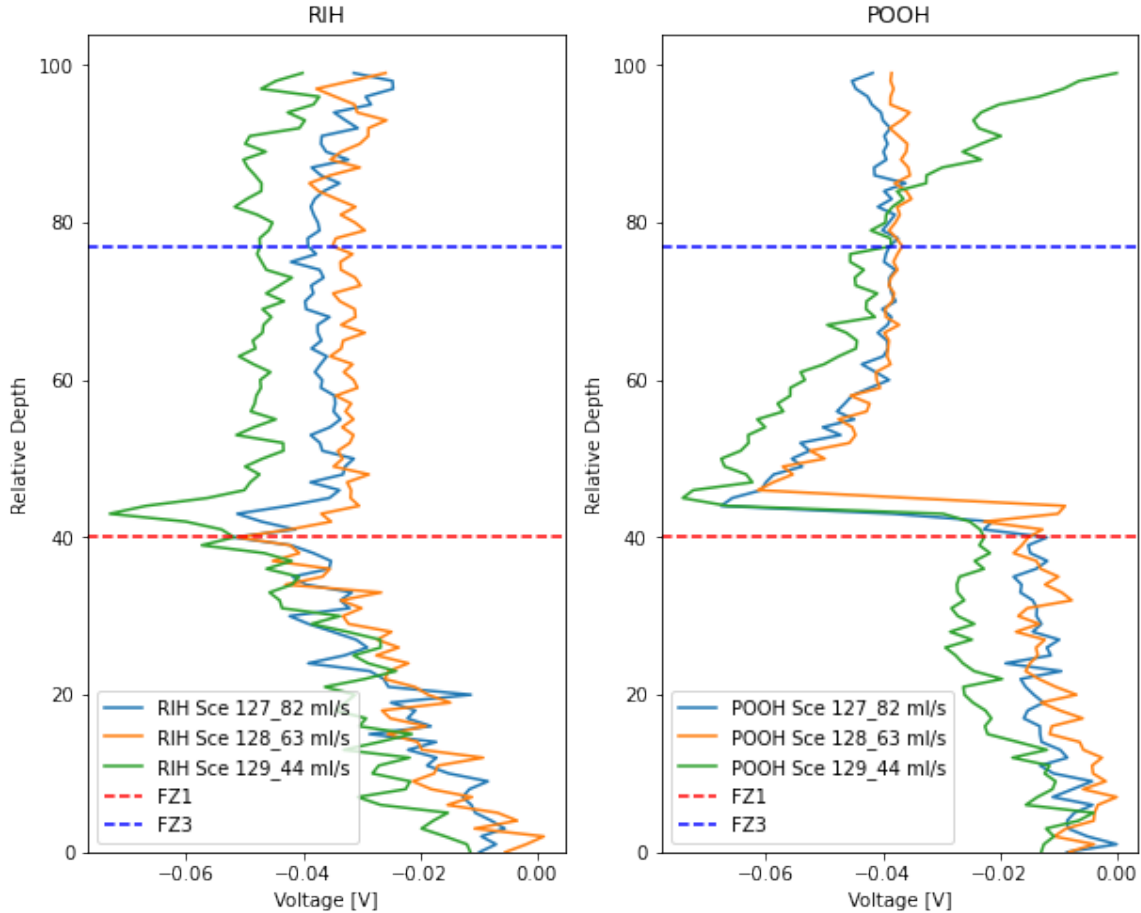


**Figure 4-26:** Dynamic measurement injection flow rate variation.

### ***Multiple Fracture Inflow***

Experiments involving multiple feed zones were also conducted using the version 1 tool connected to the DAQ device and the modified artificial well system with reservoir tank 2. A total of seven measurements were performed, involving two feed zones (feed zone 1 and feed zone 3) and varying ranges of injection rates, downhole flow rates, and chloride concentrations (**Table 4-2**). The injection rates for these measurements ranged from 9.46 to 100.94 ml/s, while the downhole flow rates varied between 521.63 and 638.81 ml/s. The chloride concentration injected from the feed zone ports ranged from 0.05 to 0.1 M.

In Scenarios 156 to 158, the injection rate of the lower feed zone (FZ1) was adjusted while the injection rate of the upper feed zone (FZ3) remained constant. The purpose of these scenarios was to observe the effect of varying the injection rate in the lower feed zone while keeping the upper feed zone consistent. The chloride concentration was maintained the same for both feed zone ports.

On the other hand, Scenarios 161 to 164 involved adjusting the injection rate of the upper feed zone (FZ3) while keeping the injection rate of the lower feed zone constant. The objective of these scenarios was to analyze the impact of varying the injection rate in the upper feed zone while maintaining a constant rate in the lower feed zone. Similar to the previous scenarios, the chloride concentration was consistent for both feed zone ports.

**Table 4-2:** Dual fracture dynamic measurement scenario details.

Scenario	Injection Flow Rate (ml/s)		Down Hole Flow Rate (ml/s)	Injection Concentration (M)	
	Feed zone 1	Feed zone 3		Feed zone 1	Feed zone 3
156	100.94	18.93	559.43	0.05	0.05
157	69.40	18.93	559.43	0.05	0.05
158	44.16	18.93	559.43	0.05	0.05
161	28.39	9.46	529.19	0.1	0.1
162	28.39	22.08	529.19	0.1	0.1
163	28.39	34.70	525.41	0.1	0.1
164	28.39	44.16	521.63	0.1	0.1

Based on the measurement results and analysis of Scenario 156-158 presented in Figure 4-27, it can be observed that the voltage measurements successfully captured the drop in voltage around the depth of the lower feed zone (FZ1), both during the RIH (Run In Hole) and POOH (Pull Out of Hole) motions. However, there was no distinct drop in voltage observed at the depth of the upper feed zone (FZ3).

Upon examining the injection rates, it is evident that the varying injection rates of FZ1 were significantly higher than the injection rate of FZ3, with values ranging from 44.16 to 100.94 ml/s compared to 18.93 ml/s. This difference in injection rates is suspected to be the reason for the lack of a visible drop in voltage at the location of the upper feed zone. It is possible that due to the low injection rate in FZ3, the injected fluid did not reach the centralized downhole tool effectively. The flow rate from the upper feed zone (FZ3) would have been around 3% compared to the wellbore's overall flow rate. This low percentage might not have been sufficient to reach the centralized downhole tool and produce a visible drop in voltage that could be captured during the time of os measurements as the tool moved past the feed zone.

Another factor that may have contributed to the lack of a distinct voltage drop at the upper feed zone (FZ3) is the high injection rate at the bottom feed zone (FZ1). The downhole flow in the wellbore already had a certain chloride concentration due to the high injection rate at the bottom feed zone. Therefore, the additional lower flow rate from the upper feed zone may not have been sufficient to change the overall chloride concentration of the wellbore fluid sufficiently to be visually identified in the voltage measurements.

In comparison to the previous multiple feed zone measurements, Scenario 161-163 (Figure 4-28) had injection ranges that were within the same ranges between FZ1 and FZ3. FZ1 was kept constant at 28.39, while FZ3 was adjusted for each scenario to range from 9.46 to 34.7 ml/s.

It can be observed that during the RIH (Run in Hole) motion, indications of both the lower feed zone (FZ1) and upper feed zone (FZ3) were present. However, during the POOH (Pull Out of Hole) motion, the lower feed zone consistently showed a drop in voltage in Scenario 161 and 162, while the upper feed zone only exhibited an indication of inflow in Scenario 162. Furthermore, in the RIH measurement of the upper feed zone, it is evident that the scenario with the higher injection rate (Scenario 163,

represented by the green line) resulted in a larger drop in voltage compared to the other scenarios. On the other hand, at the lower feed zone, the drop in voltages across the different scenarios was relatively similar. These observations confirm the findings from previous measurements, indicating that higher injection rates lead to a greater decrease in voltage.

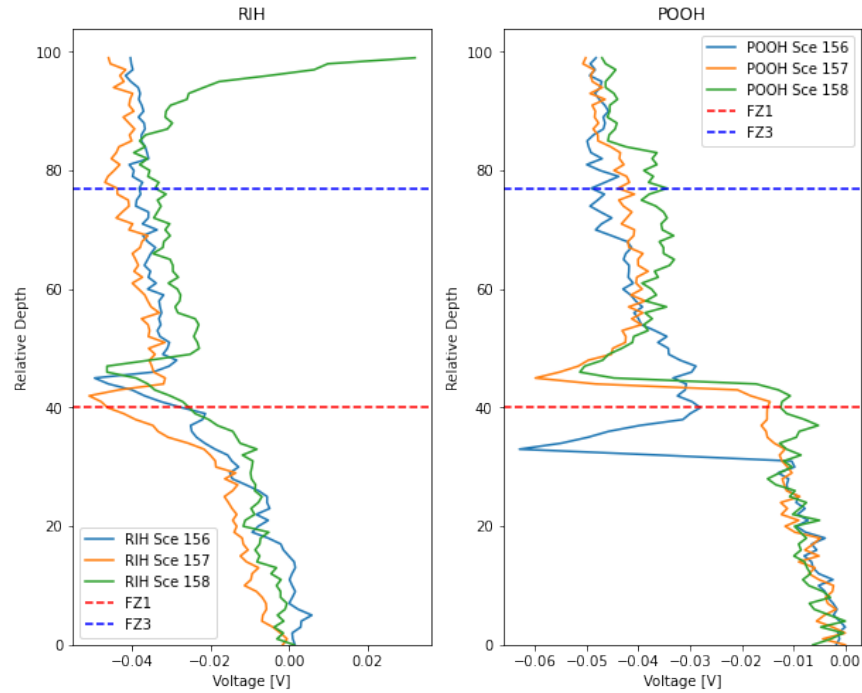


**Figure 4-27:** Dynamic measurement multiple feed zone injection 1.

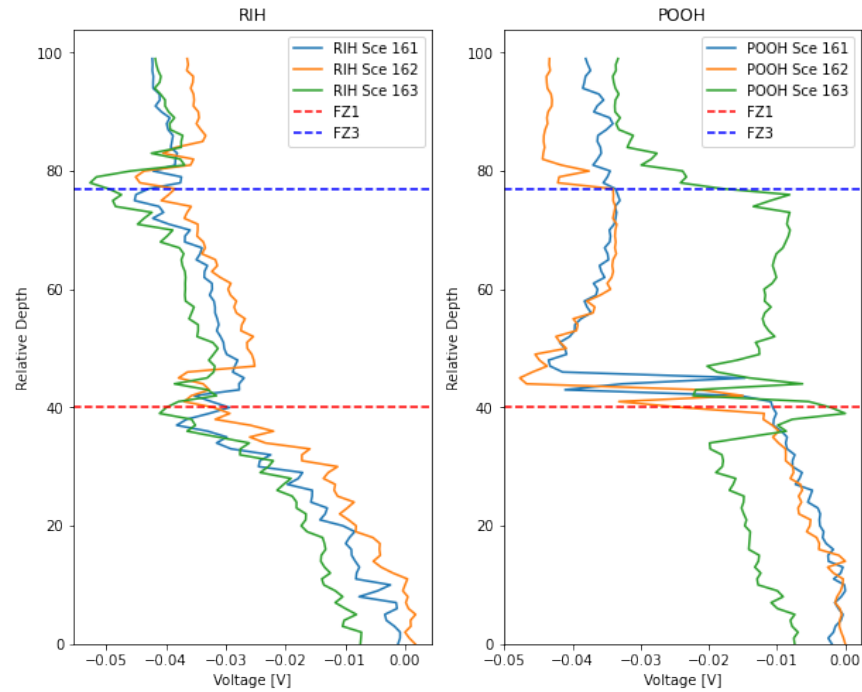


**Figure 4-28:** Dynamic measurement multiple feed zone injection 2.

## 4.1.2 Round 1 Numerical Simulation

The numerical simulation aimed to test assumptions about the dispersion of chloride concentrations and inform a methodology that could produce reliable results in field deployment.

### 4.1.2.1 Simulation Setup

The simulations in Round 1 involved miniature and laboratory scales. The miniature scale applied miniaturized and simplified geometry to quickly verify different setups before delving into larger-scale cases. The laboratory scale was designed to be as close as possible to the artificial well system to draw a comparison to the laboratory experiment results.

The miniature scale's geometry, boundary conditions, and mesh cross-section are shown in Figure 4-29. The laboratory scale geometry, boundary conditions, and mesh cross-section with a single feed zone are depicted in Figure 4-30, which was considered the base case setup. The multiple feed zone cases in the laboratory scale would follow the base case setup but with the number and location of the feed zones being modified. Other aspects of the base case setup may also be adjusted according to the tested scenarios, such as different feed zone radii. The different wellbore configurations and inflow scenarios tested across over 80 simulation cases are summarized in Table 4-3.

The Computational Fluid Dynamics (CFD) simulations were performed using ANSYS Fluent software and assisted with ANSYS Workbench software for organizing and automating the simulation workflows. COMSOL software was also evaluated against ANSYS Fluent, and it was concluded that ANSYS Fluent was better suited for this study's objectives. The resulting comparison between ANSYS Fluent vs. COMSOL is detailed in Section 4.1.2.10.

Multiple operating conditions and solution methods in the CFD software were tested to arrive at a consistent physics that could work on a wide array of scenarios, which were described as follows:

- The simulation scenarios were run in a steady state. Additional transient cases were added when there was a need to compare with video footage.
- The turbulent viscosity equations employed realizable  $k$ - $\epsilon$  with standard wall function. This particular set of equations could model flow features with strong streamline curvature, vortices, and rotation (Fluent Inc., 2006).
- Both saline and freshwater materials were present in the main wellbore, and multiphase principles governed the mixing between them. While this setup might not be ideal compared to chemical diffusion, it ensured model convergence.
- Operating conditions were set under standard gravity with no heat transfer, as the laboratory experiments involved standard temperature and pressure.
- Three boundary conditions were present: the main wellbore inlet, the feed zone inlet, and the wellbore top outlet. The inlet flow rates varied with scenarios, while the wellbore top outlet was set as a pressure outlet except for scenarios involving closed wellheads.

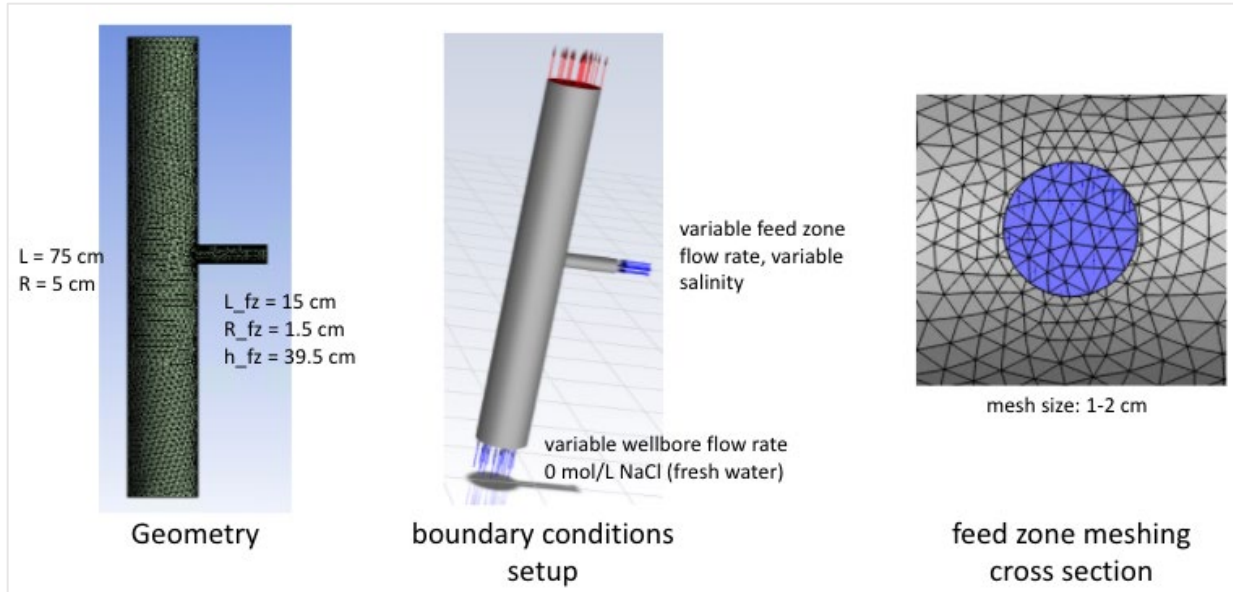


**Figure 4-29:** The geometry setup, boundary conditions, and meshing cross-section of Model S1 (single feed zone), miniature scale.

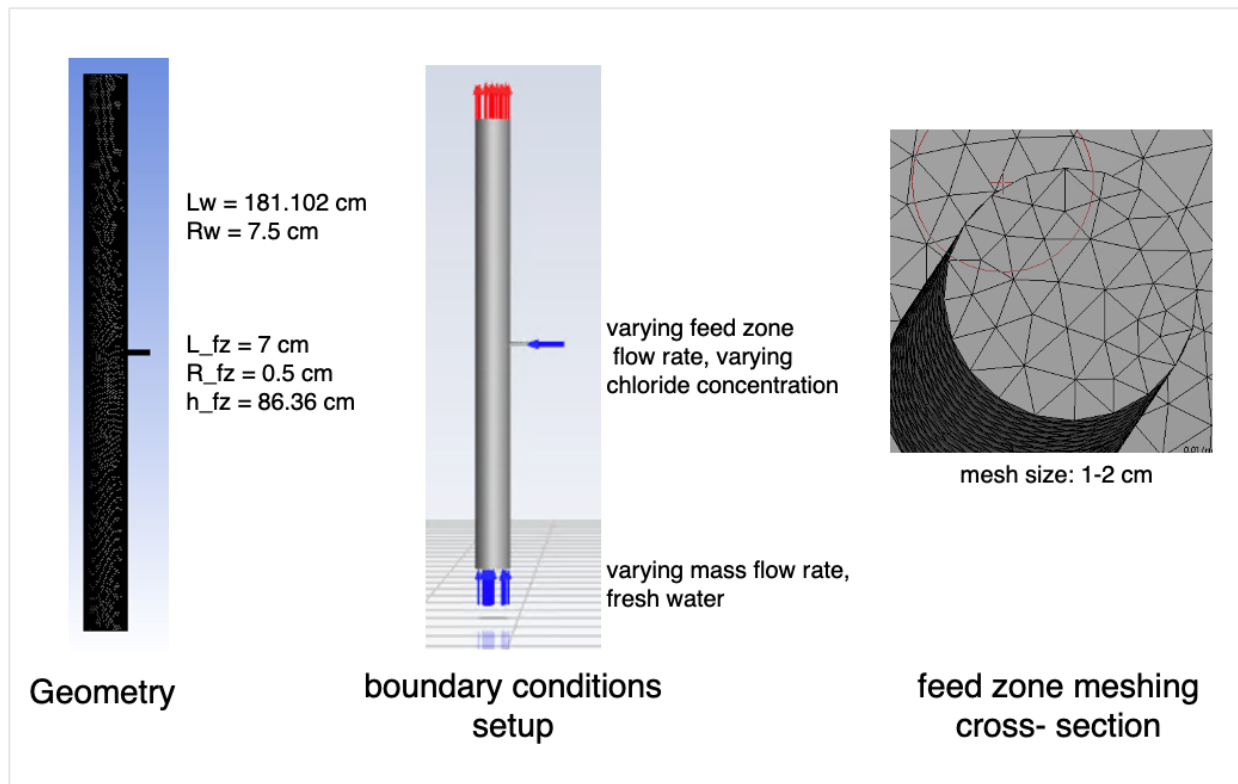


**Figure 4-30:** The geometry, boundary conditions, and meshing cross-section of Model S1 (single feed zone), laboratory scale. The laboratory scale mimicked the dimensions of the well system at the Stanford Geothermal Laboratory. Certain aspects of the geometry, such as feed zone radius, would be tweaked as part of the modeling scenarios.

**Table 4-3:** Scenario parameters for numerical simulations. Note that a scenario can have one or more variations of the parameters.

Scenario parameters	Description	Case ranges
<b>Feed zone radius</b>	Testing different feed zone radius at a well with single feed zone	0.1 cm, 0.5 cm, and 0.7 cm
<b>Wellhead opening</b>	Testing cases with open and flowing wellhead vs closed wellhead	Open wellhead, closed wellhead
<b>Main wellbore flow rate</b>	Testing different wellbore flow rates which represents the internal wellbore flow	Between 500 to 2000 ml/s
<b>Feed zone inflow rate</b>	Testing different feed zone inflow rates	Between 20 to 100 ml/s
<b>Number of feed zones</b>	Testing different number of feed zones and various configuration of flow rates between the feed zones	One feed zone, two feed zones
<b>Chloride concentration</b>	Testing different chloride concentration from the feed zones. The chloride concentration of the bottom wellbore is zero, as the fluid is fresh water.	Between 0.05 to 0.1 mol/L
<b>Tool presence</b>	Observing fluid flow behavior with and without the tool present	Undisturbed state, disturbed state
<b>Log extraction positions</b>	Testing different positions across the well cross section to extract the volume fraction log.	Five positions across wellbore

#### 4.1.2.2 Results of Miniature Scale Simulations

The miniature scale consisted of two cases, S1-Mini1 and S1-Mini2, with parameters summarized in Table 4-4. The S1-Mini1 case explored fluid behavior with a small delta between the main wellbore and feed zone flow rates with entirely freshwater fluid. Meanwhile, S1-Mini2 explored a large flow rate delta and introduced saline inflow from the feed zone.

The simulation results for the miniature case (Figure 4-31) showed that a smaller flow rate delta (S1-Mini1) would cause more turbulent flow and better fluid mixing in front of the feed zone, which would allow tool positioning at any distance from the feed zone inlet. In contrast, a larger flow rate delta (S1-Mini2) demonstrated the formation of a blind spot, starting halfway across the diameter. Measurements taken in this area will underestimate the chloride concentration.

**Table 4-4:** Miniature Scale Simulation Cases, Parameter Summary

Case ID	S1-Mini1	S1-Mini2
Description	miniature scale, freshwater inflow	miniature scale, saline inflow
Main wellbore flow rate	0.5 kg/s	6.7 kg/s
Feed zone flow rate	0.865 kg/s	1 kg/s
Flow rate delta (kg/s)	0.365	5.7
NaCl concentration at feed zone	Zero mol/L	0.23 mol/L
NaCl concentration delta (mol/L)	0	0.23

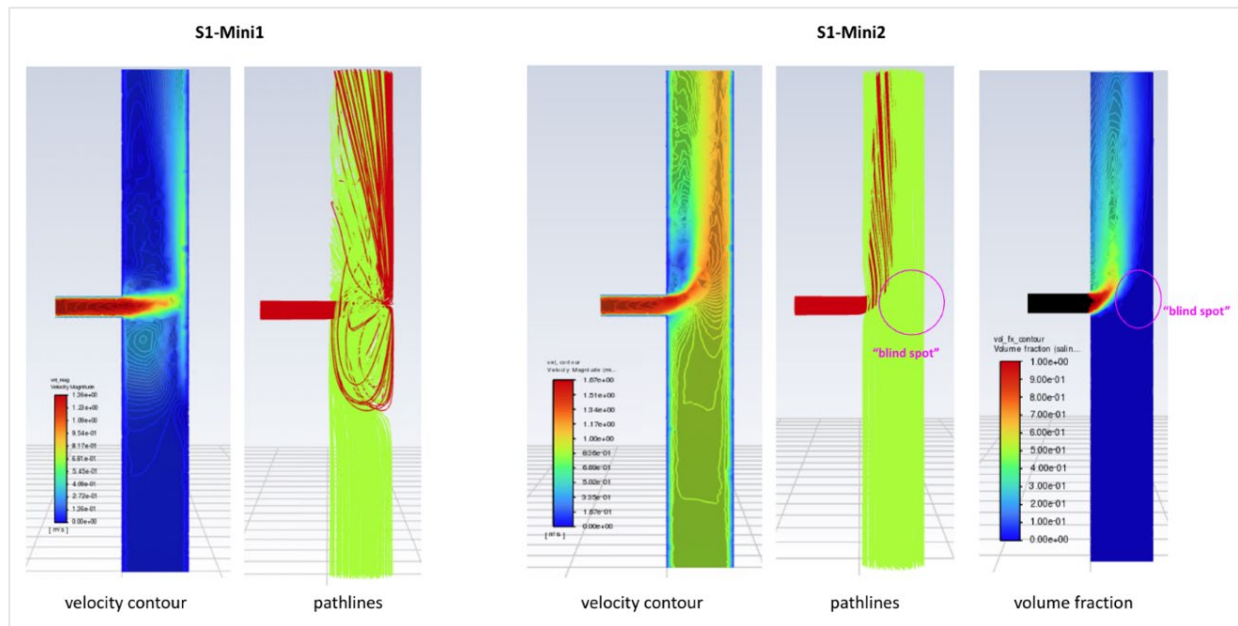


**Figure 4-31:** Simulation results of S1-Mini1 and S1-Mini2, with the latter case showing blind spot formation away from the inlet.

#### 4.1.2.3 Dye Tracer Test Comparison

Upon successful miniature-scale simulations, subsequent simulations focused on simulating the dye tracer test experiments, which includes the numerical simulation base case. The base case referred to the laboratory scale simulations with flow rates following the values observed during the dye tracer test, which was 2.09 kg/s for the wellbore flow rate and around 112.2 ml/s for the feed zone inflow rate. The feed zone inflow rate varied between 20 to 200 ml/s in the follow-up simulation cases. The simulation results were subsequently compared with dye tracer test video footage from above and in front of the well system. Note that the base case validation did not involve any presence of the chloride tool yet, thus is referred to as the undisturbed state in this report.

The comparison showed that the numerical simulations could reproduce the observed features in the dye tracer test (**Figure 4-32**). For instance, the dye tracer tests and numerical simulations showed

periodic turbulence leading to alternating fluid flow paths between curved and straight configurations. The numerical simulations also replicated blind spots at two locations identified in the dye tracer test: above the feed zone inlet and around half the diameter behind the inflow path, similar to what was observed in the miniature cases.

Furthermore, the volume fraction result of the 200 ml/s inflow case revealed a downward distribution of feed zone fluid, which was not evident in the pathlines diagram. This observation suggests that the downward distribution is likely due to the chloride concentration diffusion from regions of higher concentration to areas of lower concentration.

A further comparison between the footage of the lab experiment captured from the top of the well and the feed zone fluid volume fraction (the horizontal cross-sections shown in Figure 4-33) demonstrated consistent behavior in blind spot formation and the inflow fluid reaching the opposite wall before circulating along the perimeter. These comparisons between the numerical simulations and the laboratory experiments validate the reliability and accuracy of the base cases and serve as a foundation for further investigations and scenario analyses.

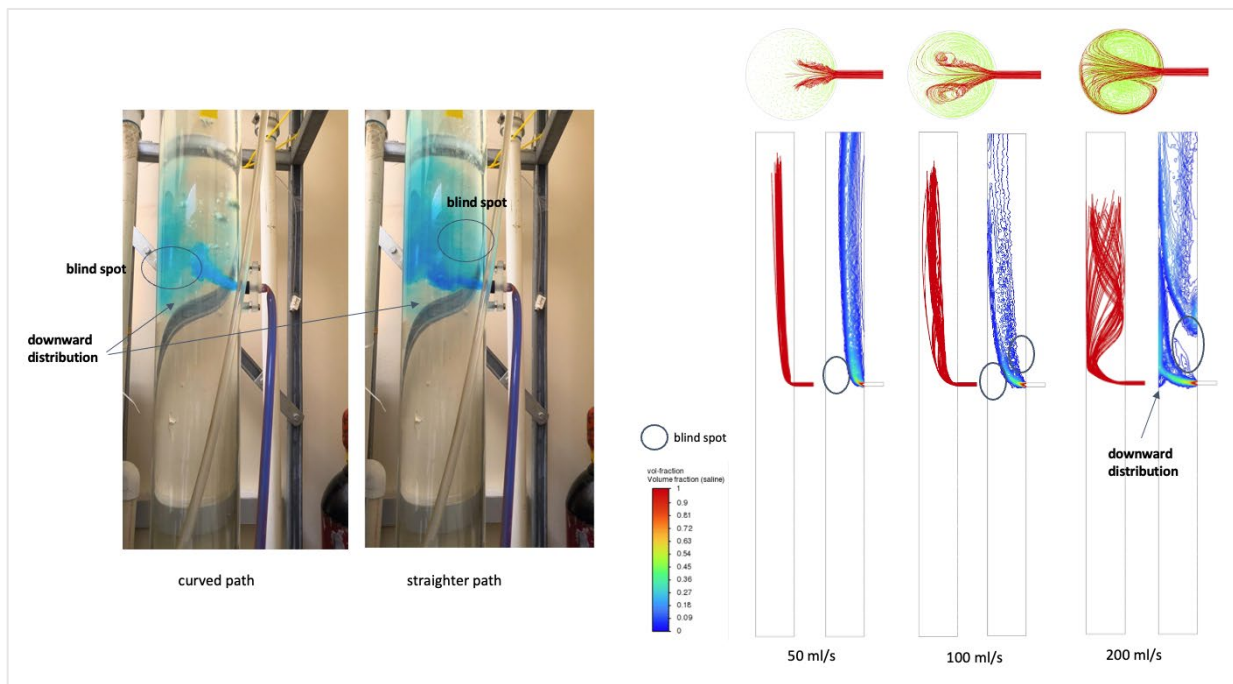


**Figure 4-32:** Comparison between laboratory dye tracer test and the undisturbed state cases at different feed zone inflow rates, shown as pathlines and volume fraction graphics horizontal cross-section along with pathlines vertical cross-section at the inlet location.

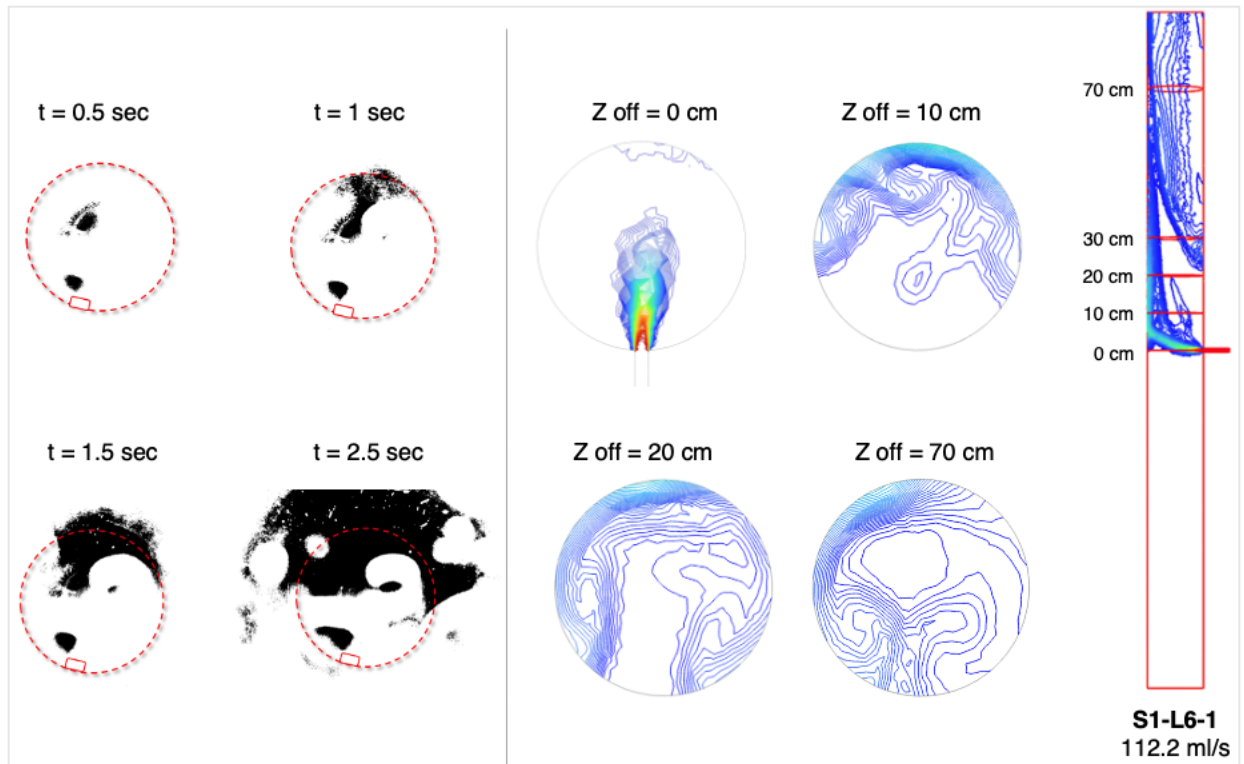


**Figure 4-33:** Lab experiment results recorded from the top of the well compared with horizontal sections of the undisturbed state base case at different height (z-value) offsets. The contours show the volume fraction of the inflow fluid, which is a NaCl solution of 0.05 mol/L concentration.

#### 4.1.2.4 Closed Wellhead Simulations

Different cases were analyzed to investigate fluid flow behavior in both flowing (closed wellhead) and static (open wellhead) conditions, as depicted in Figure 4-34. The variations in wellbore internal flow rate (kg/s) and feed zone flow rate (ml/s) are also indicated in the figure.

When the wellhead was closed, and there was no internal flow, the fluid flow demonstrated adequate mixing in front of the feed zone, even at the slowest inflow rate of 20 ml/s. In contrast, when the wellhead was open and flowing, the feed zone inflow could only enter the main wellbore when the internal flow was not too strong. When the wellbore flow rate became excessively large, the feed zone inflow could not enter the main wellbore. Instead, backflow into the feed zone was observed.

For the development of the chloride tool, the inflow needs to reach the center of the wellbore to enable meaningful measurements. Additionally, geothermal wells are expected to have some internal flow even when shut in, making the open and flowing wellbore cases more realistic. For this particular laboratory scale setup, it was observed that a minimum difference of 2.04 kg/s between the internal flow and feed zone inflow was required for the feed zone fluid to reach the center of the wellbore adequately.

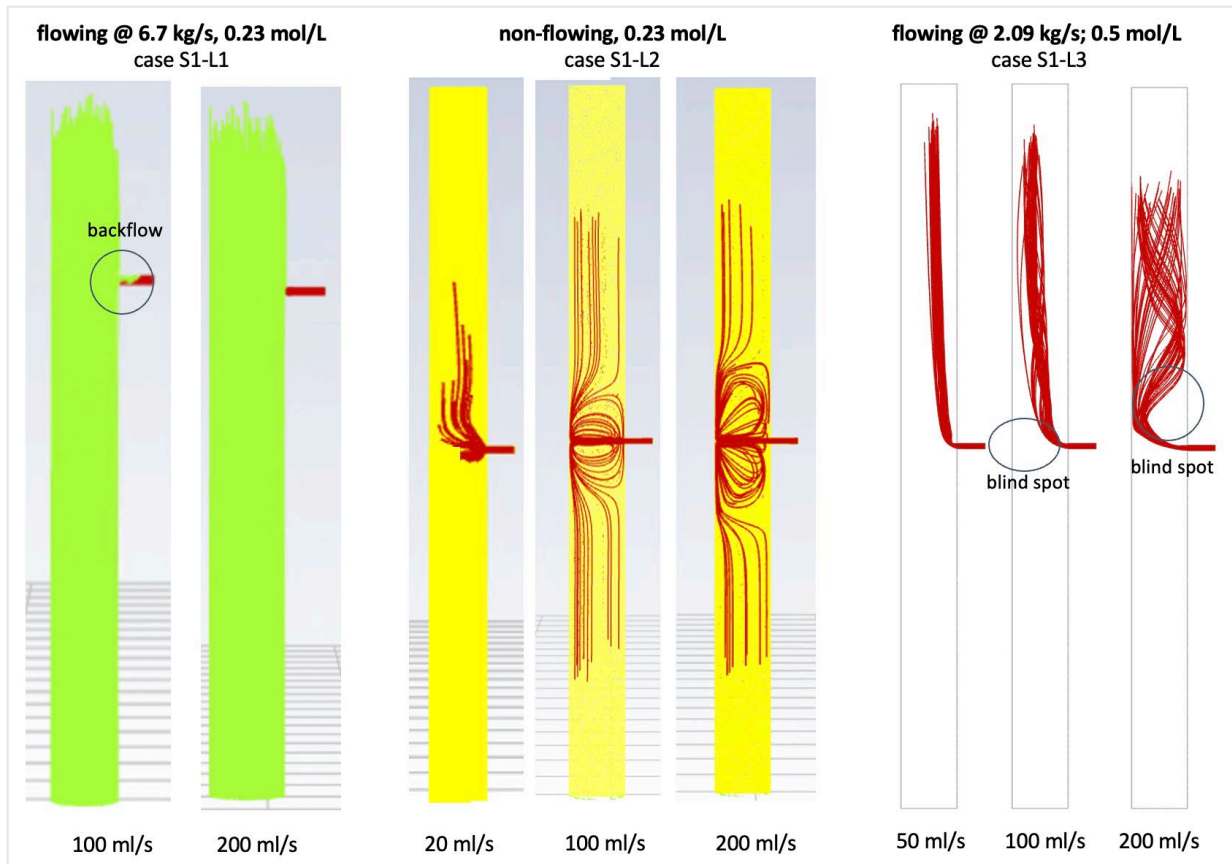


**Figure 4-34:** Simulation results of flowing (open wellhead) vs. non-flowing wells (closed wellhead). The wellbore flow rate is denoted in kg/s at the top of the graphics, while the feed zone inflow rate is denoted in ml/s at the bottom.

A multipronged electrode design could be considered to circumvent the minimum flow rate delta requirement. Such a design would allow measurements at multiple locations within the same depth, enabling the chloride tool to detect feed zones with low inflow rates more effectively.

#### 4.1.2.5 Varying Feed Zone Radius

In cases involving a smaller feed zone inlet radius (**Figure 4-35**), a slight increase in the radius from 0.5 cm to 0.7 cm while maintaining the feed zone flow rate resulted in weaker feed zone inflow capable of reaching the opposite wall. However, when the radius was too small, the feed zone inflow could not enter the main wellbore as the feed zone flow was weaker than the internal flow in the wellbore.

These observations were valid for the point-source feed zone. Different feed zone geometries, such as inclining planes resembling fracture intersections, might exhibit different behavior from this particular group of cases. Furthermore, larger feed zone radii were typically accompanied by larger inflow rates, which might result in stronger feed zone inflow which would be more accurately measured by the chloride tool. Thus, it was only sometimes the case that a larger feed zone radius for point-source feed zones would result in weaker inflow.

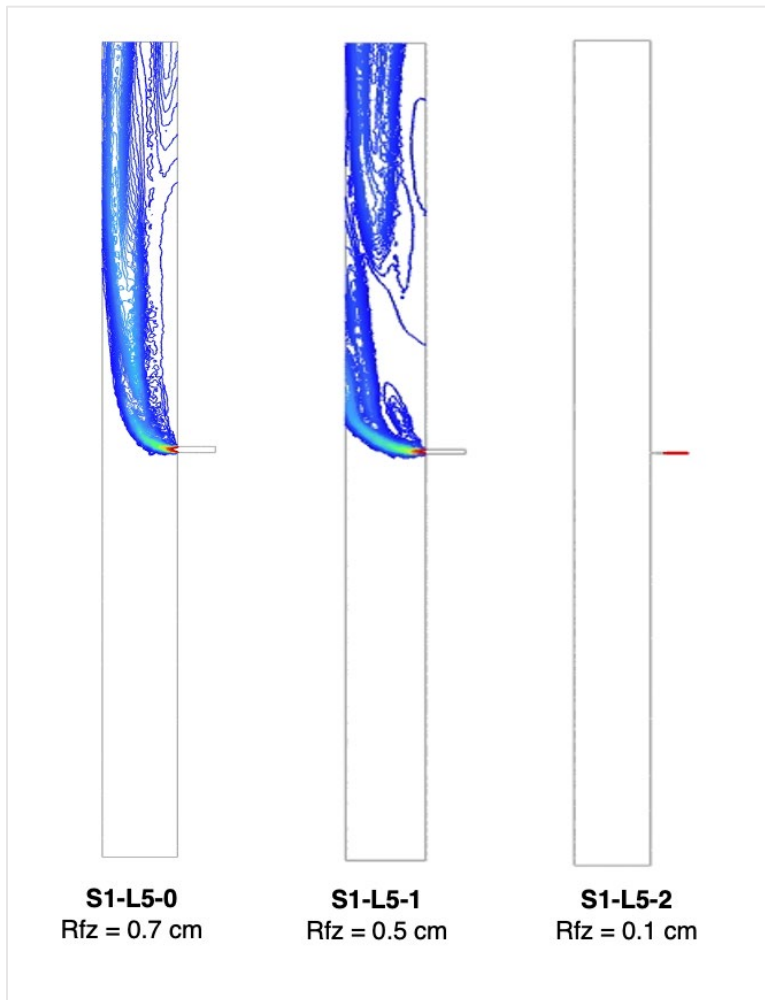


**Figure 4-35:** Simulation results in laboratory scale with different feed zone radii.

#### 4.1.2.6 Varying Log Extraction Position

**Figure 4-36** illustrates the effect of different tool positions across the wellbore width on the extracted chloride concentration log data. The chloride concentration at the inflow was set at 0.5 mol/L. It was observed that extracting data from positions within the feed zone jet, such as the center of the wellbore (midline position in the figure) and the opposite wall (wall-line-4 in the figure), yielded the valuable inlet front peak pattern, which aided in locating and quantifying the feed zone inflow.

In contrast, extracting data from outside the jet concealed the inlet front peak pattern, making it challenging to identify the feed zone and accurately measure the flow rate. Therefore, the tool design must ensure that chloride data can be collected within the feed zone jets along the well, which could be accomplished by employing a centralizer. Furthermore, a multipronged tool design would aid in measuring chloride concentrations at different locations at once, providing more validation points and increasing accuracy.

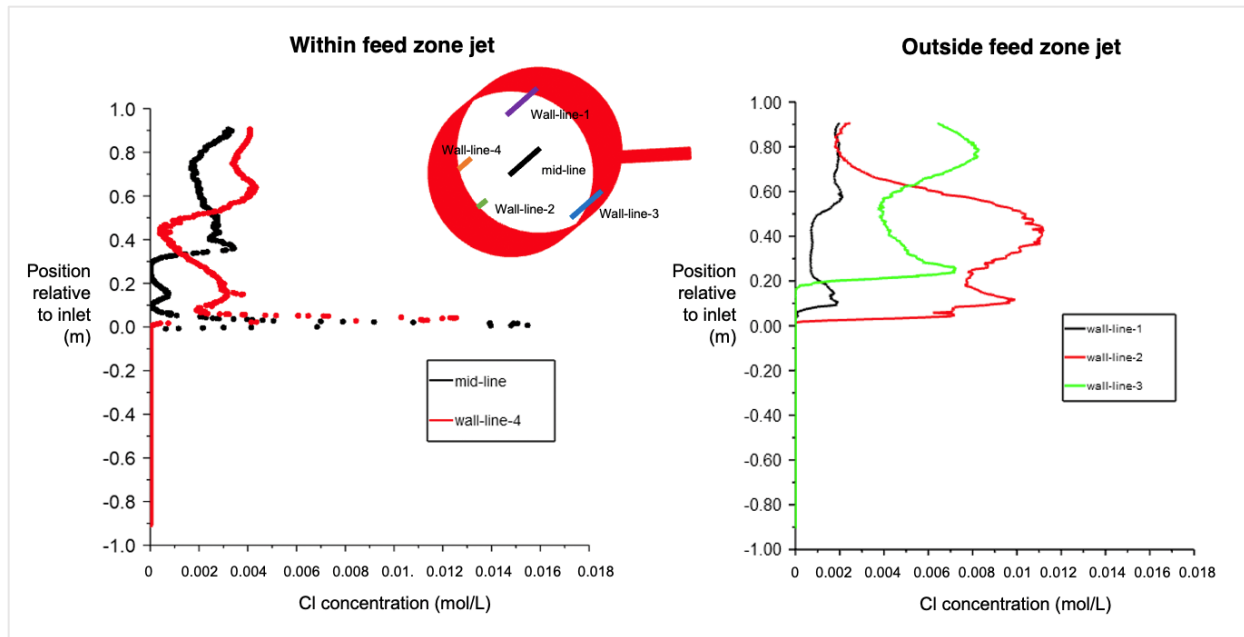


**Figure 4-36:** Comparison of the undisturbed state cases and the chloride concentration change along the wellbore height. The chloride concentration at the feed zone inflow was 0.5 M.

#### 4.1.2.7 Log Data at Varying Flow Rates

Chloride concentration log data from different inflow rates is presented in Figure 4-37, extracted from the wall-line-4 position opposite the feed zone inlet. The inflow rates were divided into two groups: high-flowrate (above 112.2 ml/s) and low-flowrate (below 112.2 ml/s).

In the high-flowrate group, a distinct pattern was observed across the z-direction. It began with an inlet front burst right in front of the feed zone, followed by a decrease zone above, and topped by a rebound zone. On the other hand, the low-flowrate group exhibited a less precise and more chaotic pattern. However, both groups showed a common feature: an inlet front chloride peak. This finding indicated that the chloride tool could consistently detect the feed zone location.

Regarding the magnitude of chloride concentration, all results underestimated the actual concentration of 0.05 mol/L. The measured values ranged from 0.01 to 0.017 mol/L, representing approximately 20% to 35% of the actual concentration. It was understood that the dispersed feed zone inflow would naturally lead to a diluted chloride concentration when measured at any location within the wellbore except right in front of the inlet. However, the discrepancy was expected to be less pronounced and more consistent in the disturbed state simulation, particularly when the tool is positioned at the center of the wellbore.

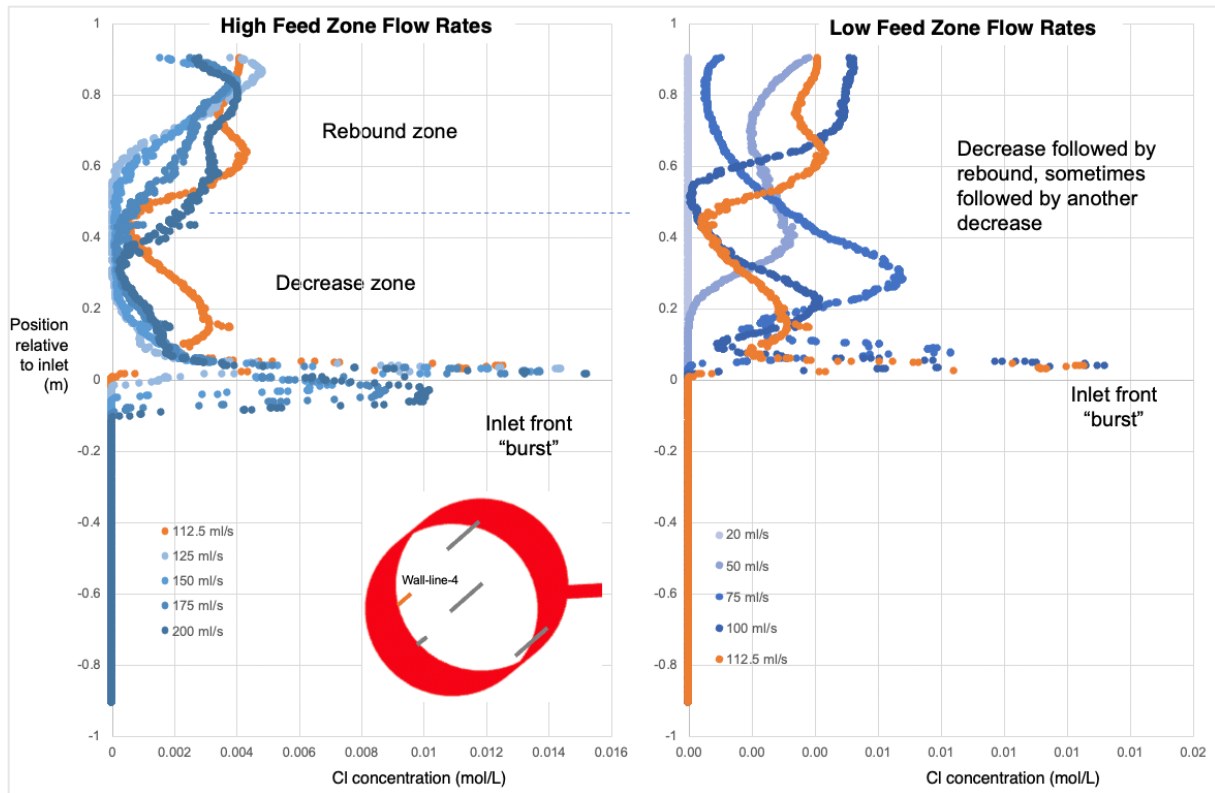


**Figure 4-37:** Comparison of the undisturbed state case and the Cl concentration change along the wellbore height at different feed zone flow rates. The results were extracted from the wall-line-4 position across the feed zone inlet. The left image shows the base case inlet flow rate (112.2 ml/s) and higher, while the right image shows the base case flow rate and lower.

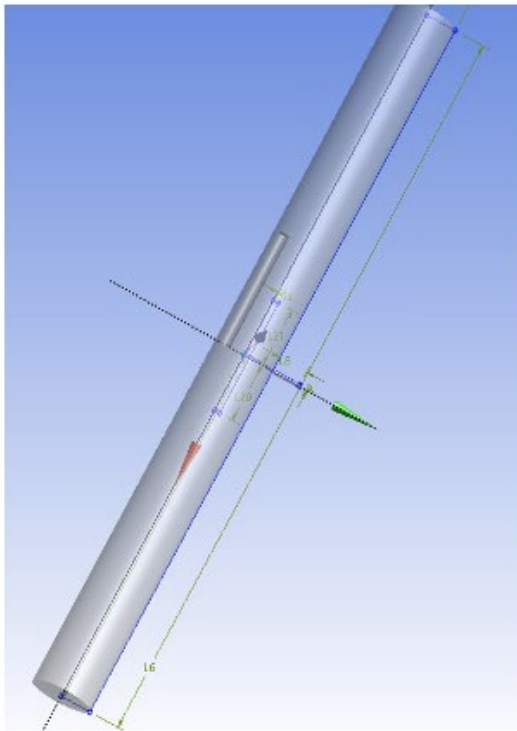
#### 4.1.2.8 Effect of Tool Presence

The disturbed case group involved the presence of the chloride tool inside the wellbore, shown as a small rectangular box near the feed zone in **Figure 4-38**. Two cases were considered, with parameters summarized in Table 4-5. The simulations of the disturbed state provided a more accurate representation of chloride concentration log data compared to the undisturbed state. Figure 4-39 presents the simulation results of the disturbed state case group, depicted in a vertical section. Additionally, Figure 4-40 displays the same results in a horizontal cross-section intersecting at the feed zone height.

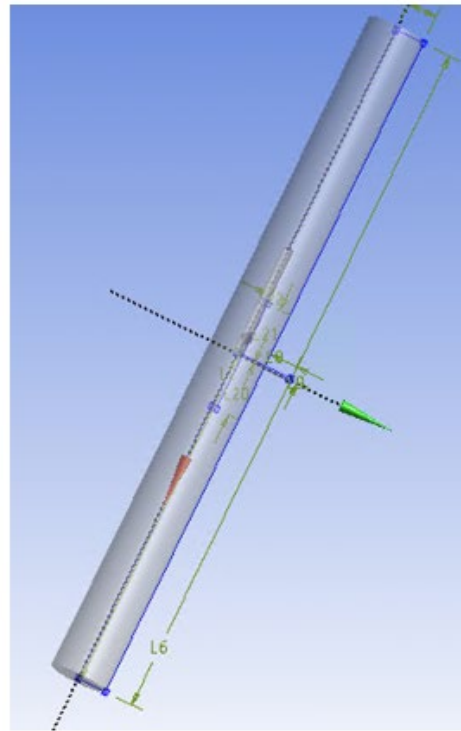
Figure 4-39 and Figure 4-40 show slightly better fluid mixing than the undisturbed state cases. For instance, positioning the tool at the center of the wellbore enhanced the visibility of chloride concentration and brought it to 30% to 35% of the actual chloride concentration. Similarly, placing the tool on the opposite wall increased the inflow concentration by 50%. These findings are supported by the dye tracer test with the chloride tool (Figure 4-41), showing better mixing of the feed zone fluid (dyed blue) compared with the undisturbed state.

Figure 4-39 also presents the results of similar tool placements without internal wellbore flow, showing the feed zone fluid dispersing in all directions. The concentration ranged between 30% and 70%, with an observed peak concentration at approximately 70% at the inlet. Therefore, variations in internal wellbore flow significantly impact the quantification of chloride concentration and, subsequently, the flow rate estimation.

Incorporating the disturbed state in the simulations enhanced their realism and reduced the chloride concentration discrepancy. The discrepancy could be further narrowed by incorporating wireline assembly design elements, such as additional housing units and mixers.



**S1-L7-1**  
Stationary at wall-line-4,  
probe end place at inlet mouth



**S1-L7-2**  
Stationary at midline (center), probe  
end place at inlet mouth

**Figure 4-38:** Schematics and description for the disturbed state case group (S1-L7).

**Table 4-5:** Disturbed State Case Group S1-L7, Parameters Summary

<b>Case ID</b>	S1-L7-[1 to 2]
<b>Scale</b>	Lab scale
<b>Description</b>	Disturbed state with stationary chloride tool. Tool position is in the center for case 2a and 2b and 5 cm from the wall at the opposite of the inlet (wall-line-4) for case 1a and 1b.
<b>Wellhead</b>	Open
<b>Main wellbore mass rate</b>	1a & 2a - 2.09 kg/s 1b & 2b – 0 kg/s (no internal flow)
<b>Feed zone flow rate</b>	112.2 ml/s (mimicking lab experiments)
<b><math>\Delta m</math> (kg/s)</b>	1a & 2a– 1.98 1b & 2b – (-0.112)
<b>NaCl concentration at feed zone</b>	0.05 mol/L
<b>NaCl concentration delta (mol/L)</b>	0.05

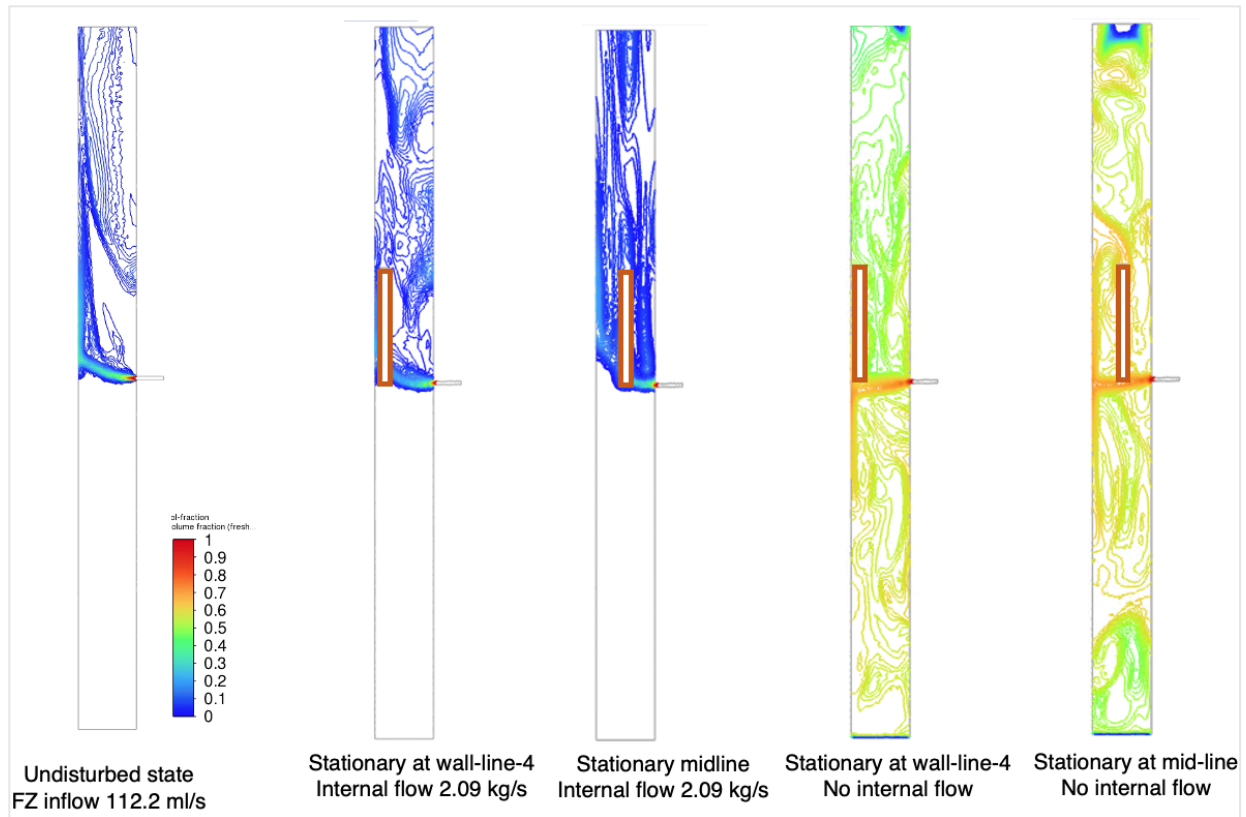


**Figure 4-39:** Comparison of the disturbed state case group, vertical section. The contours show the volume fraction of the inflow fluid, which is a NaCl solution of 0.5 mol/L concentration.

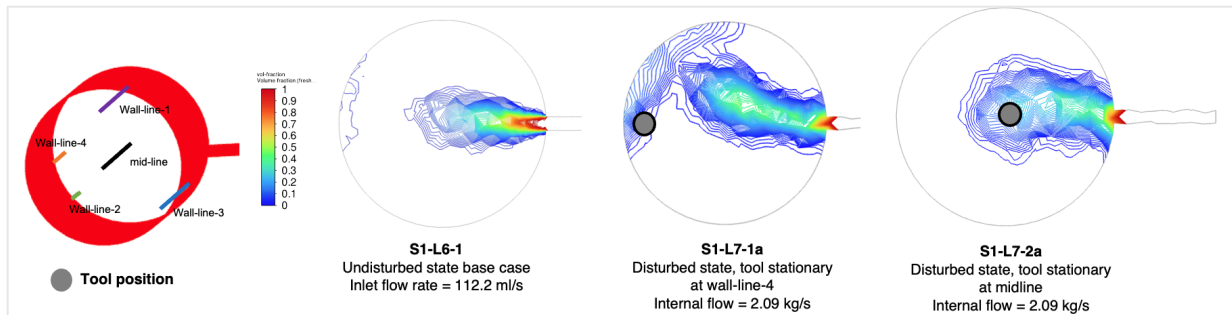


**Figure 4-40:** The horizontal section at the feed zone depth of the disturbed state cases compared with the undisturbed state base case. Reference to tool position naming is shown in the top left. The contours show the volume fraction of the inflow fluid, which is a NaCl solution of 0.5 mol/L concentration.

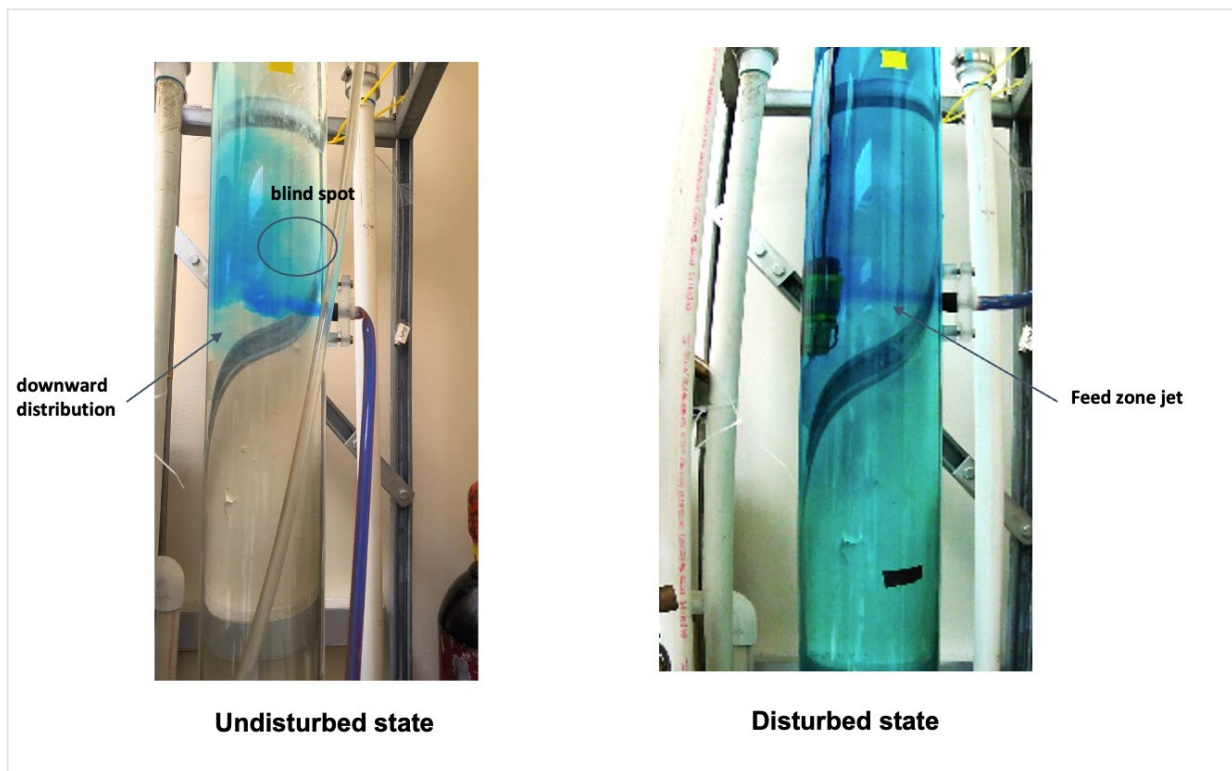


**Figure 4-41:** Dye tracer experiments in (a) undisturbed and (b) disturbed states.

#### 4.1.2.9 Multiple Feed Zones

Numerical simulations were run alongside dynamic laboratory measurements involving two feed zones. As many as 24 numerical simulation scenarios were modeled, comprising:

- five scenarios covering 20-200 ml/s inlet velocity at both feed zones at 2.09 kg/s,
- nine scenarios corresponding to the multiple-fractures dynamic lab measurements of Scenarios 151, 153, 155, 156, 158, and 161-164,

- nine scenarios following Scenarios 151, 153, 155, 156, 158, and 161-164, but with the inlet velocities being inverted.

Scenarios 156, 158, 163, and 164 parameters are summarized in Table 4-6 and shown in Figure 4-42 and Figure 4-43.

**Table 4-6:** Dual feed zones scenario parameters summary

Scenario	Injection Flow Rate (ml/s)		Down Hole Flow Rate (ml/s)	Injection (M)	Concentration	
	Feed zone 1	Feed zone 3			Feed zone 1	Feed zone 3
156	100.94	18.93	559.43	0.05	0.05	
158	44.16	18.93	559.43	0.05	0.05	
163	28.39	34.70	525.41	0.1	0.1	
164	28.39	44.16	521.63	0.1	0.1	

There were known discrepancies from the laboratory measurements that would not be replicated in the simulation results because the simulated models represented ideal conditions. For instance, it was observed that the downhole tool successfully captured the voltage drop around the depth of the feed zone port, both during the upward motion (POOH - Pull Out of Hole) and downward motion (RIH - Run in Hole) of the tool. However, the change in voltage was more pronounced during the upward than the downward motion.

Additionally, the lab experiment showed a delay in the voltage response between the POOH and RIH motions. The voltage drops during the POOH motion occurred at a greater depth than during the RIH motion, suggesting a lag in the measurement response similar to that seen in the multimeter measurement. These discrepancies related to the design and sensitivity of the chloride tool were not included in the model parameters.

Taking out the known variance from the laboratory experiments, it could be observed that the injection flow rate impacted the experiment's voltage measurement, as also evident in the simulations. In the experiments, higher injection rates generally resulted in a more significant voltage drop than lower injection rates. This observation indicated that the injection flow rate influenced the magnitude of the voltage drop, with higher injection rates leading to more significant changes in voltage. In the simulations, higher injection rates corresponded to higher chloride concentration, and vice versa.

Like the single feed zone cases in an undisturbed state, the simulation results underestimated the chloride concentration by around 30% to 40% of the actual feed zone inflow concentration. This level of underestimation was consistent across both single and multiple feed zone scenarios.

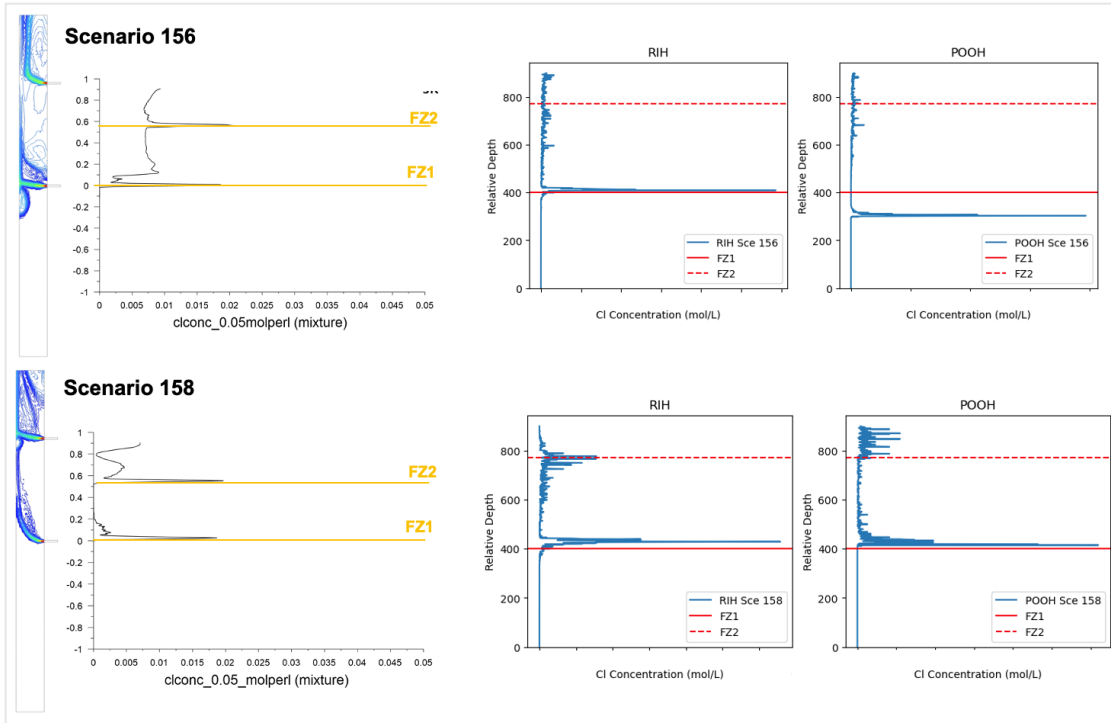


Figure 4-42: scenarios 156 (top) and 158 (bottom) showing the volume fraction vertical cross-section, simulated chloride concentration log data extracted from the center (midline) position, and the corresponding laboratory measurement results.

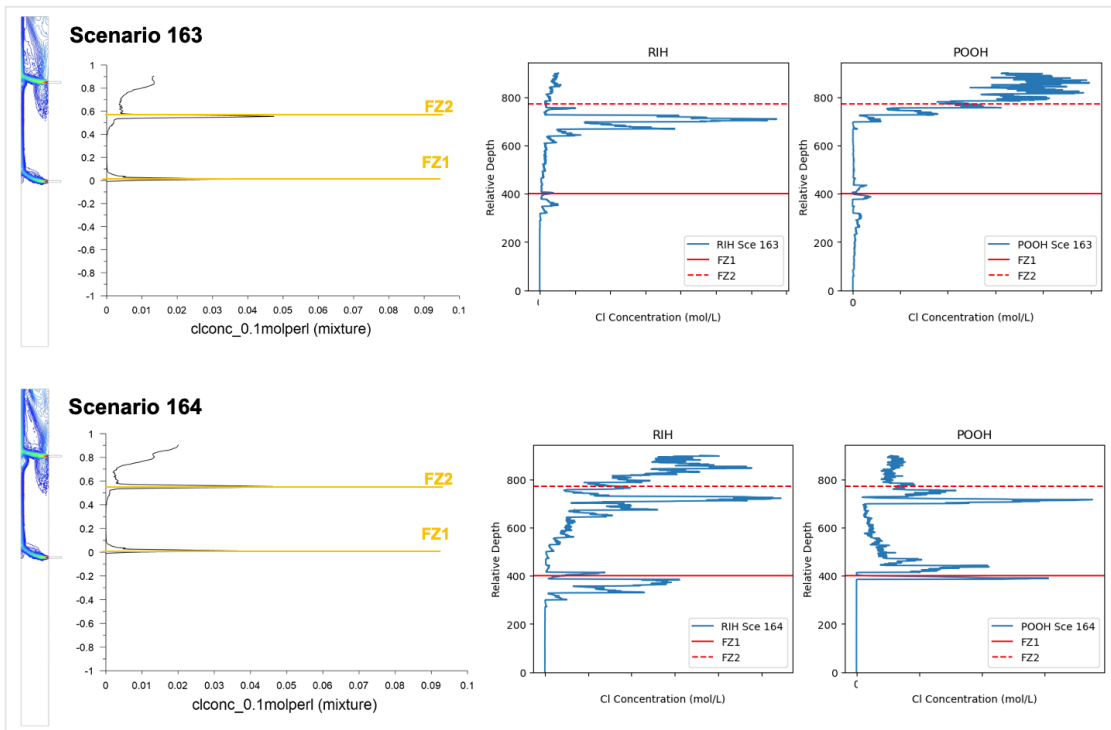


Figure 4-43: scenarios 163 (top) and 164 (bottom) showing the volume fraction vertical cross-section, simulated chloride concentration log data extracted from the center (midline) position, and the corresponding laboratory measurement results.

#### 4.1.2.10 ANSYS vs. COMSOL simulations

Comparable simulation results were performed using COMSOL software and compared to the ANSYS simulations and lab experiments to see whether COMSOL software would be a better simulation software tool. Firstly, the modeling was done in a simplified (faster running) geometry labeled Mini Scale to verify that the setup could work well. Two Mini Scale cases were considered: without and with a feed zone. The mini scale is 1 meter deep with a 10 cm feed zone radius at the midlength.

Then, the actual lab-scale model was constructed directly in COMSOL as a 1.81 m deep well with a feed zone inlet of 1 cm radius at 0.86 m height for one feed zone case and an additional feed zone at 1.31 m height for two feed zone cases. Three types of multiphysics were also considered:

- **Reacting flow with diluted species multiphysics** consisted of Laminar Flow and Transport of Diluted Species physics. Concentrated chloride at the inlet was dispersed using diffusion and Navier-Stokes fluid flow equations.
- **Two-phase flow with wetted wall multiphysics and laminar flow** consisted of Laminar flow and Level Set physics. The two phases were fresh water and saline water, and Wetted Wall was added to allow the fluid-fluid interface to move along the well. The governing equations for the level set field methods were a convection–diffusion equation, with the advective velocity coming from the Navier–Stokes equations.
- **Two-phase flow with wetted wall multiphysics and turbulent flow** consisted of Turbulent flow and Level Set physics. The method was similar to the previous one, with the difference being that turbulent flow is used rather than laminar flow.

Figure 4-44 shows the lab scale modeling results with three different multiphysics. The reacting flow with diluted species Multiphysics was the closest to real-life conditions, where both flowing solvent and diffusion disperse a concentrated source of chloride at the feed zone.

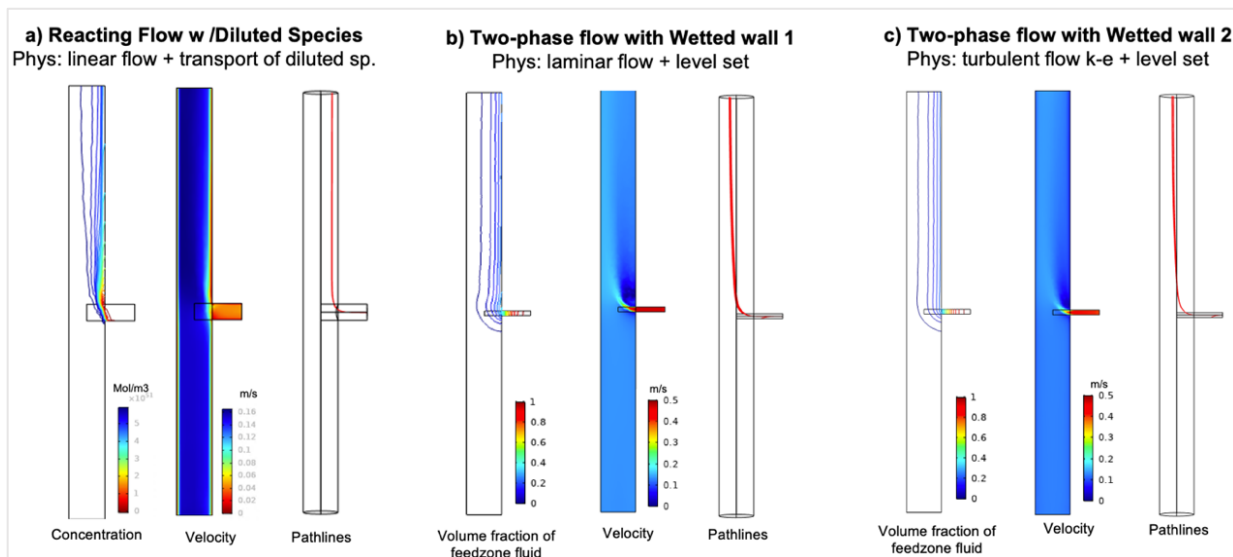


**Figure 4-44:** I initial lab-scale modeling results with three different Multiphysics applied. The following boundary conditions were put in: The mass rate at wellbore = 2.09 kg/s; Mass rate at feed zone is 0.1155 kg/s; Concentration at feed zone is 500 mol/m<sup>3</sup>.

Unfortunately, the model would not converge using the actual feed zone radius at 1 cm; only when the feed zone radius is increased to 3.5 cm would the model converge. The convergence failure happened at the feed zone inlet concerning the  $c$  species, indicating instability with the species dispersion physics in a relatively small feed zone radius. Furthermore, COMSOL could only allow laminar flow in the Reacting Flow with Diluted Species multiphysics, which would be another source of discrepancy between lab experiments exhibiting turbulent behavior such as the formation of eddies.

Even then, the converged modeling result with an enlarged feed zone radius could have been better as the concentration boundary condition was not honored, and the resulting concentration dispersion (Figure 4-44a) exceeded the boundary condition placed. This result was disappointing as the multiphysics was unavailable in the ANSYS Fluent software and could have been the advantage that using COMSOL might carry over using ANSYS Fluent. Fortunately, the two-phase flow with the wetted wall multiphysics converged, as shown in Figure 4-44b and c for laminar and for turbulent flow k-e, respectively.

Upon further comparison with calibrated ANSYS models and lab experiments, the COMSOL models could only exhibit the downward distribution feature without changing mass rate boundary conditions, as shown by the volume fraction graph in Figure 4-45b and Figure 4-45c. The blind spot formation was not being replicated, even with the turbulent flow, which should have shown some form of eddies. Only when the feed zone mass rate was inflated were the defining characteristics observed in the COMSOL model, such as by increasing the mass rate twice as much (Figure 4-45a) and four times as much (Figure 4-45c). Turning off the backflow suppression setting and turning on gravity did not provide meaningful change, as seen in Figure 4-45b.

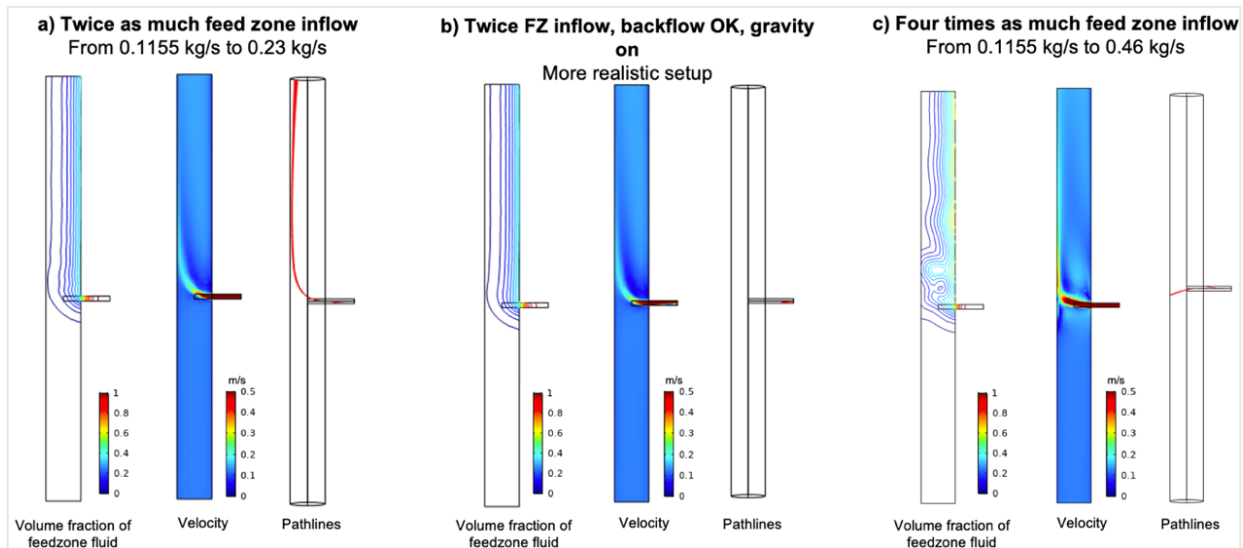


**Figure 4-45:** modified and iterated lab-scale modeling to mimic phenomena and characteristics observed in the lab experiments. The following boundary conditions were put in: The mass rate at wellbore = 2.09 kg/s; Concentration at FZ = 500 mol/m<sup>3</sup>.

Figure 4-46 shows the modeling results of the two-feed zone case with a comparison with previously modeled ANSYS Fluent and dynamic laboratory tests. The COMSOL model could replicate the peak concentration at the front of the feed zone inlets, which was a step in the right direction. Still, the concentration drop between the feed zones evident in both lab experiments and ANSYS Fluent modeling was not replicated in COMSOL.

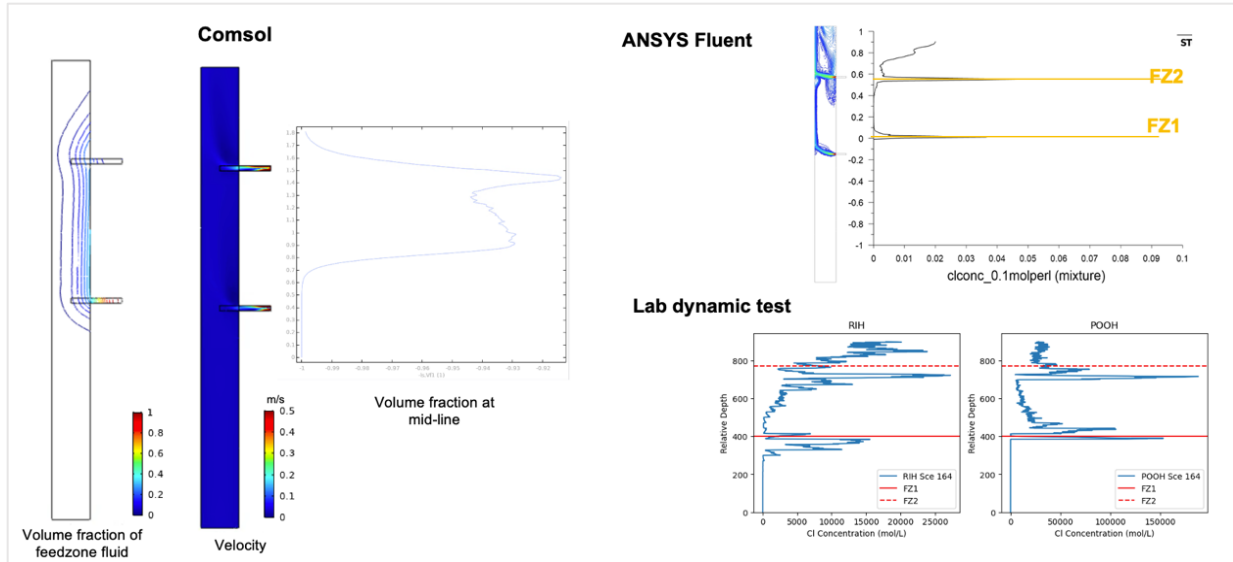


**Figure 4-46:** modeling results of the 2-feed zone case in COMSOL. Comparison with previously modeled ANSYS Fluent and dynamic laboratory tests was shown.

After closely comparing the COMSOL and ANSYS simulation results, it was concluded that the most appropriate software product for the research was ANSYS Fluent. While COMSOL had a strong suit in solid mechanics applications, ANSYS still came ahead for fluid dynamics modeling for the purpose of this study.

## 4.2 Round 2 Experiments and Simulations

Round 2 experiments and simulations focused on preparing for the deployment at Utah FORGE wells. In Round 2, numerical simulations under Utah FORGE pressure and temperature were conducted to investigate flow behaviors in the downhole conditions. Numerical simulations also tested various housing unit designs, ultimately selecting the caged housing design. This design was fabricated into an updated laboratory prototype to be used for further experiments at the Stanford Geothermal Laboratory. The detail of the fabrication process is explained in Section 2.2.

### 4.2.1 Round 2 Numerical Simulations

#### 4.2.1.1 Simulations with Downhole Temperature and Pressure

Numerical simulations were previously conducted at the laboratory scale based on the artificial well system's dimensions and under ambient pressure and temperature conditions. To prepare for the field tests, numerical simulations were initiated at the field scale. The same base case scenarios from the laboratory scale were used, but they were run under Utah FORGE temperature and pressure conditions, which are 225°C and 5000 psia, respectively. Two cases were run: one with the tool inside the wellbore and one without it, known as the undisturbed and disturbed state, respectively.

As shown in Figure 4-47, there was no substantial difference in fluid flow behavior between the pressure and temperature conditions encountered downhole and those at ambient conditions. This result is expected because the phase of the fluid remains in a liquid state despite the marked difference

in temperature and pressure. Hence, the flow behavior should be similar to the laboratory-scale simulations, given that the wellbore dimension or inflow rate was kept the same.

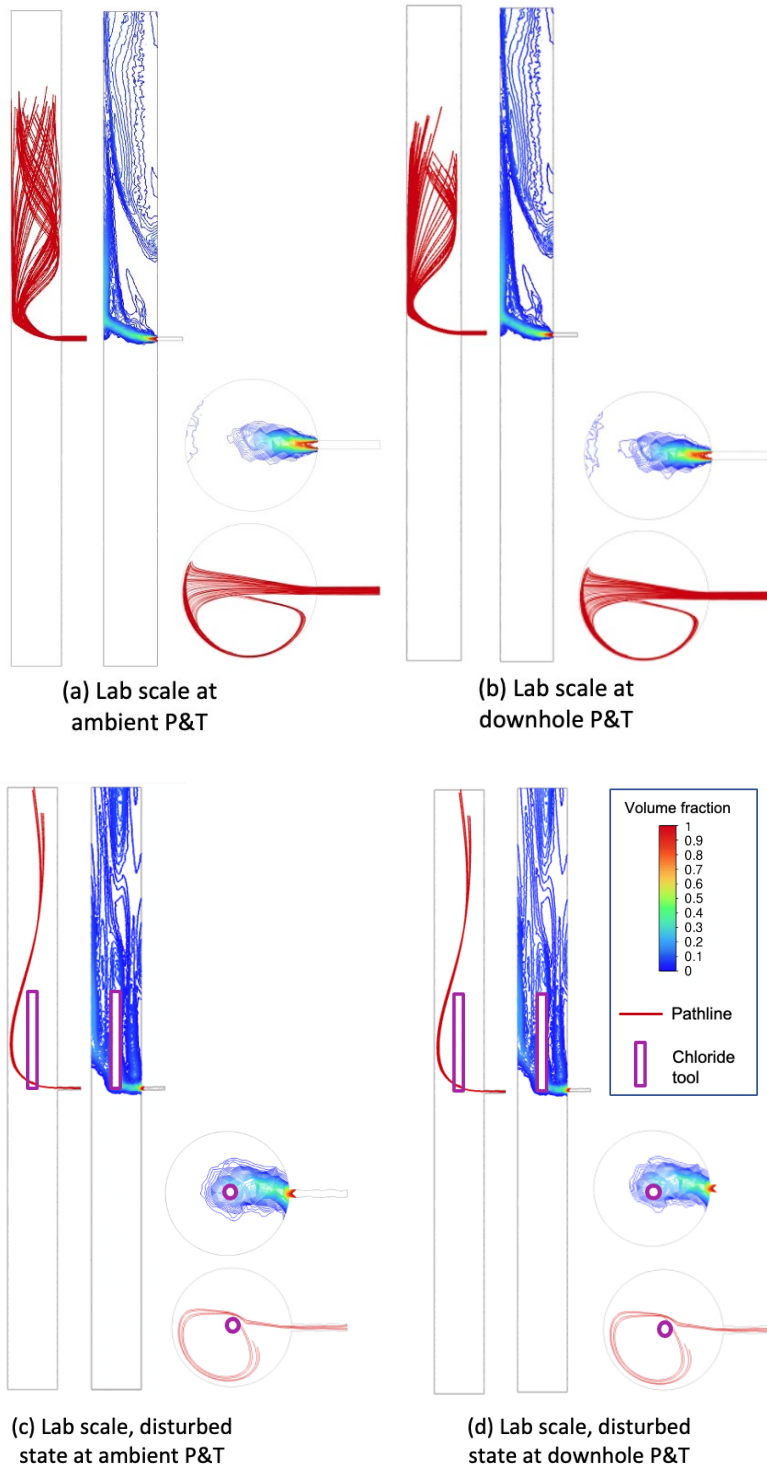


**Figure 4-47:** Comparison of the laboratory base cases of the undisturbed (a and b) and disturbed (c and d) states at laboratory ambient temperature versus at Utah FORGE downhole pressure and temperature.

#### 4.2.1.2 Housing unit design

Several iterations of the housing unit were created (Figure 4-48) using 3D modeling software and then numerically simulated to assess their effectiveness in fluid mixing, accuracy of concentration readings, and ability to anticipate the positions of unknown feed zone jets (Figure 4-49). Version 1 involved adding a spiral attachment to the end of the lab tool dimension to enhance fluid mixing. In Version 2, a new design for the attachment aimed to allow the sensors to be exposed to the fluid while being protected from damage. However, in both versions, simulation results showed that the four pillars surrounding the centralized sensor could hinder the feed zone inflow from reaching the sensor.

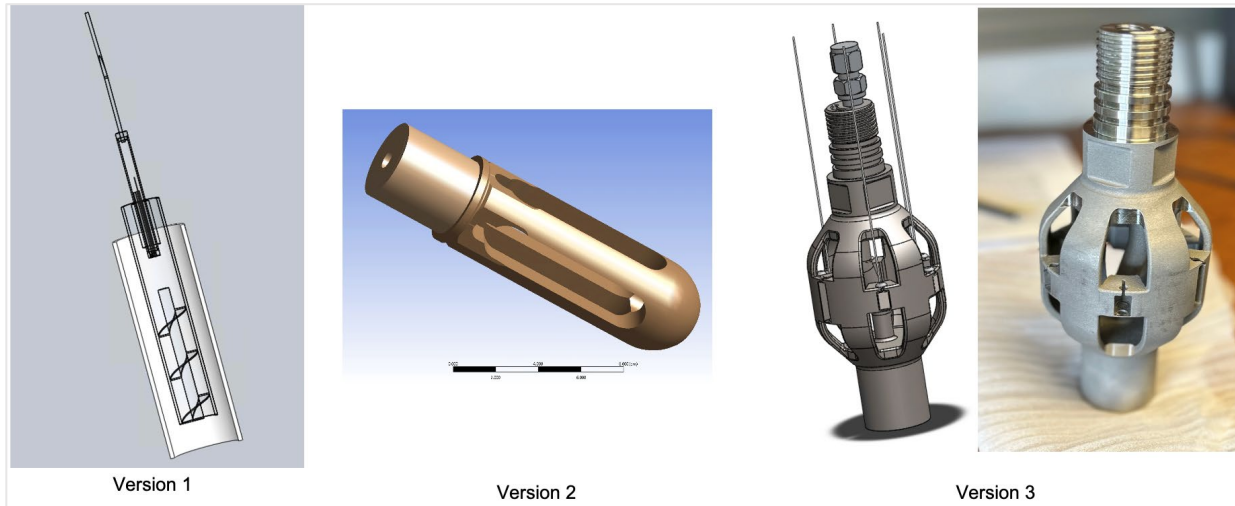


**Figure 4-48:** Iterations of the housing unit. Version 3 is the final design that was produced for the wireline tool assembly and the updated laboratory prototype.

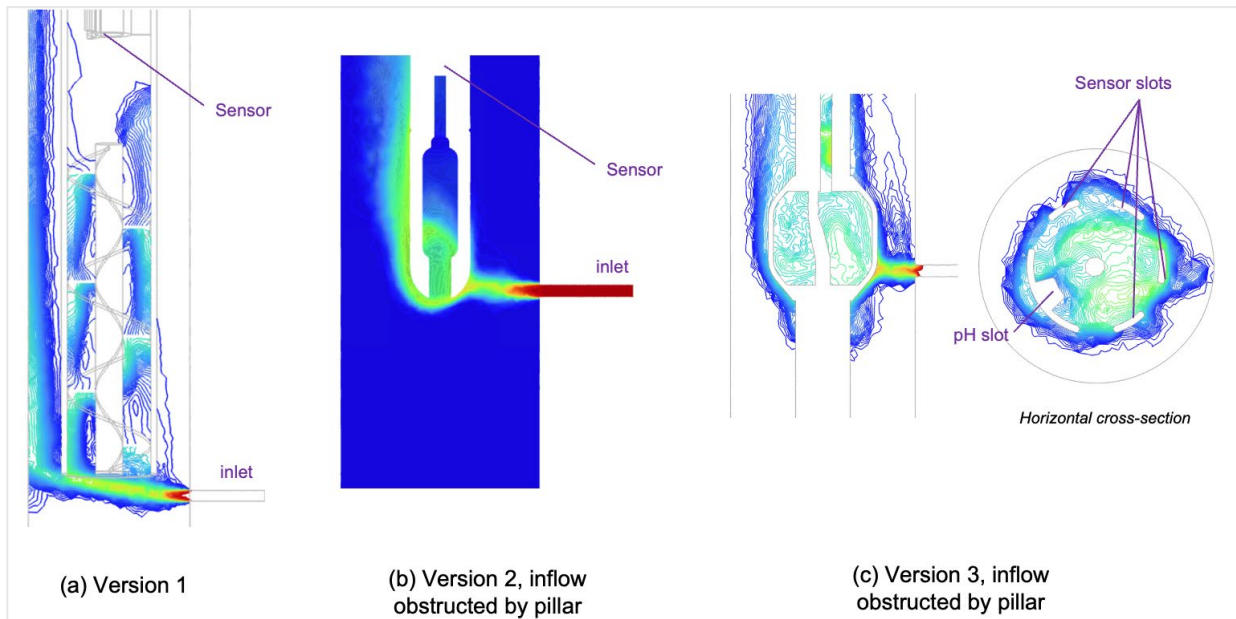


**Figure 4-49:** A summary of fluid flow simulations to evaluate the effectiveness of the field tool designs. Version 3 shows the reliable distribution of chloride concentration all around the sensors, even when the pillar obstructs the inflow.

Version 3 was the final design chosen for the wireline tool assembly and the latest iteration of the lab-scale prototype. This version includes multiple housings for up to five ion-selective electrodes and a pH sensor. The simulation results indicated that field tool Version 3 can still accurately receive voltage readings even when the feed zone is oriented to meet the pillar. In addition, the multipronged caged design is able to gather data from different positions across the wellbore. The following sections describe the detailed procedure and findings of the numerical simulations for the versions of the housing unit.

### Housing Unit Version 1

The housing unit design for Version 1 from Sandia National Laboratory was conceived for an 8-inch well internal diameter (ID). To fit the laboratory setup, the housing unit in the model was modified to a 3.5-inch outer diameter (OD), which will fit the 5.9-inch well ID with some extra space. Another design was considered by modifying the housing unit into a 2-inch OD to consider fitting into the well lubricator. The designs are illustrated in Figure 4-50. The resulting simulations for the Version 1 Modified-1 design for two different placements are shown in Figure 4-51. Placing the unit slightly above the inlet promotes better fluid mixing; however, the spiraling design did not allow the feed zone fluid to reach the chloride tool adequately.

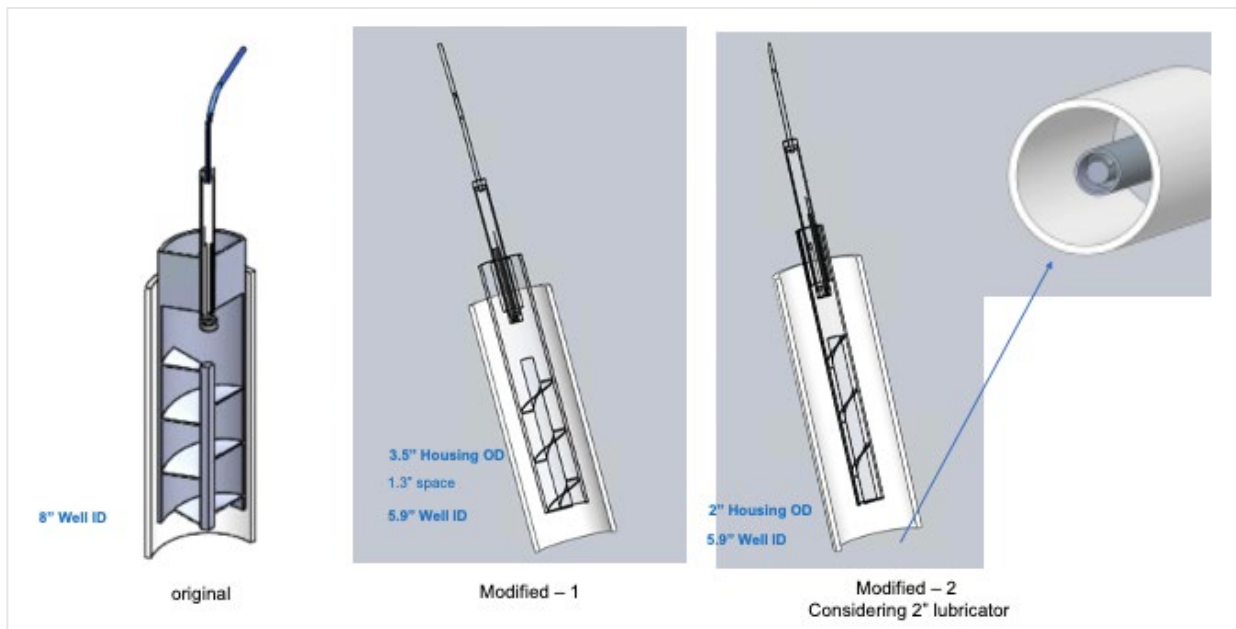


**Figure 4-50:** variations of the chloride tool housing unit designs for Version 1.

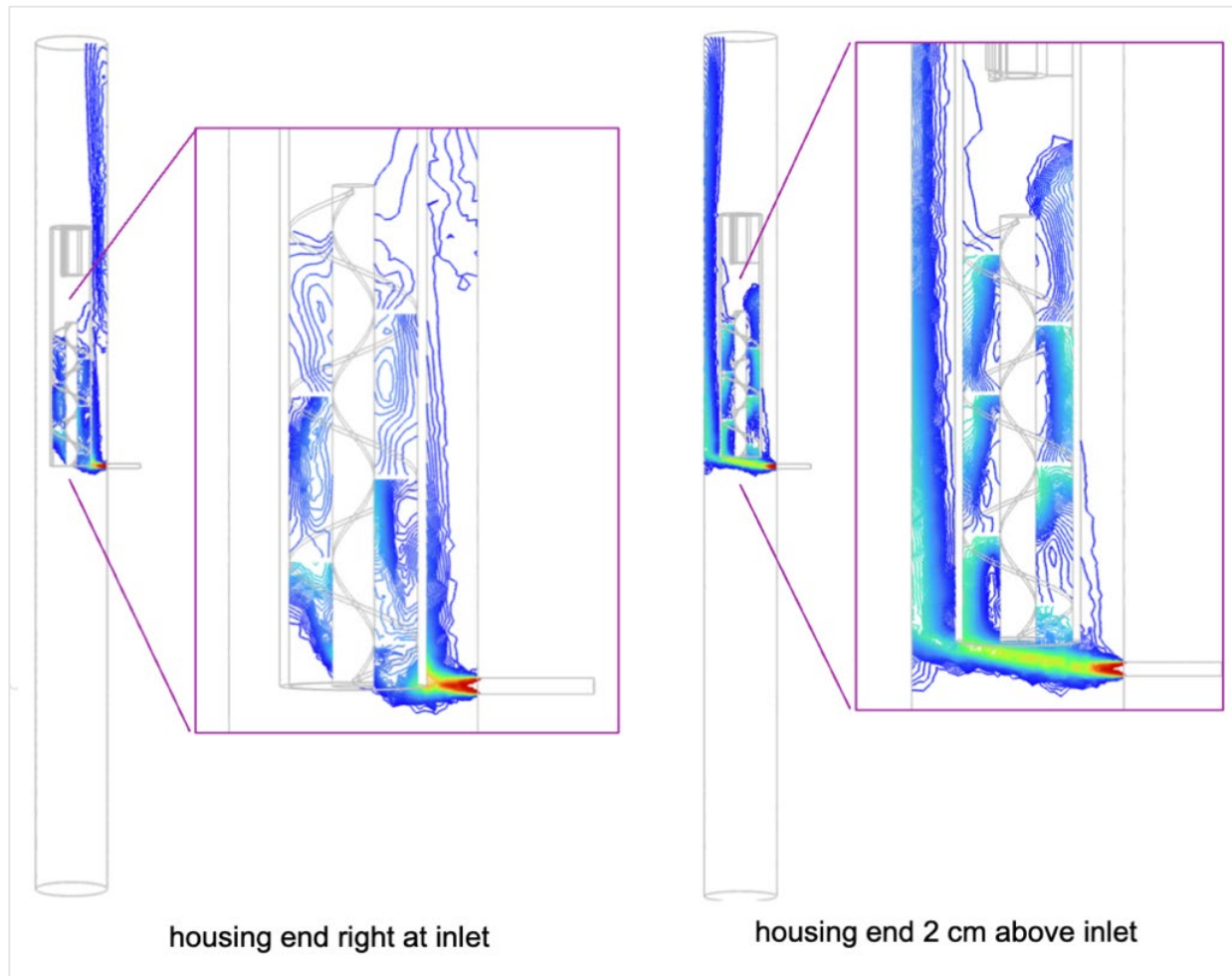


**Figure 4-51:** resulting simulations for Version-1 Modified-1 housing unit design at different tool placements.

### **Housing Unit Version 2**

Subsequent simulations were conducted involving Version 2 of the tool housing, which had four pillars surrounding a centralized ISE probe and allowed the lab-scale prototype to be plugged in (Figure 4-52). To ensure effective meshing and avoid excessive simulation time, the design was simplified down to the essential shape that still affects flow behavior without the additional complexities involving nuts, bolts, and ridges.

The main issue to test for this design was the change in flow behavior when the feed zone encounters the pillars in the tool housing design, known as the obstructed flow case. This case needs to be avoided, as the obstruction would inhibit the feed zone inflow from reaching the ISE probes located at the center of the housing, resulting in flow rate underestimation. The ideal scenario for this design would be the free flow case, as the feed zone jet can reach the ISE probes at the center directly.

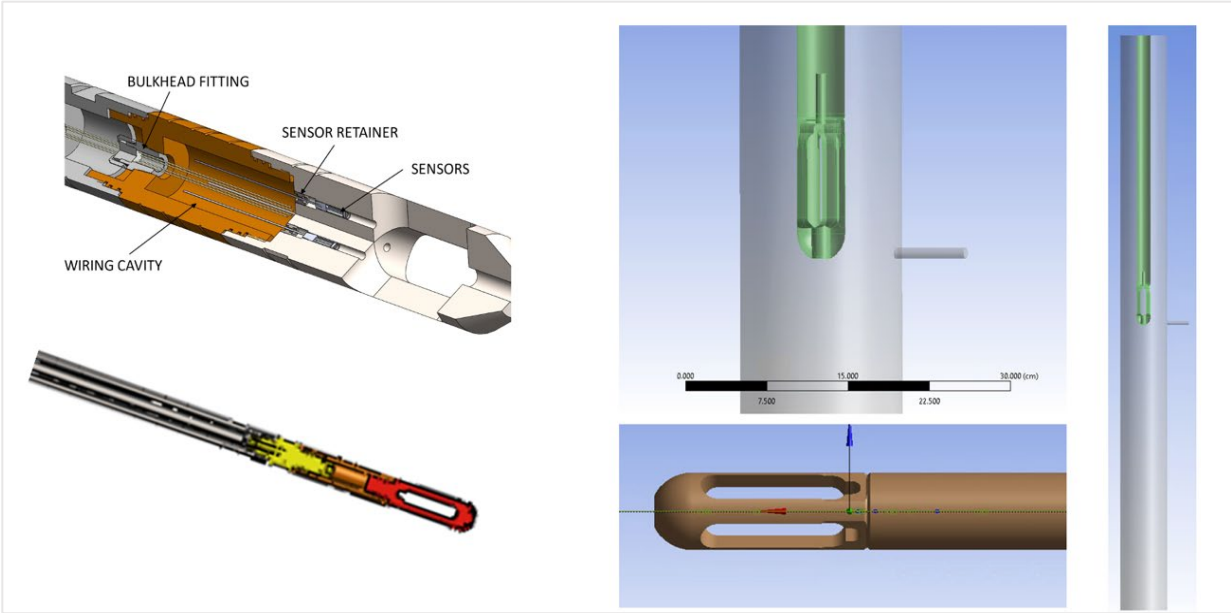


**Figure 4-52:** Original Version 2 housing design (left) and the simplified dimension for numerical simulation purposes (right).

The results of the obstructed flow and free-flow cases are shown in Figure 4-53 and Figure 4-54, respectively. These figures display the tool's progressive motion as it runs down the wellbore. It is important that sufficient chloride concentration reaches the middle crevice, where the chloride tool will be situated.

In the obstructed case, it is observed that only a small chloride concentration, ranging from 0% to 0.2% of the original volume fraction, can reach the center of the housing. The highest chloride concentration can reach the lower center of the housing when the tip of the tool faces the feed zone. In this case, the concentration can reach around 50% of the original, as shown in Figure 4-54a. Meanwhile, the free-flow case (Figure 4-54c) shows that the inflow can easily reach the center while retaining a volume fraction of around 85%.

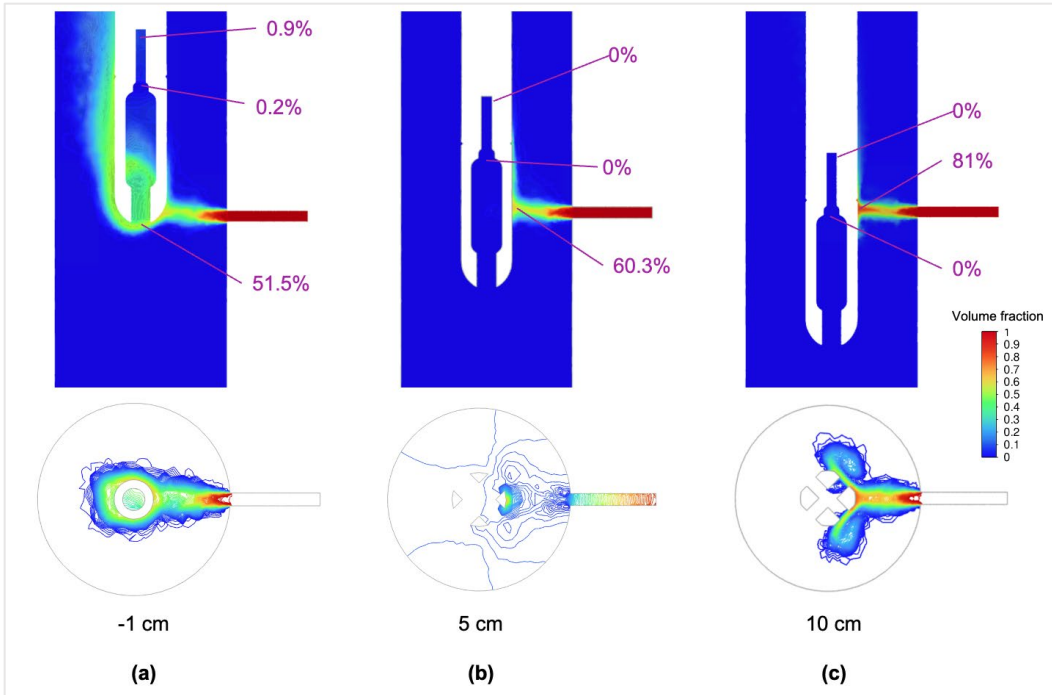


**Figure 4-53:** Simulation results of the unobstructed flow case of housing design version 2; (a, b, c) represent the progression of the tool housing penetrating through the wellbore at a certain offset of the feed zone height. The upper graphics show the vertical cross-section, while the lower graphics show the horizontal cross-section at feed zone height.

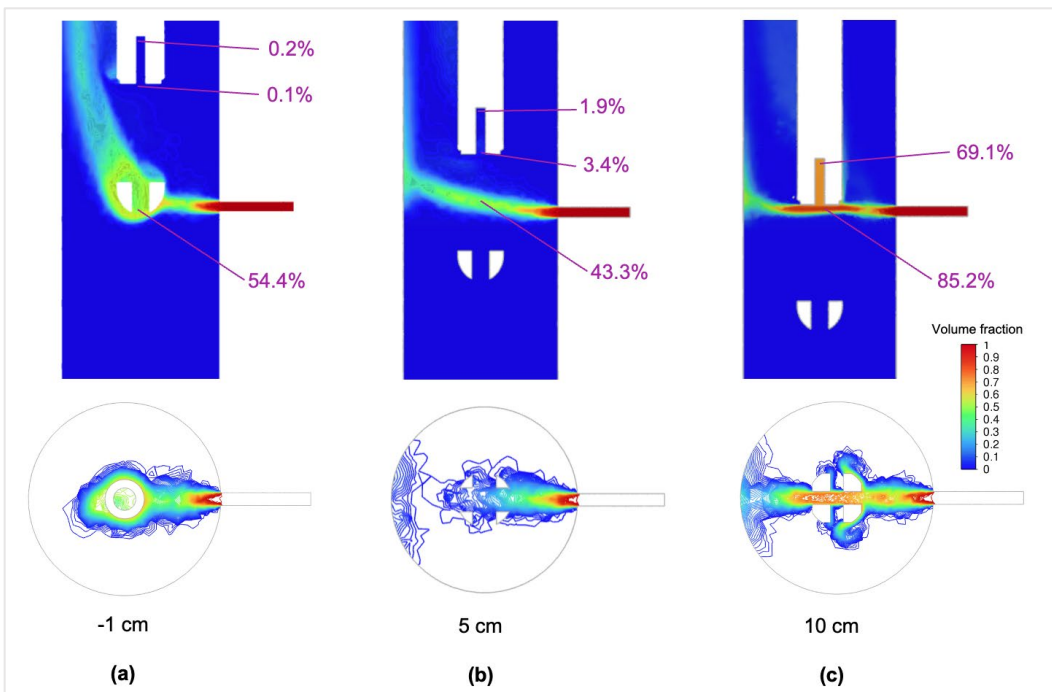


**Figure 4-54:** Simulation results of the free-flow case of the housing design version 2; (a, b, c) represent the progression of the tool housing penetrating through the wellbore at a certain offset of the feed zone height. The upper graphics show the vertical cross-section, while the lower graphics show the horizontal cross-section at feed zone height.

### Housing Unit Version 3

Version 3 of the field tool comes with a housing that has six pillars and a retainer placed at the edges. The retainer has slots to accommodate three ISE sensors, one reference sensor, and two pH sensors. To conduct simulations, we used a simplified version of the housing, as illustrated in Figure 4-55.

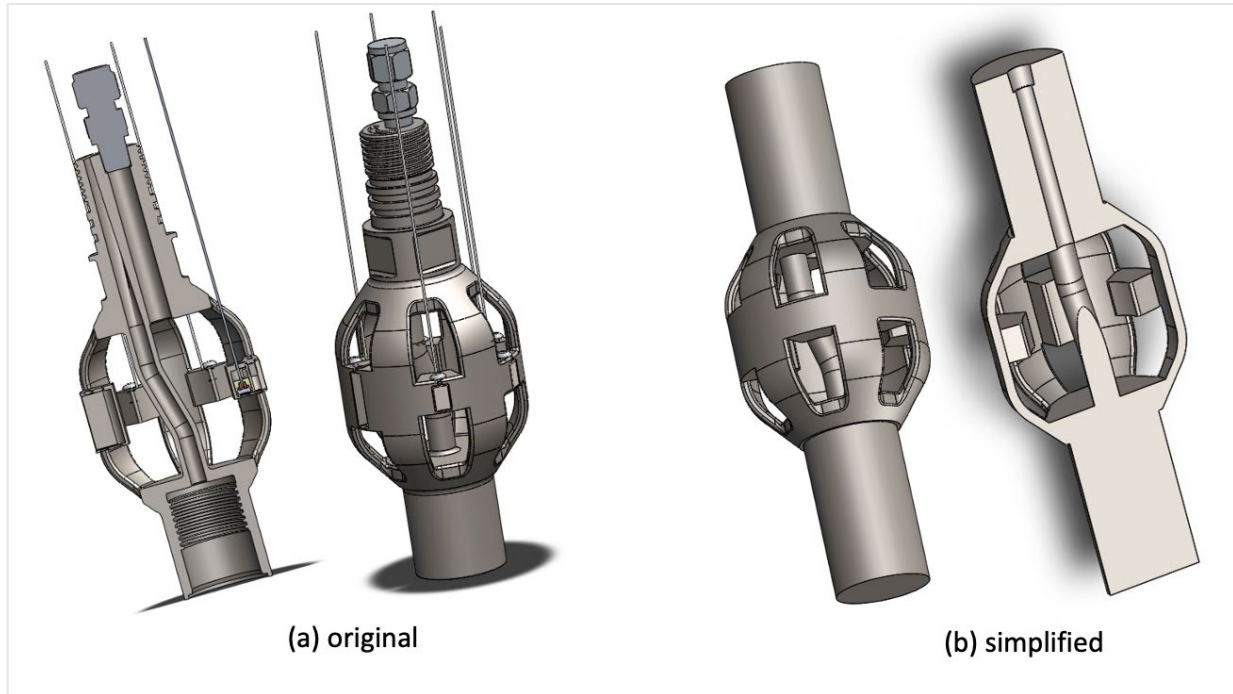


**Figure 4-55:** Simplified housing and tool dimension in preparation for numerical simulation cases for tool housing version 3.

The simulations for Version 3 were similar to Version 2, and they focused on the positioning of the ISE sensors in relation to the feed zone inflow. Five locations were tested and identified as positions *a* to *e* in Figure 4-56. These positions represent the relative location of the feed zone inflow and the tool body when it is inserted into the wellbore in the Run-in-Hole (RIH) motion. The number in cm shows the feed zone height offset relative to the center of the housing, ranging from 2.7 cm below the center (i.e., position *a* at -2.7 cm) to 2.7 cm above the center (i.e., position *b* at +2.7 cm).

The boundary conditions were kept the same as all the base cases and mimic the laboratory base case setup, i.e., two inlets and an outlet. The first inlet is from the feed zone at 112.2 ml/s, and the second inlet is from the bottom of the well at 2.09 kg/s representing the wellbore internal flow. Finally, the pressure outlet is at the top of the well, representing the wellhead. Two types of scenarios were tested for each position: when the feed zone inflow entered the crevice of the housing and when the feed zone inflow faced one of the pillars, which was at a 30-degree angle from the center of the crevice. The case groups representing the two scenarios are called free-flowing and obstructed case groups, respectively, the same as simulations for Version 2.

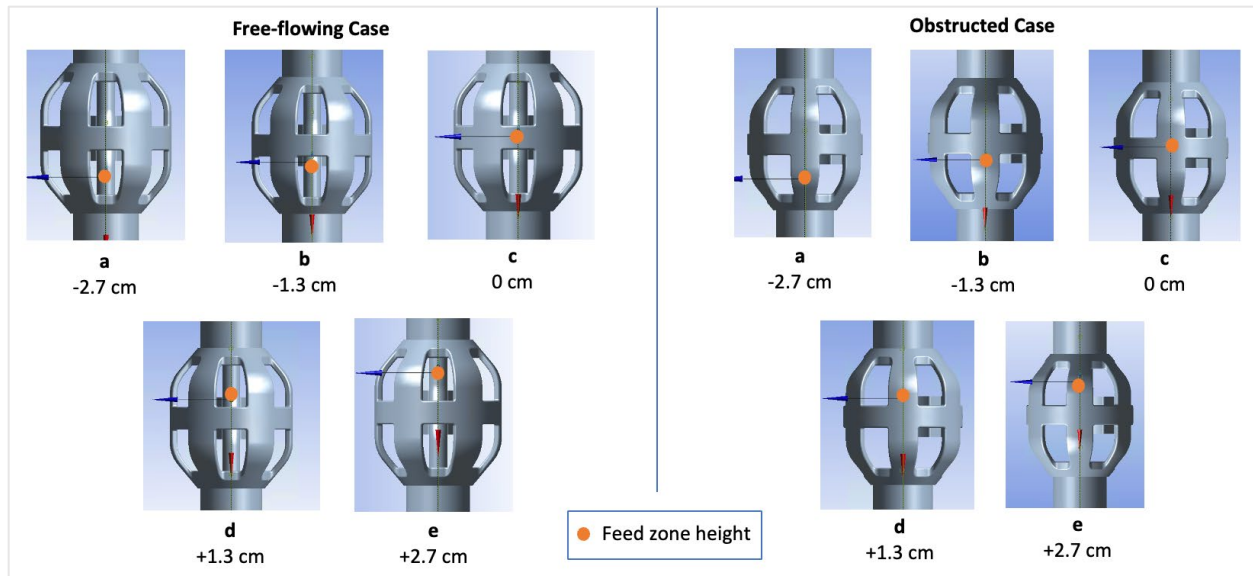


**Figure 4-56:** Five positions of the tool housing relative to the feed zone height labeled from a to e. Positions are chosen to represent the Ream in Hole (RIH) motion of the chloride tool. The number in cm shows the feed zone height offset relative to the center of the housing. Two case groups are simulated: the free-flowing case group (left), where the feed zone inflow faces the opening; and the obstructed case group (right), where the feed zone inflow faces one of the pillars.

The modeling results are shown in Figure 4-57 as horizontal cross-section and in Figure 4-58 as a vertical cross-section at sensor height, which is 1.4 cm below the center of the housing. The horizontal cross-section illustrates the inflow behavior in and around the housing as the tool progressed in RIH motion, while the vertical cross-section depicts the distribution around the tool sensor.

The free-flow case group allows the inflow to form a jet, passing through the housing. The ISE probe located right in front of the feed zone records the highest concentration at around 50-60%. The concentration disperses to 30-40% within the jet stream coverage. However, outside the jet stream coverage, the concentration drops significantly to 0-20% of the original volume fraction. Position *a* and *b*, achieved at the beginning of the tool reaming in, show the strongest and most uniformly distributed chloride concentration.

In the obstructed flow case group, the inflow jet is blocked by a pillar, which causes the fluid to be diverted around the perimeter. Figure 4-58 shows that the two nearest ISE probes on the right and left of the pillar will receive the highest concentration readings between 40% and 50%. The rest of the probes would receive almost no fluid. However, the most uniformly distributed chloride concentration is observed in position *a*, shown in Figure 4-58. The distribution is rather circular, encompassing all six sensor placements in the housing. Having the inflow jet facing the pillar allows the jet to be distributed around the perimeter of the housing, uniformly hitting all the sensors. Based on simulations at different positions and timing standpoints, it appears that the best signal will be recorded at the beginning of the RIH motion when the lower part of the housing meets the feed zone.

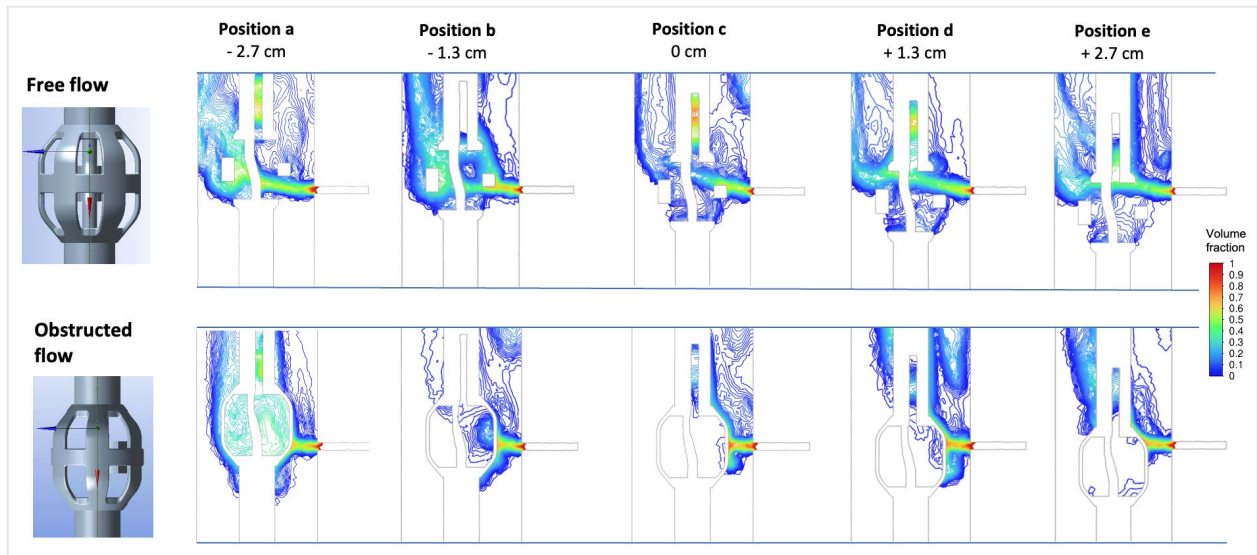


**Figure 4-57:** Modeling results are shown as vertical cross sections; the case group at the top represents the free-flow case, and the case group at the bottom represents the obstructed-flow case.

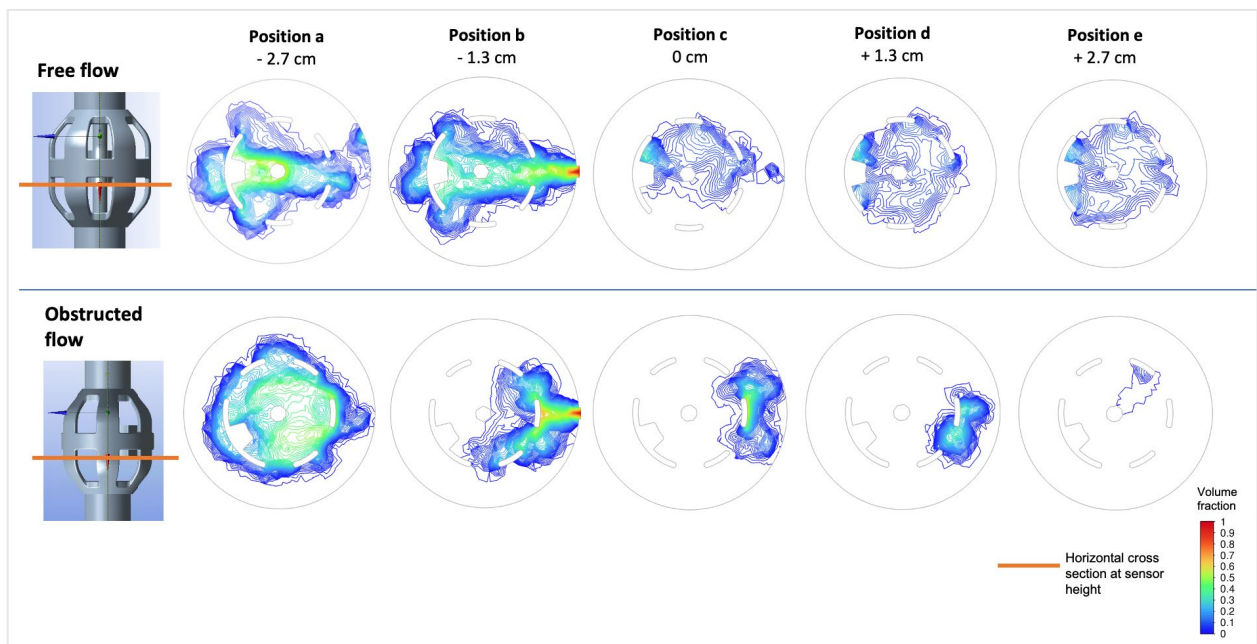


**Figure 4-58:** Modeling results are shown as horizontal cross sections at the sensor height, indicated by the orange line; the case group at the top represents the free-flow case, and the case group at the bottom represents the obstructed-flow case.

## 4.2.2 Round 2 Laboratory Experiments

### 4.2.2.1 Artificial Well System Modifications

Figure 4-59 and Figure 4-60 provide a labeled diagram and image of the artificial well system's most updated configurations. In mid-to-late 2023, pump and water lines were updated, EMF interference was reduced, and the pulley system was modified.

The Submersible Pump 3 is responsible for providing the flow of fluid into the main wellbore. The pump is a Daibao® submersible pump that provides a maximum 3,200 gal/hr (12,100 L/hr) of fluid at a power consumption of 88 W (0.118 hp). However, three power settings of 50 W (0.067 hp), 64 W (0.086 hp), and 77 W (0.103 hp) were used for this project. The fluid is cold tap water, which is transported into the Inflow Reservoir, a Hyper Tough™ trash can with a capacity of 32 gallons (121 L), from three faucets.

When the fluid exits the top of the main wellbore, it falls into the Outflow Box. From there, the spent fluid falls through three circulation pipes into the Outflow Reservoir, which is a plastic storage container with a volume of approximately 200 L. Then, Submersible Pump 1 (Little Giant™ 505176) and Submersible Pump 2 (Homdox® 1.5 hp Submersible Pump) discard the fluid to sinks in the laboratory.

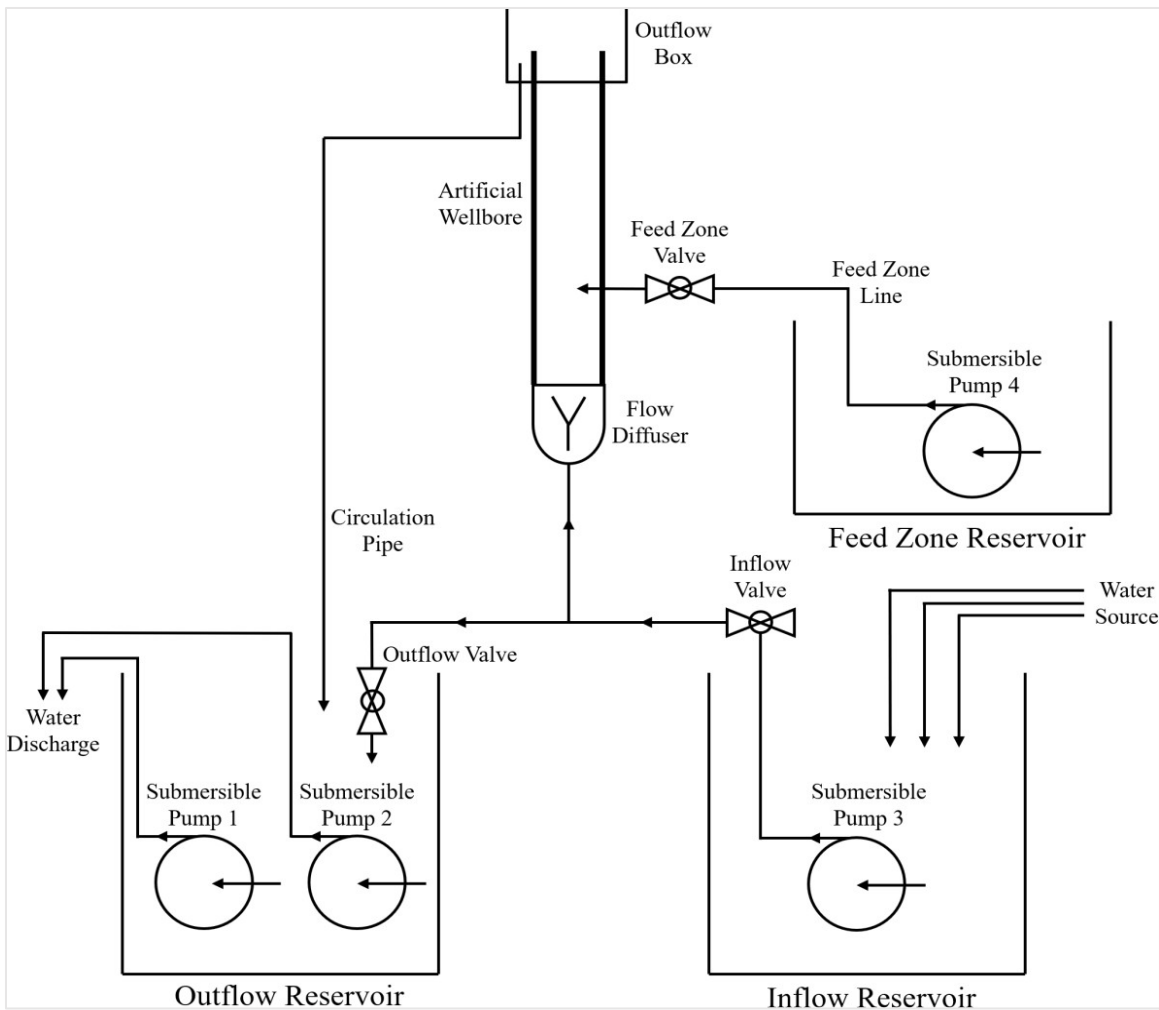


**Figure 4-59:** Schematic of the Artificial Well System in the Stanford Geothermal Laboratory.

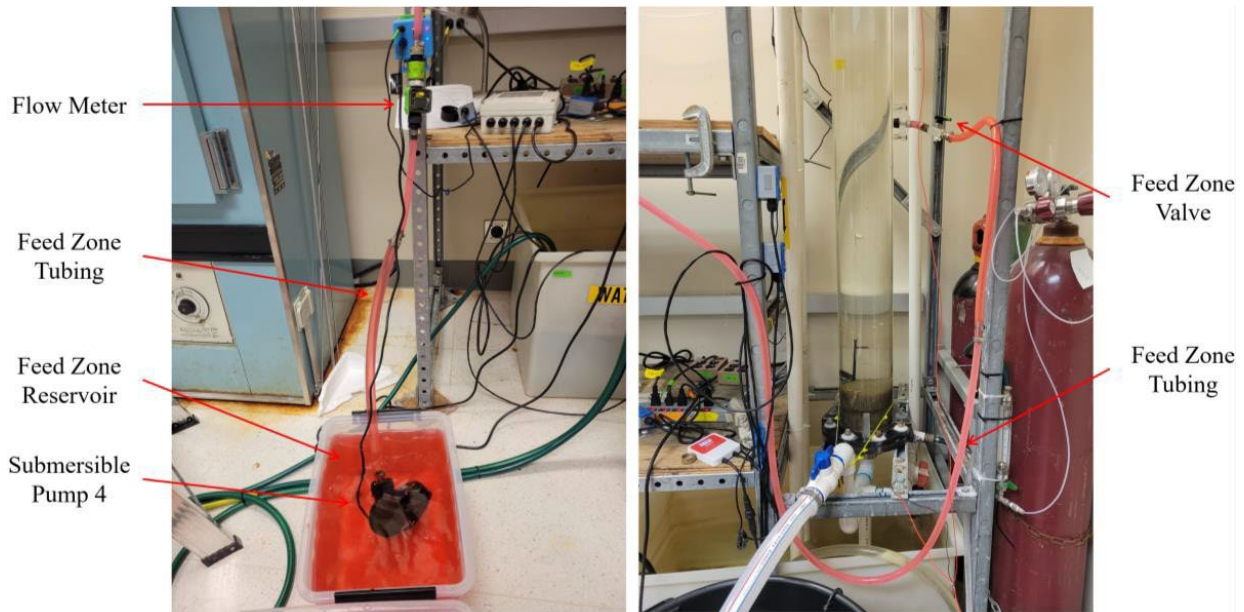
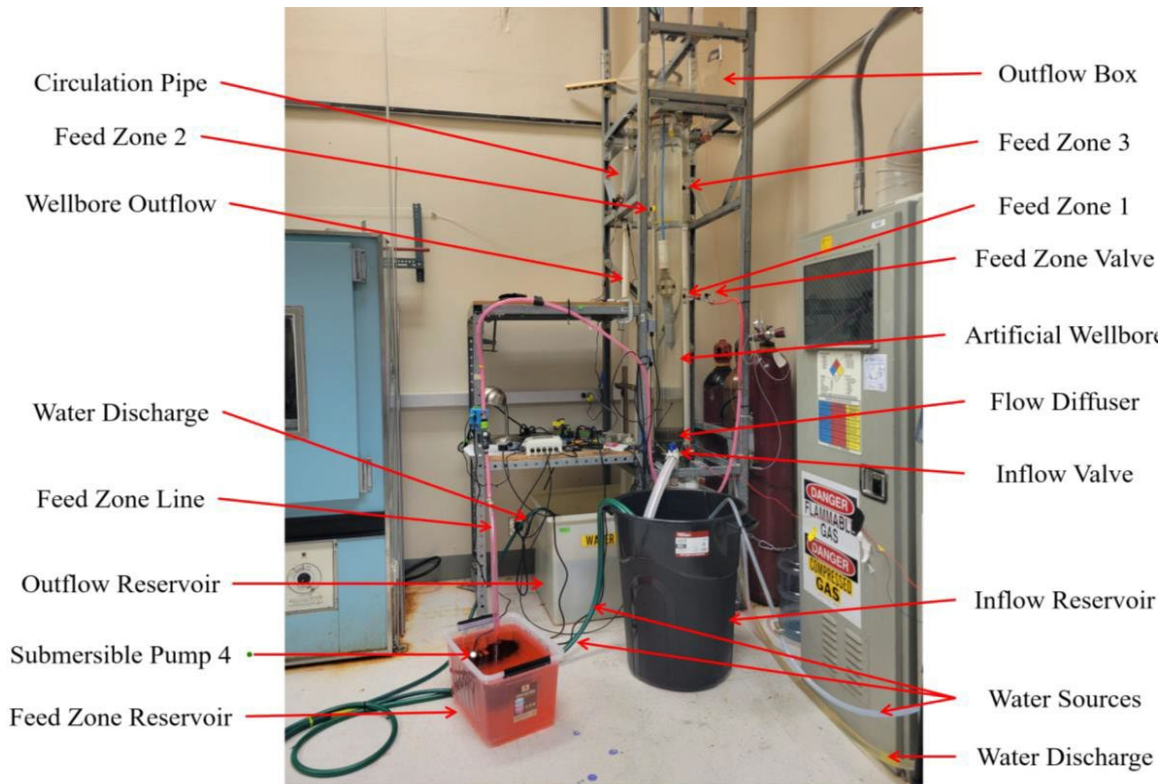


**Figure 4-60:** Labeled image of the Artificial Well System in the Stanford Geothermal Laboratory.

To determine the mass flow rate and the velocity of the fluid moving through the main wellbore, the time needed for the fluid to travel 12 vertical inches (30.5 cm) of the wellbore was used. Note that this length began approximately 10 inches (25.4 cm) above the feed zone port to determine the mass flow rate in the wellbore above the feed zone  $m_{above}$  for Equation (3-3). Table 4-7 details the assumed, measured, and calculated values needed to calculate the mass flow rate and flow velocity at the three different power settings.

**Table 4-7:** Calculation of flow rate and flow velocity in the main wellbore at three power settings of Submersible Pump 3

Parameter	Value			Unit	Method of Determination
Fluid Density	997	997	997	kg/m <sup>3</sup>	Assumption
Power	50	64	77	W	Specified
Time	7.36	6.30	5.59	s	Measured
Diameter	6.0	6.0	6.0	in	Measured
Height	12	12	12	in	Measured
Mass Flow Rate	0.753	0.880	0.992	kg/s	Calculated
Flow Velocity	$4.14 \times 10^{-2}$	$4.84 \times 10^{-2}$	$5.45 \times 10^{-2}$	m/s	Calculated

### *Pump and Water Line Modifications*

Modifications of the pump and water lines are shown in Figure 4-61. An Inflow Valve was installed to the fluid inflow apparatus, as shown in image Figure 4-61a. The Inflow Valve regulates flow between the Inflow Reservoir and the main wellbore. When closed, this valve traps fluid in the wellbore, enabling experiments requiring a static fluid. Additionally, the Outflow Valve was replaced to allow the flow from the Inflow Reservoir, or any backflow from the main wellbore, to be diverted into the Outflow Reservoir. This valve allowed the fluid in the wellbore to be discarded without needing to relocate Submersible Pump 3 into the Outflow Reservoir. This modification had the added benefit of preventing the unintentional disconnection of the main wellbore from the fluid inflow apparatus, which resulted in the total loss of fluid in the wellbore.

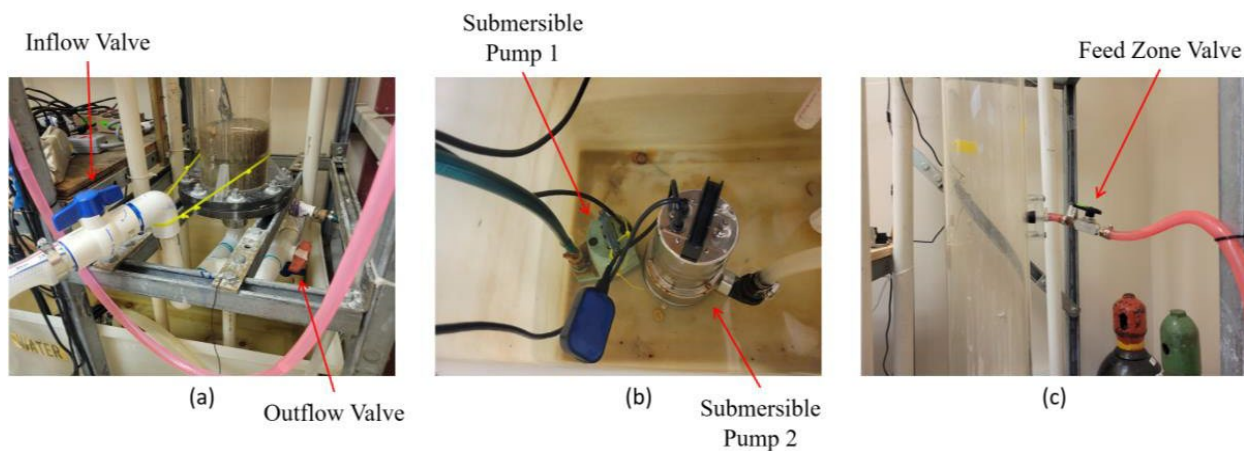


**Figure 4-61:** Updated (a) fluid inflow system, (b) Outflow Reservoir, and (c) feed zone injection line for the artificial well system.

Submersible Pump 2 was added to the Outflow Reservoir. This pump increased the total rate at which spent fluid in the Outflow Reservoir was discharged. With this addition, experiments with flowing fluid lasting more than 20 minutes (1200 seconds) were enabled. This is because the rate at which fluid was discarded from the main wellbore was greater than the pumping rate of Submersible Pump 1. This mismatch of flow rates previously required manually bailing water from the Outflow Reservoir to prevent it from overflowing.

The Feed Zone Valve was relocated along the feed zone tube to be approximately an inch (2.5 cm) from the main wellbore. The new placement of the valve reduced the volume of residual fluid following feed zone inflow, reducing the opportunity for experimental error associated with the unexpected mixing of feed zone fluid with the wellbore fluid.

A third line from the water source was added to increase the total rate at which tap water was added to the Inflow Reservoir. With this addition, experiments with flowing freshwater fluid can be run continuously. This is because the rate at which freshwater fluid is added to the Inflow Reservoir, the pumping rate of Submersible Pump 3, and the combined discharge rate of Submersible Pumps 2 and 3 could be matched. This allowed the freshwater fluid in the artificial well system to be in a steady state. Before these modifications, a mismatch of flow rates required the manual addition of water to the Inflow Reservoir. The longest duration of continuous experimentation without needing to manually add or bail water was eight hours, verifying steady-state operation.

### ***Pulley System Updates***

In Round 1, a motor-and-pulley system was used to control the speed and direction of the motion of the chloride tool. This system was removed to allow the motion of the tool to be manually driven by the shielded electrical cable that connected the chloride tool with the data acquisition hardware. Changing this operation allowed for increased stability because of the thicker diameter of the electric cable compared with the previous single-strand cable. However, this change had the drawback of requiring manual operation, which introduces variability in the experimentation process. Figure 4-62 shows the rerouted shielded electrical cable exiting the artificial wellbore system to connect with the data acquisition hardware. Changes were made to this routing by adding two pulleys to lower friction associated with the movement of the chloride tool and prevent interference with the scaffolding of the artificial well system.

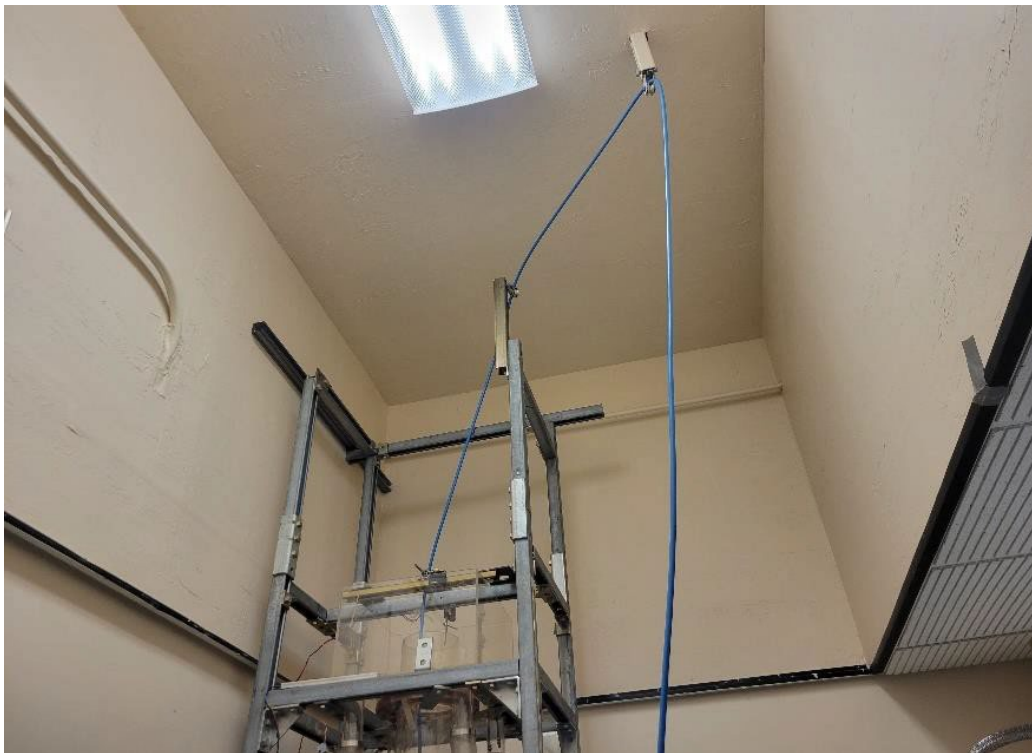


**Figure 4-62:** Updated routing of the shielded electrical cable for the artificial wellbore.

### ***EMF Interference Reductions***

Electromagnetic field (EMF) interference with the data acquisition hardware were investigated using an EMF meter to identify sources producing high levels of EMF. The main EMF sources that interfered was found to be the AC submersible pump, and thus this was subsequently exchanged for a DC pump. Additionally, the power supply transformers, which are responsible for converting alternating current (AC) to direct current (DC) for the submersible pumps, also emitted high EMF levels. Faraday mesh was used to shield the devices, as shown in Figure 4-63. Additionally, Faraday mesh was added to surround the Inflow Reservoir.



**Figure 4-63:** Faraday mesh applied to the power supply transformers of the submersible pumps in the Stanford Geothermal Laboratory

#### **4.2.2.2 Data Acquisition Modifications**

The same data acquisition (DAQ) device utilized in Round 1 was also used in Round 2 experiments. The copper silver plated pellet wires attached to the chloride ISE probes were connected with the positive ports of the AI channels of the DAQ device to connect the chloride tool and the DAQ device. Specifically, ISE probe #2 was connected with the positive port of the AI #2 channel, and ISE probe #3 was connected with the positive port of the AI #3 channel. To create an electric potential difference, the reference electrode needed to be connected with both the negative ports of the AI #2 and AI #3 channels. Given that there was only one reference electrode, its wire was spliced to allow its signal to feed into both negative ports. The resulting configuration of the DAQ device and its connections with the wires from the chloride tool are shown in Figure 4-64. Note that the spliced reference electrode wire can be seen connecting the light green and yellow wires.

To control the software settings of the DAQ device, the code shown in Figure 4-65 was written in LabVIEW®. This code controlled the sampling frequency and enabled the specification of which AI channels in the DAQ device were read. For the majority of the experiments presented in this report, the sampling frequency was set to 2 samples per second.

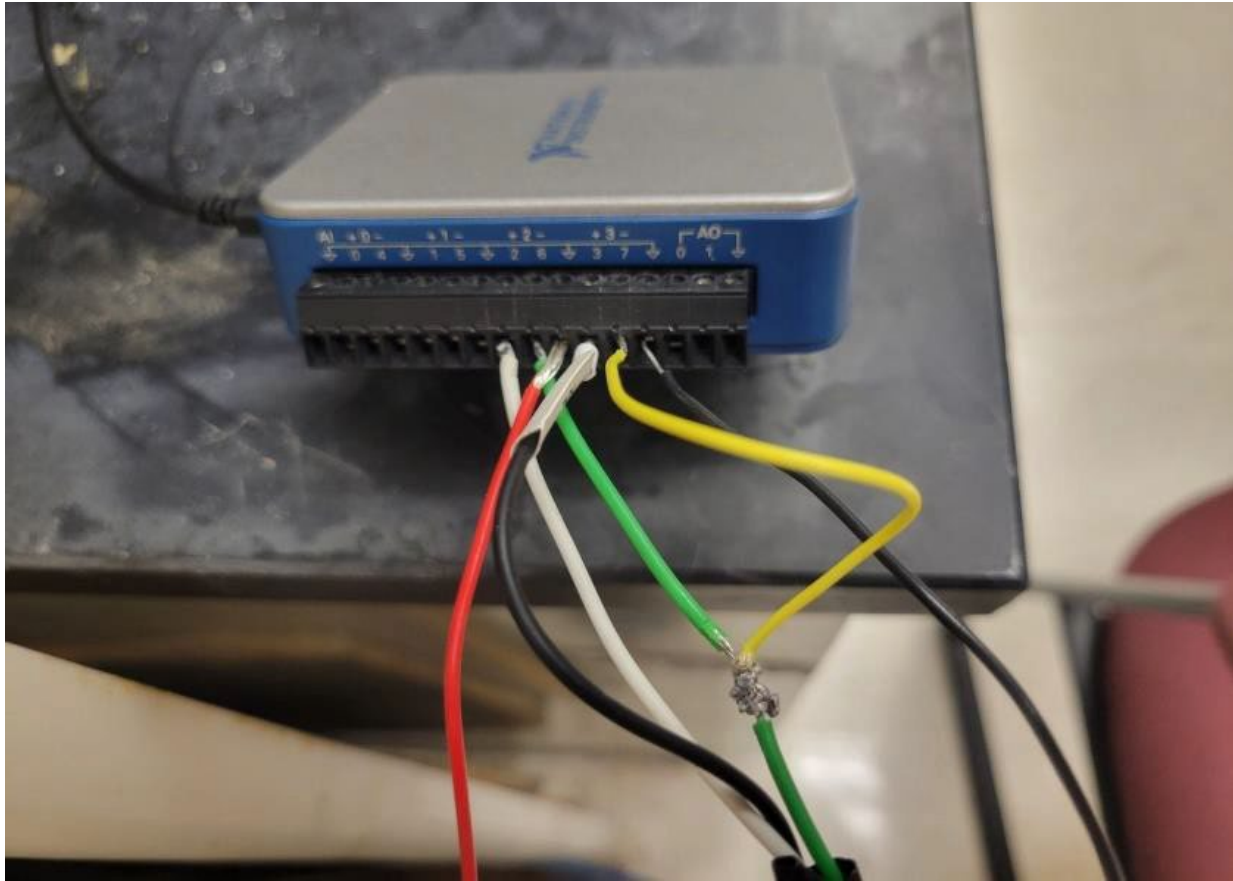


**Figure 4-64:** Configuration of the Data Acquisition Device (DAQ).

To reduce interference from any electrical noise received by the chloride tool and the overall configuration, the DAQ device was grounded. The newest version of the chloride tool did not contain a graphite ground like those found in the two prior iterations of the tool. To ensure that the tool was grounded, wires were connected with the ground ports of the AI #2 and AI #3 channels. These wires were attached to the scaffolding of the artificial well apparatus and spliced together approximately a foot (25 cm) from the main wellbore. These wires were then connected to a third wire that ran along the outside of the main wellbore and was fixed such that it resided in the outflow of the top of the wellbore.

Additionally, the two ground wires were spliced together approximately a foot (25 cm) from the DAQ device to connect with a monitor power cable. The female end of the monitor power cable and its power prongs were removed to isolate its ground wire. After plugging the monitor power cable into an electrical socket and soldering the monitor cable's ground wire with the two ground wires for the DAQ device, the overall hardware configuration for the data recording apparatus was sufficiently grounded.

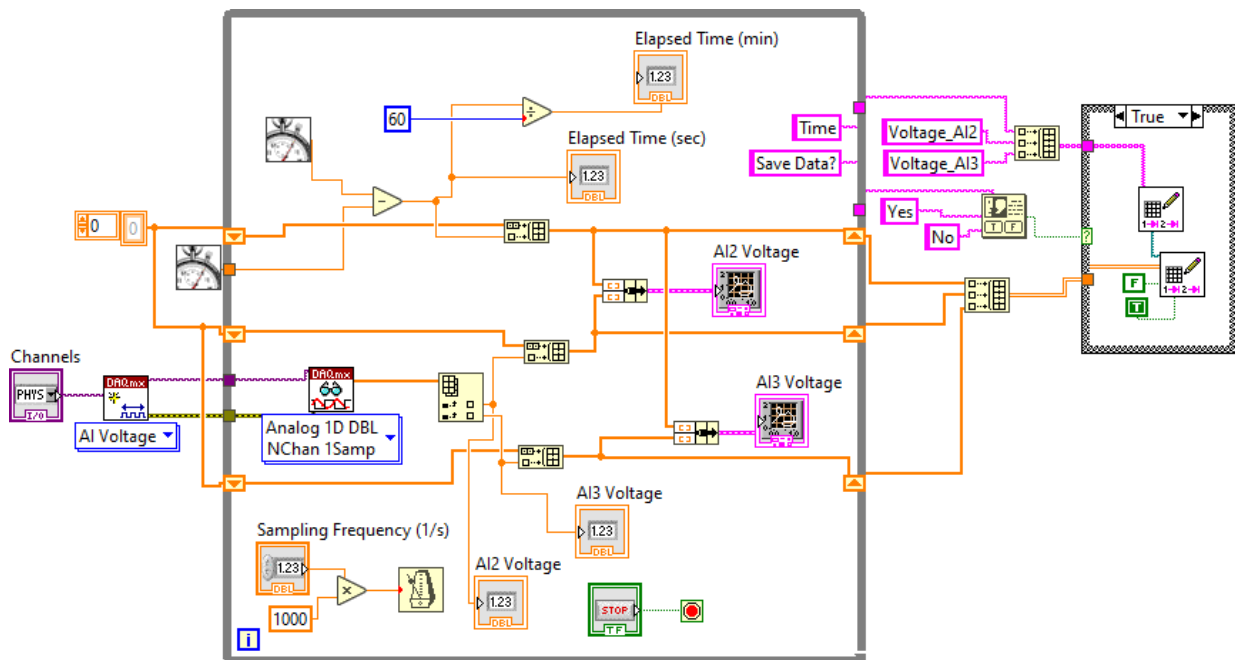
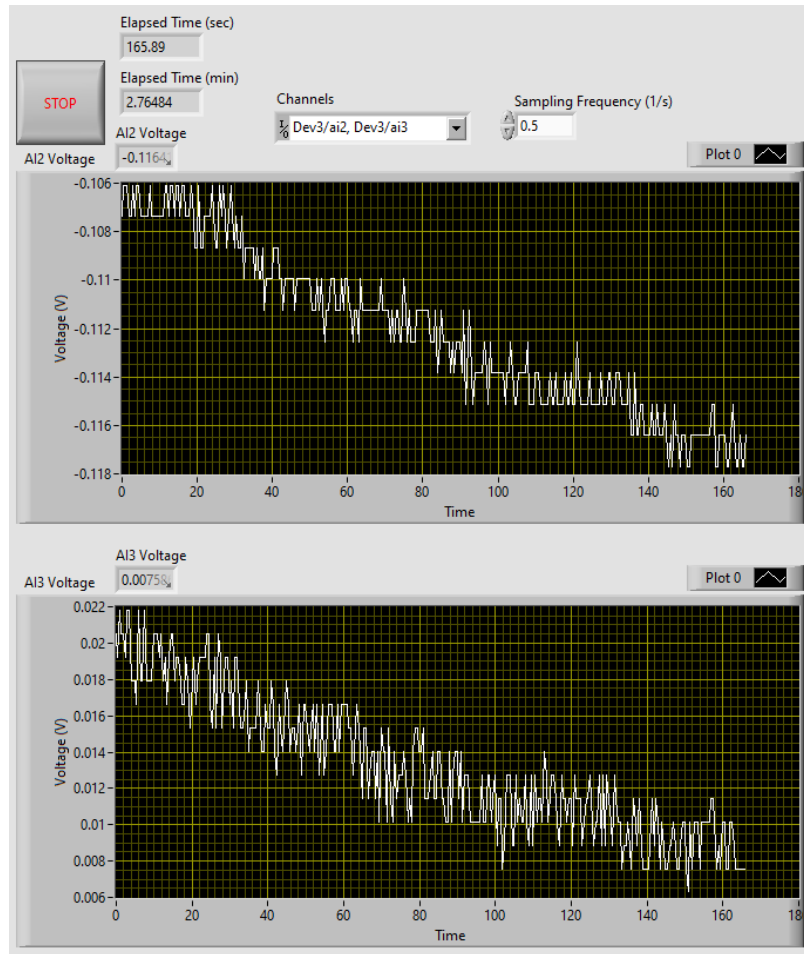


**Figure 4-65:** LabVIEW program block front panel and diagram that records voltage outputs from two chloride ISE probes.

#### 4.2.2.3 Round 2 Tool Calibration

Similar to Round 1 calibration, the Round 2 calibration was done on the lab-scale tool with housing on the bench. A coffee pot was filled with 1.6 liters of fresh tap water. The unconventional choice of using a coffee pot for a storage vessel was made because its large opening and comparatively small volume reduced the amount of salt needed for the calibration process. Additionally, the coffee pot supported the chloride tool, preventing it from falling over. The experimental configuration for the calibration process is shown in Figure 4-66. An initial voltage reading of pure tap water was taken to serve as a baseline with the assumption that the fluid had a chloride concentration of 0.0 mol/L.

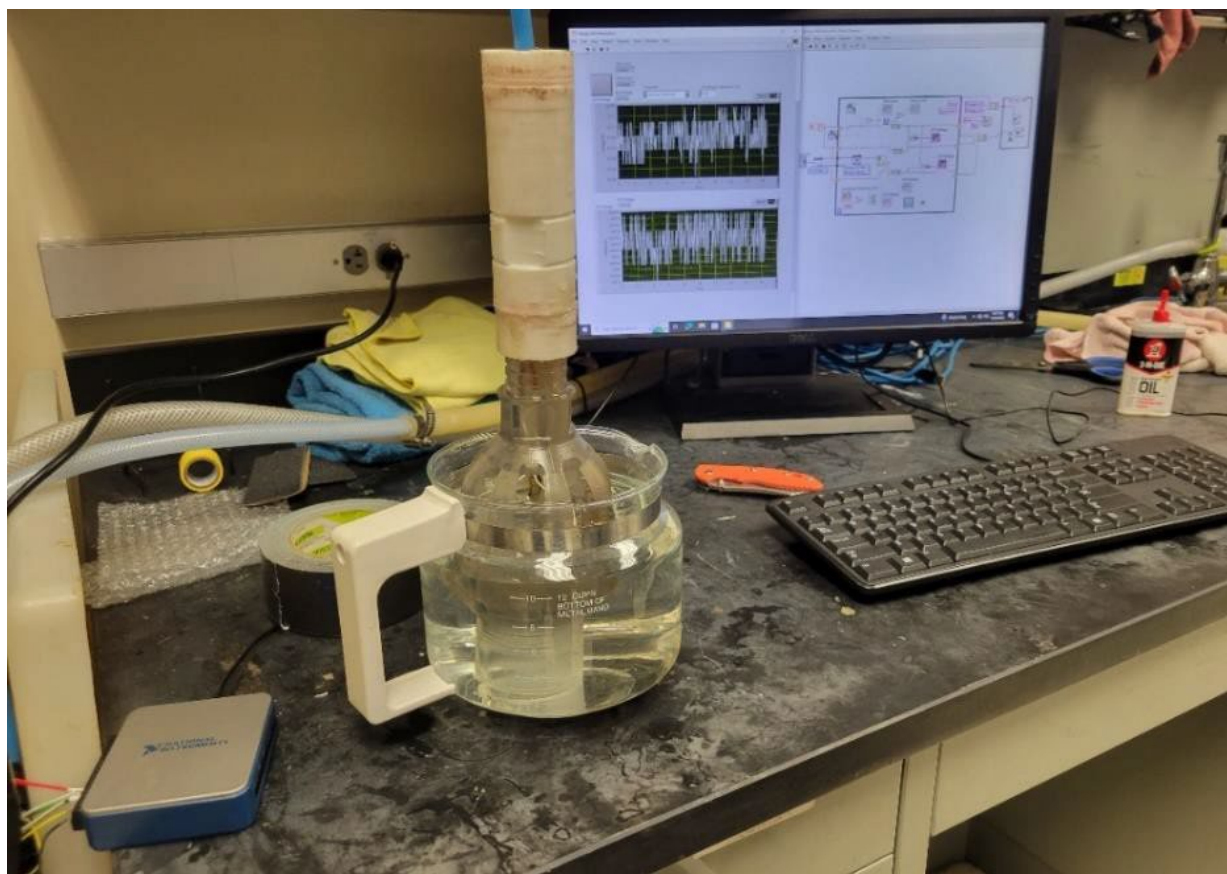


**Figure 4-66:** Experimental configuration for the calibration process

To create the chloride solution for each stage of the calibration process, the proper mass of sodium chloride was added to the fluid in the coffee pot. Note that the molecular weights of water and sodium chloride were assumed to be 18.02 g/mol and 58.44 g/mol for determining the necessary mass of sodium chloride. The necessary mass of sodium chloride for each solution was determined by multiplying the molecular weight of sodium chloride by the desired molarity and the volume of water present. To ensure that the sodium chloride was completely dissolved, the solution in the coffee pot was stirred vigorously for 60 seconds. Then, the voltage readings from both ISE probes were recorded during a 15 minutes (900 seconds) period, which was sufficient time for the voltage signals to stabilize. The baseline readings and the time series of the voltage readings for chloride concentrations ranging from  $5 \times 10^{-4}$  to  $1 \times 10^0$  mol/L are shown in Figure 4-67.

To determine a relationship between the chloride concentration and the voltage readings for both ISE probes, the negative common (base 10) logarithms of the tested molarities were plotted against their

corresponding voltage values. These plots are shown in Figure 4-68 and their linear regressions serve as the calibration curves for both ISE probes. The common logarithm of the molarities was chosen because of the logarithmic relationship between the potential difference and the ion concentration in the Nernst Equation (Equation 3-13).

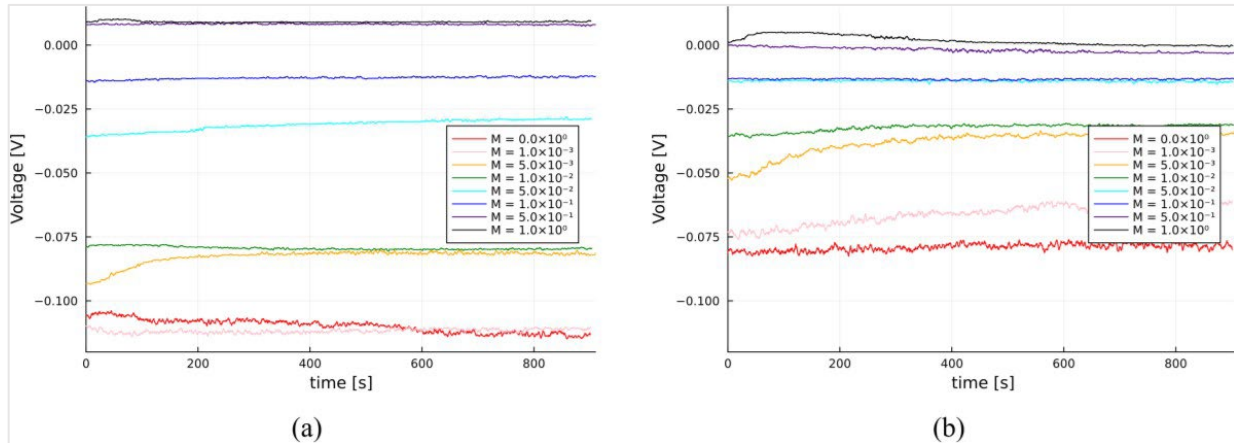


**Figure 4-67:** Voltage time series for (a) ISE probe #2 and (b) ISE probe #3 for various chloride concentrations during the calibration process

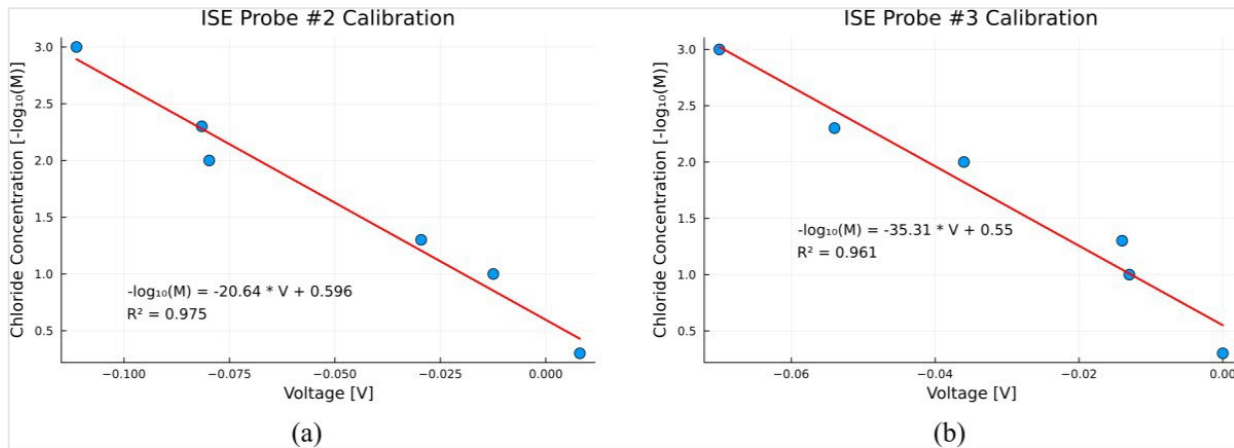


**Figure 4-68:** Linear regression of data points from the calibration process for (a) ISE probe #2 and (b) ISE probe #3

As shown in Figure 4-68, a strong linear relationship exists between the negative common logarithms of chloride concentration and the voltages produced by ISE probe #2 ( $R^2 = 0.975$ ) and ISE probe #3 ( $R^2 = 0.961$ ). The equations for the linear regressions of ISE probe #2 and ISE probe #3 are provided in Equations (4-1) and (4-2), respectively. Note that  $M$  is the chloride concentration in mol/L and  $V$  is the electric potential difference between the respective ISE probe and the reference electrode in volts.

$$-\log_{10}(M) = -20.64 * V + 0.596 \quad (4-1)$$

$$-\log_{10}(M) = -35.31 * V + 0.550 \quad (4-2)$$

Equations (4-1) and (4-2) give a negative direct relationship between the common logarithm of chloride molarity and the voltage reading. This is the opposite behavior of the calibrations conducted

by Gao (2017) and the Round 1 calibration. This discrepancy is likely caused by gradual changes to the baseline readings of chloride ISE probes, which are discussed in Section 4.2.2.4.

It was further noted that the slope of the linear regression for ISE probe #2 is significantly less than the slope of the linear regression for ISE probe #3. This discrepancy increases the sensitivity of ISE probe #3 to chloride concentration changes. As such, distinguishing smaller changes in chloride concentration is more difficult for ISE probe #3. However, as discussed in Section 3.3, the theoretical value for the slope of the linear regression is  $-17.13 \text{ } -\log_{10}(\text{M})/\text{V}$  as given by the Nernst Equation. This value is more similar to the slope of ISE probe #2, suggesting that its linear regression may be more reasonable and reliable for determining the chloride concentration of a solution.

One characteristic of the linear regressions of the calibration curves in Figure 4-68 was their divergence from the data points at the highest chloride concentration. This behavior suggests that the chloride tool underestimated the chloride concentration of fluids containing high chloride concentrations. An explanation for this phenomenon is that the ISE probes have a functional range of chloride concentrations of  $5 \times 10^{-3}$  to  $5 \times 10^{-1}$  mol/L as mentioned in Section 2.1.2. Of note, the voltage series for the chloride concentration of  $1 \times 10^0$  mol/L were excluded from the calibration curves because they exist outside the functional range of the ISE probes. This provides evidence that the chloride tool is best utilized in wells with chloride concentrations within or slightly below the functional range of the ISE probes. Fortunately, this is possible at the Utah FORGE project because the highest chloride concentration of the samples was  $1.24 \times 10^{-1}$  mol/L (see Table 4-16).

#### 4.2.2.4 Round 2 Static and Dynamic Experiments Overview

Round 2 experiments were conducted in static and dynamic manners to investigate variables that may be important for field data acquisition. Static experiments involved placing the lab-scale tool inside the artificial wellbore without moving the tool upwards or downwards. Dynamic experiments consisted of moving the tool in Run-in-Hole (RIH) and Pull-out-of-Hole (POOH) motions to replicate field deployment. The variables were as follows:

- Chloride concentration relative to tool positions (static) and tool motion (dynamic)
- Angular sensitivity (dynamic)
- Feed zone inflow rate sensitivity (static and dynamic)
- Wellbore flow rate sensitivity (dynamic)
- Ion sensitivity (static and dynamic)

#### ***Static Experiment Procedures***

A summary of the events in the procedure of a static experiment and their corresponding times are provided in Table 4-8. To conduct static experiments, the Inflow Reservoir was filled with tap water. Then, Submersible Pump 3 was turned on to provide flow into the main wellbore. To allow continuous flow, the taps providing fresh water for the Inflow Reservoir were turned on. After the fluid discharged from the main wellbore began to fall into the Outflow Reservoir, Submersible Pumps 1 and 2 were turned on to discard the outflowing fluid. With this experimental configuration, continuous flow through the artificial well system was established, allowing experimental trials to be conducted

sequentially without needing to wait for either fluid addition to the Inflow Reservoir or fluid discharge from the Outflow Reservoir.

**Table 4-8:** Timing of events in static experiments

Activity	Time (min)
Turn on Flowing Fresh Water Wellbore Inflow	Before Trial
Turn on Data Acquisition System	0:00
Open Feed Zone Valve	5:00
Close Feed Zone Valve	6:00
Open Feed Zone Valve	15:00
Close Feed Zone Valve	16:00
Turn off Data Acquisition System	25:00
Turn off Flowing Fresh Water Wellbore Inflow	After Trial

After approximately 5 minutes (300 seconds) of continuous wellbore flow, the chloride tool was deemed to have equilibrated with the flowing fresh water. Then, the data acquisition software was turned on to begin an experimental trial. During this time, Submersible Pump 4 was turned on with the Feed Zone Valve remaining closed to allow for eventual feed zone inflow.

To provide a baseline freshwater reading for each experimental trial, an additional 5 minutes (300 seconds) of continuous freshwater flow into the wellbore occurred. At the 5-minute mark, the Feed Zone Valve was opened to begin the inflow of feed zone fluid. This occurred for one minute (60 seconds), after which the Feed Zone Valve was closed to stop feed zone inflow. Note that during this time, no changes were made to the freshwater flowing into the wellbore.

To monitor the voltage response of the chloride tool following the shut off of the feed zone, only freshwater flow into the wellbore was allowed to continue for the following 9 minutes (540 seconds). Additionally, this freshwater flow washed the ISE probes of any residual ions in their membranes, preparing them for another period of feed zone inflow.

To assess the repeatability and reliability of the chloride tool, a second minute-long pulse of feed zone inflow began at the 15-minute (900 seconds) mark when the Feed Zone Valve was opened. Again, to monitor the chloride tool's response following the shut-off of the feed zone inflow, the Feed Zone Valve was closed at the 16-minute mark, and only the flow of freshwater into the wellbore was allowed for the following 9 minutes (540 seconds).

To finish an experimental trial, the session of the data acquisition software was stopped, and the data output was saved. Then, the next experimental trial began after less than one minute (60 seconds) of downtime. When the experimental trials were completed, the Inflow Valve was closed, and the Outflow Valve was opened to dump the remaining wellbore fluid into the Outflow Reservoir.

When changing the chloride concentration of the feed zone fluid, the main wellbore was filled with fresh water, the Inflow Valve was closed, Submersible Pump 4 was turned off and relocated to the Outflow Reservoir, and the Feed Zone Valve was opened. This allowed for the backflow of fresh water through the feed zone tubing and into the Outflow Reservoir. After passing approximately 30 L of freshwater, it was assumed that the feed zone tubing was sufficiently cleaned from the preceding feed zone fluid. Then, Submersible Pump 4 was placed back into the Feed Zone Reservoir and turned on. Finally, the feed zone tubing was filled with the new feed zone fluid to allow experimental trials to be resumed.

The shielded electrical cable was used to raise or lower the chloride tool to the proper vertical position in the wellbore. Then, the shielded electrical cable was fastened to the scaffolding of the artificial well system using a zip tie to secure its position. To assess the response of the chloride tool when it was located above, even with, or below the feed zone, it was positioned such that the ISE probes were 10 inches (25.4 cm) above, 0.5 inches (1.27 cm) above, or 7 inches (17.8 cm) below the feed zone port. The locations of the chloride tool in the wellbore for these three positions are shown in Figure 4-69.

Regarding experimental methodology, all static experiments were conducted in triplicate to assess the reliability and repeatability of the chloride tool. Additionally, all recorded data were processed using an in-house code written in the Julia programming language. This code slightly smoothed the voltage readings by averaging adjacent data points to reduce the inherent noise and to produce clearer visualizations for analysis. Additionally, to adjust for the gradual drifting of the baseline voltage of the ISE probes, the readings from the initial 5 minutes (300 seconds) of freshwater flow were used to align the calibration curve with each experimental trial.

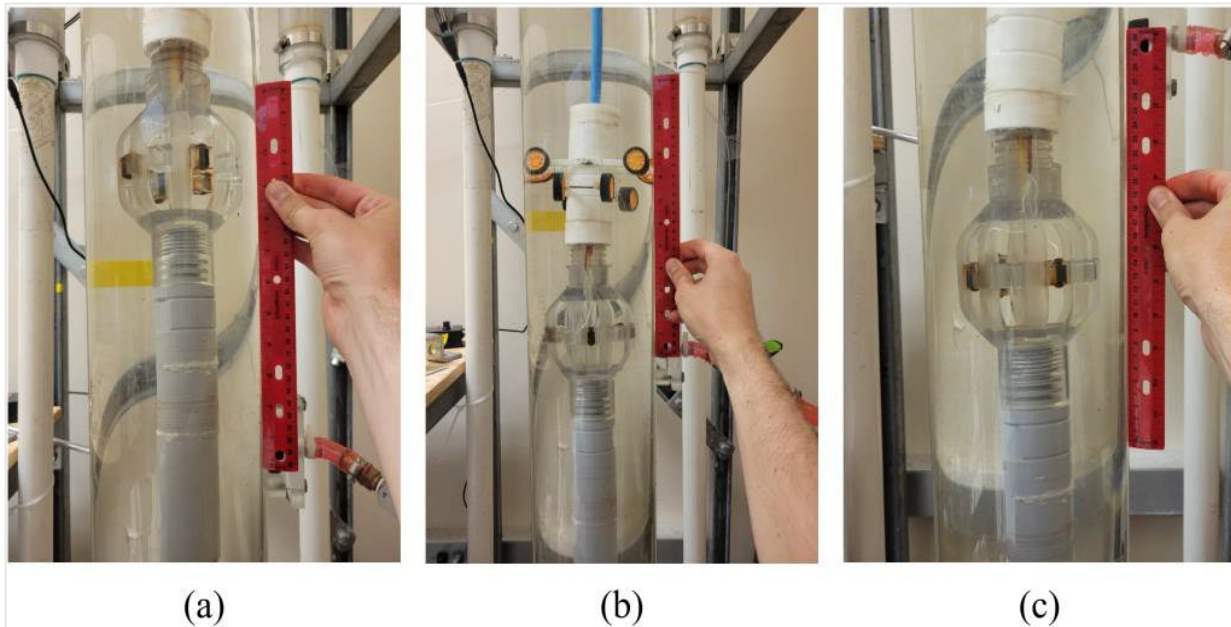


**Figure 4-69:** Position of the chloride tool in reference to the feed zone port for the (a) above, (b) even, and (c) below vertical position

### ***Discussions on ISE Noise Reduction***

Frequent rinsing of the ISE probes with isopropyl alcohol improved the consistency of the ISE probes' voltage readings. Specifically, the noise in the voltage readings decreased significantly, and the baseline voltage readings stabilized around  $-0.15$  V for ISE probe #2. However, there were still minor changes in the baseline voltage. To determine the change in baseline voltage over time, the chloride tool was left suspended in static fresh water in the artificial wellbore. Figure 4-70 displays two voltage time series lasting more than two days in which the chloride tool was left in static, freshwater conditions.

Plot (a) of Figure 4-70 began after an experiment with high chloride concentrations. As such, a significant drop in voltage during the first 10 hours is expected as the chloride ions diffuse out of the transducer and reach equilibrium with the fluid in the wellbore. Another key observation is the differing amounts of noise in the voltage readings between plots (a) and (b). Plot (a) was recorded before the

ISE probes were rinsed regularly with isopropyl alcohol, which is likely the reason for its comparatively larger amounts of noise.

The most important takeaway is the fluctuation in the baseline voltage in the latter part of plot (a) and throughout plot (b). Despite the chloride tool being subjected to static conditions, the voltage readings of both ISE probes still varied unrelated to the inflow rate variation.

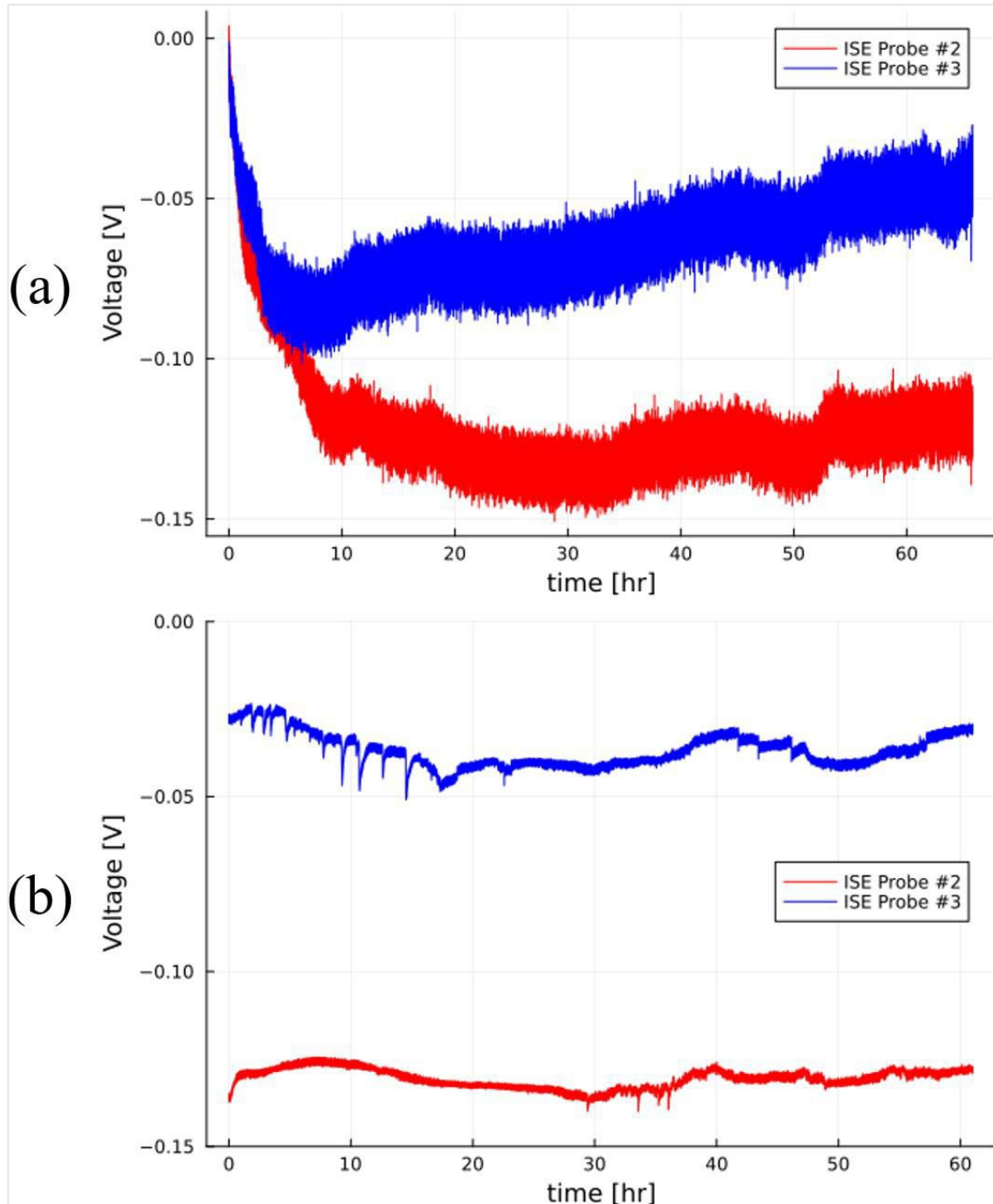


**Figure 4-70:** Two instances of varying long-term behavior of ISE probe #2 and ISE probe #3 when submerged in still freshwater in the artificial well.

### ***Dynamic Experiment Procedures***

In Round 1 dynamic experiments, strong correlations exist between the voltage drop and the feed zone location, the chloride concentration in the feed zone fluid, and radial distance of ISE probes from the feed zone. As such, in Round 2 dynamic experiments, the location of the feed zone in the wellbore and the radial distance of ISE probes from the feed zone were held constant. Specifically, only the bottom feed zone injection port was used, and the tool was held centered in the wellbore.

A summary of the experimental procedure for dynamic experiments and the times corresponding to each action are provided in Table 4-9. Before conducting a dynamic experiment, the Feed Zone Reservoir was filled with 20 L of feed zone fluid. Unlike the static experiments, two additional Feed Zone Reservoirs were created for a total of 60 L of feed zone fluid. The extra feed zone fluid was needed because the longer duration of feed zone inflow for a dynamic experiment required approximately three times the amount of feed zone fluid than a static experiment.

**Table 4-9:** Timing of events in a dynamic experimentation

<b>Activity</b>	<b>Time (min)</b>
Turn on Flowing Fresh Water Wellbore Inflow	Before Trial
Turn on Data Acquisition System	0:00
Open Feed Zone Valve	5:00
Start RIH Movement	7:00
End RIH Movement	~7:30
Pause at bottom of Wellbore	8:00
Start POOH Movement	9:00
End POOH Movement	~9:30
Turn off Chloride Tracer Feed Zone	12:00
Turn off Data Acquisition System	21:00
Turn off Flowing Fresh Water Wellbore Inflow	After Trial

To begin a dynamic experiment, the Inflow Reservoir was filled with tap water. Of note, the taps for two of these hoses remained on during the entirety of a series of dynamic flow experiments. The third hose was used to provide an additional flow of fresh water into the Inflow Reservoir approximately every 15 minutes to ensure a sufficient volume of fluid. Then, to provide inflow into the artificial wellbore, Submersible Pump 3 was turned on. After the water began falling into the Outflow Reservoir, Submersible Pumps 1 and 2 were turned on to discard the outflow fluid from the wellbore. With this configuration, continuous and sequential experimental trials were conducted.

After approximately 5 minutes (300 seconds) of continuous wellbore flow, the chloride tool was deemed to have been sufficiently acclimated to the flowing fresh water. As such, a series of experimental trials could begin. To begin an individual experimental trial, the data acquisition software was turned on. At the same time, a secondary stopwatch, typically a smartphone, was started to have concurrent timing mechanisms. The secondary stopwatch was then moved to the top of the artificial wellbore system to ensure accurate timing of the dynamic motion of the chloride tool.

A subsequent 5 minutes (300 seconds) of freshwater wellbore inflow provided a baseline reading for each experimental trial. After 300 seconds had passed from turning on the data acquisition software, the Feed Zone Valve was opened to inject feed zone fluid. Before initiating the RIH movement, two minutes (120 seconds) of feed zone inflow occurred. This time allowed the feed zone inflow to reach

a steady state concentration distribution within the wellbore. Additionally, the ISE probes equilibrated with the chloride solution flowing in the wellbore during this time.

Seven minutes (420 seconds) after beginning the experimental trial, the RIH movement was initiated. To perform this motion, the shielded electrical cable was manually actuated to drive the motion of the chloride tool. The RIH motion typically lasted for 25 to 30 seconds with variations because of manual operation. After the down-tool component contacted the flow diffuser, the motion of the tool ceased, and the time of the RIH movement was recorded. This time was used to determine the average speed of the RIH motion to make voltage and molarity plots across the vertical depth in the wellbore.

Pausing at the bottom of the wellbore allowed a sufficient amount of time before starting the POOH movement. During this time, the additional pre-prepared feed zone fluid was added to the Feed Zone Reservoir to ensure a sufficient volume for continuing the experimental trial. The chloride sensors adjusted to the freshwater flowing into the bottom of the wellbore during this time.

Nine minutes (540 seconds) after beginning the experimental trial, the POOH movement of the chloride tool was initiated. This motion was performed in the same manner and lasted for approximately the same amount of time as the RIH movement. The only difference was the pulling rather than pushing direction of motion. Also, the POOH motion lasted for approximately 30 seconds. The POOH motion was completed when the up-tool component contacted the scaffolding of the artificial wellbore system. The time at which this occurred was recorded to determine the average speed of the POOH motion, which was necessary to make voltage and molarity plots across the vertical depth in the wellbore.

Feed zone inflow continued while the tool was at the top of the wellbore after the POOH motion finished. This additional feed zone inflow occurred to monitor the response of the chloride tool following its motion in the wellbore. During this time additional pre-prepared feed zone fluid was added to the Feed Zone Reservoir to ensure it had sufficient volume. At the 12-minute mark (720 seconds), the Feed Zone Valve was closed to stop the feed zone inflow.

For the remaining 9 minutes (540 seconds) of the experimental trial, only freshwater flowed into the wellbore. This allowed the ISE probes to be washed of any residual ions in their membranes. Additionally, the behavior of the chloride tool during this time granted insight into its behavior following an experiment with brine similar to the static experiments.

Dynamic experimental trials were concluded in the same manner as the static experiments. The session of the data acquisition software was stopped, and the data output was saved. Then, the next experimental trial began after less than a minute of downtime. At the conclusion of the experimental trials, the Inflow Valve was closed to prevent flow between the wellbore and the Inflow Reservoir, and the Outflow Valve was opened to discard the remaining wellbore fluid into the Outflow Reservoir.

### ***Dynamic Experiments Initial Observations and Updated Methodology***

Initial dynamic experimentation began using a feed zone fluid with a chloride concentration of  $1 \times 10^{-1}$  mol/L and a high feed zone inflow rate (0.115 kg/s). With the modifications made to the artificial wellbore apparatus, dynamic experiments were conducted continuously with less than a minute between consecutive trials.

When the voltage time series for preliminary experimental trials were plotted sequentially, as shown in plot (a) of Figure 4-71, a clear decreasing trend in the baseline voltage of both ISE probes is evident. This shift in baseline voltage skewed the inferred molarity by an order of magnitude for Trials 4 and

5. Noticing that this behavior was present in the static experiments, albeit to a lesser degree, a method to acquire repeatable results was needed. After a discussion about the long-term behavior of the ISE probes with their fabricators at Sandia National Laboratories, a strategy of regularly rinsing the ISE probes with isopropyl alcohol was considered. Rinsing the ISE probes with isopropyl alcohol removed the ions present in the membranes, thus effectively zeroing the baseline reading of the probes.

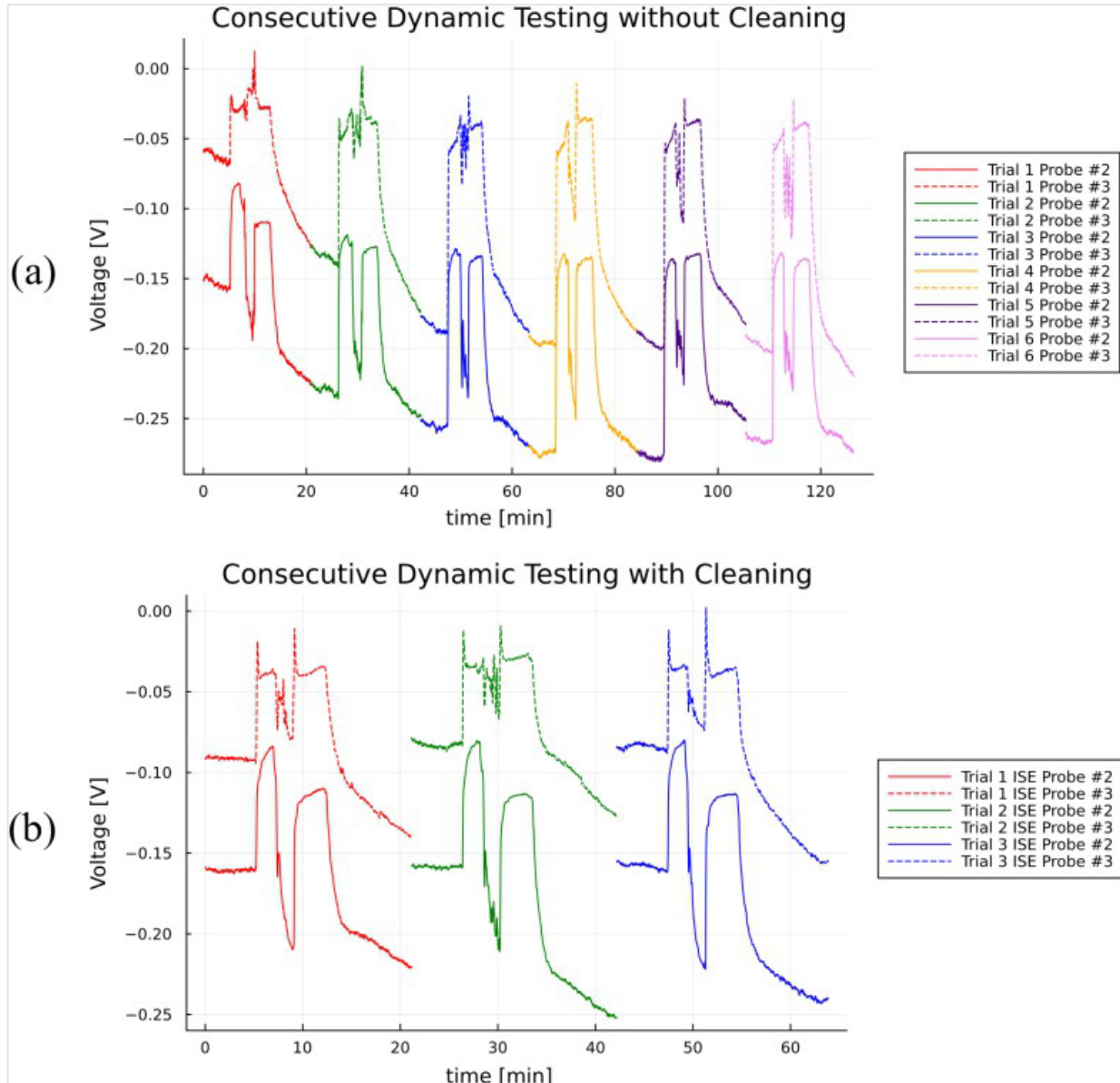


**Figure 4-71:** Voltage time series of dynamic experiments plotted consecutively (a) without and (b) with cleaning the ISE probes between trials.

Following the initial dynamic experiments, the procedure was modified such that the ISE probes were sprayed with approximately 10 mL of 91% isopropyl alcohol between trials. Then, the complete tool housing was submerged in the flowing wellbore for approximately 30 seconds to wash away any isopropyl alcohol. Using this updated procedure, the voltage-time series exhibited more consistent behavior and no shift in baseline voltage between experimental trials, as shown in plot (b) of Figure 4-71. However, these trials still exhibit a decline in voltage in the final 9 minutes (540 seconds) of each

trial when only fresh water is flowing in the wellbore, especially for ISE probe #2. This behavior suggests that a decline in voltage would occur if the ISE probes were not cleaned with isopropyl alcohol following each trial. The streaming potential and the buildup of static electricity serve as a possible explanation for this behavior, which is discussed in Section 4.2.2.5.

To highlight the repeatability of the dynamic laboratory experimental trials, Figure 4-72 displays the voltage and the corresponding molarity time series of the plot (b) from Figure 4-71 plotted concurrently. Vertical lines corresponding to the initiation and approximate completion of the RIH and POOH sections were included in interpreting these voltage time series. By rinsing the ISE probes with isopropyl alcohol, the voltage and molarity time series of the individual trials are aligned to the same extent as the static experiments. This repeatability between trials suggests that the updated methodology should be used for additional dynamic experiments. This allows the impact of changing independent variables instead of changing the baseline voltage of the ISE probes.

Of note, Figure 4-72 shows that the ISE probes exhibit behavior consistent with the static experiments. Specifically, ISE probe #2 provides more accurate measurements of the surrounding fluid's chloride concentration, and the readings from ISE probe #3 feature spikes the moment the chloride concentration changes.

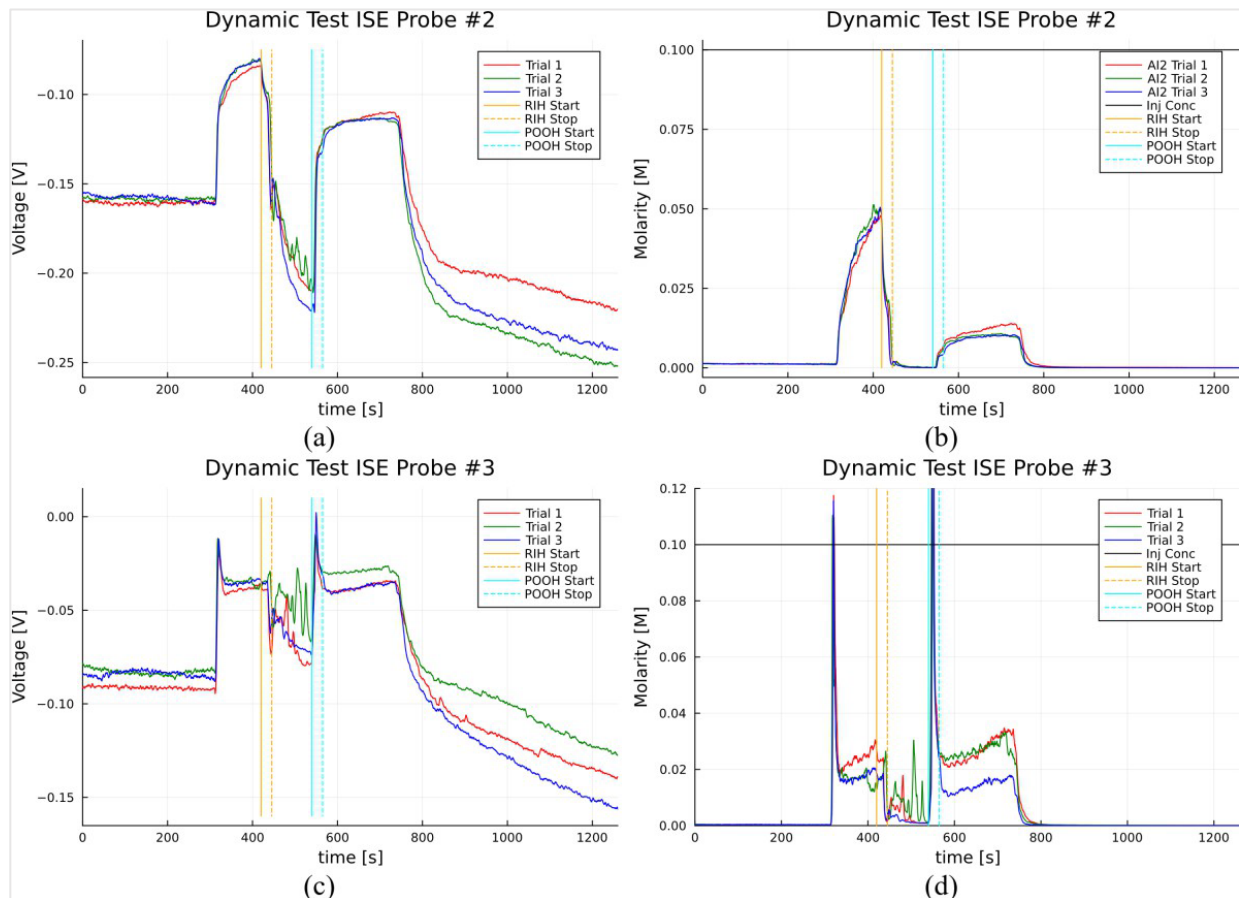


**Figure 4-72:** Concurrent voltage and molarity time series of (a and b) ISE probe #2 and (c and d) ISE probe #3 for a series of dynamic experiments.

#### 4.2.2.5 Chloride Concentration Relative to Tool Positions and Tool Motions

##### *Static Experiments of Chloride Concentration Relative to Tool Positions*

Two important parameters must be considered when considering the successful field-scale use of the chloride tool: its sensitivity to the range of chloride concentrations present in the geothermal fluid and the effects of the feed zone's vertical location relative to the chloride tool. The static experiments presented in this section were conducted to assess the chloride tool's ability to distinguish these variables.

Approximately one tablespoon (14.8 mL) of McCormick® red food coloring was added to every 20 L of feed zone fluid. Dyeing the feed zone fluid allowed for visual confirmation that the feed zone inflow was functioning properly. Additionally, the dyed feed zone fluid granted a visual assessment of the flow dynamics in the wellbore. The fluid behavior around the various vertical positions of the chloride tool after approximately 45 seconds of feed zone inflow is shown in Figure 4-73.

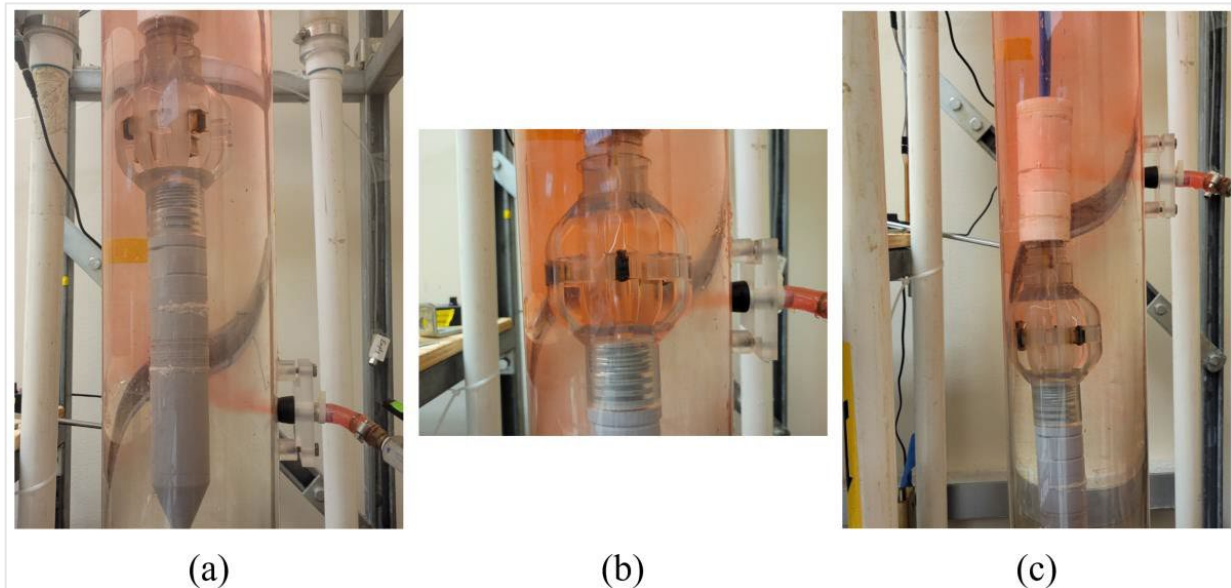


**Figure 4-73:** Flow dynamics surrounding the chloride tool in the (a) above, (b) even, and (c) below vertical position during feed zone inflow.

Qualitatively, Figure 4-73 shows that the feed zone inflow dynamics varied significantly for the different vertical positions of the chloride tool. Specifically, the amount of feed zone fluid that reached the ISE probes when the tool was in the below position was significantly less than when the tool was in the above and even positions. As such, it was expected that the chloride tool had voltage readings corresponding to lesser molarities while in this vertical position.

To assess the quantitative results when varying the chloride concentration of the feed zone fluid and the vertical position of the chloride tool, Figure 4-74, Figure 4-75, Figure 4-76, and Figure 4-77 must be interpreted together. Figure 4-74 and Figure 4-75 display the voltage time series of the two ISE probes at varying chloride concentrations of the feed zone fluid ( $1 \times 10^{-2}$  mol/L,  $5 \times 10^{-2}$  mol/L, and  $1 \times 10^{-1}$  mol/L) and at varying vertical positions. Using the linear regressions of the calibration curves, which are Equations (4-1) and (4-2), the molarity time series shown in Figure 4-76 and Figure 4-77 were created corresponding to the voltage readings of the ISE probes.

The rows of plots correspond to the vertical position of the chloride tool, and the columns correspond to the chloride concentration of the feed zone fluid. The top row has the results from the above position, the middle row has the results from the even position, and the bottom row has the results from the bottom position. Additionally, the columns are in ascending order of the chloride concentration ( $1 \times 10^{-2}$  mol/L,  $5 \times 10^{-2}$  mol/L, and  $1 \times 10^{-1}$  mol/L) of the feed zone fluid when interpreted from left to right.

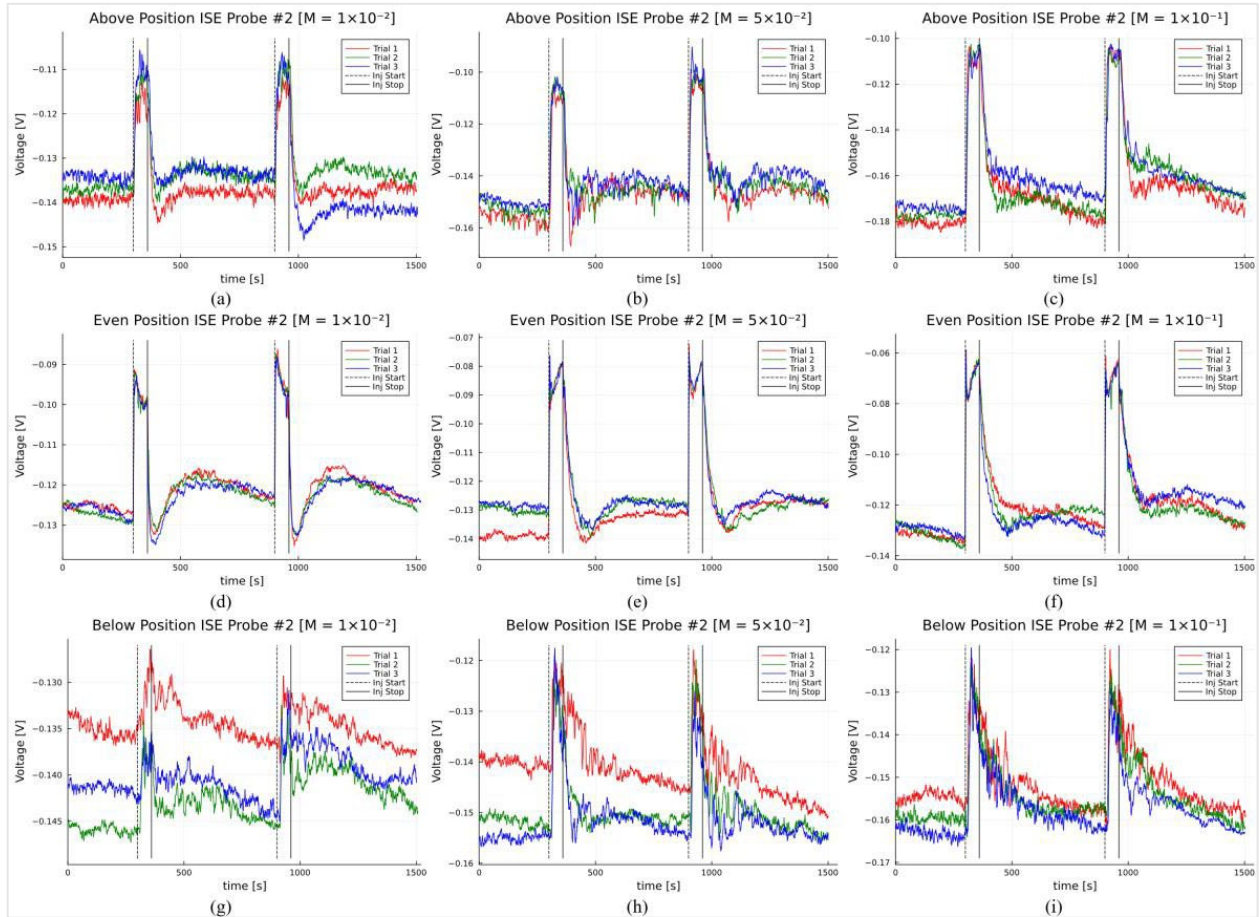


**Figure 4-74:** Voltage time series for ISE probe #2 in the above, even, and below positions for feed zone fluid chloride concentrations of (a, d, and g)  $1 \times 10^{-2}$  mol/L, (b, e, and h)  $5 \times 10^{-2}$  mol/L, and (c, f, and i)  $1 \times 10^{-1}$  mol/L.

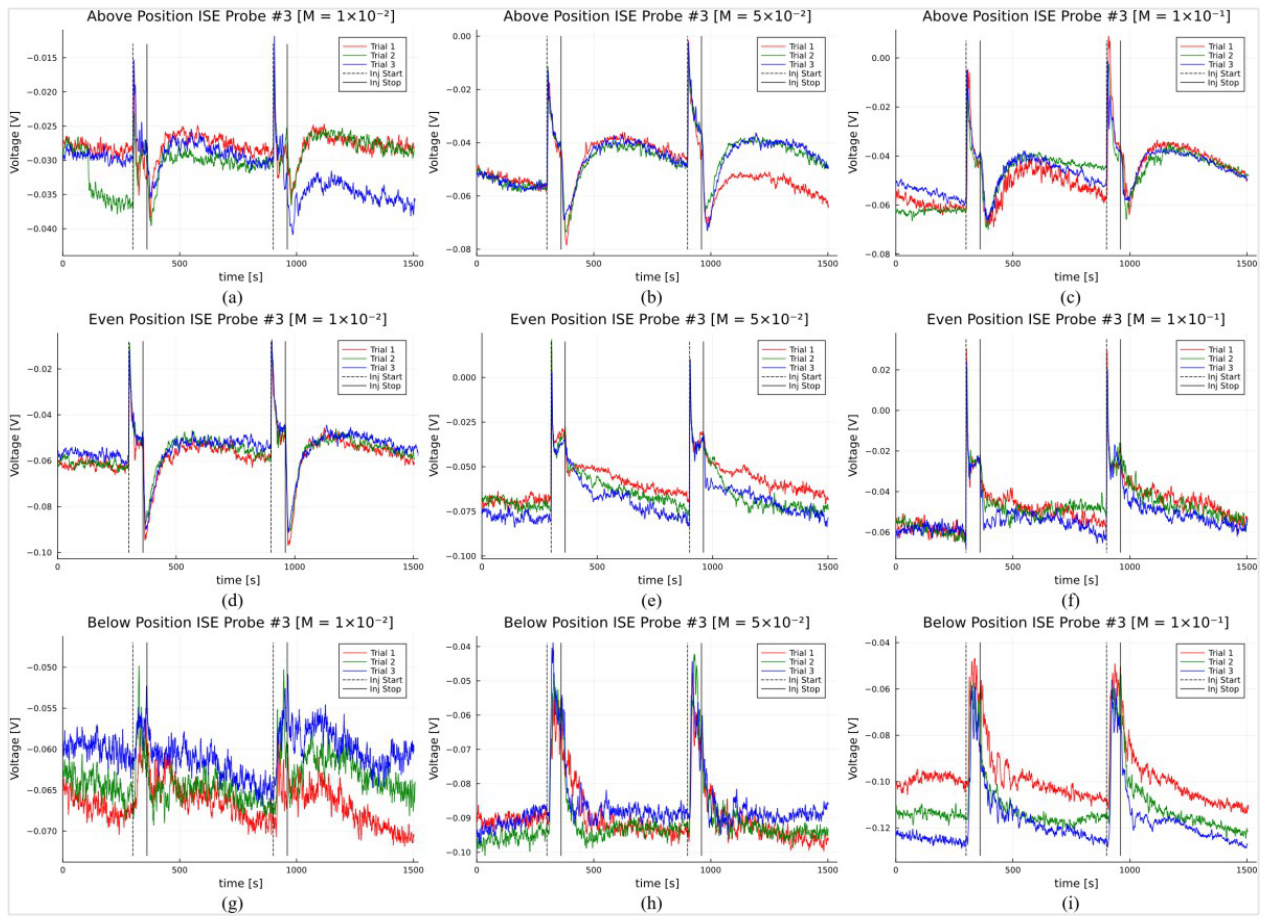


**Figure 4-75:** Voltage time series for ISE probe #3 in the above, even, and below positions for feed zone fluid chloride concentrations of (a, d, and g)  $1 \times 10^{-2}$  mol/L, (b, e, and h)  $5 \times 10^{-2}$  mol/L, and (c, f, and i)  $1 \times 10^{-1}$  mol/L.

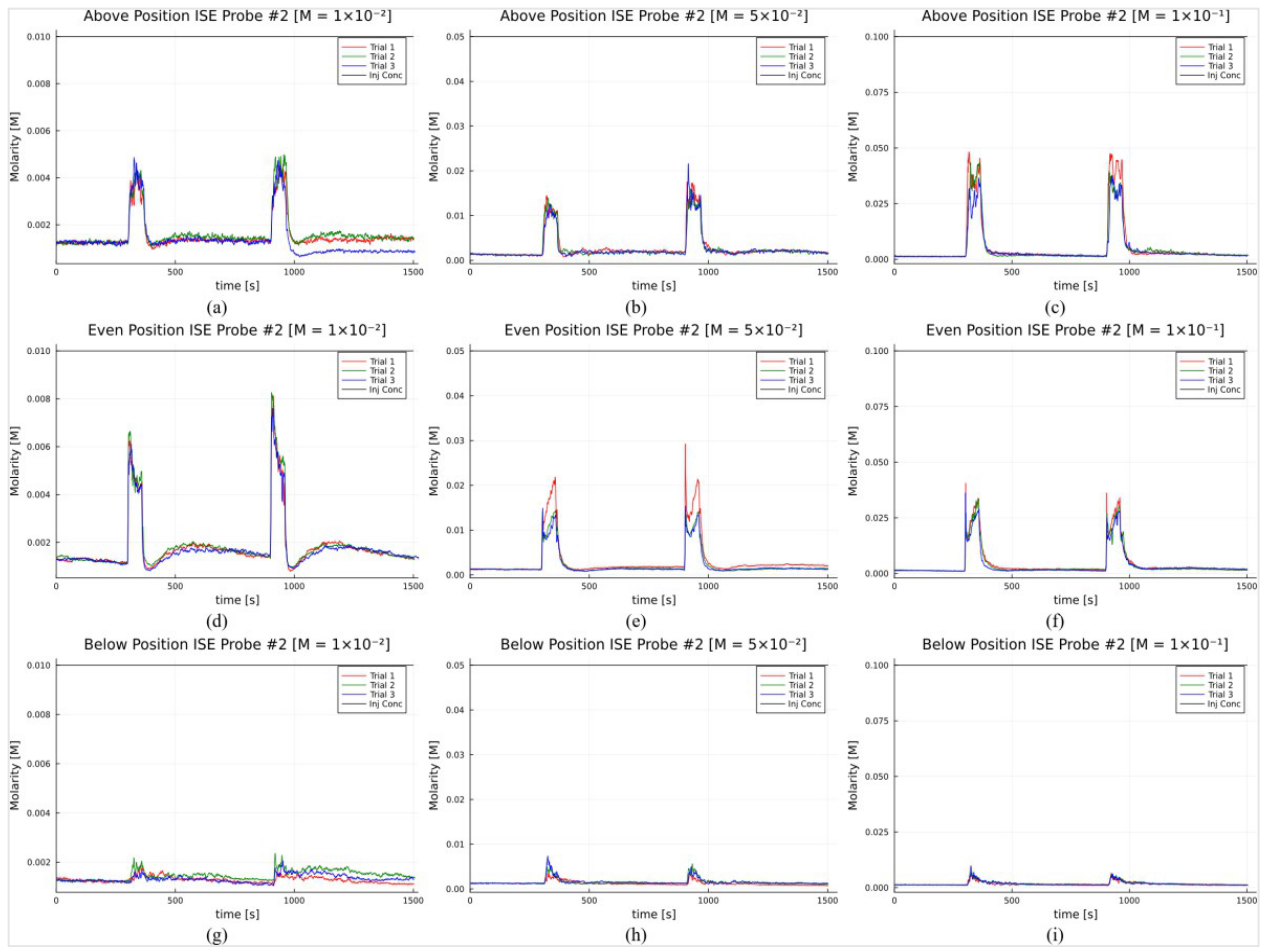


**Figure 4-76:** Molarity time series for ISE probe #2 in the above, even, and below positions for feed zone fluid chloride concentrations of (a, d, and g)  $1 \times 10^{-2}$  mol/L, (b, e, and h)  $5 \times 10^{-2}$  mol/L, and (c, f, and i)  $1 \times 10^{-1}$  mol/L

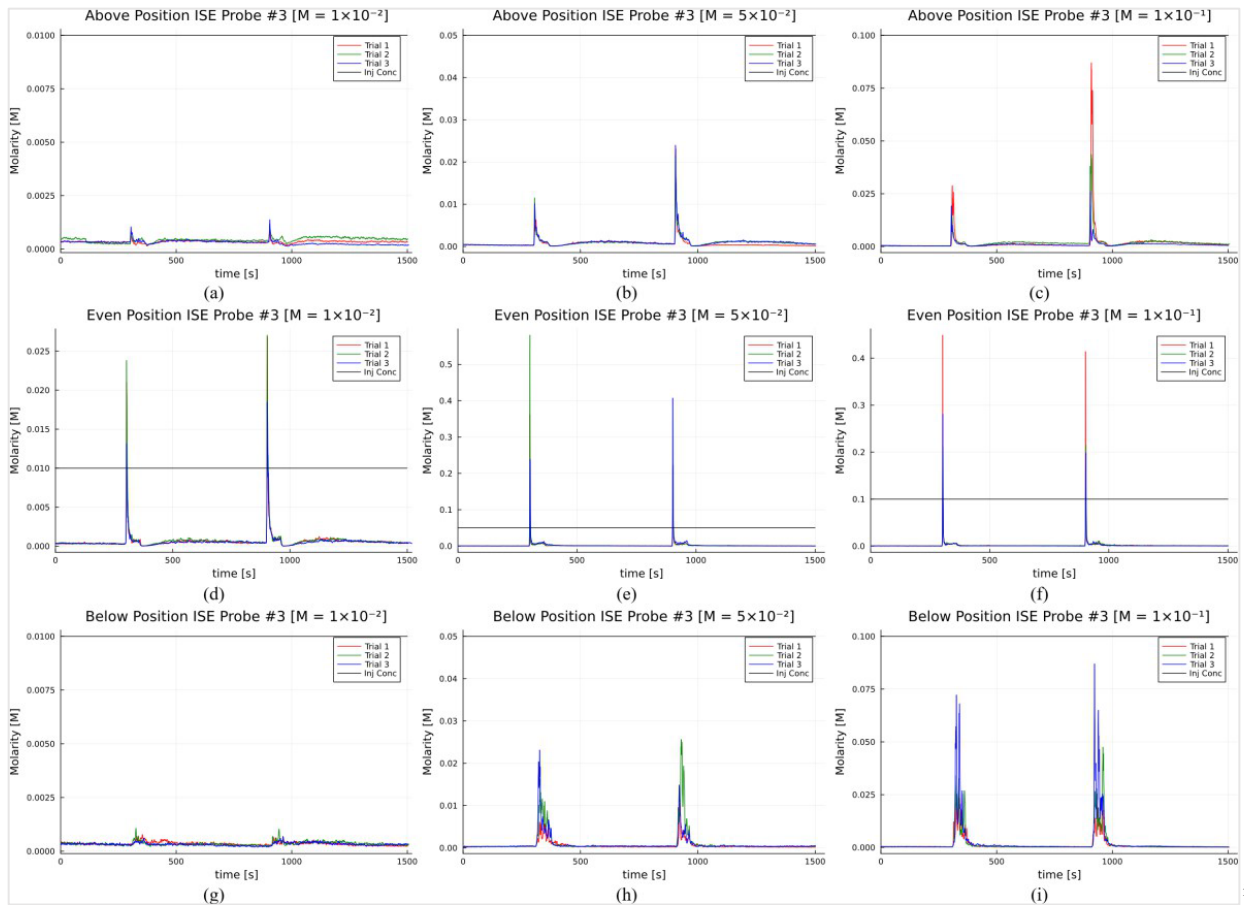


**Figure 4-77:** Molarity time series for ISE probe #3 in the above, even, and below positions for feed zone fluid chloride concentrations of (a, d, and g)  $1 \times 10^{-2}$  mol/L, (b, e, and h)  $5 \times 10^{-2}$  mol/L, and (c, f, and i)  $1 \times 10^{-1}$  mol/L

A direct observation from the plots is that the voltage and molarity readings for ISE probe #2 differ significantly from those of ISE probe #3. This is likely caused by inconsistent voltage responses of ISE probe #3, as first noticed when the slope of its calibration curve was approximately double the theoretical value, as highlighted in the chloride calibration discussion (Section 4.2.2.3). One of the largest irregularities with the behavior of ISE probe #3 was the large and steep spike in the voltage response, and thus, molarity was observed the moment that the feed zone fluid contacted the probe. Then, the voltage readings decreased and sometimes resulted in rebound spikes in the opposite direction, such as those in plot (d) of Figure 4-75. This is inconsistent with the expected behavior of an ISE probe in response to a greater chloride concentration, as predicted by the calibration curves presented in Figure 3-3 and the Nernst Equation.

An additional observation is a significant change to the behavior of the voltage and the molarity readings that occurred when the vertical position of the tool and the chloride concentration of the feed zone fluid were varied. The most consequential change was the significantly lower response of the chloride tool when it was located in the below position. In corroboration with Figure 4-73, the spikes in the molarity readings for the below position, especially for ISE probe #2, reached a maximum chloride concentration that was approximately 15% of the concentration of the feed zone fluid. Note that the concentration of the feed zone fluid is denoted with a horizontal black line. This reduced response was

caused by the fluid dynamics in the wellbore resulting in significantly less feed zone fluid reaching the ISE probes while the chloride tool was in the below position.

Additionally, Figure 4-76 shows that the spikes in the molarity readings of ISE probe #2 corresponding to feed zone inflow for the above position reached approximately 40% to 50% of the known chloride concentration of the feed zone fluid. In contrast, the spikes in the molarity readings for the even position of ISE probe #2 ranged from 30% to 70% of the chloride concentration of the feed zone fluid. Additionally, the spikes for the even position had a more variable behavior depending on the chloride concentration of the feed zone fluid.

An explanation for the greater magnitude of the molarity readings in the even position is that the feed zone inflow had less time to diffuse into the rest of the wellbore fluid. As shown in Figure 4-73, the feed zone jet was more concentrated in the even position (image (b)) and diffused to form a more homogeneous solution when it reached the above position (image (a)). Additionally, the greater variation in the readings of the even position can also be explained by this phenomenon. Slight changes to the position of the tool in the even position caused by the force of the feed zone jet likely caused movement of the chloride tool, thus moving the ISE probes. Considering the greater angular variation of the chloride concentration in the wellbore fluid in the even position, the chloride tool's readings were more sensitive to these minor perturbations in angular location when compared to the above position.

The differing voltage and molarity readings produced by the chloride tool at varying vertical positions suggest viability for inferring the feed zone inflow rate using the method discussed in Section 3.1. This is because the changing molarity readings at different depths in the wellbore can be used with Equation (3-3) to quantify a vertical series of chloride concentrations in the wellbore fluid as a result of feed zone inflow.

### ***Dynamic Experiments of Chloride Concentration Relative to Tool Motions***

Dynamic experiments were performed with three feed zone chloride concentrations ( $1 \times 10^{-1}$  mol/L,  $5 \times 10^{-2}$  mol/L, and  $1 \times 10^{-2}$  mol/L) following the updated methodology described in Section 4.2.2.4, which involves a round-trip of Run-in-Hole and Pull-out-of-Hole.

To fully assess the results of varying the feed zone chloride concentration in dynamic experimentation, Figure 4-78, Figure 4-79, Figure 4-80, and Figure 4-81 must be interpreted together. Figure 4-78 and Figure 4-79 display the voltage readings from both ISE probes against their relative depth in the wellbore during both the RIH and POOH motions for the varying feed zone chloride concentrations. Using the linear regressions of the calibration curves in Equations (4-1) and (4-2), Figure 4-80 and Figure 4-81 display the corresponding molarities for these voltages against the relative depth in the wellbore. The rows of plots correspond to the chloride concentration of the feed zone fluid in decreasing order ( $1 \times 10^{-1}$ ,  $5 \times 10^{-2}$ , and  $1 \times 10^{-2}$  mol/L), and the columns correspond to the direction of motion of the chloride tool in the wellbore.

For this project, relative depth is defined as the depth at which the ISE probes are located in the wellbore. Relative depth was chosen to account for the location of the ISE probes in the Chemical Sensor Housing. By specifying the relative depth, the top 6 inches (15.2 cm) and bottom 14 inches (35.6 cm) of the wellbore are excluded from consideration. This is because the ISE probes are located 6 inches (15.2 cm) below the top of the wellbore when the up-tool component contacts the scaffolding of the artificial well system. Additionally, when the chloride tool was at the bottom of the wellbore,

the ISE probes were located 14 inches (35.6 cm) above the flow diffuser. Consequently, the ISE probes only took voltage readings corresponding to 54 inches (137.2 cm) of the height of the wellbore during a dynamic experiment. This is the reason why the y-axes have a range of 0 to 54 inches (0 to 137.2 cm).

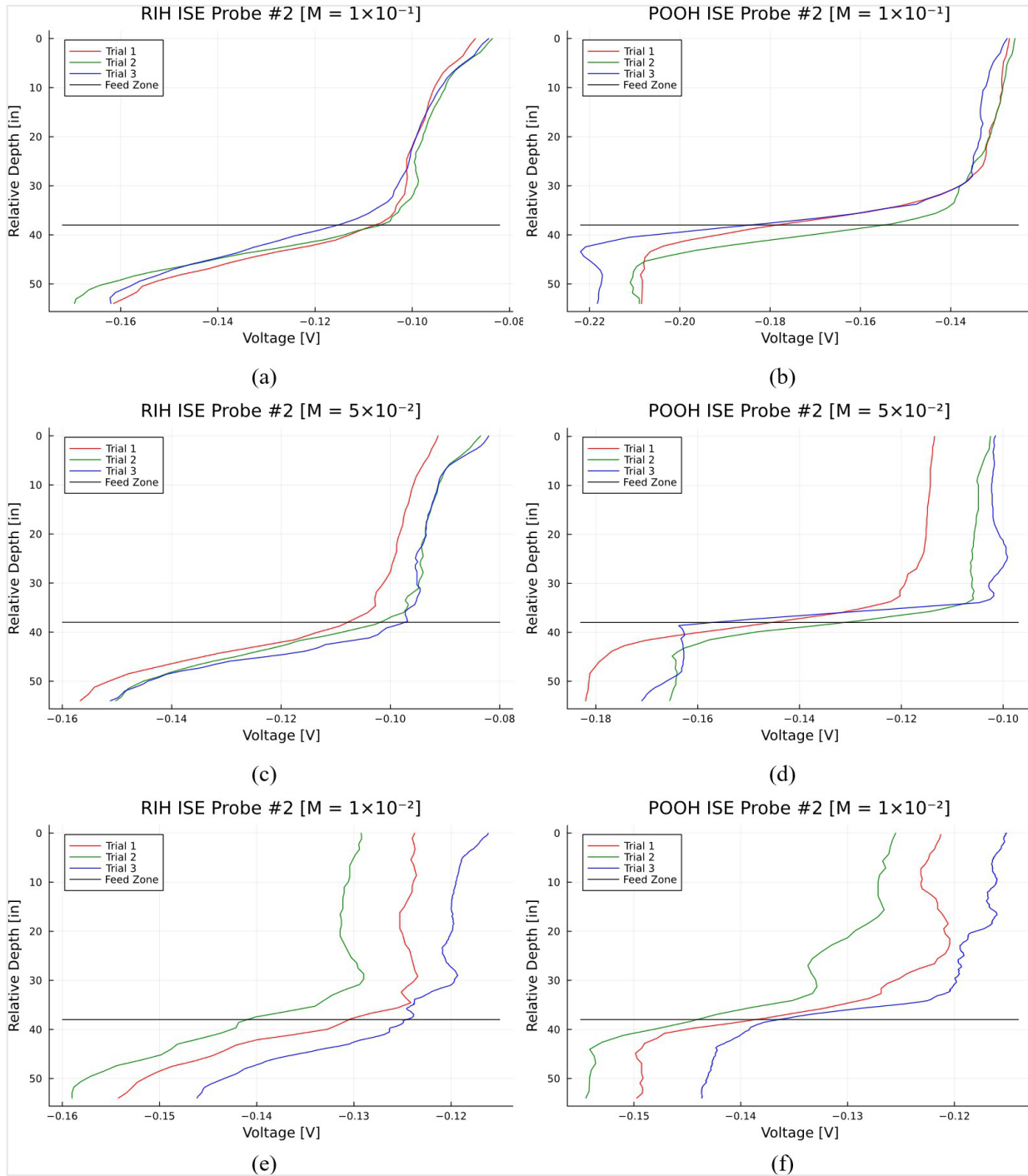


**Figure 4-78:** Voltage vs. Depth for ISE probe #2 in the RIH and POOH directions for feed zone fluids with chloride concentrations of (a and b)  $1 \times 10^{-1}$  mol/L, (c and d)  $5 \times 10^{-2}$  mol/L, and (e and f)  $1 \times 10^{-2}$  mol/L.

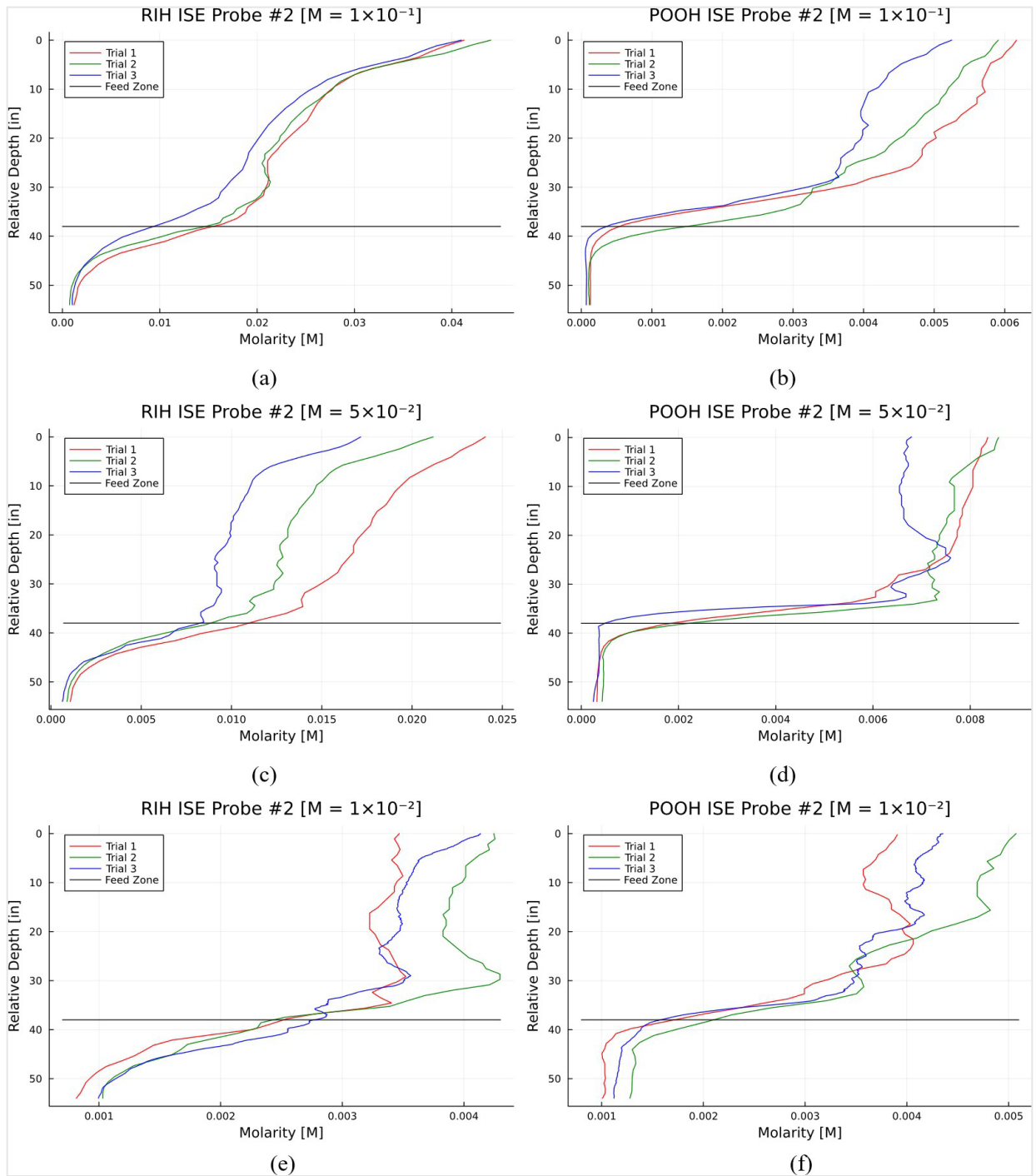


**Figure 4-79:** Voltage vs. Depth for ISE probe #3 in the RIH and POOH directions for feed zone fluids with chloride concentrations of (a and b)  $1 \times 10^{-1}$  mol/L, (c and d)  $5 \times 10^{-2}$  mol/L, and (e and f)  $1 \times 10^{-2}$  mol/L.

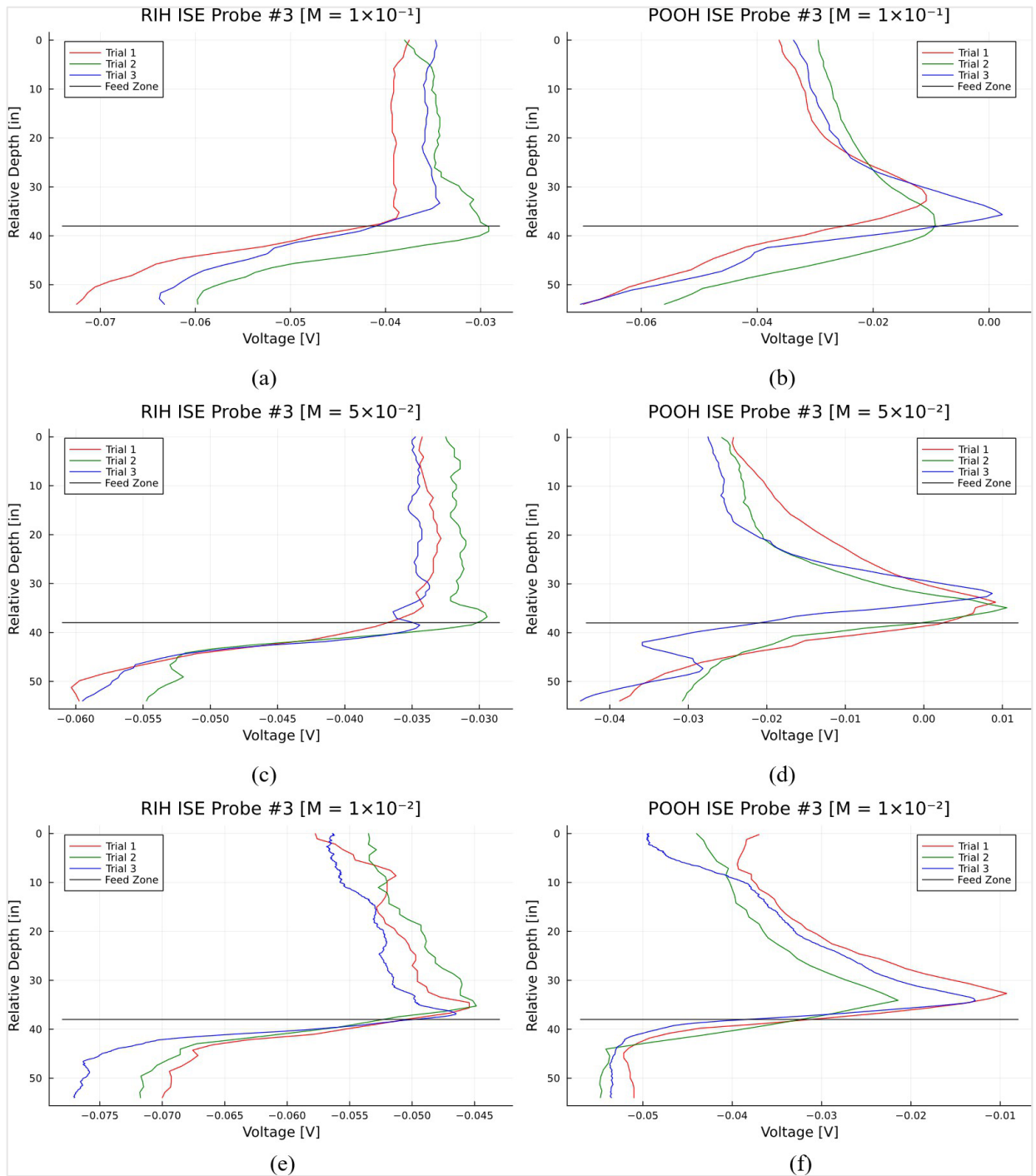


**Figure 4-80:** Molarity vs. Depth for ISE probe #2 in the RIH and POOH directions for feed zone fluids with chloride concentrations of (a and b)  $1 \times 10^{-1}$  mol/L, (c and d)  $5 \times 10^{-2}$  mol/L, and (e and f)  $1 \times 10^{-2}$  mol/L.

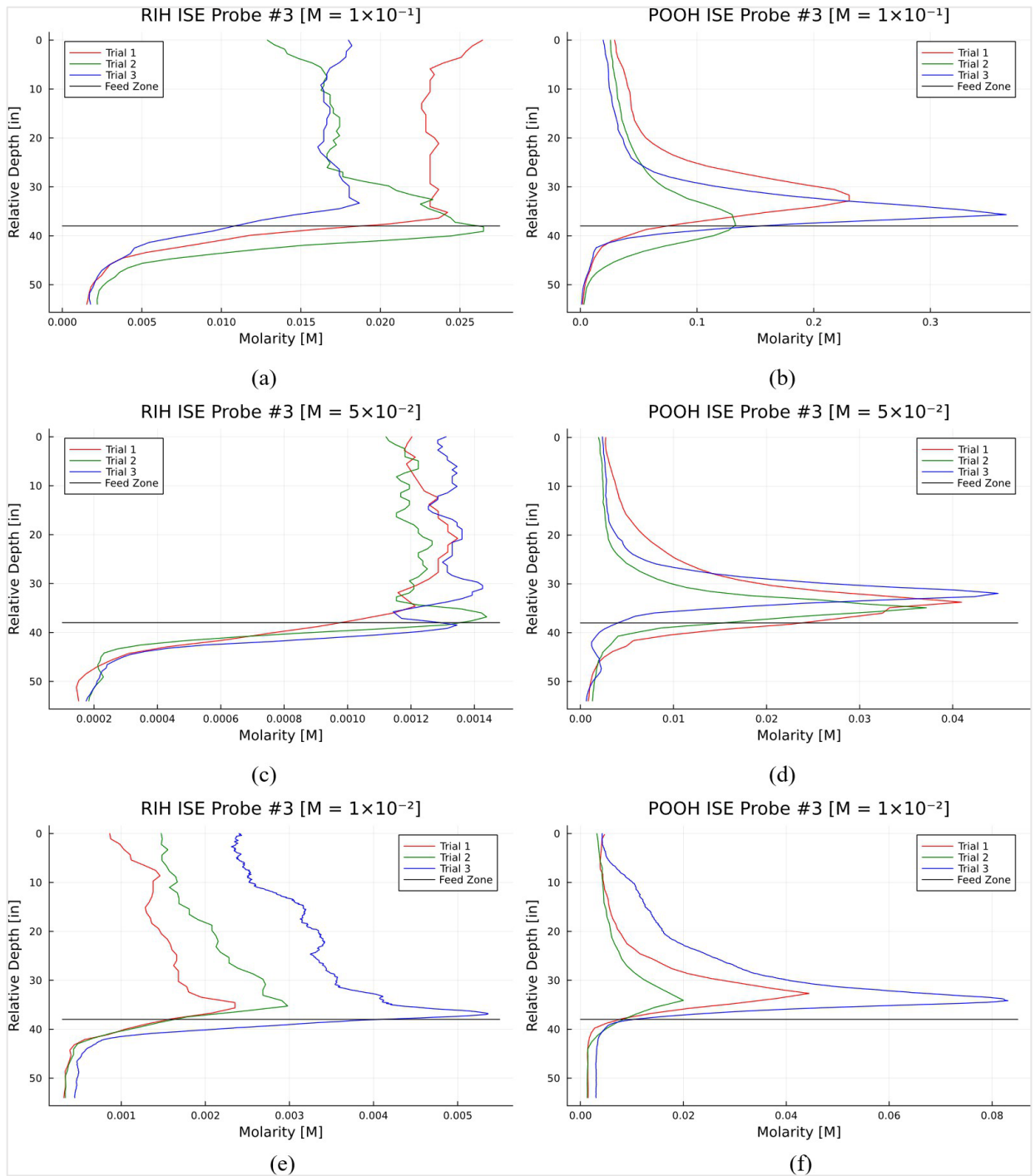


**Figure 4-81:** Molarity vs. Depth for ISE probe #3 in the RIH and POOH directions for feed zone fluids with chloride concentrations of (a and b)  $1 \times 10^{-1}$  mol/L, (c and d)  $5 \times 10^{-2}$  mol/L, and (e and f)  $1 \times 10^{-2}$  mol/L.

Using Equation (3-3), the mass inflow rate  $m_{in}$  for a single feed zone was estimated using the molarity vs. depth plots in Figure 4-80 and Figure 4-81. To determine the chloride concentrations above the feed zone  $Cl_{above}$ , at the feed zone  $Cl_{in}$ , and below the feed zone  $Cl_{below}$ , the mean concentration of the top 13 inches (33.0 cm) of relative depth, the maximum concentration in the middle 17 inches (43.2

cm) of relative depth, and the mean concentration of the bottom 9 inches (22.9 cm) of relative depth were used respectively.

These concentration values and the calculated feed zone mass inflow rate are provided in

Table 4-10. Note that the value of 0.880 kg/s was used for the mass flow rate above the feed zone  $\dot{m}_{above}$  as it was calculated in Section 4.2.2.1. Additionally, the value of 0.115 kg/s was calculated as the actual feed zone mass inflow rate. The column for mass inflow rate  $\dot{m}_{in}$  in

Table 4-10 is color-coded to visually highlight which experimental trials have the closest calculated feed zone rate to the value of 0.115 kg/s. The color green corresponds to the closest values, and the red corresponds to the farthest values.

**Table 4-10:** Chloride concentrations and calculated feed zone inflow rates for the various scenarios at different chloride concentrations of the feed zone fluid

Scenario	Trial #	ISE Probe	Feed Zone Chloride Concentration	$C_{labove}$ (mol/L)	$C_{lin}$ (mol/L)	$C_{lbelow}$ (mol/L)	$\dot{m}_{in}$ (kg/s)
RIH	1	#2	$1 \times 10^{-1}$ mol/L	0.0329	0.0251	0.0023	1.1790
RIH	2	#2	$1 \times 10^{-1}$ mol/L	0.0333	0.0235	0.0014	1.2734
RIH	3	#2	$1 \times 10^{-1}$ mol/L	0.0309	0.0212	0.0016	1.3170
POOH	1	#2	$1 \times 10^{-1}$ mol/L	0.0058	0.0050	0.0001	1.0174
POOH	2	#2	$1 \times 10^{-1}$ mol/L	0.0054	0.0046	0.0001	1.0300
POOH	3	#2	$1 \times 10^{-1}$ mol/L	0.0044	0.0040	0.0001	0.9824
RIH	1	#3	$1 \times 10^{-1}$ mol/L	0.0241	0.0242	0.0023	0.8760
RIH	2	#3	$1 \times 10^{-1}$ mol/L	0.0155	0.0239	0.0034	0.5209
RIH	3	#3	$1 \times 10^{-1}$ mol/L	0.0171	0.0187	0.0023	0.7943
POOH	1	#3	$1 \times 10^{-1}$ mol/L	0.0372	0.2305	0.0043	0.1278
POOH	2	#3	$1 \times 10^{-1}$ mol/L	0.0293	0.1315	0.0084	0.1494
POOH	3	#3	$1 \times 10^{-1}$ mol/L	0.0241	0.3652	0.0037	0.0496
RIH	1	#2	$5 \times 10^{-2}$ mol/L	0.0211	0.0178	0.0019	1.0627
RIH	2	#2	$5 \times 10^{-2}$ mol/L	0.0169	0.0133	0.0015	1.1471
RIH	3	#2	$5 \times 10^{-2}$ mol/L	0.0130	0.0100	0.0012	1.1841
POOH	1	#2	$5 \times 10^{-2}$ mol/L	0.0081	0.0077	0.0003	0.9228
POOH	2	#2	$5 \times 10^{-2}$ mol/L	0.0080	0.0075	0.0004	0.9425
POOH	3	#2	$5 \times 10^{-2}$ mol/L	0.0066	0.0076	0.0003	0.7645
RIH	1	#3	$5 \times 10^{-2}$ mol/L	0.0012	0.0013	0.0002	0.7783
RIH	2	#3	$5 \times 10^{-2}$ mol/L	0.0012	0.0014	0.0002	0.7419
RIH	3	#3	$5 \times 10^{-2}$ mol/L	0.0013	0.0014	0.0002	0.7985
POOH	1	#3	$5 \times 10^{-2}$ mol/L	0.0035	0.0410	0.0012	0.0497
POOH	2	#3	$5 \times 10^{-2}$ mol/L	0.0023	0.0372	0.0016	0.0183
POOH	3	#3	$5 \times 10^{-2}$ mol/L	0.0026	0.0449	0.0014	0.0248
RIH	1	#2	$1 \times 10^{-2}$ mol/L	0.0035	0.0035	0.0010	0.8549

RIH	2	#2	$1 \times 10^{-2}$ mol/L	0.0041	0.0043	0.0013	0.8171
RIH	3	#2	$1 \times 10^{-2}$ mol/L	0.0037	0.0036	0.0012	0.9244
POOH	1	#2	$1 \times 10^{-2}$ mol/L	0.0037	0.0041	0.0010	0.7800
POOH	2	#2	$1 \times 10^{-2}$ mol/L	0.0048	0.0045	0.0013	0.9792
POOH	3	#2	$1 \times 10^{-2}$ mol/L	0.0041	0.0041	0.0012	0.8984
RIH	1	#3	$1 \times 10^{-2}$ mol/L	0.0012	0.0024	0.0004	0.3676
RIH	2	#3	$1 \times 10^{-2}$ mol/L	0.0016	0.0030	0.0004	0.3990
RIH	3	#3	$1 \times 10^{-2}$ mol/L	0.0025	0.0048	0.0005	0.4133
POOH	1	#3	$1 \times 10^{-2}$ mol/L	0.0044	0.0444	0.0015	0.0610
POOH	2	#3	$1 \times 10^{-2}$ mol/L	0.0040	0.0200	0.0014	0.1243
POOH	3	#3	$1 \times 10^{-2}$ mol/L	0.0074	0.0831	0.0030	0.0475

To summarize

Table 4-10, the inferred flow rates of the three individual trials of each scenario were averaged. These values and their percentage error from the actual feed zone inflow rate of 0.115 kg/s are provided in Table 4-11.

**Table 4-11:** Average inferred feed zone inflow rate and percentage error for the various scenarios at different feed zone chloride concentrations

Feed Zone Chloride Concentration	Scenario	ISE Probe	Average Inferred Flow Rate (kg/s)	Percentage Error
$1 \times 10^{-1}$ mol/L	RIH	#2	1.256	993%
$1 \times 10^{-1}$ mol/L	POOH	#2	1.010	778%
$1 \times 10^{-1}$ mol/L	RIH	#3	0.730	535%
$1 \times 10^{-1}$ mol/L	POOH	#3	0.109	-5%
$5 \times 10^{-2}$ mol/L	RIH	#2	1.131	884%
$5 \times 10^{-2}$ mol/L	POOH	#2	0.877	662%
$5 \times 10^{-2}$ mol/L	RIH	#3	0.773	572%
$5 \times 10^{-2}$ mol/L	POOH	#3	0.031	-73%
$1 \times 10^{-2}$ mol/L	RIH	#2	0.866	653%
$1 \times 10^{-2}$ mol/L	POOH	#2	0.886	670%
$1 \times 10^{-2}$ mol/L	RIH	#3	0.393	242%
$1 \times 10^{-2}$ mol/L	POOH	#3	0.078	-33%

#### 4.2.2.6 Analysis of the Dynamic Experiment Results

As shown in the experiment results, the ability to estimate the feed zone inflow rate differs significantly across the various experimental scenarios. Specifically, there are clear relationships between the ability to infer the feed zone inflow rate and the direction of tool motion, the chloride concentration of the feed zone fluid, and the specific ISE probe.

Firstly, the direction of motion of the chloride tool appears to be the largest determining factor for the performance at estimating the feed zone inflow rate. Specifically, the POOH direction had significantly better performance than the RIH. The likely explanation for this behavior is the relative chloride concentration distribution within the wellbore. When moving in the RIH direction, the ISE probes experience gradual changes to the chloride concentration of its surrounding fluid until they pass through the feed zone jet. In contrast, when moving in the POOH direction, the ISE probes begin in fresh water and are suddenly hit by the feed zone jet at a high chloride concentration. As such, the dramatic spike in chloride concentration experienced when crossing the feed zone jet in the POOH direction provided the best signal for inferring the feed zone inflow rate. However, this behavior may not be representative of a geothermal well because most of the wellbore fluid may have a chloride concentration greater than fresh tap water.

Another observation is that ISE probe #3 provided the most accurate estimations for the feed zone inflow rate compared to ISE probe #2, especially in the POOH direction. This is despite ISE probe #3 having less precision in measuring fluid chloride concentrations, as determined in the static experiments. Visually, these estimations are associated with the spiked molarity plots shown in plots (b), (d), and (f) of Figure 4-81. In contrast, the molarity plots of ISE probe #3 in the RIH direction exhibit a dogleg shape, and the molarity plots of ISE probe #2 in both the RIH and POOH directions exhibit a sigmoid shape.

The sigmoid shape of ISE probe #2 suggests that it responded to gradual changes in chloride concentration above the feed zone. In contrast, the straight nature of the RIH molarity curve of ISE probe #3 suggests that it responded to roughly constant chloride concentrations before reaching the feed zone. However, the RIH and POOH molarity plots of ISE probe #2 and the RIH plots of ISE probe #3 all show distinct changes in chloride concentration with an inflection point located at the feed zone depth. As such, despite being marginally useful for estimating the feed zone inflow rate, the presence of an inflection point at similar depths in all of the trials suggests that the tool is useful for identifying the location of a feed zone.

One possible explanation for the differing behavior of the ISE probes is their different locations in the Chemical Sensor Housing, as shown in Figure 4-89. For these experiments, the feed zone jet was normal to Space a, corresponding to a 0° rotation. As such, it is possible that ISE probe #2 was blocked from fully sensing the feed zone jet, resulting in its different behavior and less accurate feed zone inflow rate estimations than ISE probe #3. To address this possibility, Section 4.2.2.10 investigates the effects of the angular location of the ISE probes relative to the feed zone jet.

Consistent with the static experiments, the molarity readings recorded by ISE probe #2 during the RIH motion were approximately 40% of the actual chloride concentration in the feed zone fluid. In contrast, the molarity readings for ISE probe #2 in the POOH were significantly lower than the actual chloride concentration in the feed zone fluid. Of note, the difference between the measured chloride concentration and the actual chloride concentration was greatest for the greater feed zone fluid chloride concentrations. This behavior suggests that absolute measurements of the chloride concentration in a

geothermal well should be assessed in the RIH direction, and relative measurements should be assessed in the POOH direction. In contrast, ISE probe #3 underestimated the chloride molarity in the RIH direction and generally overestimated the chloride molarity in the POOH direction. However, as discussed in the static experiment results, ISE probe #3 was shown not to reliably determine the chloride concentration of its surrounding fluid.

Of note, the changes in the voltage and molarity plots associated with the feed zone consistently occurred above the actual depth of the feed zone. For example, the spikes in POOH plots of ISE probe #3 were approximately 5 inches (12.7 cm) above the actual feed zone location. One explanation for this phenomenon is the inconsistent velocities of the chloride tool in the wellbore, as further discussed in the 'Experimental Error' section. An additional explanation for the lower depth of the feed zone responses is that the flow in the wellbore pushed the jet of the feed zone upwards, as shown in Figure 4-82. This would be responsible for the higher location of the feed zone response, especially at lower feed zone inflow rates. An investigation into this possibility is discussed in Section 4.2.2.7.

Another observation is that more noise appears when the chloride tool is above the feed zone jet, especially during the RIH motion. This behavior is likely caused by the fluid dynamics in the wellbore fluid preventing a homogenous distribution of chloride. Until sufficient mixing of the feed zone fluid in the wellbore fluid occurs, noisy measurements by ISE probes above the feed zone should be expected. Additionally, the increased amount of noise in the RIH direction is likely caused by the opposing direction of the tool's motion and the fluid in the wellbore. The different direction of the velocity vectors of the chloride tool and wellbore fluid likely exacerbates the heterogeneous chloride distribution caused by the fluid dynamics of the system. Additionally, the actuation of the tool in the RIH motion is less smooth. As such, the noisier results in the RIH direction can be explained.

### ***Sources of Experimental Error in the Dynamic Experiments***

The most prominent source of error was the imprecision associated with recording the time needed for the tool to complete the RIH and POOH movements. The experimenters' active engagement reduced their ability to record precise times. To account for this complication, all dynamic experimental trials were video recorded. Using these two sources, the time needed for the motion of the chloride tool was quantified more accurately.

Another source of error inherent to the manual operation of the chloride tool was its inconsistent velocity. During experimental trials, the speed of the tool varied, and the motion was unsmooth. To reduce this issue, zip tie loops were made to hold the shielded electrical cable of the chloride tool to the wellbore scaffolding. This had the benefit of centralizing the shielded electrical cable in the wellbore and smoothening the motion of the tool. However, the inconsistent motion of the tool likely accounted for some of the noise in the results. Of note, the motion of the tool was more even and controlled for the POOH motion. This is because the wellbore fluid lubricated the contact between the shielded electrical cable and the zip tie loops, thus creating a smoother POOH motion. This phenomenon may be one of the reasons why the POOH plots have less noise than the RIH plots.

As mentioned in the experiment methodology (Section 4.2.2.4), the decline in voltage readings following the RIH motion of a dynamic experiment might introduce errors and alter the interpretation of the results. A possible explanation for this behavior is the streaming potential and the buildup of static electricity. Streaming potential is defined as the electric potential that is generated when an electrolyte solution flows. Because the tap water used for the experiments conducted in this project likely contained small concentrations of ions, the flowing fluid and the inner surface of the acrylic wellbore likely resulted in a small streaming potential.

#### 4.2.2.7 Feed Zone Inflow Rate Sensitivity

In geothermal wells, the feed zone inflow rate is not known and will likely change with time. As such, an assessment of varying the feed zone inflow rate on the behavior and response of the chloride tool was warranted.

##### ***Static Experiments on Feed Zone Inflow Rate Sensitivity***

To conduct this sensitivity analysis with static experiments, the chloride tool was held statically in the above position, as shown in Figure 4-69, and a feed zone fluid chloride concentration of  $1 \times 10^{-1}$  mol/L was used. Additionally, the experimental procedure detailed in Table 4-8 was used to compare the results with those of the other static experiments. To vary the feed zone inflow rate, the power adjuster on Submersible Pump 4 was set to medium 6.0 L/min (0.100 kg/s) and low 4.9 L/min (0.083 kg/s) flow rate settings.

Considering that the high 6.9 L/min (0.115 kg/s) flow rate setting was used for all the static experiments presented in Section 4.2.2.5, duplicating these experiments was deemed unnecessary. A time series of images displaying the flow dynamics in the main wellbore at the various feed zone inflow rates are shown in Figure 4-47. The voltage and corresponding molarity time series for each feed zone inflow rate are given in Figure 4-48. Only the results from ISE probe #2 are shown because its behavior provides more accurate measurements of the chloride concentration. Note that the high flow rate results were taken from the (c) plots of Figure 4-74 and Figure 4-75.

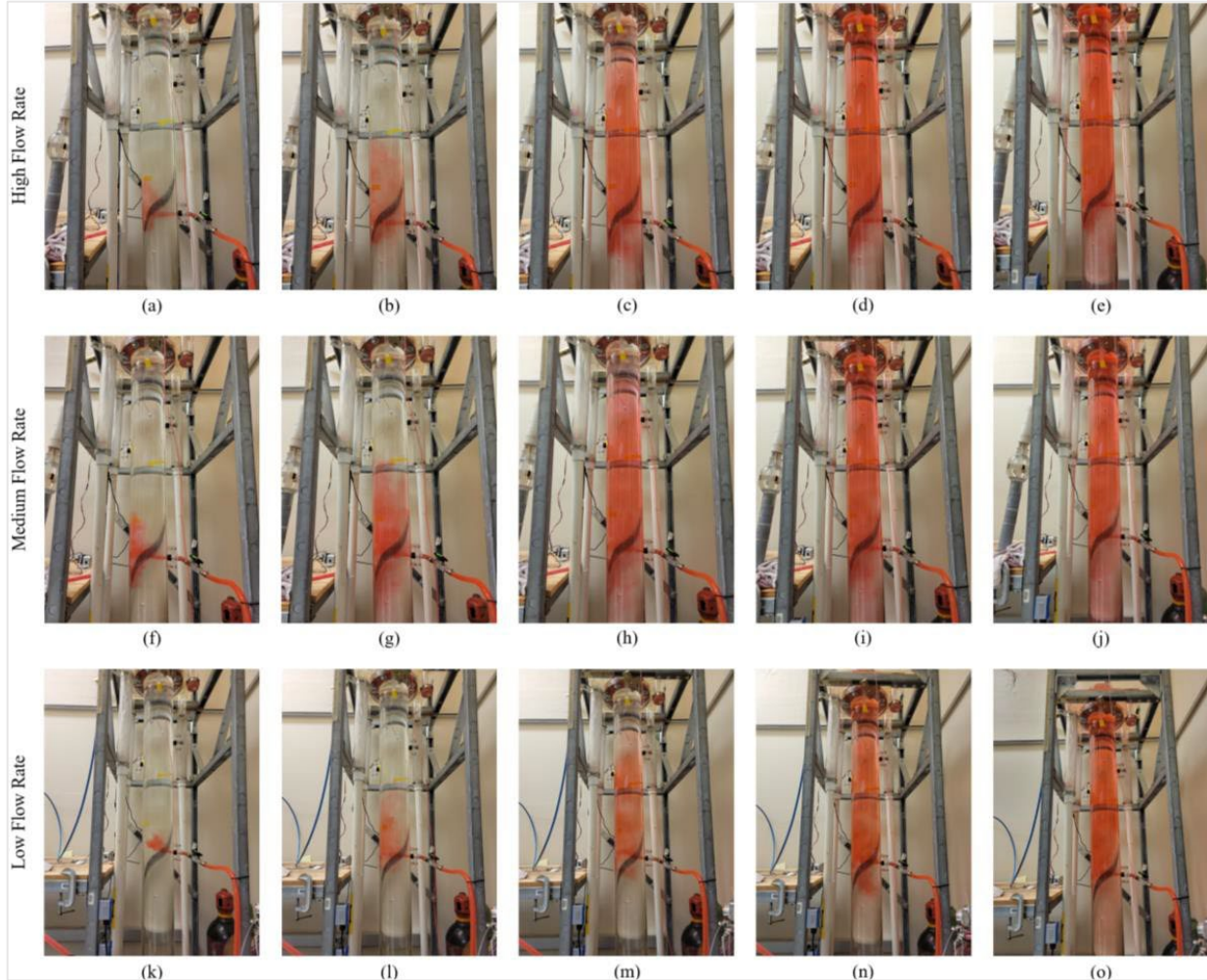


**Figure 4-82:** Flow dynamics in the wellbore at high (0.115 kg/s), medium (0.100 kg/s), and low (0.082 kg/s) feed zone flow rates after (a, f, and k) 2 seconds, (b, g, and l) 5 seconds, (c, h, and m) 15 seconds, (d, i, and n) 30 seconds, and (e, f, and o) 60 seconds.

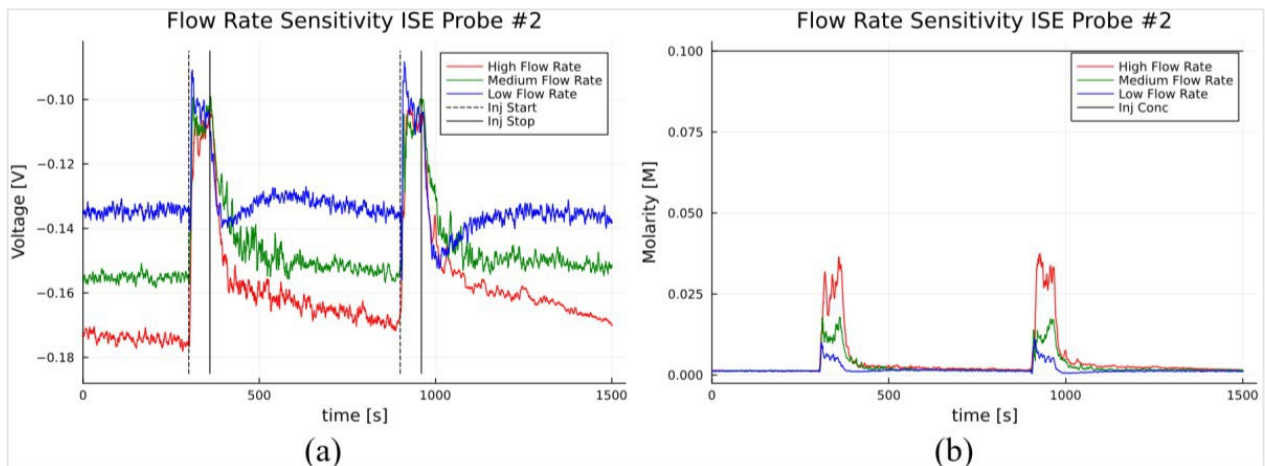


**Figure 4-83:** (a) Voltage and (b) molarity time series of ISE probe #2 at high (0.115 kg/s), medium (0.100 kg/s), and low (0.082 kg/s) feed zone flow rates.

As shown in Figure 4-83, the magnitudes of both the voltage and molarity spikes are directly proportional to the flow rate of the feed zone. This relationship is expected because the higher feed zone inflow rates inject a greater number of chloride ions, resulting in a greater chloride concentration of the wellbore fluid. As such, the ISE probes produced a greater voltage response. To quantify the relationship between the chloride concentration recorded by ISE probe #2 and the feed zone inflow rate, the mean chloride concentration during the two one-minute intervals of feed zone inflow was calculated. These values are provided in Table 4-12.

The coefficient of determination for the data in Table 4-12 is  $R^2 = 0.918$ , suggesting a strong linear relationship between the feed zone inflow rate and the measured chloride concentration. This correlation suggests that the chloride tool can accurately infer feed zone inflow rates when used in a geothermal well.

**Table 4-12:** Relationship between feed zone inflow rate and measured chloride concentration for static experimentation

Feed Zone Inflow Rate (kg/s)	Measured Chloride Concentration (mol/L)
0.115	0.02379
0.100	0.01087
0.082	0.00548

#### 4.2.2.8 Dynamic Experiments on Feed Zone Inflow Rate Sensitivity

The dynamic experiments to investigate inflow rate sensitivity were conducted using chloride concentrations of  $1 \times 10^{-1}$  mol/L. Similar to the static experiments, Submersible Pump 4 was adjusted to both the medium (0.100 kg/s) and low (0.083 kg/s) flow rate settings. For the high (0.115 kg/s) flow rate setting, the dynamic experiment results from the tool motion sensitivity presented in Section 4.2.2.5 were used. For reference, Figure 4-82 displays the flow dynamics in the wellbore for the various feed zone inflow rates using time series images.

The molarity vs. relative depth plots presented in Figure 4-96 and Figure 4-97 were made for these experiments. These figures display the three trials for the RIH and POOH motions for both ISE probes at the varying feed zone inflow rates. Note that the results for the high feed zone inflow rate are the same as those shown in plot (a) and plot (b) of Figure 4-80 and Figure 4-81. The most prominent observation is the clear difference in the behavior of the ISE probes in the RIH and POOH directions. Similar to the static experiment results, the readings from neither ISE probe display a prominent single spike corresponding to the feed zone inflow in the RIH direction. However, in the POOH direction, ISE probe #3 shows a distinct spike when it passes the feed zone. This is likely caused by the relative changes in chloride concentration, as discussed in the static experiment results.

An additional observation is that the molarity spikes of ISE probe #3 in the POOH direction corresponding to the feed zone for the low feed zone inflow rate occurred at a lower depth than the other results in this section. This phenomenon is likely caused by the greater vertical motion of the feed zone jet at the low flow rate, as shown in Figure 4-82. Another explanation for this phenomenon is the inaccurate recording of the times recorded during the experimental procedure. However, this is less likely to be the cause of the higher feed zone molarity spikes.

Another observation is the significant decrease in molarity above the feed zone in the RIH scenario, as shown in Figure 4-96. This behavior is not exhibited to the same extent in any of the results presented in the tool motion analysis in Section 4.2.2.5 or the angular sensitivity in Section 4.2.2.10. The likely explanation for this behavior is that the feed zone jet created an eddy because of the fluid dynamics in the artificial wellbore. This phenomenon, known as a rebound zone, was observed in numerical simulations during Round 1 (see Section 4.1.2.7), which caused fluctuating chloride concentrations above the feed zone. As such, the fluid dynamics within the wellbore provide an explanation for this behavior.

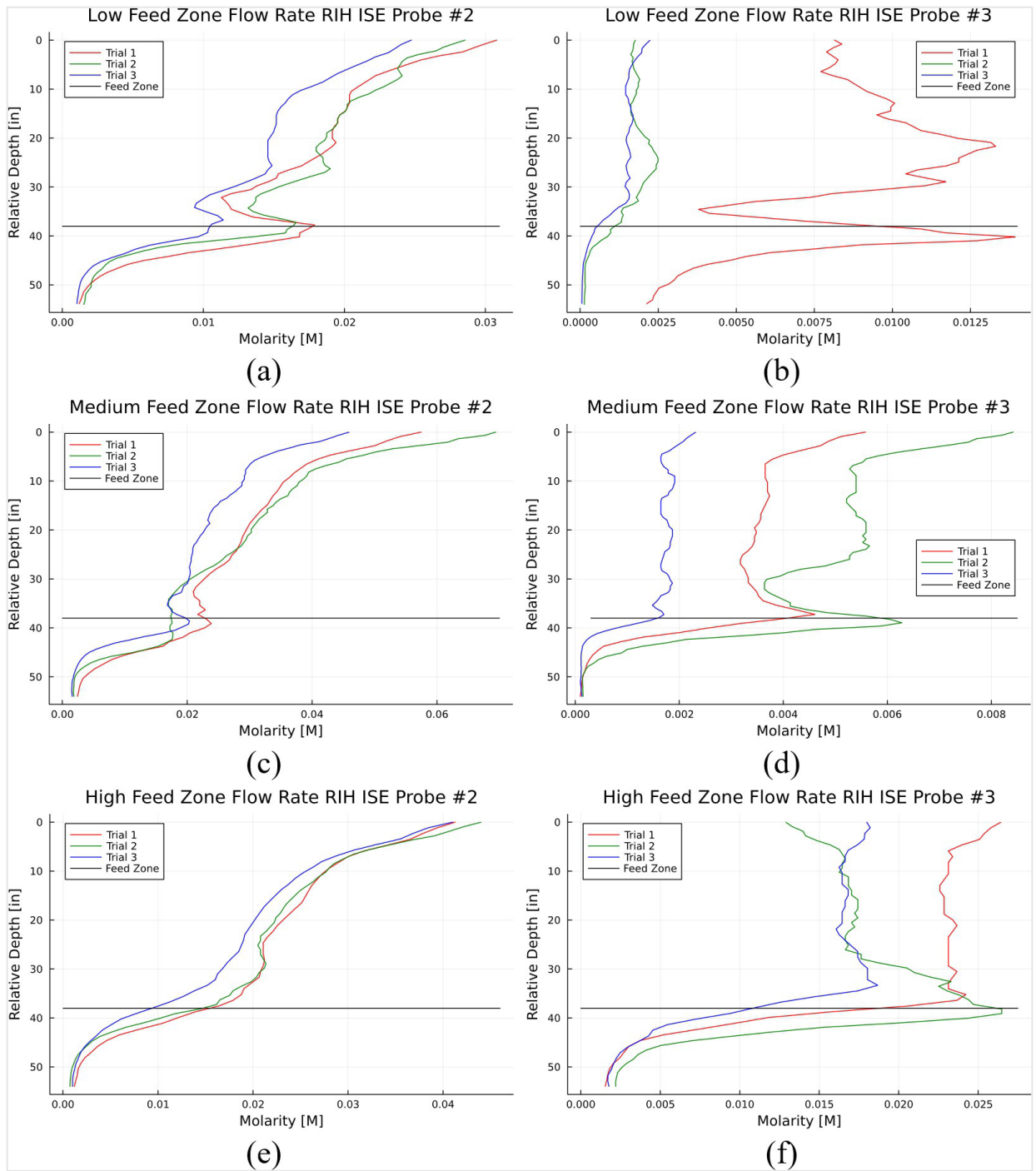


**Figure 4-84:** Molarity vs. Depth for ISE probe #2 and ISE probe #3 in the RIH direction with feed zone inflow rates of (a and b) 0.115 kg/s, (c and d) 0.100 kg/s, and (e and f) 0.082 kg/s.

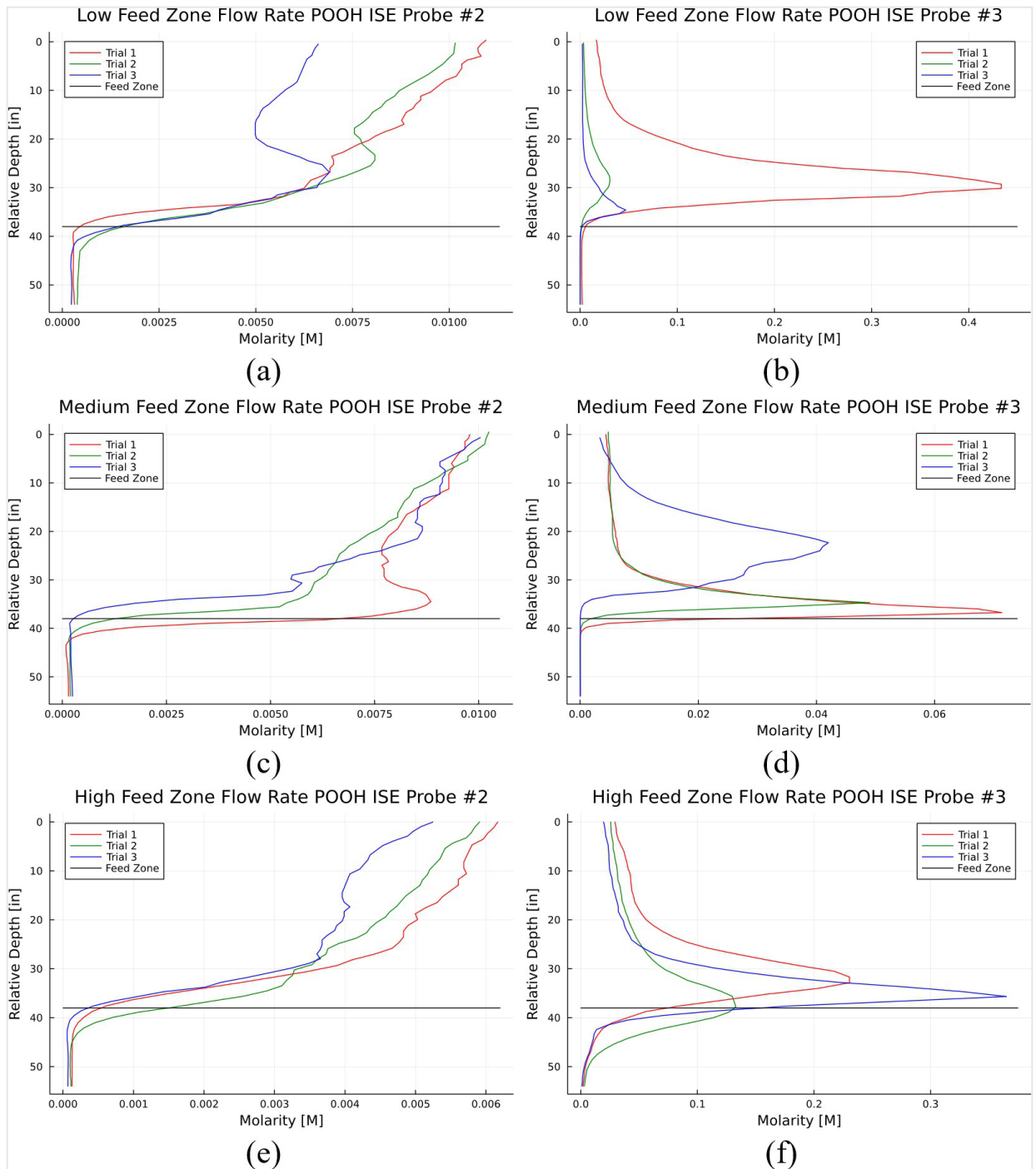


**Figure 4-85:** Molarity vs. Depth for ISE probe #2 and ISE probe #3 in the POOH direction with feed zone inflow rates of (a and b) 0.115 kg/s, (c and d) 0.100 kg/s, and (e and f) 0.082 kg/s.

Using the same method used to analyze the chloride tool motion discussed in Section 4.2.2.5, the mass inflow rate  $\dot{m}_{in}$  for a single feed zone was calculated using the plots in Figure 4-96 and Figure 4-97. The fourth column of Table 4-13 provides the average value of the calculated feed zone inflow rate across the three trials for the scenario specified in the first three columns. Additionally, the table provides the actual flow rates of the corresponding scenario and the percentage error between the actual

and inferred feed zone inflow rates. Note that Conditional Formatting was used to visually present the magnitude of the percentage errors.

Table results show an overestimation of the inferred feed zone inflow rates across all flow rates, scenarios, and ISE probes, except those for ISE probe #3 during the POOH motion. These scenarios provided the most accurate results, similar to the experiments in for tool motion and angular sensitivity (Section 4.2.2.5 and 4.2.2.10, respectively). Of note, the accuracy of the inferred feed zone inflow rates did not significantly vary with the feed zone inflow rates. This behavior holds promise when using the chloride tool for field experiments in which the feed zone inflow rates are not known.

**Table 4-13:** Percentage error between the inferred and actual feed zone inflow rates for dynamic experiments with varying feed zone inflow rates

Flow Rate	Scenario	ISE Probe	Average Inferred Feed Zone Inflow Rate (kg/s)	Actual Feed Zone Inflow Rate (kg/s)	Percentage Error
High	RIH	#2	1.256	0.115	993%
High	RIH	#3	0.730	0.115	535%
High	POOH	#2	1.010	0.115	778%
High	POOH	#3	0.109	0.115	-5%
Medium	RIH	#2	1.301	0.100	1201%
Medium	RIH	#3	0.929	0.100	829%
Medium	POOH	#2	0.974	0.100	874%
Medium	POOH	#3	0.099	0.100	-1%
Low	RIH	#2	1.148	0.082	1305%
Low	RIH	#3	0.658	0.082	705%
Low	POOH	#2	0.948	0.082	1061%
Low	POOH	#3	0.075	0.082	-8%

#### 4.2.2.9 Wellbore Flow Rate Sensitivity

In the experiment setup in the artificial well system, both the feed zone inflow rate and the wellbore flow rate contribute to the overall rate of produced fluid. In addition to investigating the sensitivity of the inflow rate, the sensitivity to the wellbore flow rate was also examined. In geothermal wells, the wellbore flow rate may occur as internal upflow or as flow contribution from lower feed zone(s).

To change the wellbore flow rate, the power adjuster on Submersible Pump 3 was set to either the low (50 W) or high (77 W) power setting. Of note, the medium (64 W) power setting was used for all the other experiments (static and dynamic). As calculated in Section 4.2.2.1, the high, medium, and low power settings for correspond to wellbore mass flow rates of 0.992 kg/s, 0.880 kg/s, and 0.753 kg/s respectively. Assuming a wellbore fluid density of 997 kg/m<sup>3</sup>, the corresponding volumetric flow rates are 0.263 gal/s, 0.233 gal/s, and 0.199 gal/s respectively.

To provide context, a circulation test of well 16A(78)-32 was conducted in July 2023 to assess the recovery efficiency and conductivity at Utah FORGE. After injection at a maximum rate 210 gal/min (3.50 gal/s), the resulting production rate from well 16B(78)- 32 was 7 gal/min (0.117 gal/s) (Xing et al., 2024). As such, all wellbore flow rates tested in the experiments were smaller than those observed during the circulation test at the Utah FORGE site. However, this sensitivity analysis still affords insight into the performance of the chloride tool for varying wellbore flow rate conditions.

Using the same dynamic experiment procedure and only feed zone fluids with chloride concentrations of  $1 \times 10^{-1}$  mol/L, the results in this section can be compared with the other dynamic experiments conducted for this project. The voltage time series corresponding to the three trials of each wellbore flow rate scenario are provided in Figure 4-86. Additionally, the molarity vs. relative depth plots presented in Figure 4-87 and Figure 4-88 were created from the experiments in this section. These figures display the three trails for the RIH and POOH motions of both ISE probes at the varying wellbore flow rates. Note that the results for the medium wellbore flow rate are the same as those shown in plot (a) and plot (b) of Figure 4-80 and Figure 4-81.

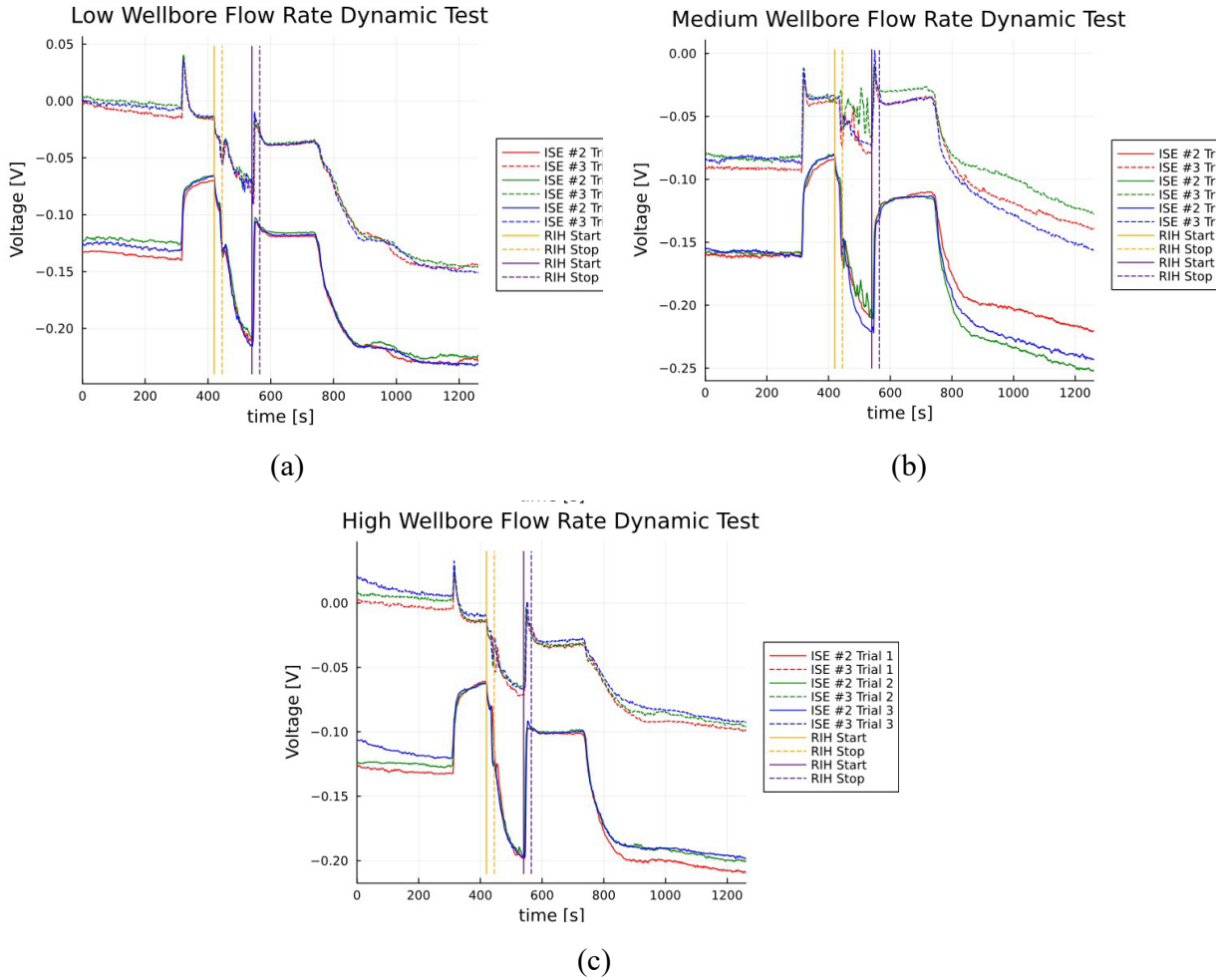


**Figure 4-86:** Concurrent voltage time series of ISE probe #2 and ISE probe #3 with wellbore flow rates of (a) 0.753 kg/s, (b) 0.880 kg/s, and (c) 0.992 kg/s.

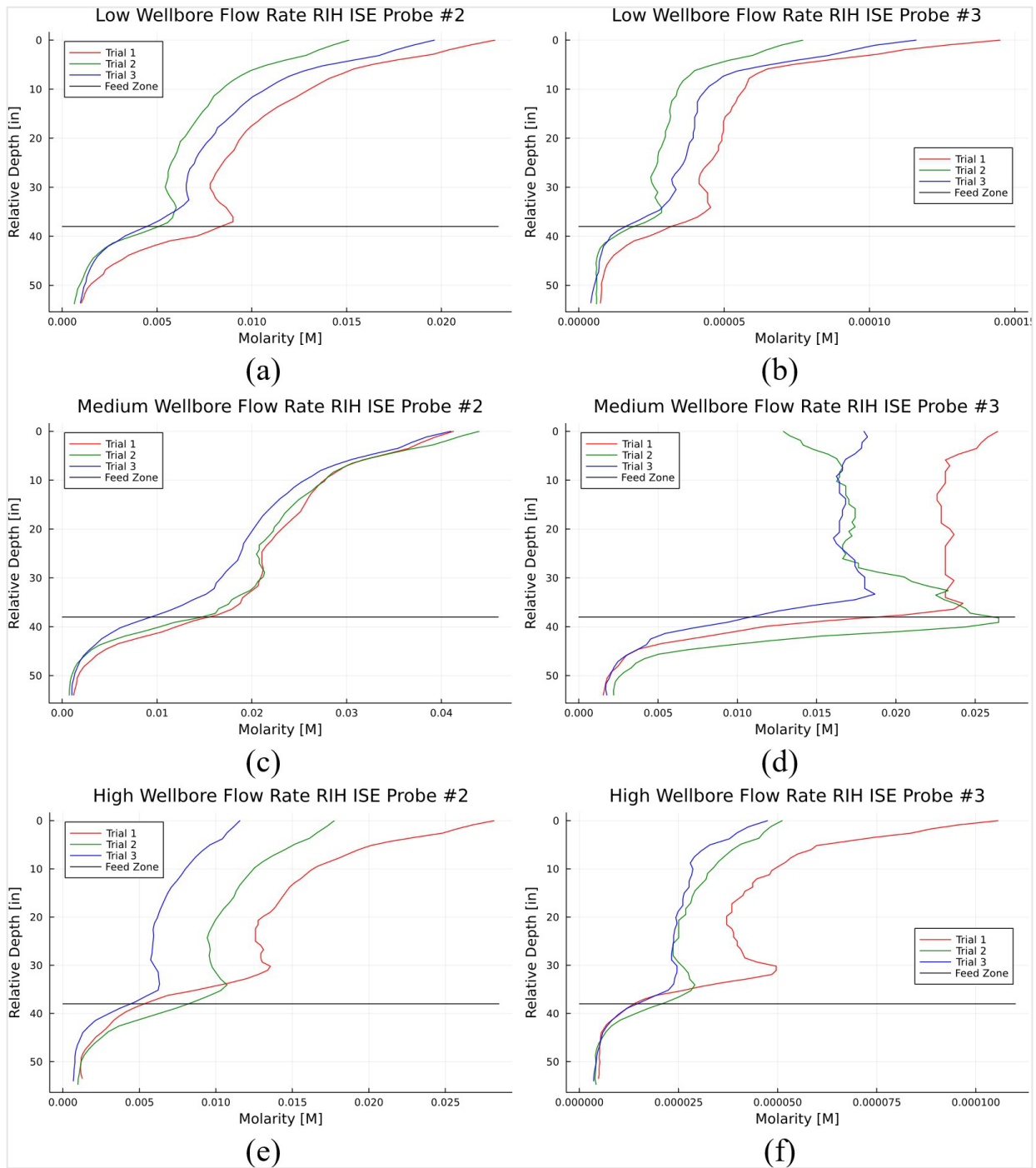


**Figure 4-87:** Molarity vs. Depth for ISE probe #2 and ISE probe #3 in the RIH direction with wellbore flow rates of (a and b) 0.753 kg/s, (c and d) 0.880 kg/s, and (e and f) 0.992 kg/s.

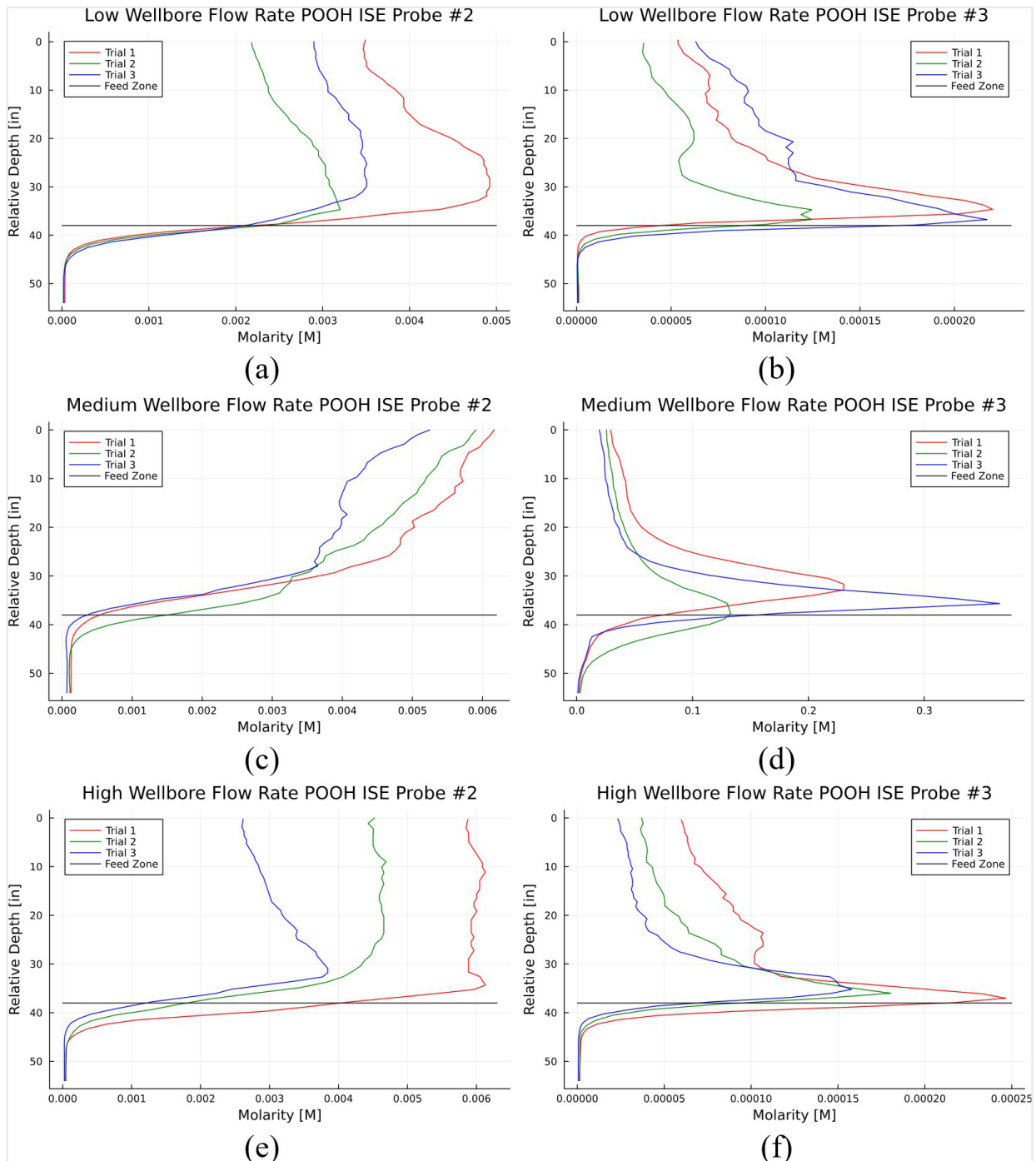


**Figure 4-88:** Molarity vs. Depth for ISE probe #2 and ISE probe #3 in the POOH direction with wellbore flow rates of (a and b) 0.753 kg/s, (c and d) 0.880 kg/s, and (e and f) 0.992 kg/s.

The mass inflow rate  $\dot{m}_{in}$  for a single feed zone were calculated using data shown on Figure 4-87 and Figure 4-88, resulting in Table 4-14. The fourth column provides the feed zone inflow rate averaged across the three trials for the scenario specified in the first three columns. Additionally, the table provides the percentage error between the actual and inferred flow rates and visually presents the magnitude of the percentage errors using a color-coding scheme.

**Table 4-14:** Percentage error between the inferred and actual feed zone inflow rates for dynamic experiments with varying wellbore flow rates

Wellbore Flow Rate	Scenario	ISE Probe	Average Inferred Feed Zone Inflow Rate (kg/s)	Percentage Error
High	RIH	#2	1.447	1159%
High	RIH	#3	1.377	1097%
High	POOH	#2	0.883	668%
High	POOH	#3	0.222	93%
Medium	RIH	#2	1.256	993%
Medium	RIH	#3	0.730	535%
Medium	POOH	#2	1.010	778%
Medium	POOH	#3	0.109	-5%
Low	RIH	#2	1.266	1000%
Low	RIH	#3	1.288	1020%
Low	POOH	#2	0.584	408%
Low	POOH	#3	0.251	118%

As presented in Table 4-14, there is a clear difference in the accuracy of the inferred feed zone inflow rates for the various wellbore flow rates. Specifically, the scenarios with the high and low wellbore flow rates both significantly overestimated the feed zone inflow rate. In contrast, the medium wellbore flow rate produced an inferred feed zone inflow rate that was remarkably similar to the actual flow rate of 0.115 kg/s.

The explanation for this behavior is seen in Figure 4-86. Specifically, the baseline voltages for ISE probe #3 during the first five minutes of freshwater flow was between 0.00 V and 0.02 V for the low and high wellbore flow rate trials. In contrast, ISE probe #3 had a baseline voltage reading of approximately -0.08 V for the medium wellbore flow rate trials. This difference caused the voltage readings of ISE probe #3 to return to the baseline voltage after beginning the feed zone inflow. Consequently, when the RIH motion began, the voltage readings decreased significantly. Then, when the POOH motion began, the voltage readings were significantly smaller in magnitude.

This inconsistent behavior was likely caused by the gradual shift in the baseline voltage readings of the ISE probes, as discussed in Section 4.2.2.4. The high and low wellbore flow rate trials were conducted almost four weeks after the medium wellbore flow rate trials. During this time, the baseline response of ISE probe #3 had changed significantly, resulting in worse performance at measuring the chloride concentration in the artificial well.

Despite the inconsistent behavior of ISE probe #3, the molarity vs. depth plots for all the wellbore flow rate scenarios exhibited similar shapes. However, there were some differences, which resulted in the high and low wellbore flow rate scenarios significantly overestimating the feed zone inflow rate. Specifically, when compared with the results of the medium flow rate, the molarity readings corresponding to the top third of the wellbore contained more noise for the low and high wellbore flow rate settings. Additionally, these sections were proportionally higher in relative value for the POOH direction.

Another difference was that the absolute value of the POOH molarity readings for ISE probe #3 were four orders of magnitude lower. Of note, this discrepancy in molarity is a result of the shifted baseline

voltage. At voltages corresponding to lower chloride concentrations, the ISE probes become more sensitive because of the logarithmic relationship between the voltage and the ion concentration described by the Nernst Equation as shown in Equation (3-13). A consequence of this increased sensitivity was a reduced accuracy at inferring the molarity of the wellbore fluid. This resulted in increased variability between trials in both the RIH and POOH directions for both ISE probes. As a consequence of the increased variability and slightly different behavior, the chloride tool was less accurate in inferring the feed zone inflow rate for the high and low wellbore flow rate scenarios.

#### 4.2.2.10 Angular Sensitivity

As discussed in the tool motion experiments (Section 4.2.2.5), a possible explanation for the differing behavior of the ISE probes during dynamic experimentation is their different locations in the Chemical Sensor Housing relative to the feed zone injection port. To assess the impact of the angular positions of the ISE probes relative to the feed zone jet, the angular position of the chloride tool in the wellbore was varied. By rotating the chloride tool about the shielded electrical cable, the angular position of the ISE probes was changed without affecting the radial position of the chloride tool in the wellbore.

Figure 4-89 shows the labeled tool with the names of the angular features. The reference electrode, ISE probe #2, and ISE probe #3 are labeled as 1, 2, and 3, respectively. The prominent angular features were named to characterize the angular location of the feed zone jet relative to the chloride tool. The chemical tool has alternating longitudinal bands of pillars and spaces.

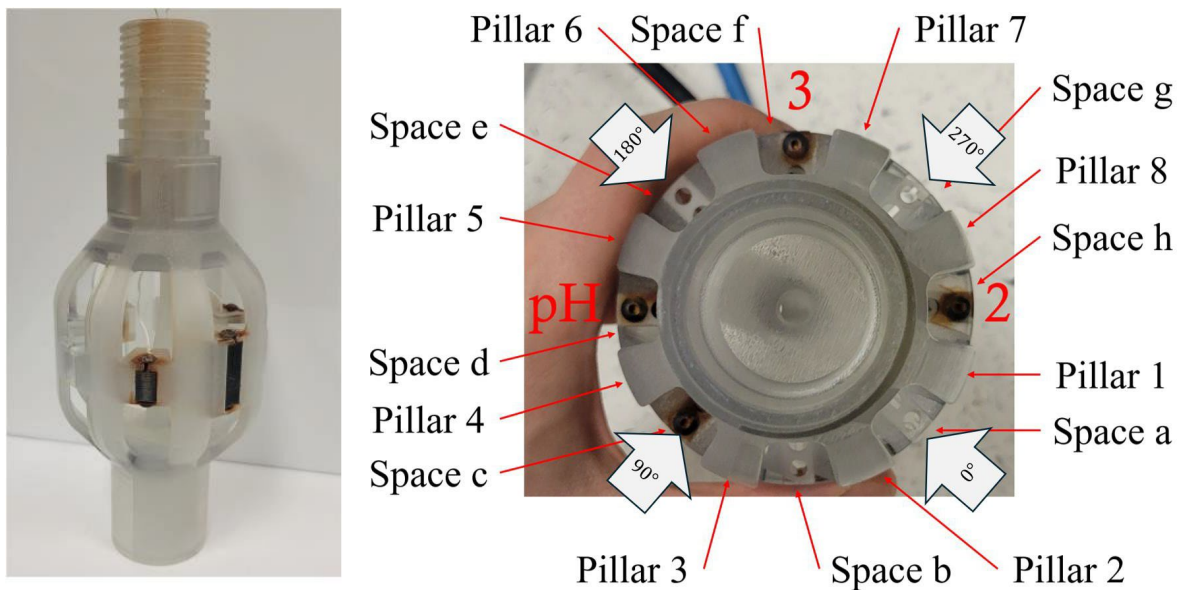


**Figure 4-89:** Chloride Sensor Housing with the labeled pillars and spaces. The varying directions of the feed zone jet tested for the angular sensitivity are denoted as arrows.

All the other experiments conducted have the feed zone jet position normal to Space a, which is a rotation of 0°. For testing the angular sensitivity, three additional sets of dynamic experiments were conducted corresponding to clockwise rotations of 90°, 180°, and 270°. These rotations resulted in the feed zone jet being normal to Space c, Space e, and Space g, respectively. The feed zone fluid for these experiments had a chloride concentration of  $1 \times 10^{-1}$  mol/L and was injected at a flow rate of 0.115 kg/s.

The molarity vs. relative depth plots for the various angular positions of the chloride tool are provided in Figure 4-90 and Figure 4-91 for the RIH and POOH motions, respectively. The mass inflow rate  $\dot{m}_{in}$  for a single feed zone was calculated and shown in Table 4-15 and the average value of the inferred feed zone inflow rate across each scenario is provided in the fourth column. Additionally, the percentage error between the actual and inferred flow rates is shown in the fifth column with Conditional Formatting coloring.

**Table 4-15:** Percentage error for the average inferred feed zone inflow rates for dynamic experiments with varying angular rotations of the chloride tool

Scenario	Angular Position	ISE Probe	Average Inferred Feed Zone Inflow Rate (kg/s)	Percentage Error
RIH	Space a	#2	1.256	993%
RIH	Space a	#3	0.730	535%
POOH	Space a	#2	1.010	778%
POOH	Space a	#3	0.109	-5.3%
RIH	Space c	#2	1.369	1091%
RIH	Space c	#3	1.218	959%
POOH	Space c	#2	0.721	527%
POOH	Space c	#3	0.041	-64%
RIH	Space e	#2	1.451	1162%
RIH	Space e	#3	1.529	1229%
POOH	Space e	#2	0.678	490%
POOH	Space e	#3	0.109	-4.9%
RIH	Space g	#2	1.426	1140%
RIH	Space g	#3	1.418	1133%
POOH	Space g	#2	0.582	406%
POOH	Space g	#3	0.088	-23%

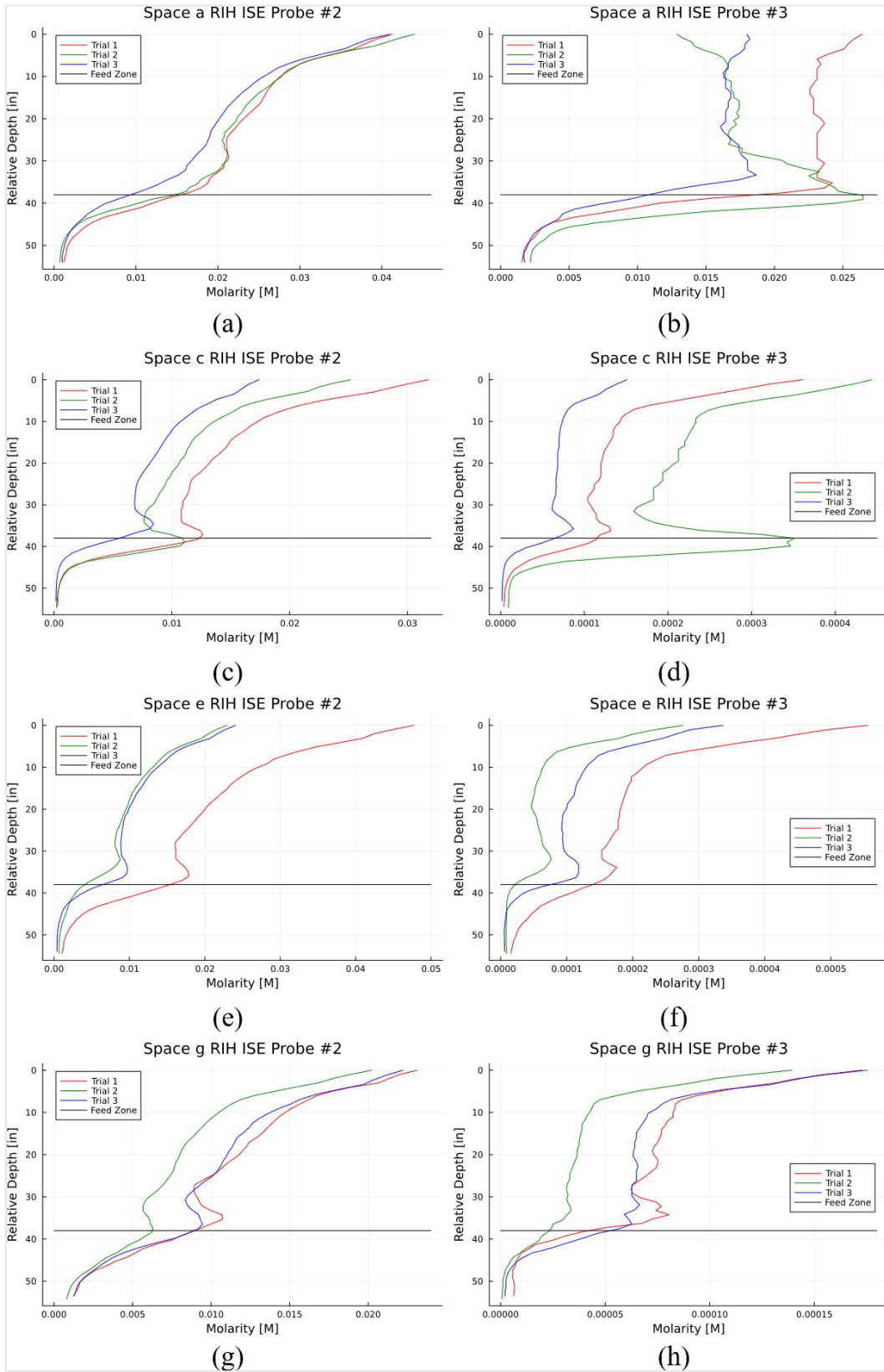


**Figure 4-90:** Molarity vs. Depth for ISE probe #2 and ISE probe #3 in the RIH motion for angular rotations of (a and b) 0°, (c and d) 90°, (e and f) 180°, and (g and h) 270°.

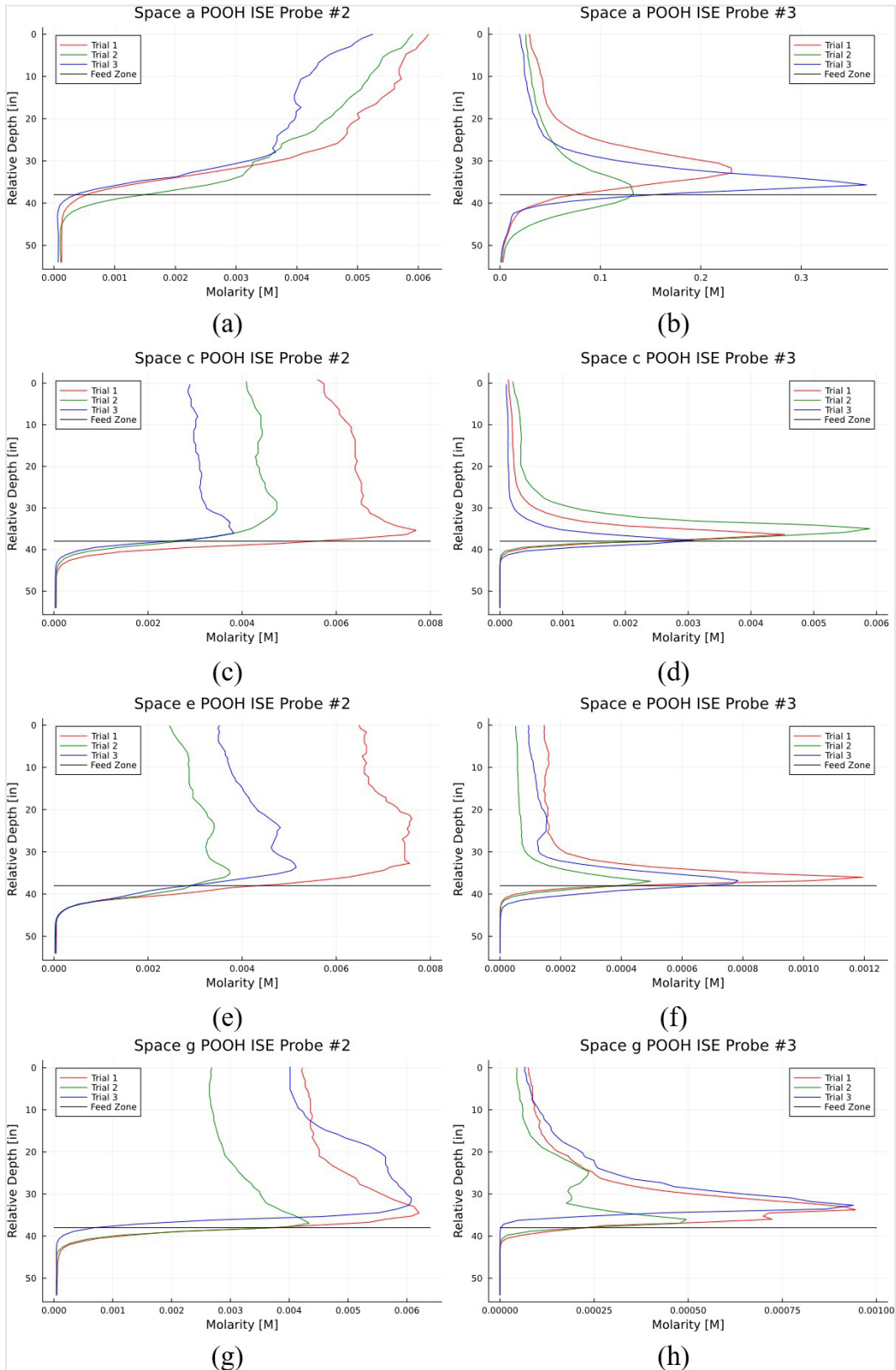


**Figure 4-91:** Molarity vs. Depth for ISE probe #2 and ISE probe #3 in the POOH motion for angular rotations of (a and b) 0°, (c and d) 90°, (e and f) 180°, and (g and h) 270°.

In Round 1 experiments, it was found that locating a feed zone and determining the chloride concentration of its fluid was more challenging when the ISE probes were located a greater distance from the injection point. This conclusion was determined using the tubular design of the chloride tool which featured one ISE probe without any obstructions. The angular sensitivity results with the updated tool and housing unit show that the most accurate inference of the feed zone inflow rate occurs when the feed zone port is normal to Spaces a and e (rotations of 0° and 180°). Both of these scenarios resulted in almost identical feed zone inflow rates, which had a remarkably small percentage error of approximately 5%. In contrast, when the feed zone jet was normal to Space c (rotation of 90°), the largest absolute magnitude percentage error of 64% occurred. In the middle, the feed zone jet being normal to Space g (rotation of 270°) resulted in an underestimation of the feed zone inflow rate of 23%. As such, there is clearly a relationship between the angular orientation of the chloride tool and the ability to accurately infer the feed zone flow rate.

The housing design of the chloride tool features a central pass-through for its electrical cable, which obstructed the ISE probes from sensing the full feed zone jet when it is located between the ISE probes and the feed zone port. This claim is supported by the 64% underestimation of the feed zone inflow rate when the port was normal to Space c. In contrast, when the feed zone jet was perpendicular to the ISE probes (normal to Space a or Space e), the inferred feed zone inflow rates were the most accurate with percentage errors of approximately 5%. For this scenario, it is plausible that the feed zone jet rebounded off of the cable’s pass-through and directly struck the ISE probes. As such, this angular position resulted in chloride concentration measurements that accurately inferred the feed zone inflow rate. Finally, when the feed zone jet was normal to Space g, the ISE probes were able to measure the chloride concentration of the feed zone jet, but this occurred after a greater amount of dilution had occurred, resulting in less accurate chloride concentration measurements for inferring the feed zone inflow rate.

#### 4.2.2.11 Ion Sensitivity

The geothermal brine in the wells at the Utah FORGE project contained multiple additional chemical species besides chloride ions, as shown in Table 4-16. Sensitivity analyses using static and dynamic experiments were performed to assess the effects that these additional ions have on the voltage readings of the chloride tool.

**Table 4-16:** Chemical composition of well samples from Utah FORGE Wells 16A(78)-32 and 16B(78)-32

Date and Time	Location	Chemical Component (mg/L)								
		Na	K	Ca	Mg	B	SiO2	Cl	SO4	HCO3
7/19/2023 20:00	16A(78)-32 Utah FORGE	621	80.2	92.3	4.13	2.07	167	1300	162	105
7/20/2023 7:50	16B(78)-32 Utah FORGE	2871	319	44	0.07	9.05	81	4384	239	383
7/20/2023 15:00	16B(78)-32 Utah FORGE	81	7	109	3.48	0.32	78	122	115	276

### *Static Experiments on Potassium Bromide Sensitivity*

For sensitivity analyses with static experiments, the chloride tool was held statically in the above position, as shown in Figure 4-69. The composition of the feed zone fluid was the only variable that was changed, allowing the results to be compared with those of other static experiments. The first sensitivity analysis involved adding potassium bromide (KBr) to the feed zone fluid. Note that KBr was selected because bromide ions have the same charge and similar properties to chloride ions. Additionally, potassium ions were present in significant concentrations in the Utah FORGE brine.

Two different solutions were used to assess the impact of KBr in the feed zone fluid. One solution had a bromide concentration of  $1 \times 10^{-2}$  mol/L, and the other solution had  $1 \times 10^{-2}$  mol/L concentrations of both bromide and chloride. To provide a comparison for a feed zone fluid with a chloride concentration of  $1 \times 10^{-2}$  mol/L, the results from Section 4.2.2.4 were used. The voltage time series for these three solutions for both ISE probes are provided in Figure 4-92, and the corresponding molarity time series are provided in Figure 4-93.

As shown in plots (a) and (b) of Figure 4-92, voltage spikes corresponding to the feed zone inflow of the bromide solution are observed from both ISE probes. Additionally, these voltage spikes are greater than those in plots (c) and (d) when only chloride was present in the feed zone fluid. This, however, is expected because bromide's hydration energy of  $-335$  kJ/mol is slightly higher than chloride's at  $-363$  kJ/mol (Marcus, 1991). Hydration energy is the energy released when ions are surrounded by water molecules. Both chloride and bromide ions have moderately high hydration energies, meaning that they form strong hydrogen bonds with water molecules. However, the slightly higher hydration energy of bromide causes it to more readily interact with the membrane of the ISE probes. Consequently, bromide ions supplant chloride ions from the membrane, thus creating greater voltage responses which result in interference and less accurate measurements. Other interfering ions with chloride are iodine, thiocyanate, salicylate, bicarbonate, and heparin. As such, the presence of these ions will also cause interference for the ISE probes.

Some concern must be given regarding the magnitude of the bromide voltage spikes. As shown in plots (a) and (b) of Figure 4-93, the bromide voltage spikes correspond to molarity spikes that are significantly greater than the actual bromide concentration in the feed zone fluid. Specifically, the bromide molarity spikes are 100% to 5,000% of the actual concentration of the ion in the feed zone fluid. In contrast with plots (c) and (d), the presence of bromide ions has a disproportionately larger impact than chloride ions for the readings produced by the ISE probes.

Additionally, plots (e) and (f) of Figure 4-92 and Figure 4-93 show a unique behavior when both chloride and bromide were present in the feed zone fluid. The voltage and molarity time series for these four trials contain minimal noise and exhibit remarkably repeatable behavior for both ISE probes. This behavior was not seen to the same extent when either bromide or chloride were present separately in the feed zone fluid. However, the corresponding molarity spikes were 10,000% and 300,000% of the actual concentration of the individual ions for ISE probes #2 and #3. As such, this behavior warrants significant concern for obtaining accurate measurements of the absolute chloride concentration in a geothermal well. However, these repeatable responses hold the potential for obtaining usable results from field-scale experiments in geothermal wells. As discussed in Section 4.2.2.11, accurate measurements of the relative changes to chloride concentration are needed to infer the feed zone inflow rate. As such, the greater array of chemical species present in geothermal brine might improve the ability to accurately infer feed zone inflow rates.

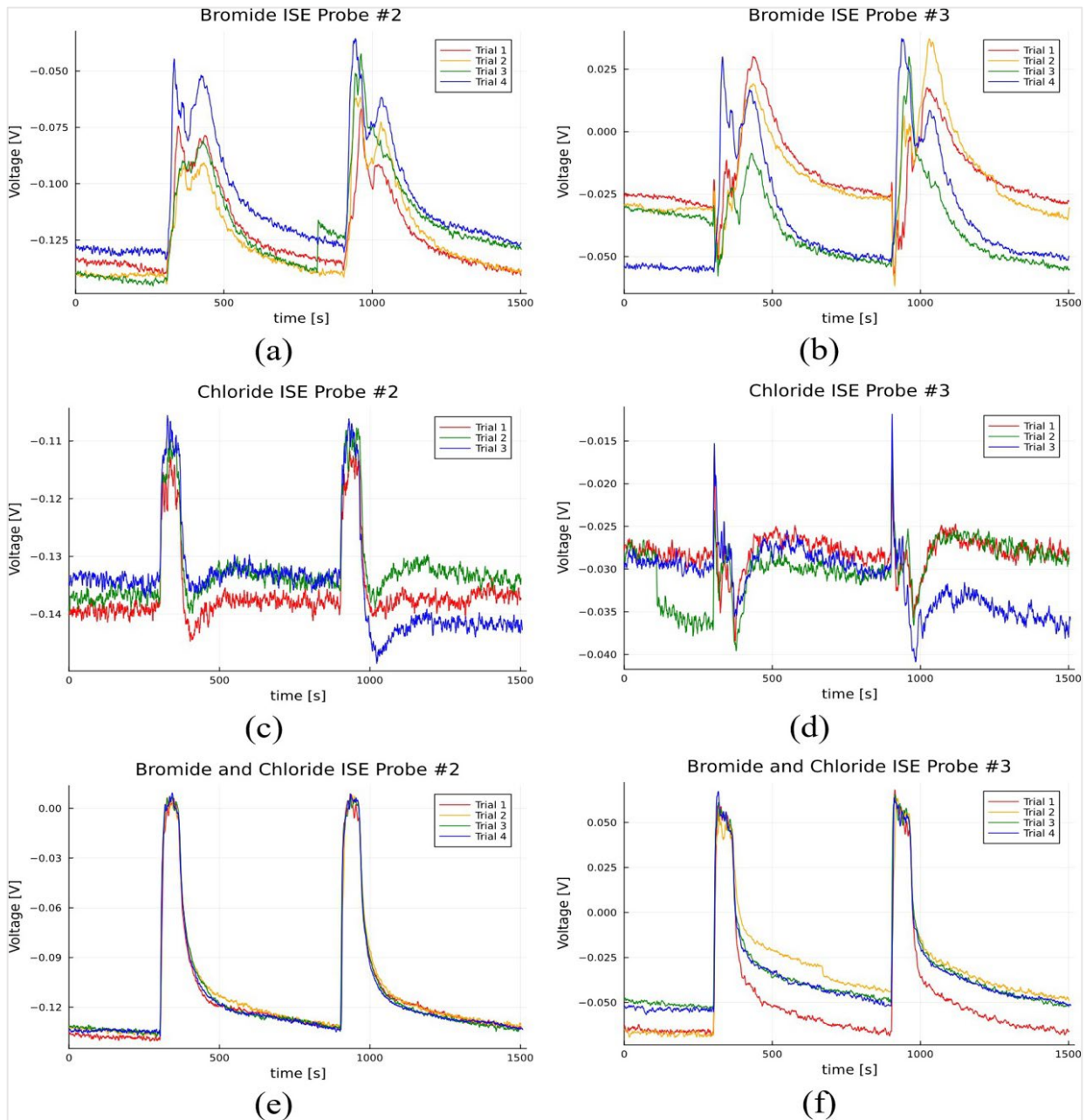


**Figure 4-92:** Voltage time series for ISE probe #2 and ISE probe #3 for feed zone fluid containing  $1 \times 10^{-2}$  mol/L concentrations of (a and b) bromide, (c and d) chloride, and (e and f) both bromide and chloride.

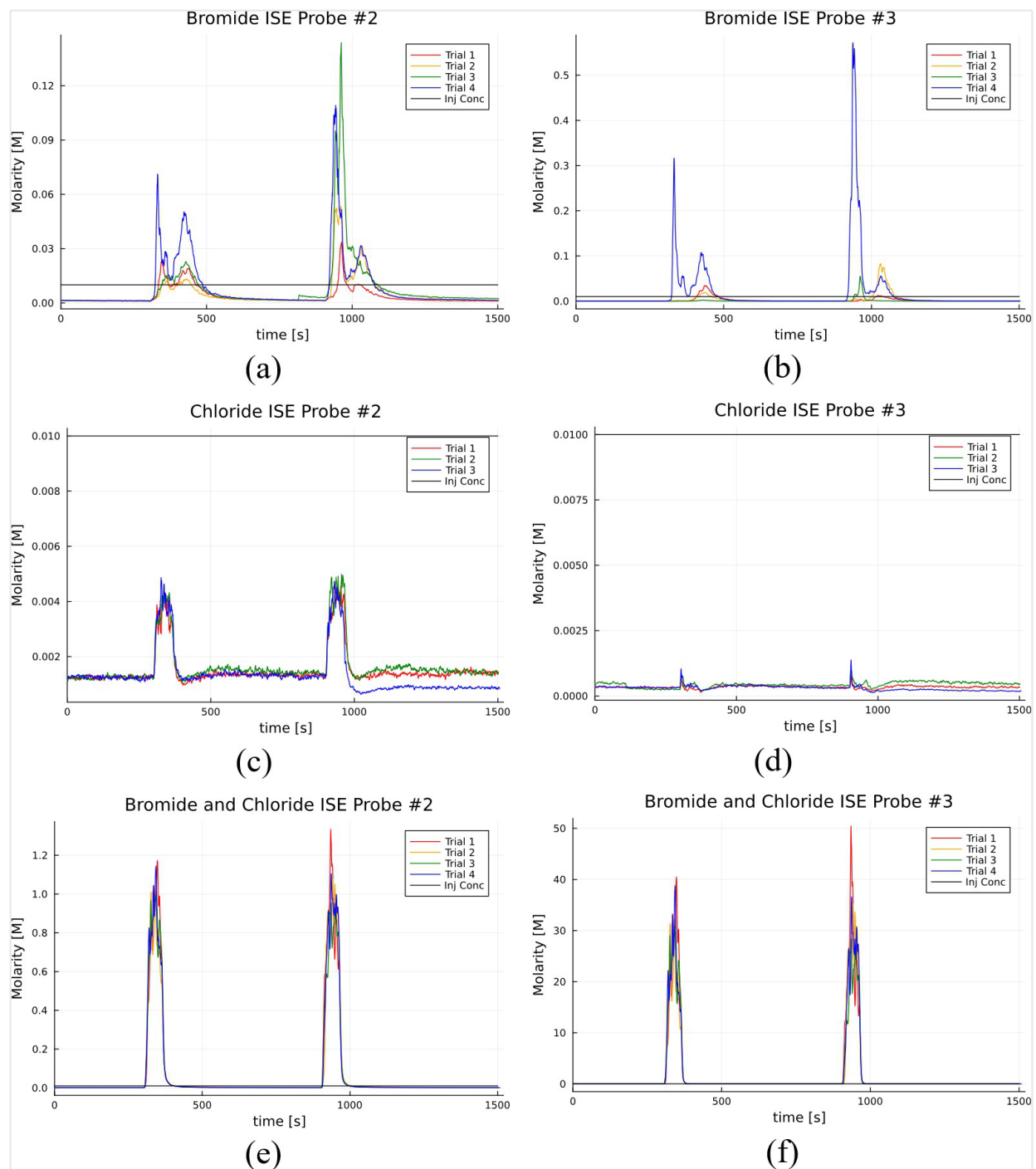


**Figure 4-93:** Molarity time series for ISE probe #2 and ISE probe #3 for feed zone fluid containing  $1 \times 10^{-2}$  mol/L concentrations of (a and b) bromide, (c and d) chloride, and (e and f) both bromide and chloride.

### ***Dynamic Experiments on Potassium Bromide Sensitivity***

The first ion sensitivity analysis for dynamic experiments involved the addition of potassium bromide (KBr) to the feed zone fluid. To assess its impact, a feed zone fluid with  $1 \times 10^{-2}$  mol/L concentrations

of bromide and chloride was used. For this feed zone fluid, three trials of dynamic experiments were conducted.

One observation from the results (Figure 4-94) is that there were significant drops in molarity that occurred above the feed zone in the RIH plots. The same behavior was present in the lower feed zone inflow rate scenario of Section 4.2.2.7, but to a lesser degree. A possible explanation for this behavior is that the effects of a rebound zone were exacerbated by the interference of bromide ions for the ISE probes.

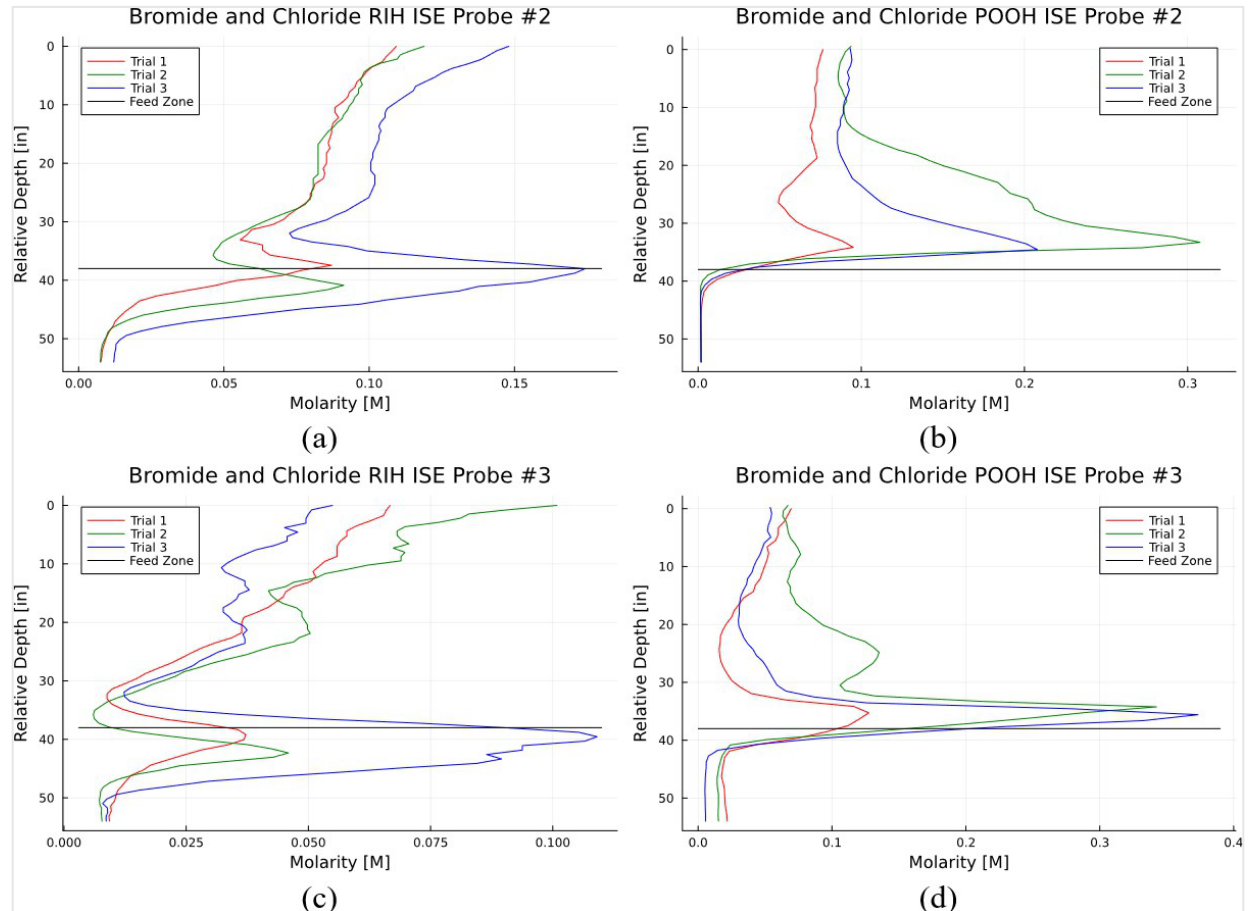


**Figure 4-94:** Molarity vs. Depth for ISE probe #2 and ISE probe #3 in the (a and c) RIH and (b and d) POOH directions for a feed zone fluid with  $1 \times 10^{-2}$  mol/L concentrations of bromide and chloride.

Using the method discussed in Section 4.2.2.5, the mass inflow rate  $\dot{m}_{in}$  for a single feed zone was calculated and Table 4-17 provides these values. Additionally, the percentage errors between these inferred feed zone inflow rates and the actual flow rate of 0.115 kg/s are provided in the final column of the table. Of note, color coding was used to visually convey the experimental trials with the smallest percentage errors. Additionally, the chloride concentrations above the feed zone  $Cl_{above}$ , at the feed zone  $Cl_{in}$ , and below the feed zone  $Cl_{below}$  are provided in the table for reference.

The results for the potassium bromide sensitivity analysis between the dynamic and static experiments were similar. Specifically, the #3 ISE probe provides the most accurate inferences of the feed zone inflow rate in the POOH direction. This probe and scenario had an average inferred feed zone inflow rate of 0.175 kg/s, corresponding to a 53% overestimation of the actual value. This large overestimation

is likely caused by the presence of bromide ions, which interfered with the membranes of the ISE probes.

**Table 4-17:** Chloride concentrations and calculated feed zone inflow rates for the dynamic experimentation sensitivity trials with bromide ions

Scenario	Trial #	ISE Probe	$Cl_{above}$ (mol/L)	$Cl_{in}$ (mol/L)	$Cl_{below}$ (mol/L)	$\dot{m}_{in}$ (kg/s)	Percentage Error
RIH	1	#2	0.0973	0.0865	0.0112	1.0059	775%
RIH	2	#2	0.0999	0.0824	0.0143	1.1060	862%
RIH	3	#2	0.1214	0.1160	0.0287	0.9343	712%
POOH	1	#2	0.0723	0.0951	0.0020	0.6644	478%
POOH	2	#2	0.0892	0.3076	0.0018	0.2515	119%
POOH	3	#2	0.0908	0.2079	0.0016	0.3804	231%
RIH	1	#3	0.0579	0.0418	0.0118	1.3527	1076%
RIH	2	#3	0.0710	0.0504	0.0106	1.3354	1061%
RIH	3	#3	0.0424	0.0375	0.0229	1.1803	926%
POOH	1	#3	0.0545	0.1275	0.0200	0.2825	146%
POOH	2	#3	0.0691	0.3424	0.0149	0.1456	27%
POOH	3	#3	0.0465	0.3735	0.0054	0.0983	-15%

Similar to the static results, the molarity readings of the dynamic experiments were significantly greater than the actual concentration of bromide and chloride in the feed zone fluid. However, the absolute value of the molarity readings did not seem to be significant because the relative changes to the measured concentration can be used to infer the feed zone inflow rate. Despite the presence of the interfering bromide ion, the molarity vs. relative depth plots for this scenario provided an accurate estimation of the feed zone inflow rate.

### ***Static Experiments on Potassium Sulfate Sensitivity***

The second set of sensitivity analyses involved adding potassium sulfate ( $K_2SO_4$ ) to the feed zone fluid.  $K_2SO_4$  was selected because of its lower hydration energy of  $-1,145$  kJ/mol (Marcus, 1991). As such, its presence should not significantly interfere with chloride for the readings of the ISE probes. Additionally, sulfate was present in the samples of Utah FORGE brine.

For this sensitivity analysis, three different solutions of feed zone fluid were made. One solution had a sulfate concentration of  $1 \times 10^{-2}$  mol/L, another solution had sulfate and chloride concentrations of  $1 \times 10^{-2}$  mol/L, and the final solution had sulfate, chloride, and bromide concentrations of  $1 \times 10^{-2}$  mol/L. The voltage time series for these three solutions for both ISE probes are provided in Figure 4-95, and the corresponding molarity time series are provided in Figure 4-96.

Similar to the results of the potassium bromide sensitivity, there are distinct voltage spikes corresponding to the feed zone inflow of the sulfate solution for both ISE probes. However, unlike bromide, sulfate is not classified as an interfering ion, so these voltage spikes should not be present. As such, investigating these anomalous voltage spikes should be considered for future work. One possible explanation for the voltage spikes is that degradation of the materials in the membranes, or the coating of the ISE probes reduced their specificity.

Despite the presence of voltage spikes, the greatest concentration of sulfate found in Utah FORGE brine was  $2.5 \times 10^{-3}$  mol/L. As such, the sulfate concentrations of the Utah FORGE brine samples were one-quarter as concentrated as the solutions used in these experiments. Consequently, the magnitude of the voltage spikes corresponding to the presence of sulfate in a field experiment will likely not be as large as those seen in plots (a) and (b) of Figure 4-95.

Unlike bromide, the presence of sulfate did not appear to greatly increase the molarity readings of the chloride tool. As shown in plot (c) of Figure 4-93 and plots (a) and (c) of Figure 4-96, there was no significant change in the magnitude of the molarity spikes when chloride, sulfate, or both chloride and sulfate were present in the feed zone fluid for ISE probe #2. This behavior was largely the same for ISE probe #3. There was no significant difference in the molarity response of ISE probe #3 when only chloride or sulfate was present in the feed zone fluid. However, plot (d) of Figure 4-96 shows that the molarity reading was approximately 25% of the actual concentration of the bromide and chloride ions in the feed zone fluid. This behavior better aligns with the results presented in Section 4.2.2.5, suggesting that molarity readings of ISE probe #3 improved with additional chemical species.

Similar to the results of Section 4.2.2.11, a unique behavior was observed when multiple ions were present in the feed zone fluid. As shown in plots (c) and (f) of Figure 4-95, the voltage-time series contained minimal noise and exhibited remarkably repeatable behavior for both ISE probes when sulfate, chloride, and bromide were present in equal concentrations in the feed zone fluid. This behavior was not seen to the same extent when sulfate and chloride, just sulfate, or just chloride, were present in the feed zone fluid. As such, this repeatable behavior was attributed to the greater array of chemical species present in the fluid.

As shown in plots (e) and (f) of Figure 4-96, the molarity readings when sulfate, chloride, and bromide were present in the feed zone fluid were significantly greater than the actual concentration of the individual components in the feed zone fluid. This was similar to the behavior observed in Figure 4-93 when bromide ions were present. For ISE probes #2 and #3, the molarity spikes were 5,000% and 150,000% of the actual concentration of the individual ions. Of note, these values are half of those shown in plots (e) and (f) of Figure 4-93. This suggests that the presence of sulfate ions in the feed zone fluid stabilized the readings of the chloride tool compared to a feed zone fluid with bromide and chloride ions. In addition to the increased repeatability exhibited when sulfate ions were present, this stability holds the potential for obtaining reliable results from a field-scale experiment, which can be used to accurately infer feed zone inflow rates.

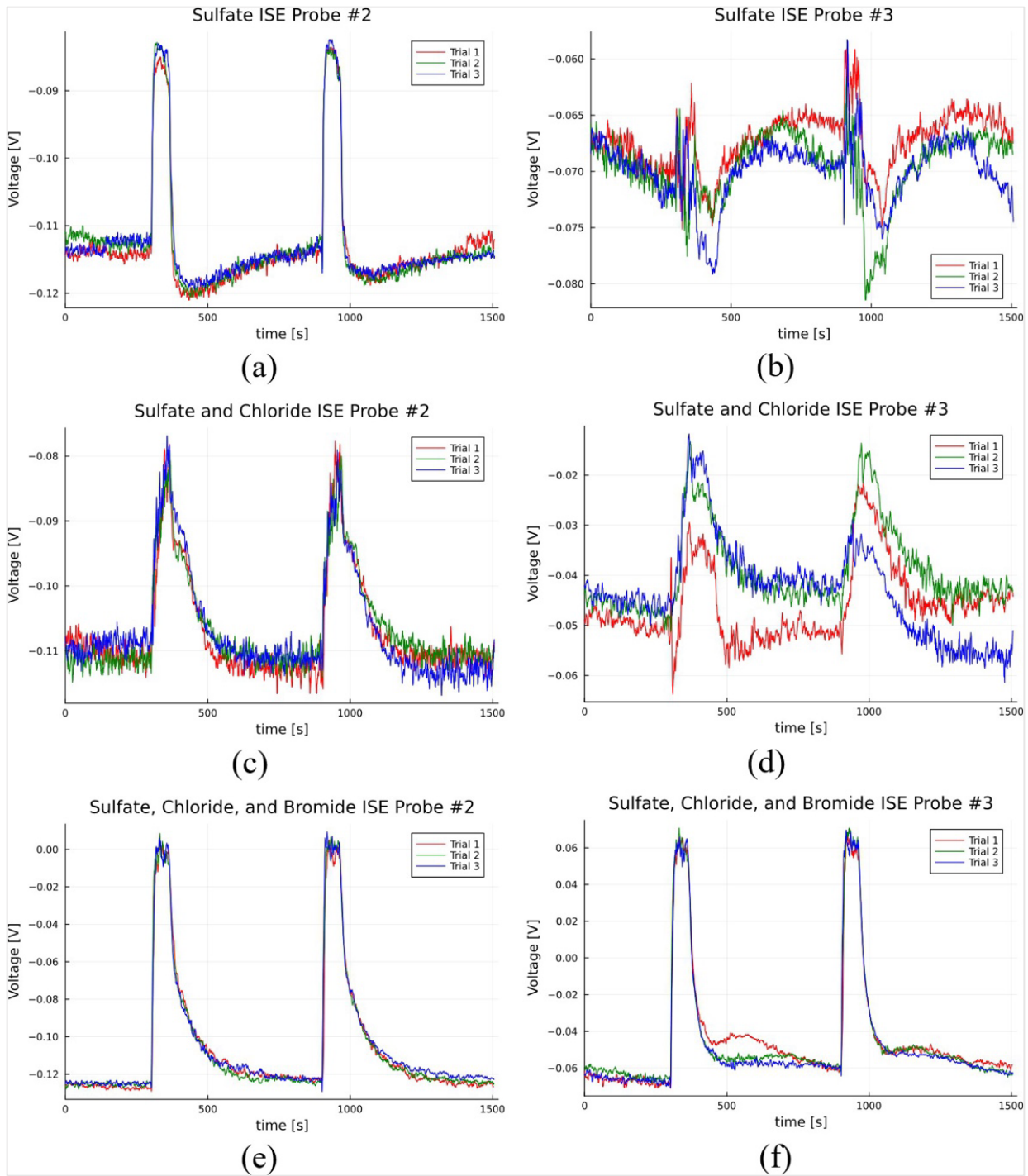


**Figure 4-95:** Voltage time series for ISE probe #2 and ISE probe #3 for feed zone fluid containing  $1 \times 10^{-2}$  mol/L concentrations of (a and b) sulfate, (c and d) sulfate and chloride, and (e and f) sulfate, chloride, and bromide.

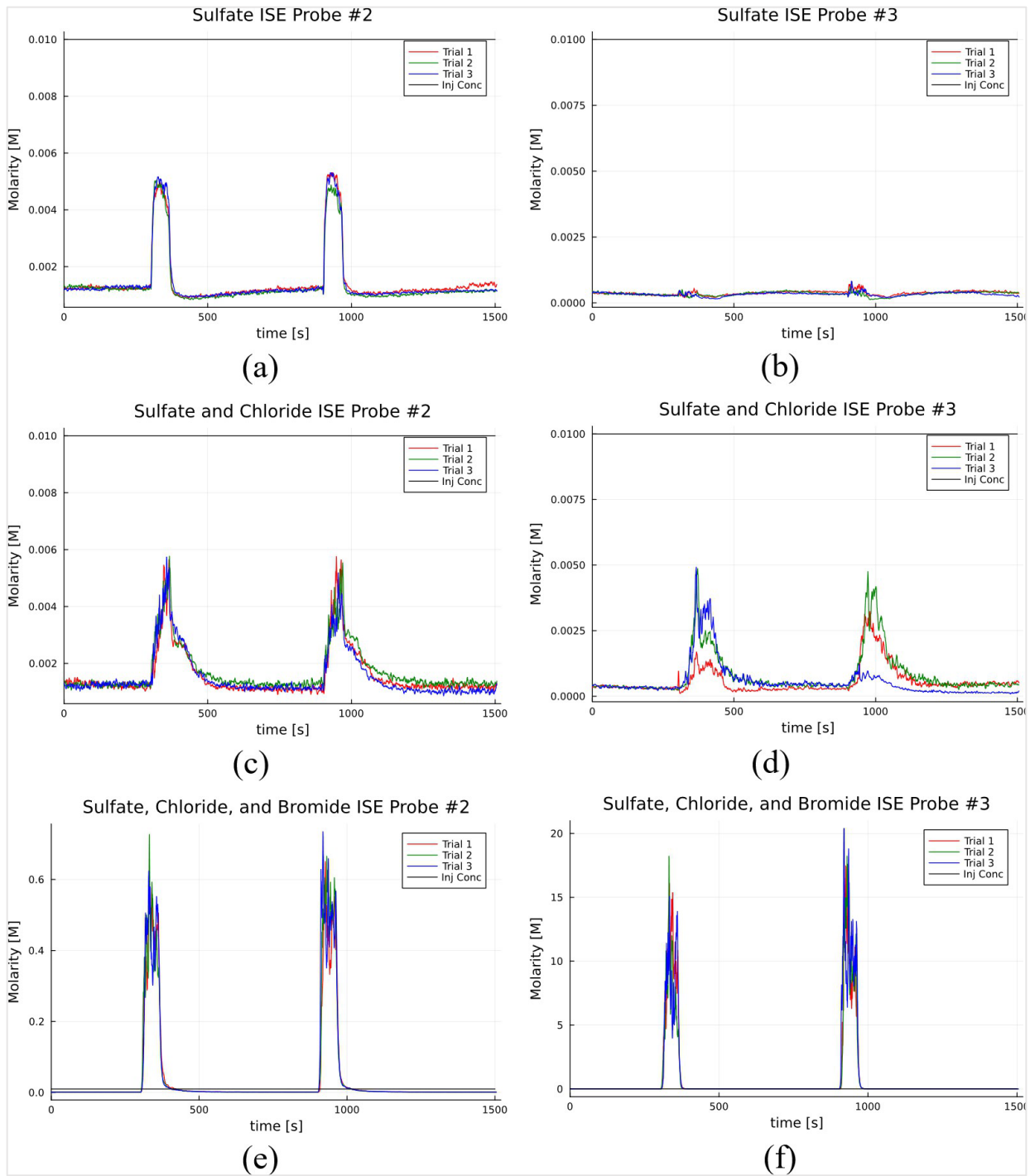


**Figure 4-96:** Molarity time series for ISE probes #2 and ISE probe #3 for feed zone fluid containing  $1 \times 10^{-2}$  mol/L concentrations of (a and d) sulfate, (b and e) sulfate and chloride, and (c and f) sulfate, chloride, and bromide.

### Dynamic Experiments on Potassium Sulfate Sensitivity

Three trials of dynamic experiments with a feed zone fluid with sulfate and chloride concentrations of  $1 \times 10^{-2}$  mol/L were conducted. Unlike the results of the bromide sensitivity, the molarity readings in Figure 4-97 at the depth of the feed zone are equivalent to those in the static experiments, especially for ISE probe #2. This corroborates the results presented earlier, which suggest that the presence of sulfate ions in the feed zone fluid does not significantly affect the absolute chloride concentration readings of the ISE probes.

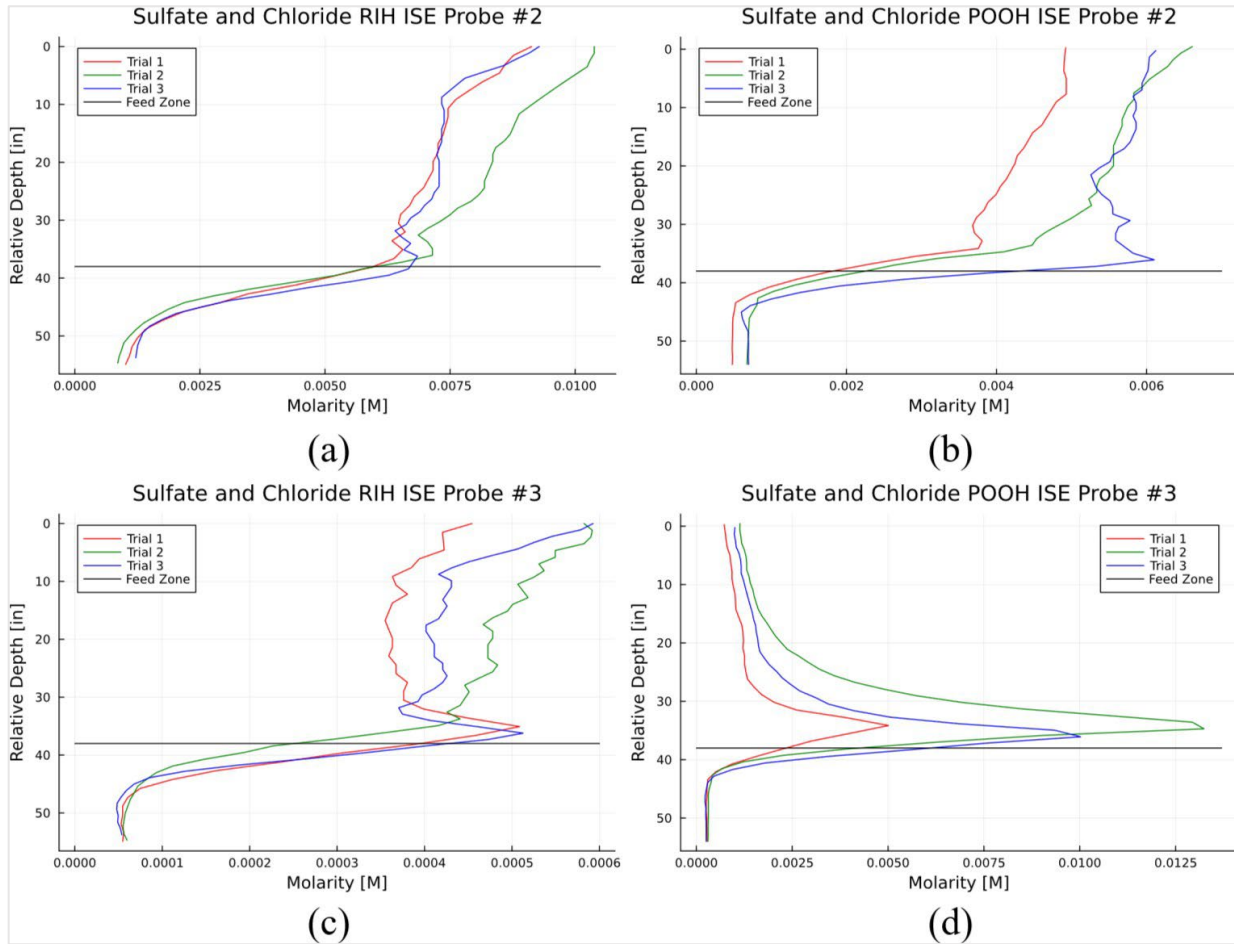


**Figure 4-97:** Molarity vs. Depth for ISE probe #2 and ISE probe #3 in the (a and c) RIH and (b and d) POOH directions for a feed zone fluid with  $1 \times 10^{-2}$  mol/L concentrations of sulfate and chloride.

One observation from Figure 4-97 is that there were slight spikes in molarity in the RIH direction above the feed zone location, especially for ISE probe #3. This behavior was not seen to the same extent in other dynamic experiments. The ability to identify these increases in chloride concentration associated with the feed zone jet was likely caused by the stabilizing effect of sulfate ions on the ISE probes' readings discussed in the static experiment results. However, using Equation (3-3) on this isolated section overestimated the feed zone inflow rate at approximately 0.63 kg/s. This value is still significantly less accurate than the inferred feed zone inflow rates of the POOH motion. This is likely because of the relative chloride concentration distribution within the wellbore, which results in a more accurate reading of the POOH motion discussed in Section 4.2.2.5.

The addition of sulfate ions did not alter the ISE probes' ability to detect relative changes in the chloride concentration in the wellbore fluid. As such, the plots were used to infer the feed zone inflow rate  $\dot{m}_{in}$  for a single feed zone, as provided in Table 4-18. Note that a color-coding scheme was used to visually indicate which experimental trials have the closest calculated feed zone inflow rate  $\dot{m}_{in}$  to the actual value of 0.115 kg/s.

**Table 4-18:** Chloride concentrations and calculated feed zone inflow rates for the dynamic experimentation sensitivity trials with sulfate ions

Scenario	Trial #	ISE Probe	$Cl_{above}$ (mol/L)	$Cl_{in}$ (mol/L)	$Cl_{below}$ (mol/L)	$\dot{m}_{in}$ (kg/s)	Percentage Error
RIH	1	#2	0.0082	0.0073	0.0016	1.0216	788%
RIH	2	#2	0.0097	0.0084	0.0012	1.0359	801%
RIH	3	#2	0.0080	0.0073	0.0017	0.9884	759%
POOH	1	#2	0.0048	0.0043	0.0005	1.0039	773%
POOH	2	#2	0.0060	0.0056	0.0007	0.9589	734%
POOH	3	#2	0.0059	0.0061	0.0007	0.8513	640%
RIH	1	#3	0.0004	0.0005	0.0001	0.6664	479%
RIH	2	#3	0.0005	0.0005	0.0001	1.0140	782%
RIH	3	#3	0.0005	0.0005	0.0001	0.9290	708%
POOH	1	#3	0.0009	0.0050	0.0003	0.1154	0%
POOH	2	#3	0.0013	0.0132	0.0003	0.0700	-39%
POOH	3	#3	0.0012	0.0100	0.0002	0.0851	-26%

As mentioned in the other sections of this chapter, the most accurate results are those for ISE probe #3 in the POOH motion. Unlike the results in the static experiments of the potassium sulfate, however, the inferred feed zone inflow rate for this scenario was underestimated, with an average value of 0.090 kg/s. The accuracy of this scenario suggests that the sulfate ions in the feed zone fluid did not affect the ability of the chloride tool to infer feed zone inflow rates. However, all other scenarios resulted in overestimations of the feed zone inflow rate.

To compare the effects of chloride ions, bromide and chloride ions, and sulfate and chloride ions being present in the feed zone fluid, their inferred feed zone inflow rates will be compared. Table 4-19 provides the average inferred feed flow rates across the three trials for both ISE probes in the RIH and POOH motions for these feed zone fluid compositions.

**Table 4-19:** Average inferred feed zone inflow rates for the dynamic experimentation ion sensitivity analysis

Scenario	ISE Probe	Inferred Feed Zone ( $Cl^-$ ) Inflow Rate (kg/s)	Inferred Feed Zone ( $Br^-$ and $Cl^-$ ) Inflow Rate (kg/s)	Inferred Feed Zone ( $SO_4^{2-}$ and $Cl^-$ ) Inflow Rate (kg/s)
RIH	#2	0.8655	1.0154	1.0153
RIH	#3	0.3933	1.2895	0.8698
POOH	#2	0.8859	0.4321	0.9380
POOH	#3	0.0776	0.1755	0.0902

The inferred feed zone inflow rates showed overestimations for almost all scenarios and feed zone fluid compositions. However, the ISE Probe #3 underestimated the feed zone inflow rate in POOH direction with a feed zone fluid containing only chloride ions or both sulfate and chloride ions. For this probe in this scenario, the addition of bromide increased the value of the inferred feed zone inflow rate and increased the magnitude of the percentage error. However, this inferred value is still equivalent to those from dynamic experiments in other sections. Despite the large discrepancies to the absolute value of the molarity readings for the ion sensitivity scenarios, the relative molarity changes were used to accurately infer the feed zone inflow rate.

The greater spikes in the POOH direction for ISE Probe #2, when chloride and bromide were present in the feed zone fluid, resulted in more accurate feed zone inflow rate inferences by 400% in absolute terms. This is likely because of the smoothing effect caused by bromide ions discussed in the static experiments of potassium bromide. However, it is not known why the smoothing effect of sulfate ions did not result in the same behavior. However, the inferred feed zone inflow rates for the other scenarios performed consistently with the other experiments in this chapter. As such, the wide array of chemical species present in geothermal brine may not impair the chloride tool's ability to obtain accurate results from field-scale experiments, especially in the POOH direction.

# Chapter 5

## Field Deployment

### 5.1 Field Deployment Summary

The field-deployable version of the chemical tool was deployed in FORGE Wells 58-32, a vertical monitoring well with a total depth of 7,536 ft, and Well 16B(78)-32, a deviated production well drilled to a total depth of 10,947 ft. For 58-32, the weight of the tool was sufficient to lower the tool with gravity; however, in 16B(78)-32, a wireline roller was needed to help convey the tool through the well deviation. Figure 5-1 shows the wells on the Utah FORGE site, and Table 5-1 provides an overview of the two FORGE wells and their deployment techniques.

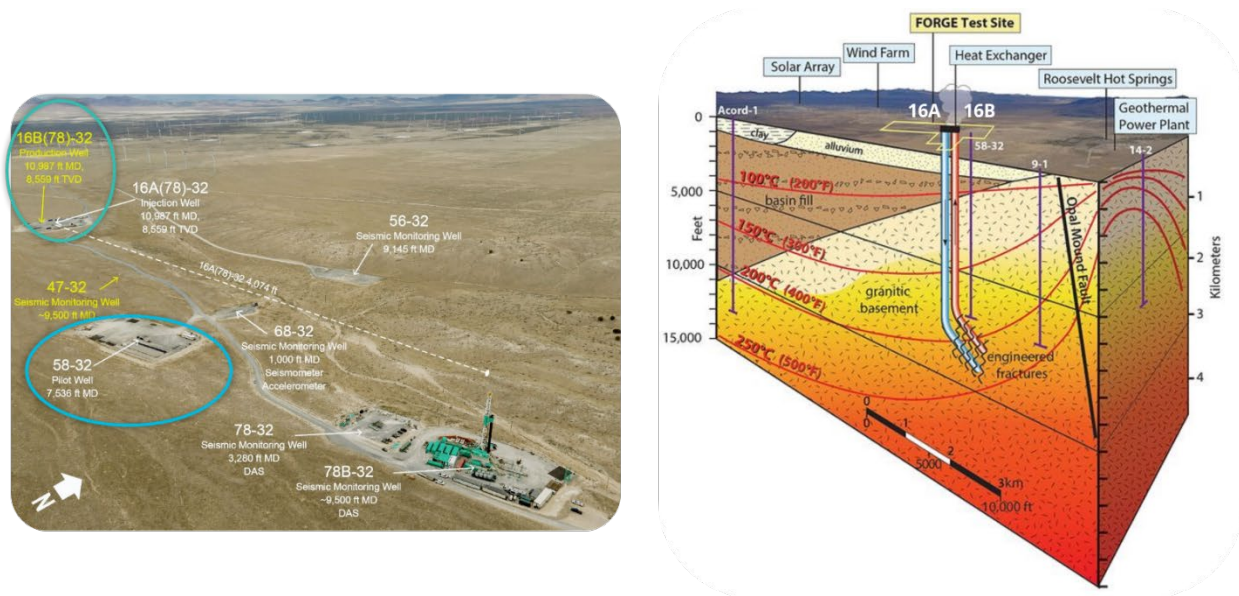


**Figure 5-1:** Utah FORGE site with planned deployment wells circled (left) and geological and heat model of the Utah FORGE site (right). Source: Utah FORGE.

**Table 5-1:** Overview of tool deployment scenarios in Utah FORGE wells 58-32 and 16B(78)-32.

FORGE Well	Well Type	Curve Profile	Total Depth	Deployment Technique
58-32	Vertical Pilot Well	N/A	7,536 ft	Tool deployed on Sandia wireline with weight of tool
16B(78)-32	Directional Production Well	5°/100 ft	10,947 ft	Tool deployed through wireline service company with conveyance rollers to assist with well deviation

The field-deployable chemical tool assembly incorporates the Mitco PTS sensor package and a tip centralizer at the leading edge of the tool. This is used for secondary downhole measurements to compare the geochemistry-based alternative method to the commonly used PTS measurements. A wire guide component was developed to adapt the PTS tool to the FORGE chemical sensor housing. The sensor wires from both the Mitco PTS tool and the chemical sensors pass through a wire feedthrough in the chemical sensor housing to the high-temperature logging tool in the electronics housing. The electronics housing connects to the wireline via a 4-conductor feedthrough that is adapted to a 7-pin conductor feedthrough that matches the wireline connection. The full assembly schematic is shown in Figure 5-2 and the development is detailed in Section 2.3.

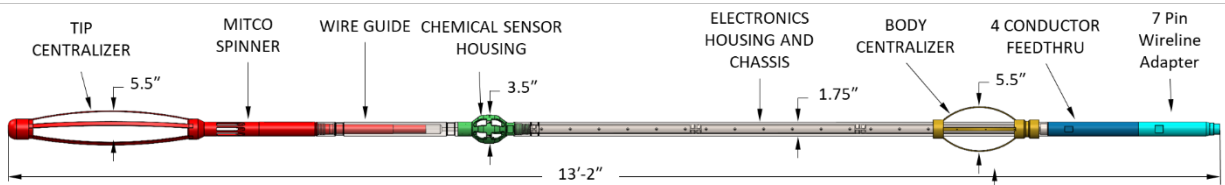


**Figure 5-2:** Field-deployable chloride tool schematics, including an existing PTS tool adapted to the chloride-based wireline tool and high-temperature developed by Sandia National Laboratory.

## 5.2 FORGE Well 58-32 Deployment

The well 58-32 deployment at Utah FORGE occurred on June 12-14, 2024, and was intended as a test run to assess the capabilities and limitations of the field-scale tool in preparation for the main deployment, which was at well 16B(78)-32. Well 58-32 is a vertical pilot well of 7,536 ft depth with two cased and perforated zones (Zones 2 and 3) and an open hole section (Zone 1) with a 7-inch casing. The logging was paused in five test locations above, below, and within the cased and perforated zones to gather stronger indicators of inflow, if any, as shown in the deployment plan in Figure 5-3. The logging was planned to stop short of entering Zone 1, as a component in the open hole section could potentially get stuck. Figure 5-4 shows the chemical sensor housing (i.e., the geochemistry-based tool) and the wireline assembly lifted by the Sandia wireline truck and ready to trip into well 58-32. The first two tools encountered issues due to leaks in connections and a problem with the microcontroller board, thus they were unable to collect any data. The third tool was able to successfully log data in each test location during the trip in and out of the hole.

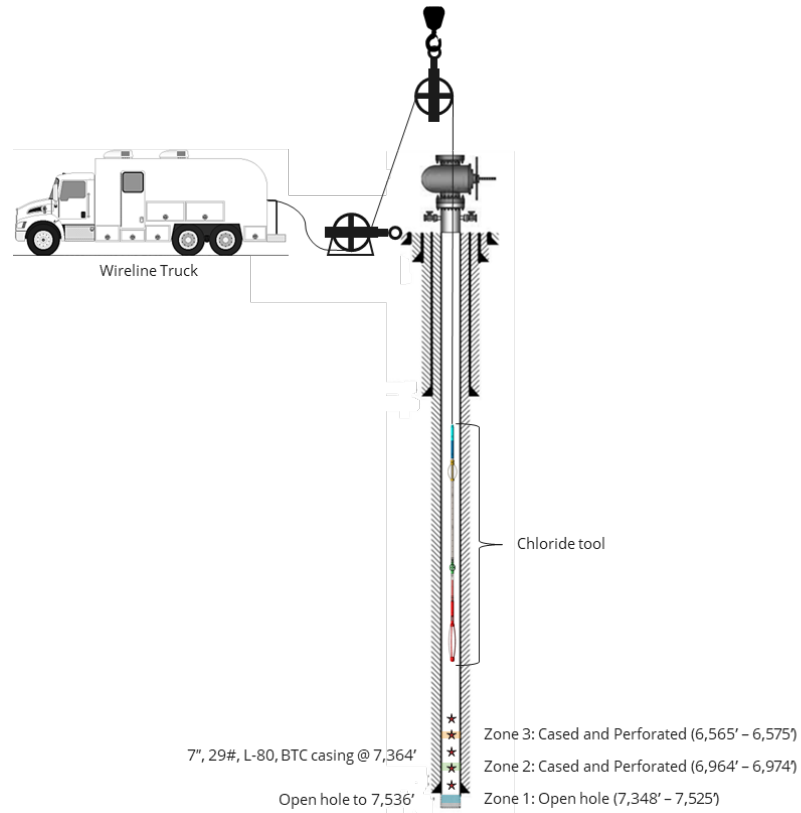


**Figure 5-3:** Illustration of tool deployment plan at well 58-32.



(a) Field tool component



(b) Wireline tool ready to trip in

**Figure 5-4:** (a) the chemical sensor and housing as part of the wireline tool assembly, and (b) the assembly ready to trip in.

The logging results are shown in Figure 5-5 for the run-in hole (RIH) and Figure 5-6 for the pull-out of the hole (POOH). The first two columns display data from two chemical sensors, while the following two columns show the PTS and CPU temperature data. The CPU temperature data is considered more accurate in magnitude for this particular run despite the lag in heating up caused by its position inside the electronics component rather than in direct contact with the fluid. The last three columns represent the flow data from the PTS sensor. The perforated zones are marked with yellow regions; the short interval creates the appearance of a line.

A decrease in voltage (i.e., a spike to the left) would correlate with an increase in chloride concentration, indicating inflow presence. If accompanied by a temperature spike coming from geofluid entering the wellbore, the voltage spike will strongly indicate inflow presence. The RIH data shows no firm indication of such a spike around Zone 2 and 3. Meanwhile, spikes in both directions are observed in the chloride voltage columns near Zone 1, which also correlates with a temperature increase. However, the PTS counter did not increase, even with a location pause. Thus, the interval is not considered to be flowing or exhibiting notable internal flow.

The POOH run provides much cleaner data than the RIH run, which is consistent with results from the laboratory experiments. However, chemical sensor voltage data from the shallower part of the POOH, as indicated in Figure 5-6, is erroneous and cannot be used for interpretation. Similar to RIH, spikes are seen near Zone 1 but are not interpreted as flow because the PTS counter did not change at all. There is a voltage spike near Zone 3, which is also accompanied by a temperature spike. However, the spike was only caused by one data point; again, no corresponding counter or direction change from PTS was present. Therefore, it is concluded that the logged interval did not indicate the presence of any inflow. If there were any internal flow happening, it may have occurred within the open hole section, which was not covered by the logging runs.

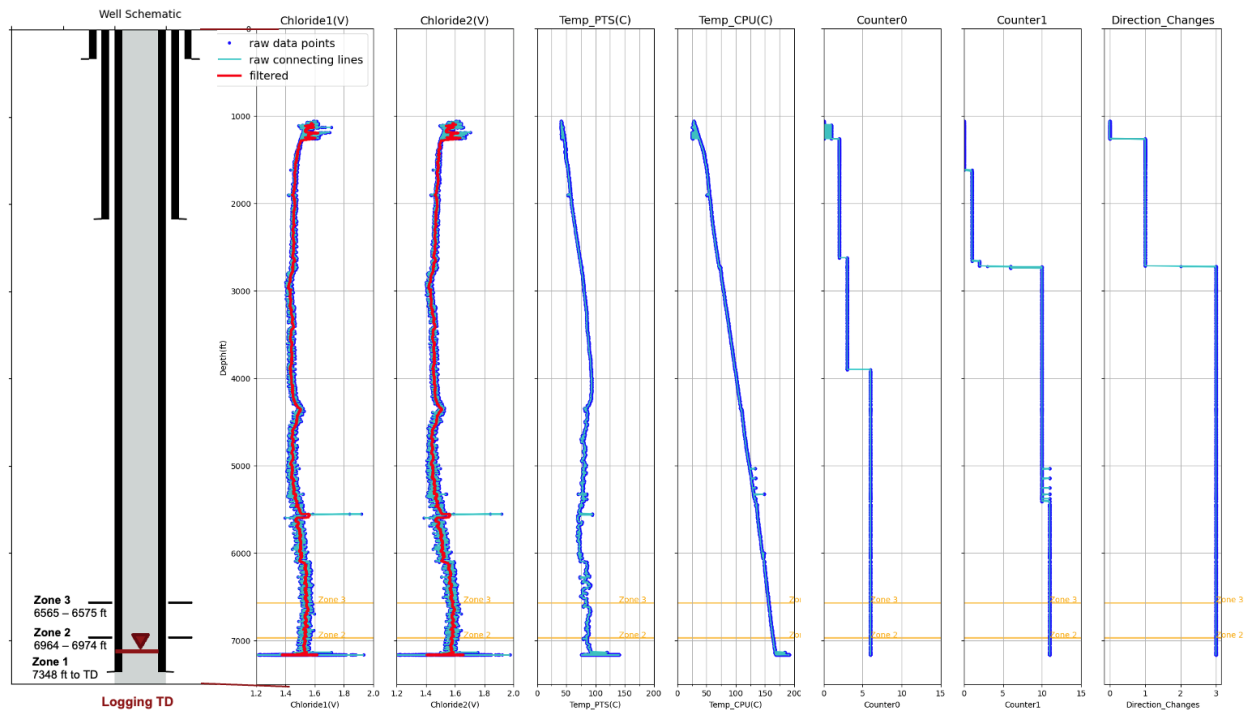
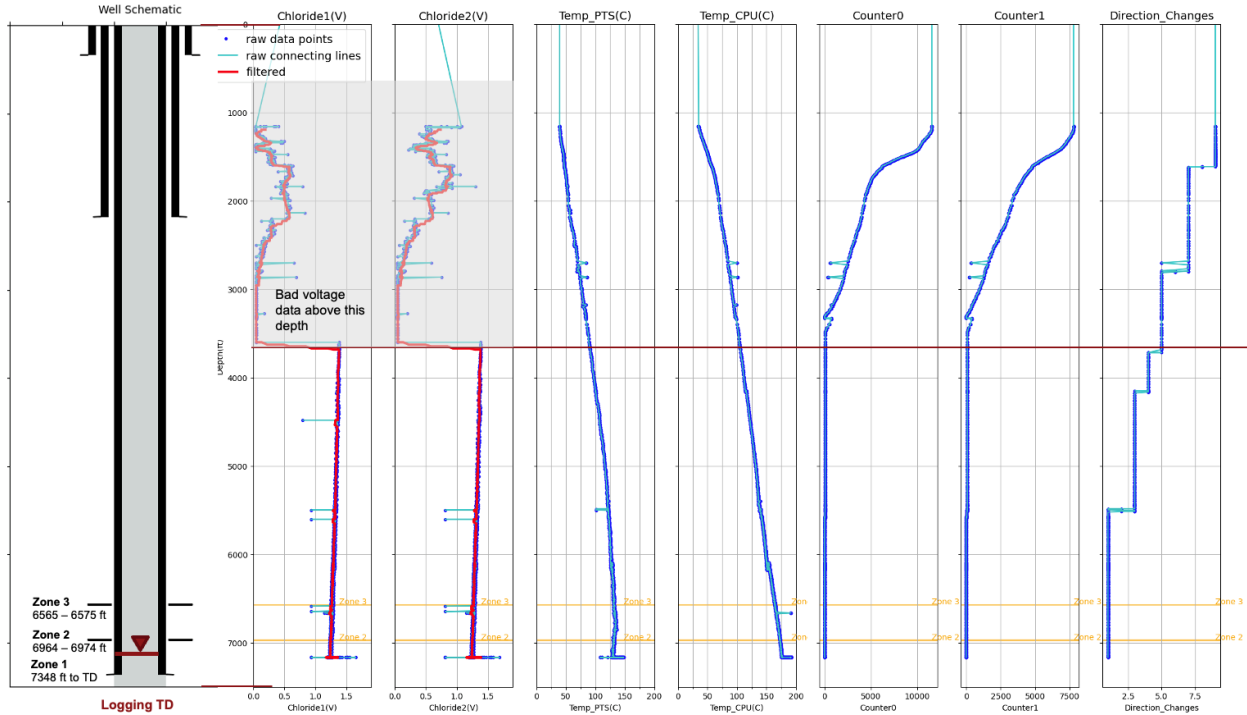


Figure 5-5: logging results during Run in Hole (RIH) at well 58-32.



**Figure 5-6:** logging results during Pull Out of Hole (POOH) at well 58-32.

The voltage signals from the two chemical sensors appear to resemble each other. Thus, the readings from the first sensor were used to evaluate converting the chemical sensor voltage into chloride concentration. Calibration for the field tool used at 58-32 was performed with KCl solution in distilled water and fluid samples from well 16A(78)-32 and 16B(78)-32. The molarity result using the best available calibration curve is shown in Figure 5-7, showing a range of around 0.2 M for RIH data and between 0.25 to 0.75 M for POOH data. However, this calibration curve is unreliable due to a discrepancy in the bench calibration after acquisition.

In **Figure 5-2** Table 5-2, the sum of the molarity of relevant chemical species that the chemical sensor would pick up ranges from 0.0046 to 0.12 M. Recent laboratory experiments have shown that in addition to chloride, the ISE is sensitive to bromide (Br) and a lesser extent, sulfate (SO<sub>4</sub>). While chloride is more common in brine water and often determines the molarity, the ISE reacts to bromide and sulfate to varying degrees. Compared to the molarity in Table 5-1, the chemical concentration obtained from the logging data (Figure 5-7) indicates that the ranges of molarity derived from the chemical sensor are generally higher than what was found in the nearby well samples 16A(78)-32 and 16B(78)-32. Some anomalous points are present and exhibit erroneous railing behavior and, therefore, may be excluded.

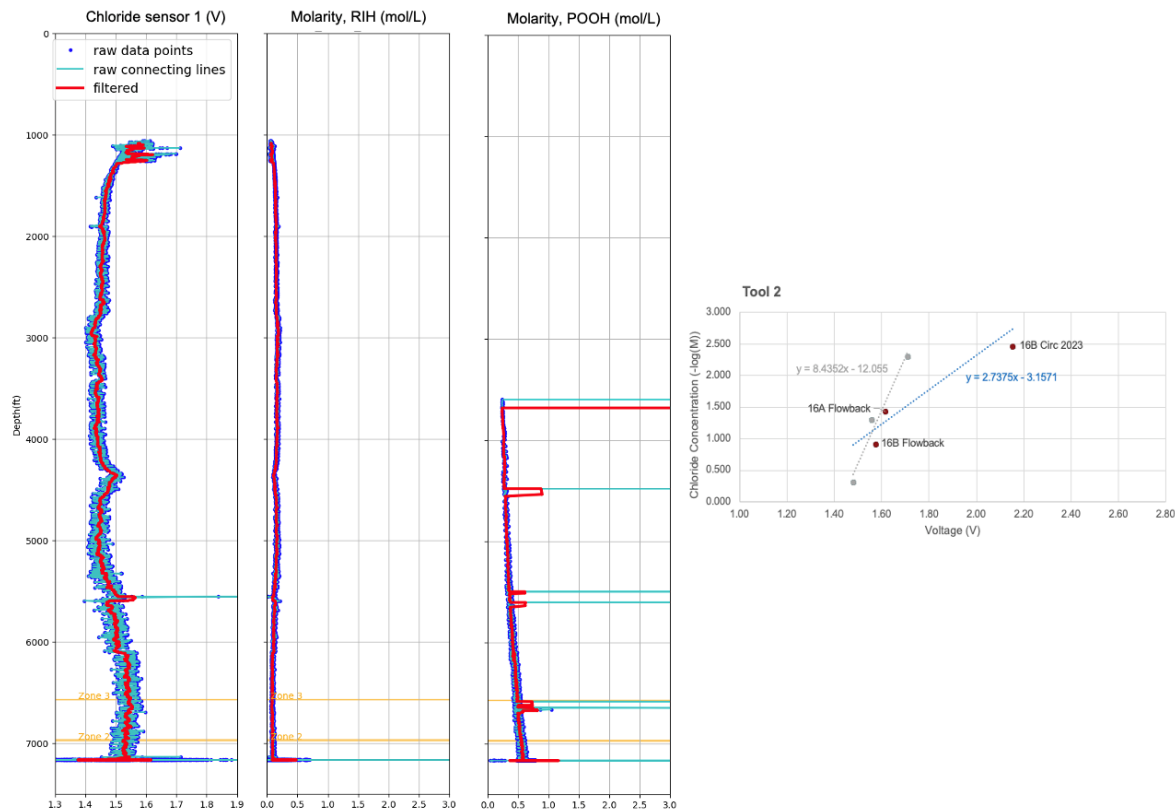


**Figure 5-7:** converted molarity from the chemical sensor 1 voltage data during RIH and POOH using Tool 2 calibration curve (blue line on the right chart).

**Table 5-2:** Relevant chemical species of well samples from Utah FORGE Wells 16A(78)-32 and 16B(78)-32

DATE & TIME	WELL	Concentration (mg/l)			Molarity (mol/l)			Sum of molarity (mol/l)
		Br	Cl	SO4	Br	Cl	SO4	
7/19/2023 20:00	16A(78)-32	2.07	1300	162	2.59E-05	3.66E-02	1.69E-03	0.0383
7/20/2023, 7:50	16B(78)-32	9.05	4384	239	1.13E-04	1.23E-01	2.49E-03	0.1261
7/20/2023, 15:00	16B(78)-32	0.32	122	115	4.01E-06	3.44E-03	1.20E-03	0.0046

### 5.3 Field Deployment at 16B(78)-32

While the field test at 58-32 demonstrated the practical application of the geochemistry-based wireline tool, and the resilience of the tool to high-temperature, a meaningful inflow signal was absent because the well was not flowing. In contrast, well 16B(78)-32 was undergoing flow through the five

stimulation stages and multiple feed zones along the deviated section. The field test at this well investigated the sensor's feasibility, tool design, and capability of data acquisition under challenging well conditions.

The second deployment occurred on August 19, 2024, at Utah FORGE Well 16B(78)-32 during a 30-day circulation test. Figure 5-8 depicts the deployment plan. Well 16B has five stages, each with 3-5 guns, allowing for mapping up to 20 fractures. For this deployment, ten test locations were planned to target measurements at and between perforations. The tool would be stationed at each test location to enable stationary measurements of the chloride sensors and PTS tool. The logging between each test location would provide a blind “fly by” measurement to assess the feasibility of mapping fractures using a running log. Two chemical tool assemblies were prepared as a contingency in the field. The tool was deployed using a Schlumberger wireline truck, weight bars, and Petromac rollers to convey it through the flowing and deviated well. Figure 5-9 shows the full chemical tool assembly attached to weight bars and being loaded into lubricators. Figure 5-10 shows the wireline tool assembly tripping in.

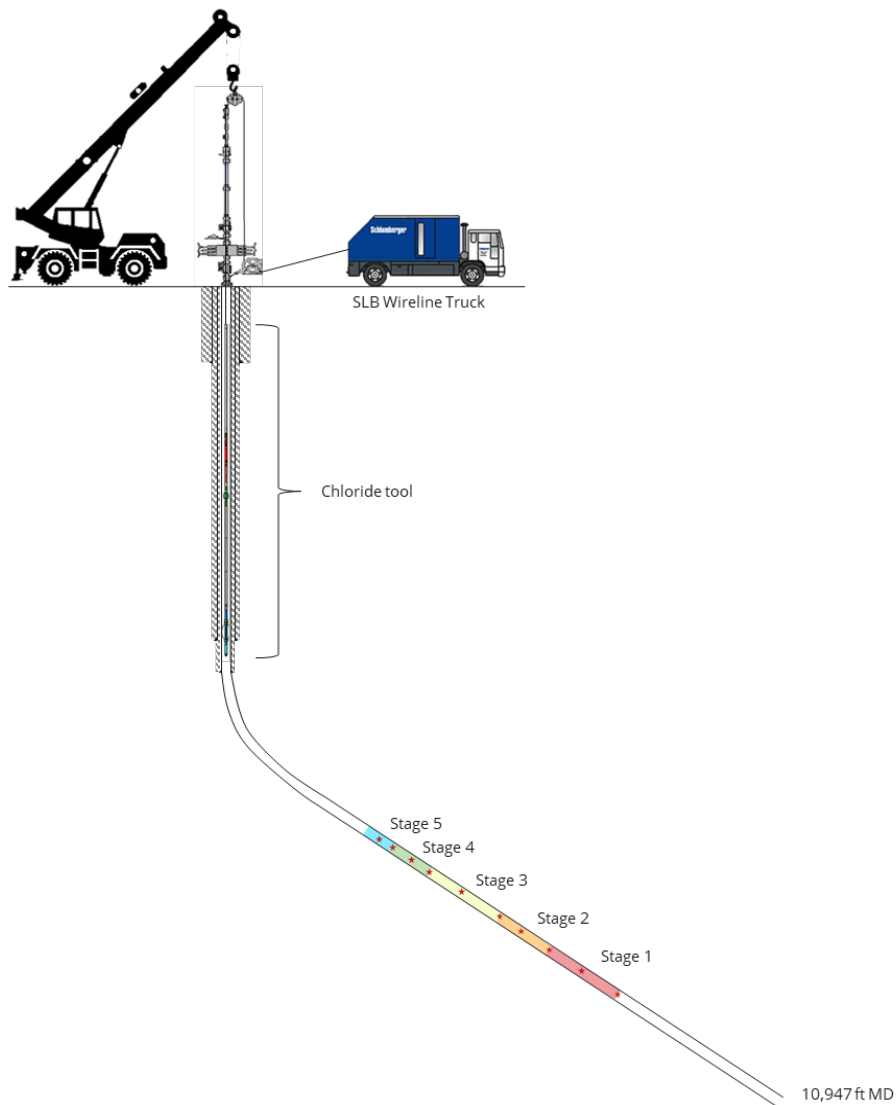


**Figure 5-8:** Illustration of tool deployment plan for Utah FORGE Well 16B(78)-32. Perforation stages are shown in highlighted zones, and planned test locations are shown as red stars.



**Figure 5-9:** Full chemical tool assembly attached to weight bars and being loaded into lubricators.



**Figure 5-10:** Utah FORGE Well 16B test site with lubricator stacks for chemical tool.

The tool was successfully deployed to approximately 9,480 ft, passing through Stage 5, Stage 4, and part of Stage 3, with a maximum measured temperature on the tool of 210°C. The logging results from well 16B(78)-32 are presented in Figure 5-11 for the run-in hole (RIH) and in Figure 5-12 for the pull-out hole (POOH). The first three columns display chloride voltage readings from the three sensors installed in the wireline tool. The following three columns represent the chloride concentration in mol/L, calculated using the calibration curve (Figure 5-13) to convert voltage to concentration. Subsequently, the Pressure-Temperature-Spinner tool readings are displayed in the following three columns, and the velocity log is derived from the spinner readings. The stages are marked in differently colored zones, and guns are marked as green lines throughout the logs.

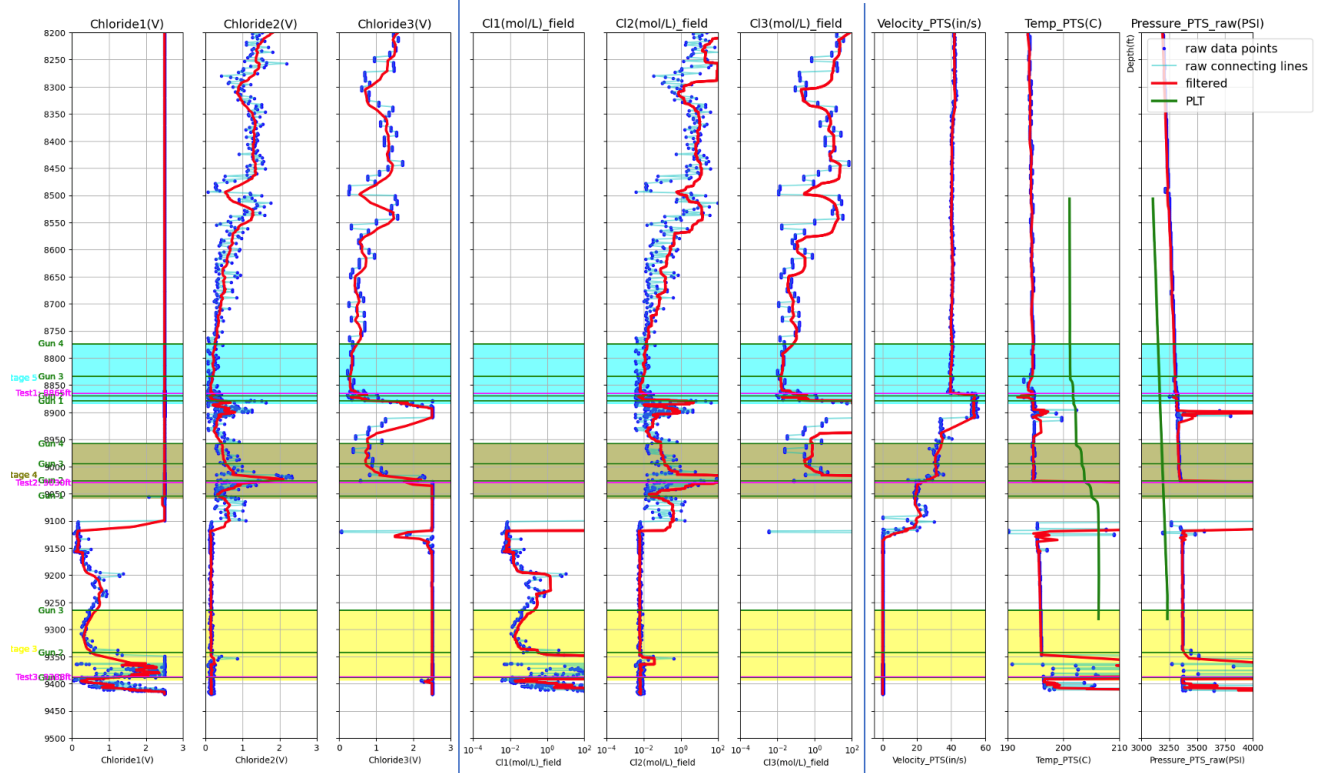


**Figure 5-11:** well logs from Run in Hole (RIH) run at 16B zonal depths.

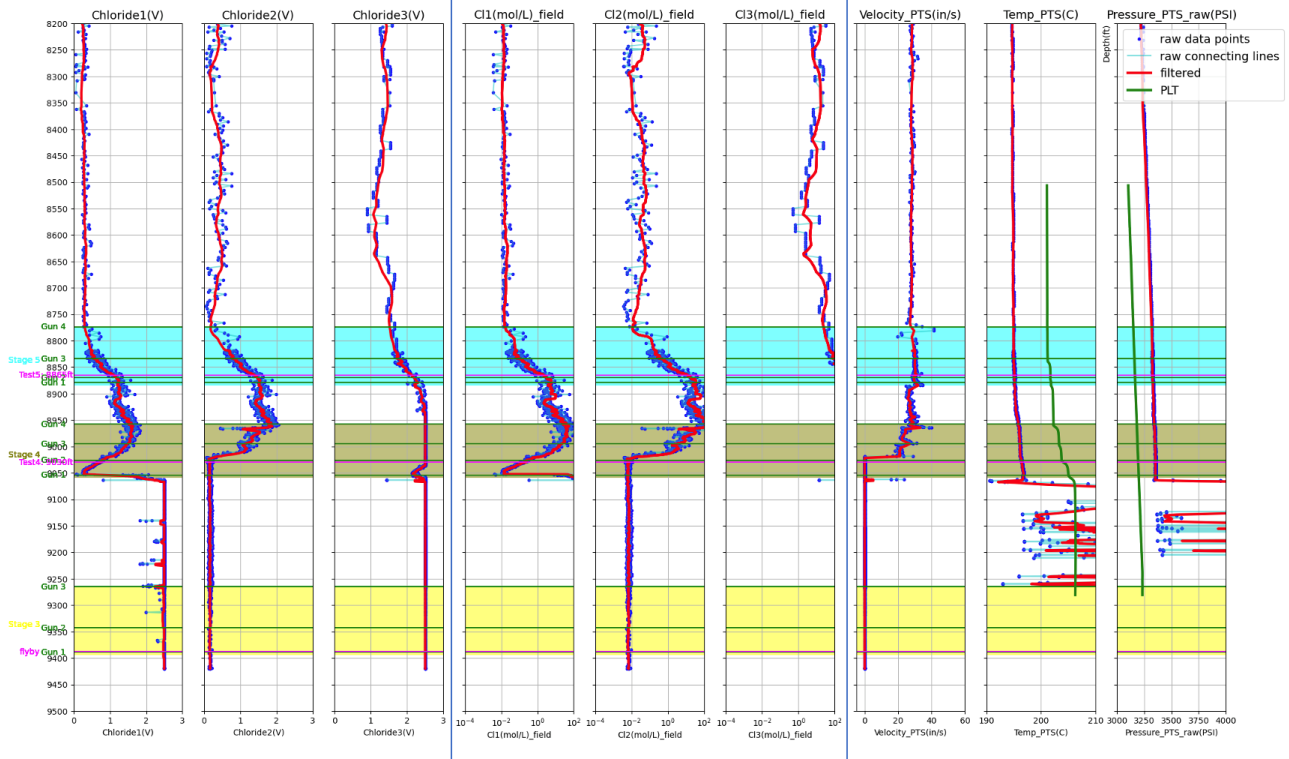


Figure 5-12: well logs from Pull out of Hole (POOH) run at 16B zonal depths.

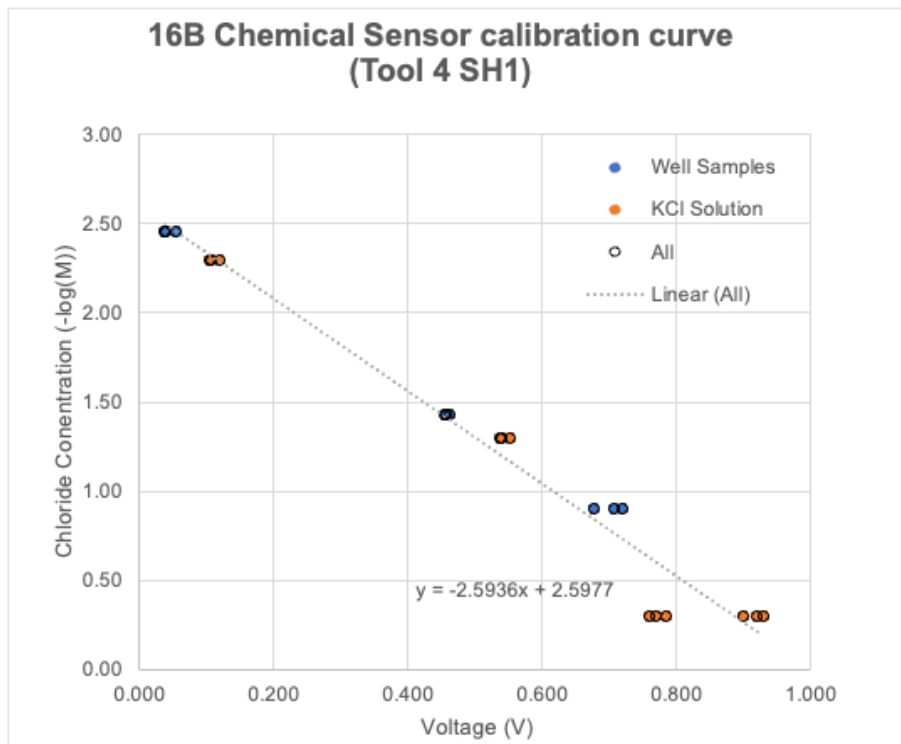
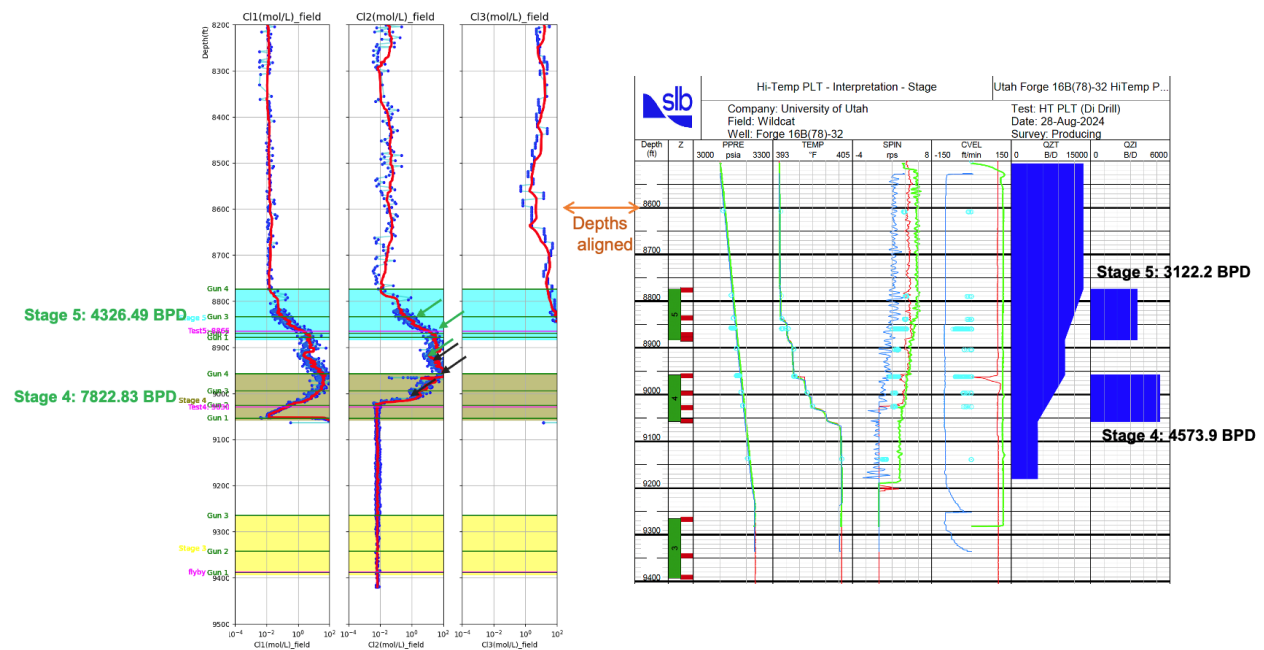


Figure 5-13: calibration curve for the chloride sensors used for 16B logging.

Similar principles apply to reading the results, which show that a spike in voltage correlates with an increase in chloride concentration, indicating inflow presence. If accompanied by a temperature spike from the geofluid entering the wellbore, the voltage spike indicates inflow. Such spikes can be observed in Stage 5 and Stage 4 in both RIH and POOH. Moreover, similar to the observations in wells 58-32 and laboratory experiments, chloride measurements at 16B(78)-32 are noticeably more stable and consistent during the POOH run than in the RIH run. Therefore, the inflow analysis was conducted using POOH data (Figure 5-14).

Utilizing the formula developed to convert chloride concentration readings into flow rates (Equation 3-3), several reading points were selected at Stage 5 and Stage 4 to provide information on chloride concentration above, at, and below the feed zones, indicated by arrows in Figure 4. The calculation yields flow rates of 4326.49 BPD for Stage 5 and 7822.83 BPD for Stage 4, respectively. Compared to the flow rate calculation from the PLT log obtained a week later by SLB, the flow rate calculated using the chloride method is within the expected range of agreement.



**Figure 5-14:** Comparison of POOH chloride signal and PLT interpretation performed by SLB on 28 Aug 2024 (around one week later).

# Chapter 6

## Post-Deployment Improvements

A series of comprehensive tests were conducted after the lab and field deployments to further evaluate the performance and reliability of ion-selective electrodes (ISEs) and determine methods for future improvements. This investigation included bench-top testing of three variations of ISEs with varied ratios of chemical compositions to assess how these modifications impacted sensor functionality. Additionally, a new platinum-iridium reference sensor was introduced, aiming to provide improved stability and accuracy in measurements. To complement these evaluations, scanning electron microscopy (SEM) images of the sensors were collected, offering valuable insights into their structural characteristics and surface morphology. The overarching goal of this additional testing was to deepen the understanding of the chemical sensors employed and to identify potential changes that could enhance the reliability and repeatability of the sensors for future applications.

### 6.1 Additional Ion Selective Electrode Studies

The additional testing involved preparing three different ratios of silver sulfide ( $\text{Ag}_2\text{S}$ ) and silver chloride ( $\text{AgCl}$ ) powders for the ion selective electrode: 25:75, 50:50, and 75:25. Each ion selective electrode (ISE) was connected to a new platinum-iridium (PI-Ir) reference electrode, chosen for its excellent conductivity and chemical stability, which should ensure a consistent reference potential in various environments. The platinum-iridium alloy's resistance to corrosion and low electrical noise should enhance measurement accuracy and reliability. As a benchmark, the  $\text{AgCl}$  reference electrode used in the lab and field scale testing was also used as a reference electrode for the newly fabricated ion-selective electrodes.

The ISEs were interfaced with a National Instruments (NI) Data Acquisition (DAQ) system for precise data collection and tested in three potassium chloride ( $\text{KCl}$ ) molar solutions: 0.005, 0.05, and 0.5 mol/L. This setup (shown in Figure 6-1) allowed for a comprehensive assessment of the sensors' performance across a range of chloride concentrations. To ensure the reliability of the results, each sensor was tested three times in each molar solution, enabling an evaluation of both repeatability and stability in the measurements obtained.

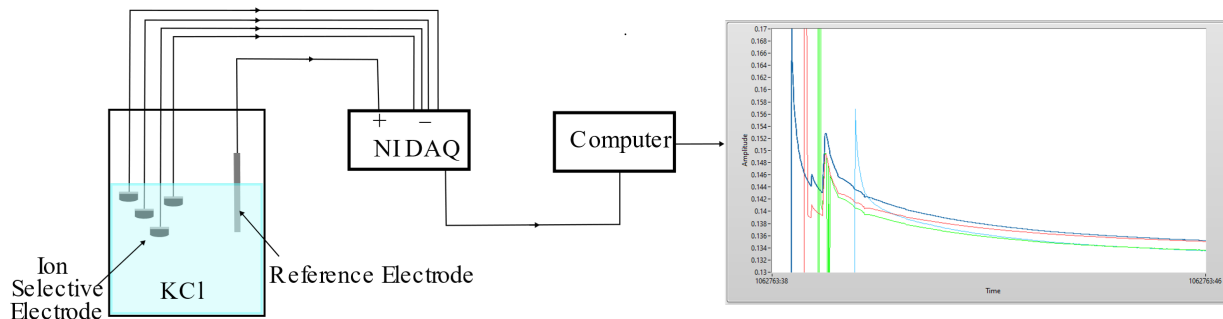


**Figure 6-1:** Benchtop test setup for ion selective electrode and reference electrode pair.

The results summarized in Figure 6-2 through Figure 6-4 indicate that the platinum-iridium reference does not provide a stable and repeatable reference for the AgCl/Ag<sub>2</sub>S CI-ISE. This reference was tested with each AgCl/Ag<sub>2</sub>S sensor variation at ambient (Figure 6-2) and elevated (Figure 6-3) temperatures and showed very low repeatability and little to no linear relationship between the molarity of the solution and the voltage output. The AgCl Reference pellet used in the lab and field scale testing was tested for a comparison to this new reference electrode. As shown in Figure 6-3, this reference provides a more stable and repeatable reference, as is indicated by the lower deviation between trials and higher R<sup>2</sup> value between the solution molarity and voltage output. More testing and studies are needed to understand why the platinum-iridium reference did not provide a more stable reference.

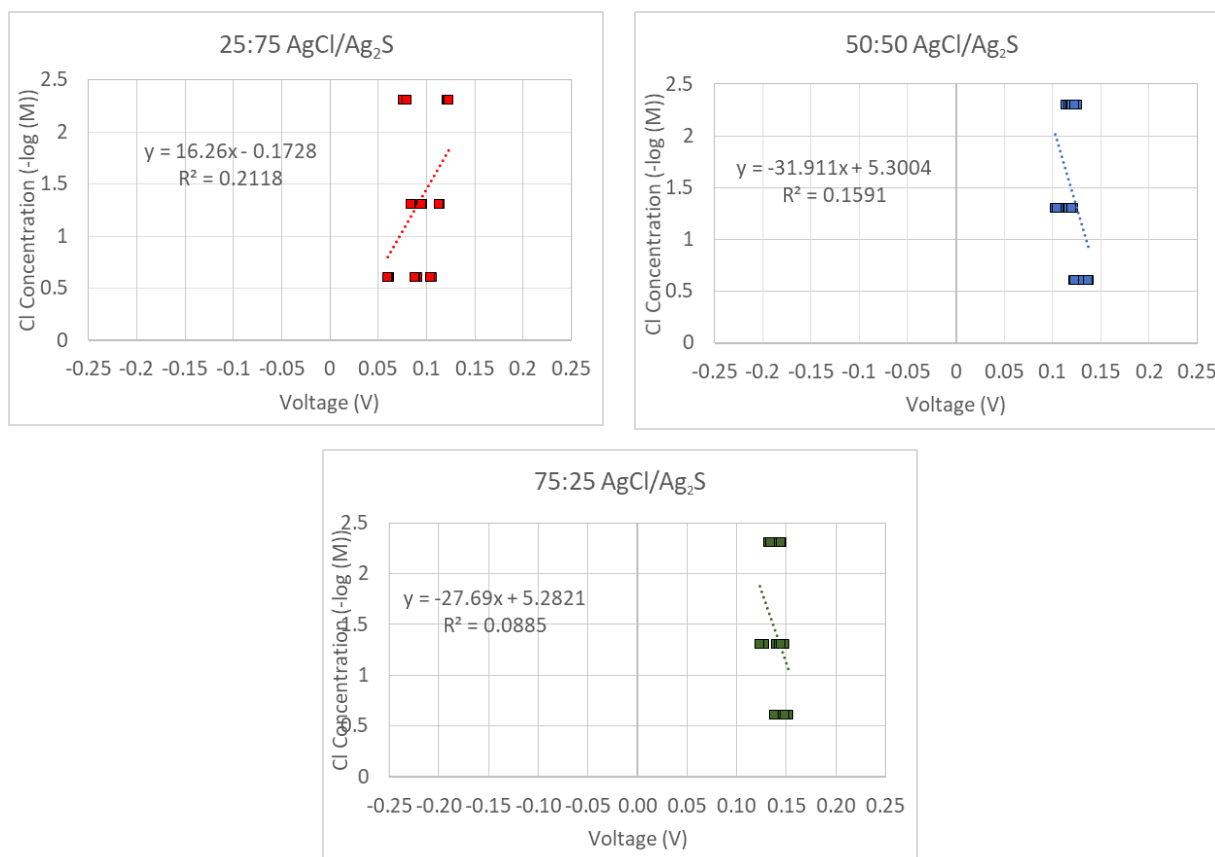


**Figure 6-2:** Calibration test of Platinum-Iridium (PI-Ir) reference electrode and AgCl/Ag<sub>2</sub>S sensor variations (25:75, 50:50, and 75:25 AgCl:Ag<sub>2</sub>S) in three molar solutions of KCl at ambient temperature.

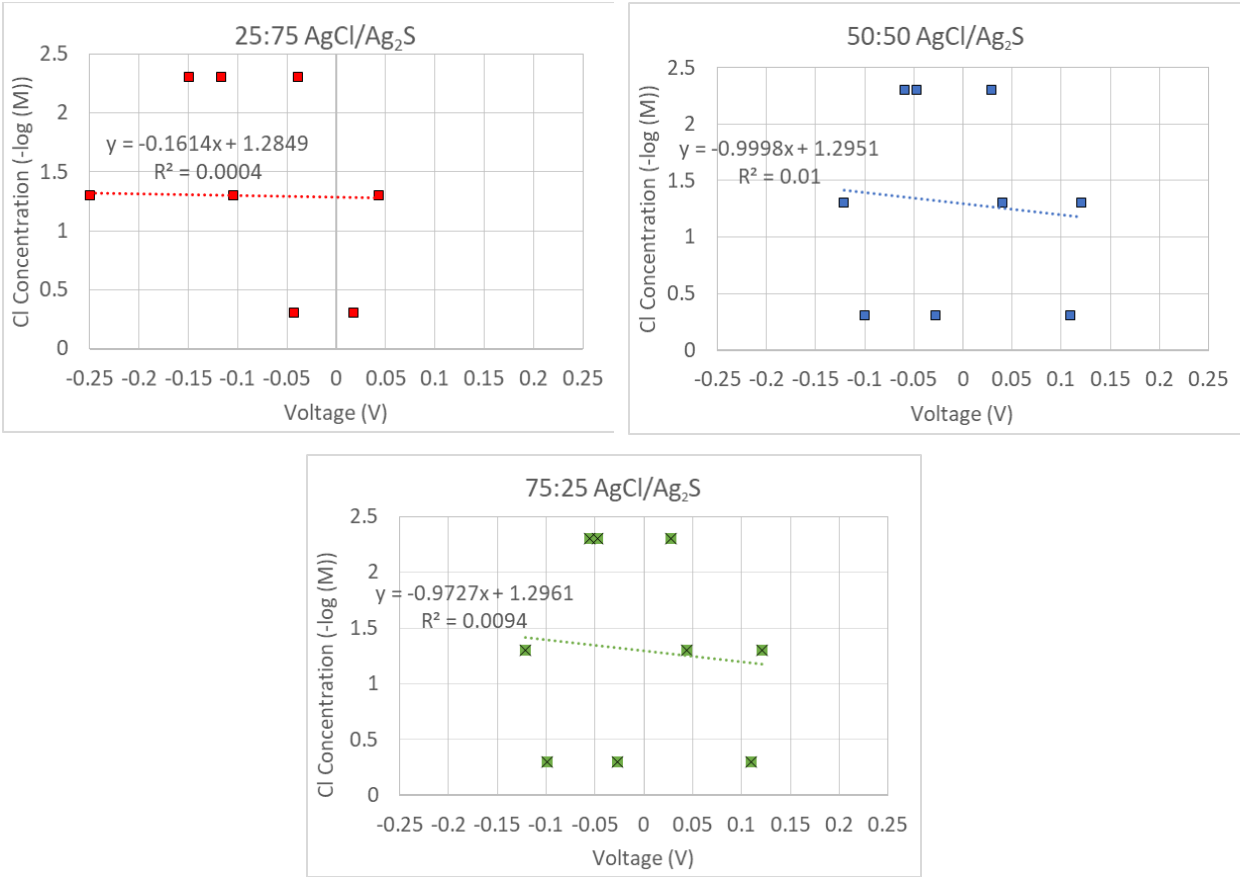


**Figure 6-3:** Calibration test of Platinum-Iridium (Pt-Ir) reference electrode and AgCl/Ag<sub>2</sub>S sensor variations (25:75, 50:50, and 75:25 AgCl:Ag<sub>2</sub>S) in three molar solutions of KCl at elevated temperature (80°C).

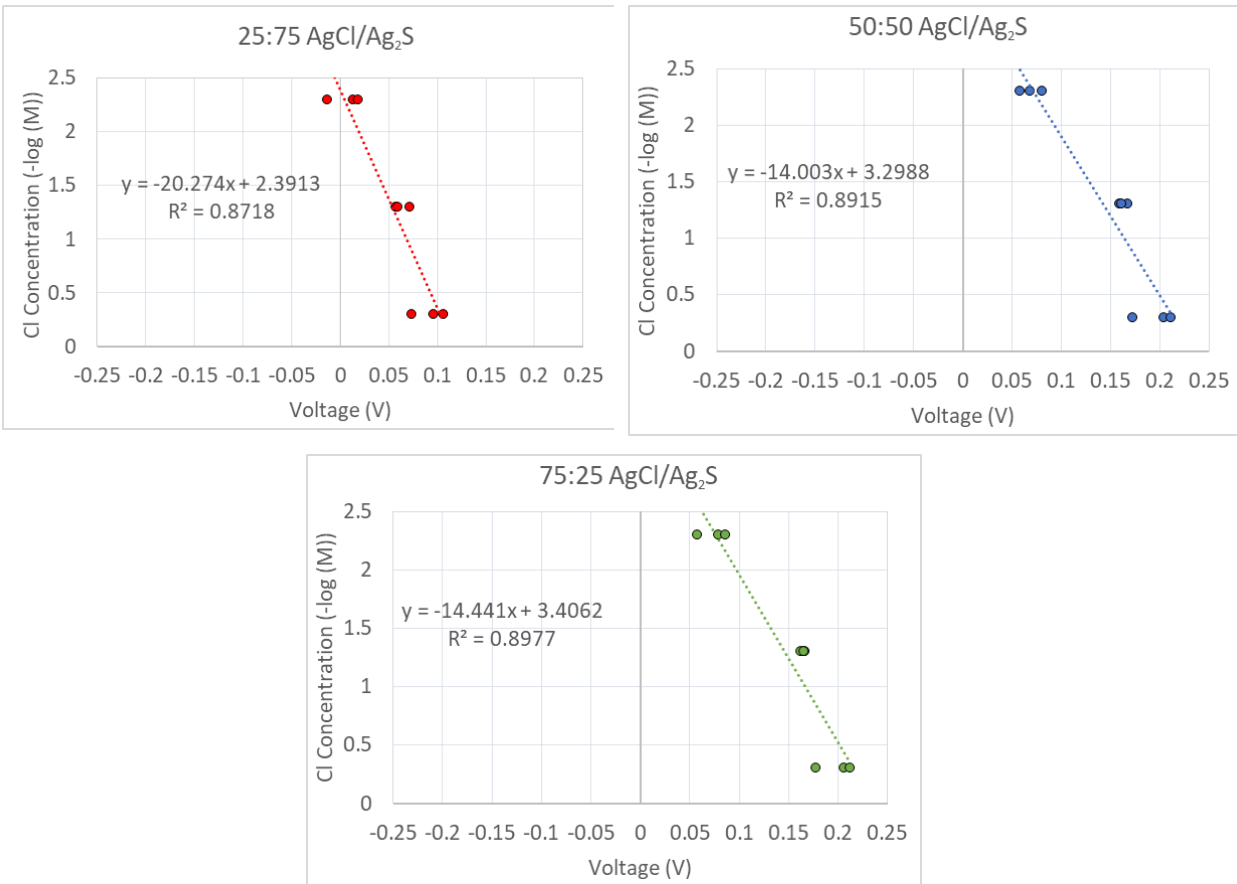


**Figure 6-4:** Calibration test of Silver Chloride (AgCl) reference electrode and AgCl/Ag<sub>2</sub>S sensor variations (25:75, 50:50, and 75:25 AgCl:Ag<sub>2</sub>S) in three molar solutions of KCl at elevated temperature (85°C).

Table 6-1 summarizes each of the tests comparing the reference electrodes and ISE variations in terms of the  $R^2$  value between voltage and the Cl concentration and the slope of the linear relationship. The ideal sensor and reference electrode pair should show a high  $R^2$ , indicating a strong relationship between voltage output and molarity, and a low slope, indicating a detectable change in voltage with changing molarity. In these terms, the ideal sensor-reference pair is the 50:50 AgCl/Ag<sub>2</sub>S ISE and the AgCl reference, which is what was used in the lab and field scale testing. Further testing is needed to determine if another reference is more suitable or if altering the ion-selective electrode in another way, i.e. varying the porosity or surface finish, would improve the repeatability and stability of the measurements.

**Table 6-1:** Summary of bench top test results comparing reference electrodes (Pt-Ir and AgCl) and ISE variations (25:75, 50:50, and 75:25).

Ion-Selective Electrode	Reference Electrode	Temperature (°C)	R <sup>2</sup>	Slope, m
25:75 AgCl/Ag <sub>2</sub> S	Pt-Ir	25	0.2118	16.260
50:50 AgCl/Ag <sub>2</sub> S	Pt-Ir	25	0.1591	-31.911
75:25 AgCl/Ag <sub>2</sub> S	Pt-Ir	25	0.0885	-27.690
25:75 AgCl/Ag <sub>2</sub> S	Pt-Ir	80	0.0004	-0.161
50:50 AgCl/Ag <sub>2</sub> S	Pt-Ir	80	0.0100	-1.000
75:25 AgCl/Ag <sub>2</sub> S	Pt-Ir	80	0.0094	-0.973
25:75 AgCl/Ag <sub>2</sub> S	AgCl	80	0.8718	-20.274
50:50 AgCl/Ag <sub>2</sub> S	AgCl	80	0.8915	-14.003
75:25 AgCl/Ag <sub>2</sub> S	AgCl	80	0.8977	-14.441

## 6.2 Scanning Electron Microscope (SEM)

In this section, we detail the data acquisition and analysis processes utilized to investigate the surface characteristics and elemental composition of ion-selective electrode pellets. Scanning electron microscope (SEM) images were collected on a SNE-ALPHA benchtop instrument by SEC at 30 kV accelerating voltage electron beam. Energy dispersive X-ray spectroscopic (EDX) data were collected in tandem with the SEM benchtop instrument using a Bruker SCU elemental analyzer.

Three pellets comprised of AgCl and Ag<sub>2</sub>S in various weight percent ratios were examined *via* SEM microscopy (Figure 6-5). At lower magnifications (500 and 1000x), each pellet displays large grooves on the surface ranging from 20 – 50 μm in width. These features are consistent between samples and do not appear to arise from any difference in composition and are likely an artifact of the pellet preparation process to sand the pellets after sintering. The 50:50 AgCl:Ag<sub>2</sub>S sample displayed a substantial amount of particulates on the surface of the pellet; these particles were approximately 10 – 20 μm in size and were uniformly distributed.

Elemental mapping of the surface of the pellets (Figure 6-6) was done to examine the distribution of AgCl to Ag<sub>2</sub>S. The distribution of chloride (pink) to sulfide (teal) for each pellet can be seen in Figure 6-3 below. In the 25:75 AgCl:Ag<sub>2</sub>S pellet, the sulfide species is clearly dominant, and the chloride particles are dispersed fairly evenly. Clear domains of AgCl are visible and range in size from 5 – 20 μm. The 50:50 AgCl:Ag<sub>2</sub>S pellet is expected to have a more equal distribution, and more chloride domains are visible than in the 25:75 sample. However, the AgCl is more localized with several large (20 – 50 μm) regions in addition to smaller 5 μm particles evenly spaced. The 75:25 AgCl:Ag<sub>2</sub>S pellet showed the expected increase in chloride distribution, and the sulfide species was distributed homogeneously. Overall, the elemental mapping data show the expected trend of increasing chloride content when increasing its weight percent during pellet preparation. This is supported by Table 6-2 below, which shows the mass % and atom % distributions for the areas imaged. The Ag content stays

mostly constant between samples as expected, and chlorine percentages increase with higher weight % loadings; the same trend for sulfur is observed.

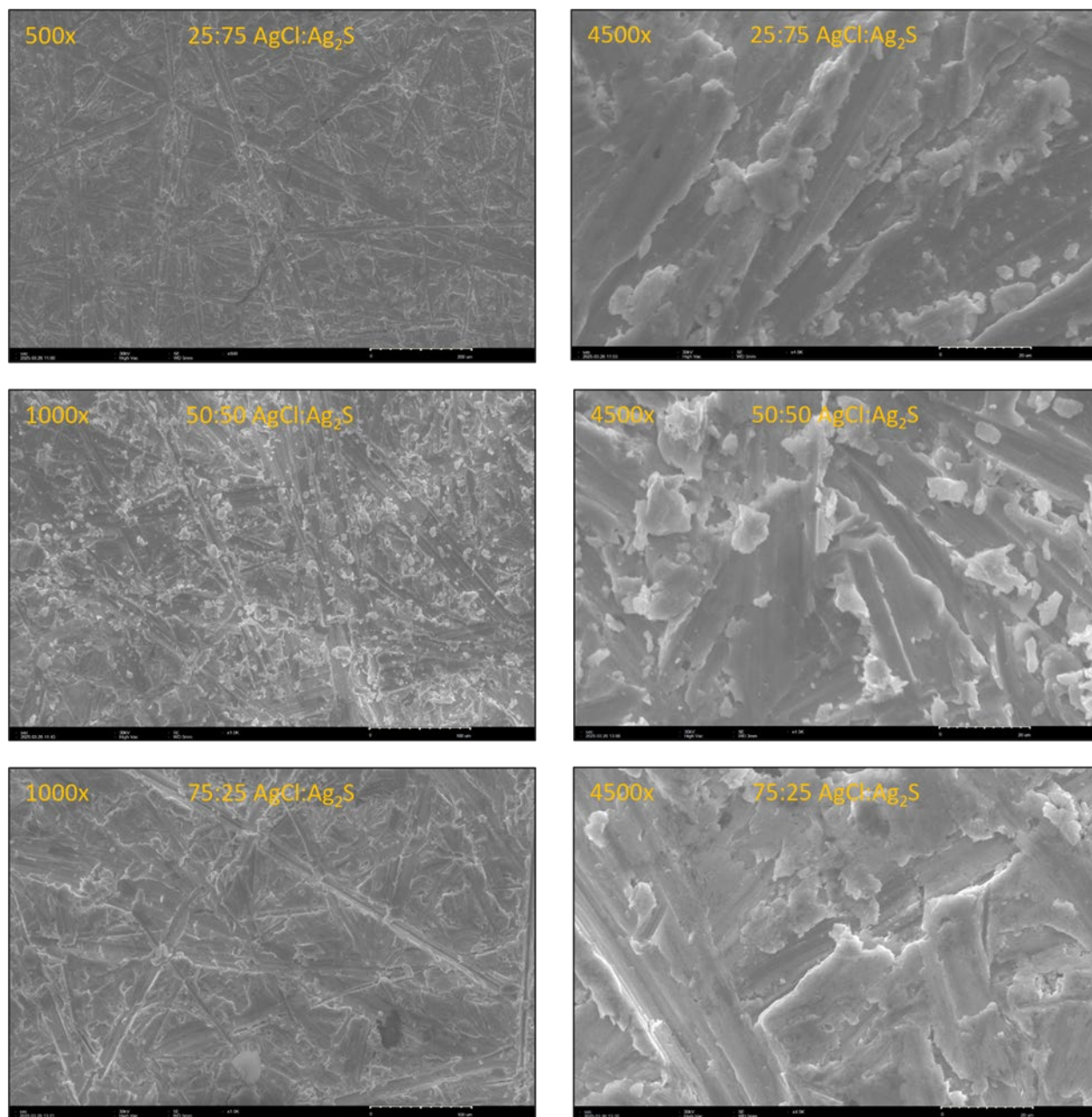


**Figure 6-5:** SEM images of three pellet samples obtained under 30 kV beam voltage.

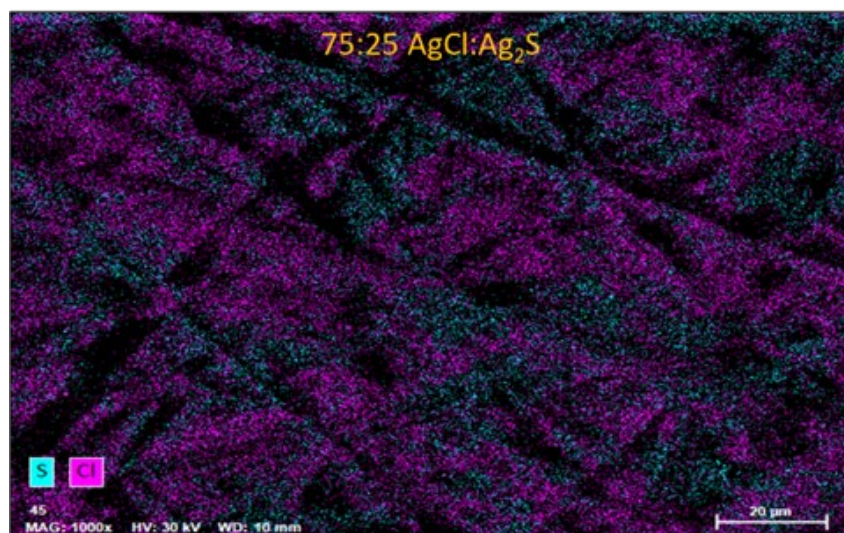
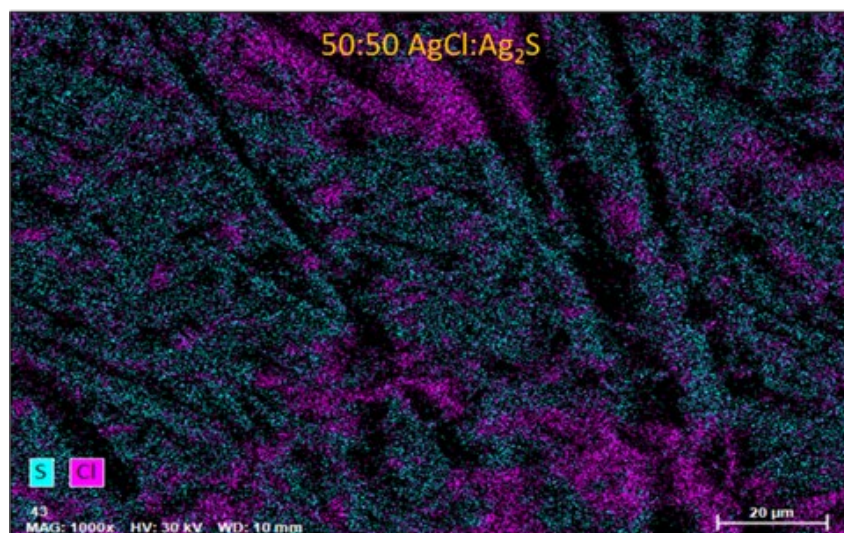
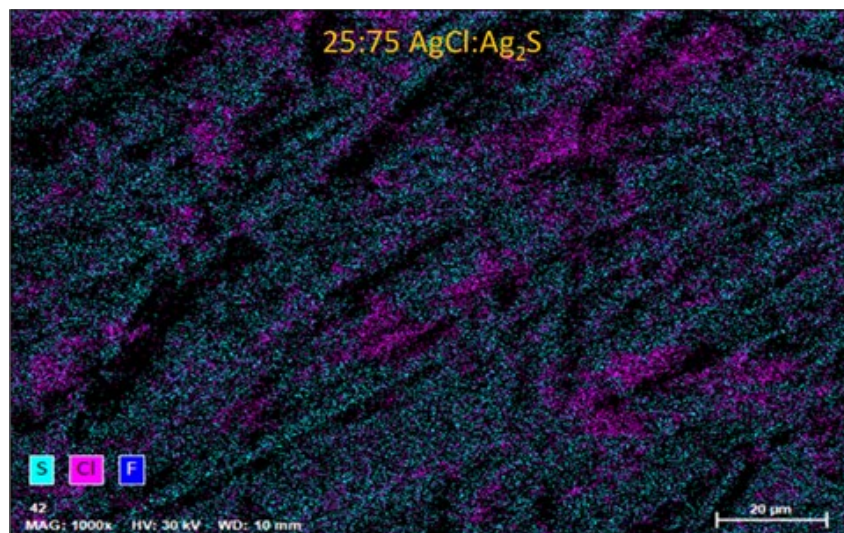


**Figure 6-6:** Comparison of the EDX elemental mapping of chlorine and sulfur atoms in the three pellets.

**Table 6-2:** EDX elemental quantification data for each sample analyzed at 1000x magnification.

Element	25:75 AgCl:Ag <sub>2</sub> S		50:50 AgCl:Ag <sub>2</sub> S		75:25 AgCl:Ag <sub>2</sub> S	
	Mass %	Atom %	Mass %	Atom %	Mass %	Atom %
Ag	52.82	25.31	51.04	24.20	47.96	22.69
Cl	8.73	12.73	15.18	21.90	36.37	52.36
S	38.45	61.97	33.79	53.90	15.68	24.95

### 6.3 Porosity

Another method to tune the sensitivity of the chloride sensors is to tune the system's porosity. Alterations to the porosity of a sensor system impact many aspects of the sensor, such as sensitivity, response time, and efficiency. These performance impacts are downstream effects from modifications to core properties such as the surface area, mass transport, accessibility to active sites, and surface-to-volume ratio. Each of these modifications can result in changes to stability, potential, and efficiency in these systems.

The sensor's porosity directly impacts the device's surface area, which impacts the sensitivity. The porosity, in terms of overall porosity and the size of the pore, changes the analyte solution's access to active sites on the sensor. A larger surface area overall leads to more accessibility of sensing sites, which increases signal response (Baig et al., 2021; Khan et al., 2024). Changes in the porosity of the system additionally impact the diffusion of analyte to the sensor, which in turn has a significant impact on critical performance properties such as response time and sensitivity. Since electrochemical sensors rely on the analyte diffusing to the electrode surface to generate a measurable signal, increased porosity can change the diffusion rate and, thus, the sensor response (Sedlak et al., 2020).

In the currently studied system, pellets were pressed at a force of 4000 lbs. By varying the pressing force, we might change the porosity in the resulting sensor pellet. Additionally, the utilization of binders or other additives might be incorporated to ensure that lower pressures still result in a robust, self-standing pellet. These samples, which have been prepared using various pressures (and presumably possessing differing porosities), would be subject to gas absorption analysis to determine the gas uptake (and porosity) of the system by determining the Brunauer-Emmett-Teller (BET) surface area (Howarth et al., 2017). Scanning electron microscopy could be used as a supplemental tool to evaluate the porosity of the systems visually.

Other factors that might impact the surface area are the particle size of the precursor materials. Ball-milling at various times could be used as a handle to modify the particle size and mixing of the precursor materials reproducibly.

# Chapter 7

## Conclusions and Future Work

### 7.1 Conclusions

A novel approach was developed to map flowing fractures and estimate their flow magnitudes in real-time at the Utah FORGE site. The research was motivated by observations from DOE's EGS Collab project, where direct visualization of water flow into production wells through fractures provided valuable insights into fracture network topology. Building upon a joint 2017 project between Sandia and Stanford that developed a downhole tool concept for measuring chloride ion concentration, our work focused on adapting this technology for FORGE deployment at 225°C temperatures. The tool's capability to accurately measure chloride concentration with slight differences from wellbore water, enabled the detection of individual fractures and estimation of their flow volumes.

The project was structured in three phases: first, modifying and stress-testing the existing Sandia downhole tool under simulated FORGE conditions; second, deploying the tool at FORGE to characterize fractures produced during previous stimulation efforts; and third, analyzing the tool's effectiveness and refining its elements based on field experience. The findings from this research is summarized in this section.

#### *Tool fabrication*

Ion-selective electrodes (ISEs) were developed to measure chloride concentrations in geothermal systems. The chloride ISE sensors were fabricated using equal parts by mass of AgCl and Ag<sub>2</sub>S powders pressed into cylindrical pellets at 4000 lbs of pressure and sintered at 200°C. Multiple reference electrode iterations were evaluated, including an experimental solid-state multilayered pellet and a single-layer AgCl pellet, with the latter ultimately selected for field deployment due to comparable performance and reduced fabrication complexity. Various sealing methods were tested to protect the electrodes in high-temperature, high-pressure environments, culminating in a final design using CuAg-plated pellet wire adapters and Gagekote #1 protective coating rated up to 455°C. Extensive autoclave testing was conducted to verify the sensors' ability to withstand Utah FORGE conditions (225°C and up to 5000 psi). The sensors demonstrated reliable performance during extended duration tests exceeding 24 hours, with consistent voltage responses that showed temperature dependence but minimal pressure sensitivity. These results confirmed that the chemical tool probes could withstand the targeted temperature and pressure conditions specified for field deployment.

A laboratory-scale tool was initially developed using a tubular housing unit with electrodes at the front end and a data transmission cable at the rear, which was later updated in 2023 to address calibration issues. For field deployment, a comprehensive system was designed incorporating the Mitco PTS sensor package for secondary downhole measurements. The field-deployable chemical sensor housing

was specially designed to allow flow interaction with the sensors and included retainer slots for ISE sensors, reference electrodes, and pH sensors. Three sensor housings were manufactured and pressure-tested to ensure safety and leak resistance. A high-temperature logging tool was developed using a Honeywell HT83C51 microcontroller and Sandia custom high-temperature Application-specific Integrated Circuit, along with a Chemical Buffer Amplifier board to accommodate additional sensor inputs. Two versions of the high-temperature logging tool were assembled and tested, with a secondary backup system using an EV-HT-200CDAQ1 platform from Analog Devices. A LabView user interface was developed for real-time data display and recording capabilities, ensuring compatibility with both primary and secondary logging tools.

### ***Analytical solution and data-driven inferences***

Analytical solutions were developed to calculate feed zone inflow rates from chloride concentration measurements in geothermal wells. The mass balance principle was applied to establish relationships between flow rates at different points in the wellbore, with equations derived for both single and multiple feed zone scenarios. Error estimation and modeling were conducted to understand how measurement errors affect flow rate calculations, revealing that errors adversely impact calculations at and below feed zones but have less effect above feed zones. The Nernst equation was utilized to relate the potential difference between reference electrodes and chloride ISE probes to ion concentration, establishing that the relationship between the negative common logarithm of chloride concentration and voltage reading.

Machine learning models were developed using data from numerical simulations and laboratory experiments to enhance feed zone detection and flow rate prediction. For simulation data, Random Forest algorithms performed best for both classification (feed zone presence) and regression (flow rate prediction) tasks, achieving up to 99.94% accuracy in predicting feed zone presence. Statistical analysis identified key variables influencing prediction accuracy, including chloride concentration, feed zone indicators, and turbulence terms. For laboratory experiment data, LGBM models demonstrated superior performance after hyperparameter tuning, achieving 87.56% accuracy in feed zone classification with feature engineering that incorporated voltage change data. The models showed particular strength in approximating feed zone locations, with accuracy increasing to 93% when allowing for minimal error tolerance. While the approach was successful for single feed zone characterization, application to dual feed zone scenarios yielded less satisfactory results, suggesting the need for additional training with dual feed zone data for future improvements.

### ***Round 1 numerical simulations and laboratory experiments***

In Round 1, laboratory experiments and numerical simulations were conducted to investigate fluid flow behavior and understand the chloride tool's capabilities. Tubular lab-scale tools (versions 1 and 2) were calibrated, showing an inverse relationship between chloride concentration and voltage measurements. Static experiments revealed that tool placement significantly affected measurement accuracy, with positioning directly in front of the feed zone yielding better results than center placement. Dye tracer tests demonstrated non-uniform mixing phenomena, including blind spots in the wellbore that varied with injection flow rates. Dynamic experiments successfully captured voltage drops around injection points, though with measurement delays between Run-in-Hole (RIH) and Pull-Out-of-Hole (POOH) motions. Numerical simulations validated these laboratory observations, showing that higher injection rates led to greater voltage drops and that approximately 20-35% of actual chloride concentration was measured due to dispersion effects. The presence of the tool in the wellbore improved fluid mixing and increased measurement accuracy to 30-70% of actual concentration.

The Round 1 investigations demonstrated that the chloride tool could effectively detect feed zones and provide qualitative indications of chloride concentration, though quantitative accuracy was influenced by several factors. It was found that tool positioning, feed zone flow rates, and wellbore internal flow significantly impacted measurement results. Simulations showed that a multipronged electrode design could improve detection capability for low inflow rates. For optimal results, it was determined that the tool should be centralized in the wellbore, and measurements should be taken within feed zone jets. These findings provided valuable insights for refining the tool design and measurement methodology for field deployment.

### ***Round 2 numerical simulations and laboratory experiments***

In Round 2, preparations were made for field deployment at Utah FORGE wells through further numerical simulations and laboratory experiments. Simulations under Utah FORGE pressure and temperature conditions (225°C and 5000 psia) showed no substantial difference in fluid flow behavior compared to ambient conditions. Various housing unit designs were tested, with the final multipronged caged design (Version 3) selected for its ability to accurately receive voltage readings regardless of feed zone orientation. The artificial well system was modified with updated pumps, water lines, and EMF interference reduction measures. Calibration of the lab-scale tool with housing showed a strong linear relationship between voltage and the negative logarithm of chloride concentration, though with opposite behavior compared to Round 1 calibrations.

Static and dynamic experiments in Round 2 revealed several important findings for field deployment. It was discovered that regular rinsing of ISE probes with isopropyl alcohol significantly improved measurement consistency by removing residual ions. The tool demonstrated sensitivity to chloride concentrations within the range expected at Utah FORGE (up to  $1.24 \times 10^{-1}$  mol/L). Vertical positioning of the tool relative to feed zones significantly affected measurements, with positions above or even with feed zones yielding better results than positions below feed zones. The experiments also showed that ISE probe #2 provided more accurate measurements than ISE probe #3, which exhibited inconsistent voltage responses. These findings provided critical insights for optimizing field deployment methodology and interpreting field data.

### ***Field deployment***

The tool was deployed successfully in two FORGE wells: the vertical monitoring well 58-32 (7,536 ft depth) and the deviated production well 16B(78)-32 (10,947 ft depth). In Well 58-32, despite initial challenges with leaks and microcontroller issues, data were successfully collected during the third deployment attempt. No significant inflow was detected in the logged interval, with voltage spikes near Zone 1 not being interpreted as flow due to the absence of corresponding PTS counter changes. The pull-out-of-hole (POOH) data provided cleaner readings than the run-in-hole (RIH) data, consistent with laboratory findings.

The deployment in Well 16B(78)-32 was conducted during a 30-day circulation test, with the tool successfully reaching approximately 9,480 ft and withstanding temperatures up to 210°C. Significant inflow was detected in Stages 4 and 5, with voltage spikes correlating with increased chloride concentration. Using the chloride concentration readings, flow rates were calculated at 4,326.49 BPD for Stage 5 and 7,822.83 BPD for Stage 4, which aligned with the Pressure-Temperature-Spinner (PLT) log obtained by Schlumberger approximately one week later. It was observed that the chloride measurements were notably more stable during the POOH run compared to the RIH run, reinforcing findings from both the 58-32 deployment and previous laboratory experiments. These results validate

the effectiveness of our geochemistry-based approach for detecting and quantifying inflow in geothermal wells.

### ***Post-deployment Improvements***

Comprehensive testing was conducted to evaluate the performance of ion selective electrodes (ISEs) with various chemical compositions. Three different ratios of silver sulfide ( $\text{Ag}_2\text{S}$ ) and silver chloride ( $\text{AgCl}$ ) powders (25:75, 50:50, and 75:25) were prepared and tested with both a new platinum-iridium reference electrode and the previously used  $\text{AgCl}$  reference electrode. These sensors were tested in potassium chloride solutions of varying concentrations (0.005, 0.05, and 0.5 mol/L) at both ambient and elevated temperatures. It was determined that the platinum-iridium reference did not provide the expected stability and repeatability, exhibiting low correlation between solution molarity and voltage output. In contrast, the  $\text{AgCl}$  reference electrode demonstrated superior performance, particularly when paired with the 50:50  $\text{AgCl}/\text{Ag}_2\text{S}$  ISE configuration that was utilized in our previous lab and field testing.

Scanning electron microscopy (SEM) and energy dispersive X-ray spectroscopy (EDX) analyses were performed to examine the surface characteristics and elemental composition of the sensor pellets. The images revealed consistent surface features across samples, with grooves of 20-50  $\mu\text{m}$  in width likely resulting from the post-sintering sanding process. Elemental mapping confirmed the expected distribution of chloride and sulfide species corresponding to the prepared ratios, with the 50:50 mixture showing more localized  $\text{AgCl}$  regions.

## **7.2 Future Work**

Proposed future studies for the geochemistry tool are as follows:

- Additional research into the causes of voltage fluctuations observed could lead to more stable sensor performance.
- Development of more robust algorithms that are less sensitive to measurement errors. In particular, integration of the analytical approach with machine learning models could provide a more comprehensive solution that leverages the strengths of both methodologies.
- Development of automated calibration procedures that account for temperature dependence would improve field measurement accuracy.
- Exploration of alternative sealing methods and materials could further improve sensor durability in extreme conditions.
- Investigation on whether alternative reference electrodes or modifications to the ISE, such as varying porosity or surface finish, could enhance measurement repeatability and stability for future applications.

# References

- Baig, N.; Waheed, A.; Said, M.; Khan, I.; Kawde, A-N.; Sohail, M. Porous graphene-based electrodes: Advances in electrochemical sensing of environmental contaminants *TrEAC*, 30, e000120 (2021).
- Burton, A.: OLS (Linear) Regression., *The Encyclopedia of Research Methods in Criminology and Criminal Justice* (pp.509 - 514), Chapter: 104, Wiley (2021).
- Cunningham, Pdraig, and Sarah Jane Delany.: k-Nearest neighbour classifiers: (with Python examples), arXiv preprint arXiv:2004.04523 (2020).
- Egan, S.: Development of a Robust Solid-State Reference Electrode, *New Mexico Institute of Mining and Technology, ProQuest Dissertations & Theses* (2020). 28157416.
- Fluent Inc., “Fluent 6.3 Getting Started Guide” (2006).
- Gao, X., Egan, S., Corbin, W.C., Hess, R.F., Cieslewski, G., Cashion, A.T., and Horne, R.N.: Analytical and Experimental Study of Measuring Enthalpy in Geothermal Reservoirs with a Downhole Tool, *GRC Transactions*, Vol. 41, (2017).
- Gao, X.: Development of a Downhole Technique for Measuring Enthalpy in Geothermal Wells. MS Thesis Report, Department of Energy Resources Engineering, Stanford University, (2017).
- Gholami, R., Fakhari, N.: Chapter 27 - Support Vector Machine: Principles, Parameters, and Applications, *Handbook of Neural Computation*, Academic Press, (2017).
- Howarth, A. J.; Peters, A. W.; Vermeulen, N. A.; Wang, T. C.; Hupp, J. T.; Farha, O. K. Best Practices for the Synthesis, Activation, and Characterization of Metal-Organic Frameworks. *Chem. Mater.*, 29, 1, 26-39 (2017).
- Khan, A. A.; Rabi, S. N.; Jamee, T.; Galib, M.; Elahi, F.; Rahman, A. Effects of Crumpling Stage and Porosity of Graphene Electrode on the Performance of Electrochemical Supercapacitor. *J. Phys. Chem. B.*, 128, 39, 9586-9597 (2024).
- Kumar, M.: Ultrasonic Rate Measurements in Two-Phase Bubble Flow. MS Thesis Report, Department of Petroleum Engineering, Stanford University, (1995).
- Nyachhyon, A.; Manandhar, K.; Pradhananga, R.R.: Preparation of halide sensors by means of co-precipitation of silver sulphide and silver halide, *J. Nepal Chem. Soc.*, 30, 168-173 (2012).
- Okoroafor, E.R., Smith, C.M., Ochie, K.I., Nwosu, C.J, Gudmundsdottir, H., Aljubran, M.: Machine Learning in Subsurface Geothermal Energy: Two Decades in Review, *Geothermics*, Volume 102, <https://doi.org/10.1016/j.geothermics.2022.102401>, (2022).
- Ranstam, J., Cook, J.A.: LASSO Regression, *British Journal of Surgery*, Vol 105, Issue 10, (2018).
- Schonlau, M., Zou, R.Y.: The Random Forest Algorithm for Statistical Learning, *The Stata Journal* 20, Number 1, pp. 3-29 (2020).

- Sedlak, P.; Kubersky, P. The Effect of the Orientation Towards Analyte Flow on Electrochemical Sensor Performance and Current Fluctuation. *Sensors*, 20, 4, 1038 (2020).
- Shahdi, S., Lee, A., Karpatne, B., Nojabaei: Exploratory Analysis of Machine Learning Methods in Predicting Subsurface Temperature and Geothermal Gradient of Northeastern United States. *Geotherm. Energy*, 9 (18), 10.1186/s40517-021-00200-4, (2021).
- Stoltzfus, J.C.: Logistic Regression: A Brief Primer. *Academic Emergency Medicine*, 18: 1099-1104, (2011).
- Tamburello, G., Chiodini, G., Ciotoli, G.: Global Thermal Spring Distribution and Relationship to Endogenous and Exogenous Factors. *Nat Commun* 13, 6378. <https://doi.org/10.1038/s41467-022-34115-w>, (2022).
- Xing, P., England, K., Moore, J., Podgorney, R., and McLennan, J.: "Analysis of Circulation Tests and Well Connection at Utah FORGE", Proceedings 49<sup>th</sup> Workshop on Geothermal Reservoir Engineering, Stanford University, Stanford, California (2024).
- Yurochkin, M., Nguyen, X., Vasiloglou, N.: Multi-way Interacting Regression via Factorization Machines, Proceedings of the 31st Conference on Neural Information Processing Systems (NIPS 2017), Long Beach, CA, USA, arXiv:1709.09301v1 (2021).

# Appendix: Publication List

## Contribution Authors and Abbreviations

Stanford	Sandia
Roland Horne (RH) Sarah Sausan (SS) Luthfan Hafizha Judawisastra (LHJ) Marshall Burdair Hartung (MBH)	Melanie Schneider (MS) Jiann-cherng Su (JS) Andrew Wright (AW) Alfred Cochrane (AC) Taylor Myers (TM) Joseph Pope (JP) Joshua Tafoya (JT) Manny Montano (MM) Sivana Torres (ST) Clayton Curtis (CC) Harrison Root (HR)

GRC: Geothermal Rising Conference

IIGCE: Indonesia International Geothermal Convention & Exhibition

Q: Quarter

SGW: Stanford Geothermal Workshop

SPE: Society of Petroleum Engineers

No	Date and event	Contents	Contributors	Publication Number
1	January 2022 (Q1 report)	<ul style="list-style-type: none"> <li>Analytical solution and error modeling</li> <li>Round 1 Initial calibration and static laboratory experiments</li> <li>Preliminary search for suitable well to deploy</li> </ul>	SS, LHJ, RH	
2	January 2022 (SGW 2022), first publication	<ul style="list-style-type: none"> <li>Analytical solution and error modeling</li> </ul>	SS, LHJ, RH	1

		<ul style="list-style-type: none"> <li>• Round 1 Initial calibration and static laboratory experiments</li> <li>• Preliminary search for suitable well to deploy</li> </ul>		
3	April 2022 (Q2 report)	<ul style="list-style-type: none"> <li>• Round 1 calibration</li> <li>• Round 1 numerical simulation on mini-scale</li> </ul>	SS, LHJ, RH	
4	July 2022 (Q3 report)	<ul style="list-style-type: none"> <li>• Round 1 static laboratory experiments with one feed zone injection, including dye tracer tests</li> <li>• Round 1 numerical simulation on mini-scale and comparative modeling with the dye tracer tests</li> </ul>	SS, LHJ, RH	
5	October 2022 (GRC 2022, IIGCE 2022)	<ul style="list-style-type: none"> <li>• Round 1 lab tool calibrations</li> <li>• Round 1 static laboratory experiments with one feed zone injection, including dye tracer tests</li> <li>• Round 1 numerical simulation on mini-scale and comparative modeling with the dye tracer tests</li> <li>• Preliminary search for suitable well to deploy</li> </ul>	LHJ, SS, RH	2, 3
6	January 2023 (Q4 report), Sandia began their work	<ul style="list-style-type: none"> <li>• Sandia was building new version of the sensors that can withstand FORGE pressure and temperature</li> <li>• Reconfiguration of laboratory measurements and numerical simulations to accommodate the upcoming sensor updates</li> </ul>	LHJ, SS, RH	
7	April 2023 (Q5 report)	<ul style="list-style-type: none"> <li>• Round 1 dynamic laboratory experiments begin</li> <li>• Data-driven inferences on flow measurements using laboratory data</li> <li>• Testing tool housing unit Version 1 (elongated spiral design)</li> <li>• Preliminary setup on autoclave testing</li> </ul>	SS, LHJ, JS, RH	
8	January 2023 (SGW 2023)	<ul style="list-style-type: none"> <li>• Sensor fabrication, focusing on reference electrode development</li> <li>• Preliminary setup on autoclave testing</li> </ul>	LHJ, SS, JS, RH	4
9	April 2023 (Q6 report), first	<ul style="list-style-type: none"> <li>• Lab-scale tool overview</li> <li>• ISE probe configuration testing for field tool; Conax compression;</li> </ul>	LHJ, SS, JS, RH	

	quarterly report with Sandia	<p>preliminary design of field tool assembly</p> <ul style="list-style-type: none"> <li>• Autoclave testing</li> <li>• Round 1 using old autoclave (not passing go/no-go target)</li> </ul>		
10	April 2023 (SPE Student Paper Contest manuscript)	<ul style="list-style-type: none"> <li>• Analytical solution and error modeling</li> <li>• Summary of the 2021 – 2023 numerical simulations (Round 1)</li> <li>• Data-driven inference from simulation data</li> </ul>	SS, RH	
11	June 2023 (GRC 2023)	<ul style="list-style-type: none"> <li>• Sensor fabrication, focusing on reference electrode development, with schematics</li> <li>• Lab-scale tool overview (also in Q6 report)</li> <li>• ISE probe configuration testings for field tool; Conax compression; preliminary design of field tool assembly (also in Q6 report)</li> </ul>	SS, LHJ, JS, MS, RH	5
12	June 2023 (Judawisastra's MS thesis)	<ul style="list-style-type: none"> <li>• 2021 – 2023 laboratory experiments (Round 1)</li> <li>• Data-driven inference from lab experiments data</li> </ul>	LHJ, RH	6
13	July 2023 (Q7 report)	Autoclave testing round 2, passes go/no-go	SS, LHJ, JS, MS, RH	
14	Aug 2023 (Sausan's MS report)	<ul style="list-style-type: none"> <li>• Analytical solution and error modeling</li> <li>• 2021 – 2023 numerical simulations (Round 1)</li> <li>• Data-driven inference from simulation data</li> </ul>	SS, RH	7
15	Jan 2024 (Q9 report), Note: no Summer quarterly report	<ul style="list-style-type: none"> <li>• High temperature (HT) Logging tool</li> <li>• Fabrication of sensor housing Version 3</li> <li>• Round 2 (2023-2024) numerical simulations on flow behavior at downhole temperature and pressure, as well as housing design iteration</li> <li>• Round 2 (2023-2024) laboratory experiments on signal interference reduction and tool running mechanism modifications</li> </ul>	MS, JS, SS, MBH, RH	

16	Jan 2024 (SGW 2024)	<ul style="list-style-type: none"> <li>• High temperature (HT) Logging tool</li> <li>• Preliminary field deployment plans</li> <li>• Round 2 (2023-2024) numerical simulations on flow behavior at downhole temperature and pressure, as well as housing design iteration</li> <li>• Round 2 (2023-2024) laboratory experiments on signal interference reduction and tool running mechanism modifications</li> </ul>	MS, SS, MBH, JS, AW, RH	8
17	April 2024 (Q10 report)	<ul style="list-style-type: none"> <li>• chemical sensor housing development (testing)</li> <li>• High temperature (HT) Logging tool; LabView</li> <li>• Fabrication of updated lab tool with housing (version 3, caged design) and additive manufacturing of additional component</li> <li>• Round 2 Numerical simulations for Version 3 housing (caged design)</li> </ul>	MS, SS, MBH, RH	
18	June 2024 (Hartung's thesis)	2023 – 2024 Laboratory Experiments (Round 2)	MBH, RH	9
19	July 2024 (Q11 report)	<ul style="list-style-type: none"> <li>• Round 2 calibrations with the updated lab tool with housing and initial data acquisition</li> <li>• Updates on laboratory experiment setup</li> <li>• Fabrication of sensor housing for field deployment</li> <li>• Preparations for 58-32 deployment</li> </ul>	MS, SS, MBH, RH	
20	Aug 2024 (Sausan PhD proposal)	<ul style="list-style-type: none"> <li>• Summary of the development of analytical solutions and error modeling</li> <li>• Summary of findings from laboratory experiments and numerical simulations (Round 1 and numerical simulations for housing design in Round 2)</li> </ul>	SS, RH	
21	October 2024 (GRC 2024)	<ul style="list-style-type: none"> <li>• Chloride tool field assembly</li> <li>• Chemical sensor fabrication and testing, focusing on ISE fabrication</li> <li>• Sensor testing using Utah FORGE brine</li> </ul>	MS, SS, MH, AW, RH, AC, TM, JP, JT, MM	10

		<ul style="list-style-type: none"> <li>• Chemical sensor housing development</li> <li>• High temperature (HT) Logging tool</li> <li>• experiments</li> <li>• Round 2 laboratory experiments on ion sensitivity, varying inflow rates, and varying chloride concentration at inflow</li> <li>• Field deployment at 58-32</li> <li>• Field deployment plan at 16(B)-32</li> </ul>		
22	October 2024 (Q12 report)	<ul style="list-style-type: none"> <li>• Round 2 static and dynamic experiments</li> <li>• Field deployment at 58-32</li> <li>• Field deployment plan at 16(B)-32</li> </ul>	MS, SS, AC, TM, JP, MBH, RH	
23	Jan 2025 (Q13 report)	Field deployment results and analysis for 58-32 and 16(B)-32	MS, SS, RH	
24	Jan 2025 (SGW 2025)	<ul style="list-style-type: none"> <li>• Round 2 laboratory experiments on ion sensitivity, varying inflow rates, and varying chloride concentration at inflow</li> <li>• Field deployment results and analysis for 58-32 and 16(B)-32</li> </ul>	MS, SS, MBH, RH, AW, MM, ST, CC, HR	11

## Publications

(The number refers to the publication number in the previous table)

1. Sausan, S., Judawisastra, L. H., Horne, R. N.: “Development of Downhole Measurement to Detect Inflow in Fractured Enhanced Geothermal Systems (EGS) Wells”, Proceedings 47<sup>th</sup> Workshop on Geothermal Reservoir Engineering, Stanford University, Stanford, California (2022).
2. Judawisastra, L. H., Sausan, S., Horne, R. N.: Experimental and Numerical Development of Inflow Measurement in Fractured Enhanced Geothermal Systems (EGS) Wells. Proceedings, GRC Transactions, Vol.46, (2022).
3. Judawisastra, L. H., Sausan, S., Horne, R. N.: Analytical, Experimental and Numerical Development Update on Inflow Measurement in Geothermal Wells from Chloride Concentration. Proceedings, 8th Indonesia International Geothermal Convention & Exhibition, (2022).
4. Judawisastra, L. H., Sausan, S., Su, J., Horne, R. N.: Development Update on Chloride-based Inflow Measurement in Fractured Enhanced Geothermal Systems (EGS) Wells. Proceedings 48th Workshop on Geothermal Reservoir Engineering, Stanford University, Stanford, California (2023).

5. Sausan, S., Judawisastra, L. H., Su, J., Horne, R. N.: Chloride-based Wireline Tool for Measuring Feed Zone Inflow in Enhanced Geothermal Systems (EGS) Wells: Experimental, Numerical, and Data-driven Updates, Proceedings Geothermal Rising Conference (GRC) Transactions, Vol. 47, (2023).
  6. Judawisastra, L.: Laboratory Experiment on Fracture Inflow Characterization Using Chloride Concentration in Geothermal Wells. MS Thesis Report, Department of Energy Resources Engineering, Stanford University, (2023).
  7. Sausan, S.: Investigating Fluid Flow Behavior in Enhanced Geothermal System (EGS) Wells: Numerical and Data-Driven Approaches. MS Thesis Report, Department of Energy Resources Engineering, Stanford University, (2023)
  8. Sausan, S., Marshall, B. H., Su, J., Schneider, M. B., Wright, A. A., Horne, R. N.: Updates on the Development of Chloride-based Wireline Tool for Measuring Feed Zone Inflow in Enhanced Geothermal Systems (EGS) Wells. Proceedings 49th Workshop on Geothermal Reservoir Engineering, Stanford University, Stanford, California (2024).
  9. Hartung, M. B.: Laboratory Characterization of Geothermal Fractures Using Chloride Concentration. MS Thesis Report, Department of Energy Science & Engineering, Stanford University, (2024).
  10. Schneider, M., Sausan, S., Hartung, M., Horne, R., Cochrane, A., Su, J., Wright, A., Myers, T., Pope, J., and Tafoya, J.: Chloride-based Wireline Tool for Measuring Fracture Inflow in Enhanced Geothermal Systems (EGS) Wells: Field Deployment Updates. Geothermal Rising Conference Transactions, Vol. 48, (2024).
  11. Sausan, S., Schneider, M. B., Marshall, B. H., Horne, R. N., Cochrane, A. H., Su, J., Wright, A. A., Myers, T., Pope, J., Tafoya, J.: Field Deployment Updates on Geochemistry-based Wireline Tool to Characterize Fractures in Enhanced Geothermal Systems (EGS) Wells. Proceedings 50th Workshop on Geothermal Reservoir Engineering, Stanford University, Stanford, California (2025).
-